THERMAL RADIATIVE PROPERTIES OF MICRO/NANOSTRUCTURED PLASMONIC METAMATERIALS INCLUDING TWO-DIMENSIONAL MATERIALS

A Dissertation
Presented to
The Academic Faculty

by

Bo Zhao

In Partial Fulfillment
of the Requirements for the Degree
Doctor of Philosophy in the
George W. Woodruff School of Mechanical Engineering

Georgia Institute of Technology
December 2016

THERMAL RADIATIVE PROPERTIES OF MICRO/NANOSTRUCTURED PLASMONIC METAMATERIALS INCLUDING TWO-DIMENSIONAL MATERIALS

Approved by:

Dr. Zhuomin Zhang, Advisor
George W. Woodruff School of Mechanical Engineering
Georgia Institute of Technology

Dr. Wenshan Cai
School of Electrical and Computer Engineering
Georgia Institute of Technology

Dr. Peter Hesketh
George W. Woodruff School of Mechanical Engineering
Georgia Institute of Technology

Dr. Andrew Peterson
School of Electrical and Computer Engineering
Georgia Institute of Technology

Dr. Satish Kumar
George W. Woodruff School of Mechanical Engineering
Georgia Institute of Technology

Date Approved: October 20, 2016

Dedicated to my family

ACKNOWLEDGEMENTS

My experience at Georgia Tech has been a wonderful journey of learning, sharing, and growing. I would like to give my sincerest appreciation to my advisor, Dr. Zhuomin Zhang, for his tutorship, guidance, and encouragement in my research career and daily life. During the most difficult times, he gave me his strong support I needed to move on. The inspiring conversations, insightful suggestions, and valuable discussions we had during my Ph.D. career will be my lifelong treasure. Without him, this dissertation would have never been possible.

I would like to extend my gratitude to my committee members: Dr. Peter Hesketh, Dr. Satish Kumar, Dr. Wenshan Cai, and Dr. Andrew Peterson. I would like to thank Dr. Hesketh for his encouraging and valuable comments on my work, and Dr. Peterson for his knowledgeable lectures and discussions on electromagnetics that helped me develop the computational program in this work. I would like to thank Dr. Kumar for his suggestions and support, especially on my career development. I would also like to thank Dr. Cai for the questions, guidance, encouragement, and support he gave me on my research and future career. A special recognition to him for his excellent book on metamaterial from which I learned so much.

Gratitude is extended to the Nanoscale Radiation Heat Transfer Group. In particular, I would like to thank Dr. Liping Wang, Dr. Xiaojia Wang, Dr. Andrew McNamara, Dr. Trevor Bright, Dr. Zihao Zhang, Dr. Yong Shuai, Dr. Atsushi Sakurai, Dr. Junming Zhao, Dr. Qiang Cheng, Dr. Han Wang, Dr. Jesse Watjen, Dr. Xianglei Liu, Peiyan Yang, Eric Tervo, and Zhaolong Wang for the help, discussions, and collaborations during my Ph.D. study. In particular, I would like to thank Dr. Liping Wang for the tutoring

and Dr. Xiaojia Wang for her helping hand at the beginning year when I first came to Atlanta. I thank Dr. Xianglei Liu for fruitful collaborations and enlightening discussions. Appreciation is extended to Dr. Jesse Watjen, for the delightful and joyful interactions in daily life and active collaborations on experimental research. I thank all my friends at Georgia Tech for their help over the past years.

I would also like to thank NSF and DOE for the financial support. Finally, I want to express my sincere gratefulness to my family, especially Jerome, who have always been there with endless love and support. I feel truly fortunate and blessed.

TABLE OF CONTENTS

LIST OF TABLES

LIST OF FIGURES

LIST OF SYMBOLS AND ABBREVIATIONS

A	area, m^2
b	slit width, m
C	capacitance, F
c'	numerical factor
c_0	speed of light in vacuum, 299 792 458 m s^{-1}
DE	diffraction efficiency
d	thickness or gap distance, m
$\mathbf{E}$	electric field, V m^{-1}
e	elementary charge, 1.6×10^{-19} C
$\mathbf{H}$	magnetic field, A m^{-1}
h	height, m
$\hbar$	the reduced Planck constant, 1.055×10^{-34} J s
i	$\sqrt{-1}$
J	current density, A m^{-2}
$\mathbf{J}$	electric current density vector, A m^{-2}
j	jth layer
LC	inductor-capacitor
L_m	inductance of two parallel strips, H
L	inductance, H
l	length, m; resonance order
$\mathbf{k}$	wavevector, m^{-1}
k	magnitude of wavevector, m^{-1}
k_B	the Boltzmann constant, 1.381×10^{-23} J K^{-1}
MP	magnetic polariton
m	order

n	refractive index or order
P	power, W
p	distance, m; order
q	heat flux, W m^{-2}
RCWA	rigorous coupled-wave analysis
R	reflectance; resistance, Ω
$\mathbf{r}$	spatial vector, m
r	reflection coefficient; length, m
SPP	surface plasmon polariton
s	length, m
TE	transverse electric
TM	transverse magnetic
TPV	thermophotovoltaic
T	spectral-directional transmittance; temperature, K
t	transmission coefficient; length, m
V	volume, m^3; voltage, V
v	speed, m s^{-1}
WA	Wood's anomaly
w	width, m; local power dissipation density, W m^{-3}
x,y,z	space coordinate, m
Z	impedance, Ω

Greek symbols

α	spectral-directional absorptance
β	parallel wavevector component, m^{-1}; angle, rad
$\boldsymbol{\gamma}$	variable, V m^{-1}
γ	scattering rate, rad s^{-1}

δ	penetration depth, m
ε	relative permittivity (dielectric function)
ε'	real part of relative permittivity
ε''	imaginary part of relative permittivity
ε_0	electric permittivity of vacuum, 8.854×10^{-12} F/m
ε_∞	high-frequency constant in the dielectric function
ε'_λ	spectral-directional emissivity
Θ	mean energy of the Planck oscillator, J
θ	zenith (polar) angle, rad
κ	extinction coefficient
Λ	period, m
λ	wavelength in vacuum, m
λ_R	resonance wavelength, m
μ	relative magnetic permeability; chemical potential of graphene, eV
μ_0	magnetic permeability of vacuum, $4\pi\times10^{-7}$ H m^{-1}
ν	wavenumber, cm^{-1}
ξ	photon tunneling probability
σ	electrical conductivity, S m^{-1}
σ_s	graphene sheet conductivity, S
τ	relaxation time, s
ϕ	azimuthal angle, rad
χ	variable, V m^{-1}
ψ	polarization angle, rad
ω	angular frequency, rad/s
ω_p	plasma frequency, rad/s

Superscripts

*	complex conjugate
i	incidence
inv	inverse
ord	ordinary
r	reflection
t	transmission

Subscripts

$\parallel$	out-of-plane or the *z*-direction
$\perp$	in-plane or the *x*- or *y*-direction
0	vacuum
1	medium 1
2	medium 2
A	asymptotic value
cond	conduction
D	Drude-like
disp	displacement
eff	effective
G	graphene
GSP	graphene surface plasmon
g	group velocity
I	interband
inc	incidence
i	incident
j	*j*th layer

k	kinetic
LO	longitudinal optical phonon mode
m,*n*	order
rib	ribbon
SP	surface plasmon
s,*p*	s- or p-polarization
sw	surface wave
TO	transverse optical phonon mode
tot	total

SUMMARY

Micro/nanoscale thermal radiation is of great importance in advanced energy systems, nanomanufacturing, local thermal management, and near-field imaging. It concerns both electromagnetic wave interactions with micro/nanostructured materials that could create unique far-field radiative properties as well as near-field radiative heat transfer between close objects. This dissertation explores the capability of micro/nanostructured plasmonic metamaterials and two-dimensional (2D) materials to control far- and near-field thermal radiation. The major goals are to (1) study the coherent far-field radiative properties of plasmonic metamaterials for thermal radiation control; (2) design unusual far-field thermal radiative properties by using the emerging 2D materials; (3) use 2D materials to enhance photon tunneling and near-field radiative heat transfer.

A 2D grating/thin-film periodic nanostructure is studied to utilize magnetic polaritons (MPs) and surface waves, including surface plasmon polaritons and Wood's anomaly, to create wavelength-selective thermal emission and improve the efficiency of thermophotovoltaics. Deep metallic gratings are investigated for their coherent radiative properties due to MPs in different wavelength ranges. The scalability of the MPs is scrutinized to reveal the role of kinetic inductance for resonances in nanometer and micrometer scale. The polarization dependence of the diffraction efficiency and radiative properties of anisotropic periodic surfaces is examined.

A graphene-covered deep metal grating is investigated where MPs in gratings couple with graphene. The coupled resonances are studied in visible and near-infrared range with an emphasis on the enhanced absorption in graphene. The plasmonic coupling between graphene ribbon array and metal gratings is explored in mid- and far-infrared. A

natural phononic hyperbolic 2D material, hexagonal boron nitride (hBN), is used with metal gratings to achieve perfect wavelength-selective absorption caused by coupling between hyperbolic phonon polaritons with MPs. Trapezoidal gratings made of hBN is also studied for its ability to support broadband perfect absorption. The directional hyperbolic phonon polaritons are inspected for its capability to create resonance absorption in resonators with different shapes.

The near-field heat transfer and photon tunneling between graphene, hBN films, and van der Waals heterostructures assembled by them are studied based on fluctuational electrodynamics. A hybrid polariton in the heterostructure, surface plasmon-phonon polariton, is discussed for its contribution to the near-field heat transfer. The effects of the thickness of hBN film, the chemical potential of graphene, as well as a second layer of graphene on the backside of the heterostructure, are investigated.

The results obtained from this thesis provide a better understanding of the radiative properties of various micro/nanostructured plasmonic metamaterials and 2D materials. The insights from combining metamaterials, micro/nanostructures with various 2D materials may open a new route to better control both near- and far-field thermal radiation. This dissertation can benefit a wide spectrum of applications with a desire of thermal radiation control, such as personal thermal management, radiative cooling, thermal imaging, solar energy harvesting, as well as thermophotovoltaics.

CHAPTER 1

INTRODUCTION

Thermal radiation originates from random fluctuations of the charges or atoms in matters. Because of this nature, radiation from a thermal source, such as an incandescent light bulb or the sun, is usually incoherent: It is broadband and weakly directional. However, at the beginning of 21st century, researchers found that the thermal radiation from a periodically patterned grating surface with a period smaller than the typical wavelength of the thermal radiation can be coherent over many wavelengths in a well-defined direction [1-3]. This finding initiated the adventure to explore new structured materials to control thermal radiation. Various subwavelength micro/nanostructure or electromagnetic metamaterials are proposed that can tailor optical and radiative properties both spectrally and directionally [4-7].

Metamaterials are artificially structured materials that can control and manipulate wave propagations such as light, phonons, and sound. The ability comes from the unit structures that are typically smaller than the wavelength of the interacting waves. Similar to a material whose properties are governed by its constitute atoms or molecules, an metamaterial attains its properties from the unit structure, which acts like the ‘atom’ in metamaterials. Therefore, their properties can be very different from the constituent materials [6]. Electromagnetic metamaterials are the ones that can manipulate the propagation of photons. Although a lot of structures are categorized as electromagnetic metamaterials, they are typically periodic engineered subwavelength structures with optical or radiative properties beyond or have not yet been found in conventional materials.

Research in electromagnetic metamaterials becomes increasingly important for their widespread applications [3], such as photodetectors [8-10], band-pass filters and extraordinary optical transmission [11-14], negative refraction [15-19], anomalous reflection [20,21], cloaking [22-25], surface-enhanced Raman spectroscopy [26], medical therapy [27], thermophotovoltaics (TPV) emitter and absorber [28-31], photovoltaic and solar thermal technology [32-36], structural color printing [37], as well as radiative cooling [38].

Tailoring radiative properties using metamaterials generally relies on various resonance modes or surface waves in these micro/nanostructures. Among them are gratings that support surface phonon polaritons (SPhPs) [2] or surface plasmon polaritons (SPPs) [39-41], hyperbolic metamaterials that can empower hyperbolic modes and epsilon-near-zero modes [42-44], and metal/dielectric/metal structures and deep gratings that can enable magnetic polaritons (MPs) [45-47]. Meanwhile, various structures like photonic crystals [48] and nanowire arrays [49] are also extensively studied for their unique radiative properties. As one kind of electromagnetic metamaterials, plasmonic metamaterials exploit plasmons, a collective oscillation of charge carriers, to achieve coherent absorption or transmission. SPPs [39] and magnetic (plasmon) polaritons or MPs [50-52] are two types of resonances that enable these amazing applications. They are produced by coupling an incident photon with a plasmon inside the structure. Due to the ability to confine light in small scale, SPPs and MPs are able to create unique spectral and directional radiative properties that are desired in applications such as energy harvesting [1,3,53], imaging [54], bio and chemical sensing [55], and optoelectronics [56].

The thermal radiative properties of micro/nanostructured plasmonic metamaterials can be tremendously different because of MPs and SPPs compared to the radiate properties of the materials in the structures. In the past decades, SPPs and MPs have been studied in visible and microwave wavelength regions, but the role of MPs and SPPs in plasmonic metamaterials for thermal radiation control are still not fully understood.

On the other hand, emerging two-dimensional (2D) materials [57,58], including graphene [59-63], hexagonal boron nitride (hBN) [64], transition metal dichalcogenides [65], and recently emerged black phosphors [66], offer exciting new elements to construct micro/nanostructures with unique optical and radiative properties. Take graphene as an example. With a layer of carbon atoms arranged in a honeycomb lattice, graphene exhibits unique electronic, thermal, mechanical, and optical properties [67-69]. Since its discovery in 2004 [59], graphene has been extensively studied for potential applications in nanoelectronics, optoelectronics, plasmonics, transformation optics, and energy conversion [70-77]. Unlike in conventional solids where electrons are described by the Schrödinger equation, electrons in graphene are governed by the Dirac equation for 2D relativistic fermions [78]. It enables saturation absorption in the visible and near-infrared region, and low-loss, actively tunable surface plasmons in mid- and far-infrared region [59,61,67], which have been demonstrated for their ability to control thermal radiation [79]. In addition, natural hyperbolic 2D materials like hexagonal boron nitride (hBN) [60,64,80-82] can support plentiful phononic resonance modes that could be used to create unusual radiative properties. Moreover, since the 2D materials are easily assembled with nanostructures, the resonances in 2D materials and the above-mentioned resonances in

metamaterials could interact with each other and plentiful coupling effects may open more pathways to control radiative properties [83].

Accompanied with the far-field radiation are the thermal evanescent field that exponentially decays away from their surface. This field is also initiated by the fluctuations of charge carriers in matters. In the far field, only the propagating waves can survive and transfer power from one object to the other. It leads to an upper bound of radiative heat transfer, which is the well-known blackbody limit predicted by Planck's law. However, when two objects are brought within a distance that is comparable to the characterized thermal radiation wavelength, the evanescent waves of the two objects can couple and create pathways for photon energy to tunnel, leading to a radiative heat flux that can be orders of magnitude larger than the far-field blackbody limit. This is the so-called super-Planckian heat transfer and is of critical importance in applications such as energy harvesting, thermal management, near-field imaging, and local heating and cooling [84-88]. The large radiative heat flux in near field is attributed to the tunneling of evanescent waves or photon tunneling, and enhancing the near-field heat transfer process is essentially seeking ways to improve the photon tunneling effect [89,90]. It has been demonstrated that photon tunneling effect can be significantly enhanced when coupled resonance modes like SPPs and SPhPs are excited [91,92]. 2D materials like graphene have been investigated for enhancing near-field thermal radiation due to SPPs supported by graphene [93-95]. However, the possibility of using emerging 2D materials like hBN and heterostructures constructed by different 2D materials to enhance photon tunneling is still unclear. These 2D materials and heterostructures made of them may enable plentiful new resonance modes that have great potential to enhance the photon tunneling effect and near-field heat transfer.

Optical and radiative properties essentially describe the way that light interacts with matters [3]. When the characteristic length of the material or structure is much larger than the wavelength of light, the polarization and vector attributes of light may be neglected, and radiative properties in this scale can be solved using ray-tracing or geometrical optics [96,97]. However, to calculate the radiative properties of subwavelength periodic nano/microstructured surfaces, Maxwell's equations have to be solved to fully consider the vector and polarization characters of electromagnetic waves [98]. Recent advances in 2D materials put new challenges on the numerical modeling of the optical and radiative properties due to their atomically thin thickness and natural anisotropy, especially when 2D materials are combined with periodic nanostructures.

This dissertation aims to study the thermal radiative properties of micro/nanostructured plasmonic metamaterials and different 2D materials in both far and near field. The objectives are to (1) investigate the radiative properties of MPs and SPPs in micro/nanostructured plasmonic metamaterials and their practical applications, including the far-field radiative properties of SPPs and MPs in 2D nanostructures for thermophotovoltaics applications, the underlying mechanism of MPs in deep gratings, and polarization dependent radiative properties of anisotropic metamaterials; (2) explore the radiative properties of nanostructures made of 2D materials as well as the coupling effect between 2D materials, such as graphene and hBN, with deep metal gratings; and (3) study near-field heat transfer and photon tunneling between 2D materials and their heterostructures.

This dissertation is organized as follows. Chapter 2 presents a theoretical background of SPPs and MPs, dielectric function models of 2D materials and metals, as

well as calculations of near-field radiative heat transfer. Chapter 3 introduces an anisotropic rigorous-coupled wave analysis (RCWA) algorithm that can model multilayer periodic micro/nanostructures involving anisotropic materials. Chapter 4 discusses the radiative properties of SPPs and MPs in metal/dielectric/metal structures and deep gratings and the applications of tailored thermal radiative properties with an emphasis on thermophotovoltaics. The polarization dependence of the radiative properties of anisotropic metamaterials is also discussed. Chapter 5 presents the unusual radiative properties of hybrid structures constructed with plasmonic gratings and 2D materials including graphene and hBN. The underlying mechanisms are discussed with an emphasis on the coupling effect between 2D materials and gratings. Additionally, the radiative properties of a trapezoidal gratings made of hBN are discussed to demonstrate the uniqueness and potential of hyperbolic materials in controlling thermal radiation. In Chapter 6, the near-field heat transfer and enhanced photon tunneling between 2D materials and their heterostructures are demonstrated. Chapter 7 summarizes the findings and conclusions of this dissertation and recommends some future research directions.

CHAPTER 2

THEORETICAL BACKGROUND

This Chapter covers the basics of surface plasmons, magnetic polaritons, 2D materials, as well as near-field radiative heat transfer. In section 2.1, fundamentals of SPPs are discussed. The dispersion and field plots are illustrated with an example of a periodic grating. Section 2.2 introduces MPs and LC circuit models. MPs in deep metal gratings are used as an example. The features of MPs as well as the prediction method are covered. Section 2.3 presents the dielectric functions of 2D materials including graphene and hBN. Fundamentals of graphene surface plasmons and hyperbolic materials are discussed. Finally, in section 2.4, the chapter is concluded with an introduction of near-field radiation and essential equations to calculate photon tunneling probability.

2.1 Surface Plasmon Polaritons

Generally speaking, the reason for the unique optical and radiative properties of the micro/nanostructures is the excitation of various polaritons. Polaritons are quasiparticles resulting from strong coupling of electromagnetic waves with an electric or magnetic dipole-carrying excitation. One of such excitations is plasmons, which are quasiparticles associated with oscillations of plasma, i.e., a collection of charged particles inside materials. External electromagnetic waves can couple with surface plasmons (SPs), which is a collective oscillation of surface charges, to form a surface plasmon polariton or SPP [40,99]. SPPs have been intensively studied for applications in lithography [100], chemical and bio sensing [101], extraordinary optical transmission [99], and optical communication [102]. Upon the excitation of SPPs, the charges close to the surface are driven by the electric field

and oscillate back and forth intensively. The field of a SP is confined near the surface with the amplitude exponentially decaying away from the interface. Not only is a surface wave induced propagating along the interface with an amplitude exponentially decaying away from the interface [39,40,99,103-105], but the oscillation of charges also dissipates the electromagnetic energy into heat, creating strong absorption at the resonance frequency.

SPPs are non-radiative surface waves since the required wavevector is larger than the free space wavevector and they do not couple with propagating electromagnetic waves in vacuum [3]. This can be seen from the magnitude of the wavevector of the SPs on a metal-dielectric interface that is expressed as [3]

$$\left|\mathbf{k}_{\mathrm{SP}}\right| = k_0 \sqrt{\frac{\varepsilon_1 \varepsilon_2}{\varepsilon_1 + \varepsilon_2}} \tag{2.1}$$

where $k_0 = \omega / c_0$ is the magnitude of the wavevector in vacuum, and ε_1 and ε_2 here are the dielectric functions of the dielectric and metal, respectively. Note that Eq. (2.1) are for nonmagnetic materials and transverse magnetic waves (TM waves or p polarization). For transvers electric waves (TE waves or s polarization), the excitation of SPs requires a magnetic material with negative permeability. The wavevector of the electromagnetic waves must have a tangential component equal to $\mathbf{k}_{\mathrm{SP}}$ to excite SPPs. Since $\left|\mathbf{k}_{\mathrm{SP}}\right|$ is greater than k_0, high index prisms can be used to increase the wavevector of the incident waves so that SPs can couple with incident light to excite SPPs [3,39,106]. Another method is to take advantage of the diffracted light by periodic micro/nanostructures, as will be explained in the following.

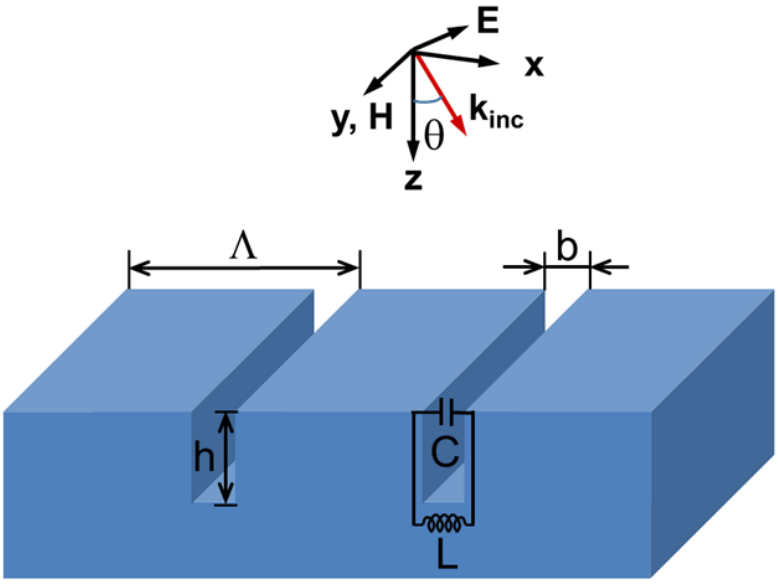

Figure 2.1 Schematic of the 1D grating with a period Λ, height or depth *h*, ridge width *w*, and trench width *b*. The equivalent LC circuit model is also shown with the capacitance *C* and inductance *L*. The wavevector $\mathbf{k}_{\mathbf{inc}}$ of the incident plane wave is in the *x*-*z* plane at an angle θ with respect to the *z*-axis.

Consider a one-dimensional (1D) silver (Ag) grating on a semi-infinite Ag substrate shown in Figure 2.1. The grating has a periodicity in the *x*-direction described by Λ = 1.7 μm. The grating height *h* = 0.1 μm and the trench width *b* = 0.595 μm. The incident plane wave is a TM wave with an oscillating magnetic field in the *y*-direction. The optical properties of Ag are obtained using a Drude model [3,96]

$$\varepsilon(\omega) = \varepsilon_\infty - \frac{\omega_p^2}{\omega(\omega + i\gamma)} \tag{2.2}$$

where the used parameters are plasma frequency $\omega_p = 1.39\times10^{16}$ rad/s , scattering rate $\gamma = 2.7\times10^{13}$ rad/s , and high-frequency constant $\varepsilon_\infty = 3.4$. For this 1D grating, the Bloch-Floquet condition, which will be explained more in the next Chapter, gives

$k_{x,m} = k_{x,\text{inc}} + 2\pi m/\Lambda$. Thus, the dispersion relation can be folded into the region for $k_x \le \pi/\Lambda$ and SPPs can be excited on a grating surface with propagating waves in air. Figure 2.2(a) shows the folded dispersion relation of SPPs for the given Ag grating. The intersections of the folded dispersion with the vertical axis identify the location where SPPs can be excited for a normal incidence, as shown in Figure 2.2(b). The excitation of surface polaritons is responsible for the dips in the reflectance, whose frequency locations agree well with predictions of the dispersion curves. Figure 2.3 illustrates an instantaneous field distribution of the SPP at $\nu = 5727$ cm^{-1} corresponding to the first reflectance dip in Figure 2.2(b). The colors represent direction and magnitude of the magnetic field and the arrows show the electric field. It is clear that this SPP is a surface wave with a wavelength that is equal to the period of the grating. Note that this surface wave is a standing wave, as will be discussed later in Chapter 5.

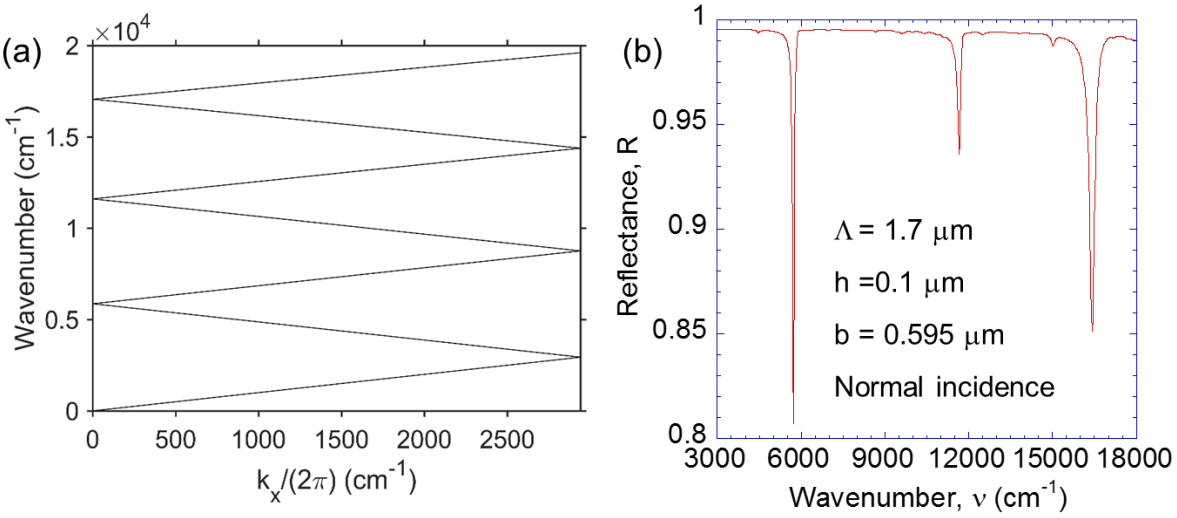

Figure 2.2 (a) Folded dispersion of SPPs for a Ag grating with Λ = 1.7 μm, h = 0.1 μm, and b = 0.595 μm. (b) Normal reflectance of TM waves for a Ag grating with the same geometries with (a).

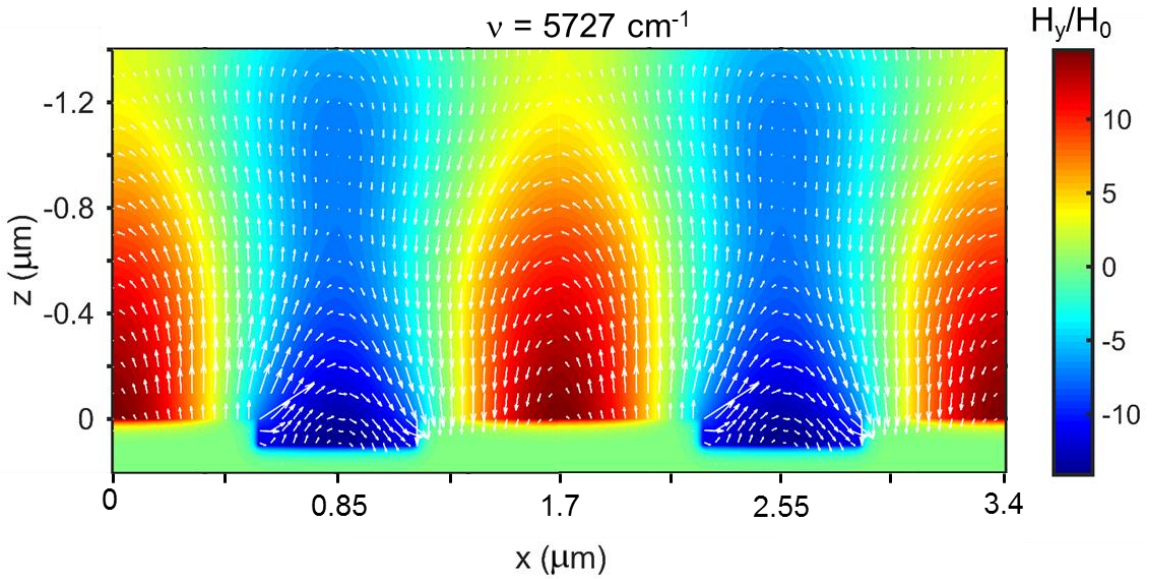

Figure 2.3 Instantaneous field distribution at the excitation of SPP at ν = 5727 cm^{-1} for a Ag grating with Λ = 1.7 μm, h = 0.1 μm, and b = 0.595 μm. The incident wave is at normal direction and TM-polarized. Color represents the relative magnetic field and the arrows show the electric field.

Note that ε_1 and ε_2 in Eq. (2.1) need to have different signs. For typical metal, since ε_2 has a negative real part whose magnitude is much larger than ε_1, the dispersion of SPP very close to the light line, which is $k_0 = \omega/c_0$. On the other hand, in some cases where ε_2 has a positive real part, another type of surface waves that has a similar dispersion called Wood's anomaly (WA) may be supported. Wood's anomaly occurs when a diffraction order shows up at the grazing angle, and its dispersion can be expressed as $\left|\mathbf{k}_{||,mn}\right| = k_0$, which is essentially the light line [14]. Both SPP and WA can be used to tailor the optical and radiative properties, as will be shown in Chapter 4.

2.2 Magnetic Polaritons and LC Circuit Model

According to Lenz's law, the time-varying magnetic field can create an oscillating current loop, which generates a magnetic field that opposes the driven magnetic field. A similar effect happens in micro/nano plasmonic metamaterials and causes resonances with a strong diamagnetic feature, which are referred to as magnetic polaritons in this work. Magnetic polaritons or MPs represent the strong coupling between the magnetic resonance inside a micro/nanostructure and the external electromagnetic waves [29,45,50,107-109]. This type of resonance was initially discovered and experimentally demonstrated in split-ring resonator [110], metal-rod pairs [111], and fishnet structures [112] that are possessed of negative permeability in microwave region. The resonance wavelength can be well explained by inductor-capacitor (LC) circuit models [113,114]. The following introduces the LC models that are used to predict the resonance wavelength of MP resonances.

Take the metal grating shown in Figure 2.1 as an example. When the incident wave has an oscillating magnetic field that is along the *y*-direction, i.e., TM waves, a current loop is induced around the trench and the equivalent LC circuit model shown in the inset can be used to predict the resonance condition. In the model, the dielectric (typically vacuum, with a positive ε') in the trenches serves as a capacitor while the surrounding material (typically metal, with a negative ε') acts as an inductor. Thus, to apply the LC models requires careful analysis of the inductance and capacitance in the circuit.

Since the walls on both sides of the groove are close to each other, mutual inductance L_{m} needs to be considered. It can be evaluated from the parallel-plate inductance formula and written as

$$L_{\mathrm{m}} = \mu_0 \frac{hb}{l} \tag{2.3}$$

where μ_0 is the permeability of vacuum and l is the length in the y-direction that can be set to unity for 1D gratings. The other contribution of the inductance comes from the kinetic energy of charges since charge current must accelerate to create the currents [113]. Thus, kinetic inductance L_k is introduced and added to the mutual inductance to form the total inductance in the circuit. It can be obtained from the frequency-dependent complex impedance of the metal:

$$Z_k \equiv R_k - i\omega L_k \tag{2.4}$$

where ω is the angular frequency. The impedance can be expressed as $Z_k = s/(\sigma A_{eff})$, where s is the total length of the current path in the metal and A_{eff} is the effective cross-section area of the induced electric current. For the deep grating structure, $s = 2h + b$ and $A_{eff} = \delta l$, where $\delta = \lambda / 2\pi\kappa$ is the penetration depth of electric field, in which κ is the extinction coefficient., $\sigma = -i\omega\varepsilon\varepsilon_0$ is the electrical conductivity. After some manipulations, the following expression can be obtained:

$$L_k = -\frac{2h+b}{\varepsilon_0\omega^2 l\delta}\frac{\varepsilon'}{\left(\varepsilon'^2 + \varepsilon''^2\right)} \tag{2.5}$$

The capacitance of the vacuum inside the trench can be approximated by

$$C = c'\varepsilon_0\frac{hl}{b} \tag{2.6}$$

where c' is a numerical factor between 0 and 1 accounting for the nonuniform charge distribution between the ridges of the grating [52,115]. Since resistance elements do not affect the resonance frequency, only the imaginary part of the total impedance of the LC circuit is considered and can be expressed by

$$Z_{\text{tot}} = i\omega\left(L_{\text{k}} + L_{\text{m}} - \frac{1}{\omega^2 C} \right) \tag{2.7}$$

By setting $Z_{\text{tot}} = 0$, one obtains the magnetic resonance wavelength as

$$\lambda_{\text{R}} = 2\pi c_0 \sqrt{\left(L_{\text{k}} + L_{\text{m}} \right) C} \tag{2.8}$$

where c_0 is the speed of light in vacuum. For other structures like slit array and metal-dielectric-metal structures [29,50], the inductance and capacitance in the circuits can be obtained in a similar way.

2.3 Graphene Surface Plasmons and Hyperbolic 2D Material hBN

The radiative properties of graphene can be described by its sheet conductivity σ_{s}, which consists of the contribution from intraband (Drude-like term) and interband transitions, i.e., $\sigma_{\text{s}} = \sigma_{\text{D}} + \sigma_{\text{I}}$, respectively [116]:

$$\sigma_{\text{D}} = \frac{i}{\omega + i/\tau} \frac{2e^2 k_{\text{B}} T}{\pi \hbar^2} \ln\left[2\cosh\left(\frac{\mu}{2k_{\text{B}} T} \right) \right] \tag{2.9}$$

and

$$\sigma_{\text{I}} = \frac{e^2}{4\hbar}\left[G\left(\frac{\hbar\omega}{2} \right) + i\frac{4\hbar\omega}{\pi} \int_0^\infty \frac{G(\xi) - G(\hbar\omega/2)}{(\hbar\omega)^2 - 4\xi^2} d\xi \right] \tag{2.10}$$

where $G(\xi) = \sinh(\xi/k_{\text{B}}T) \big/ \left[\cosh(\mu/k_{\text{B}}T) + \cosh(\xi/k_{\text{B}}T) \right]$. Here, e is the electron charge, $\hbar$ is the reduced Planck constant, μ is chemical potential, τ is relaxation time, T is temperature, and k_{B} is the Boltzmann constant. Since μ can be tuned by electrical gating or chemical doping, the optical properties of graphene can be actively tuned [59]. Figure 2.4 illustrates the effect of μ. As the plot shows, in the visible and near infrared, interband transitions dominate and graphene shows a wavelength-independent conductivity

$\sigma_s = \sigma_0 = e^2/(4\hbar)$, making graphene has no plasmonic response but has a wavelength-independent absorptivity of about 2.3% [67]. In the mid- and far- infrared region, graphene can support highly-confined SPs.

For a graphene sheet surrounded by media with dielectric functions ε_1 and ε_2 on each side of graphene, respectively, the dispersion of the graphene surface plasmon satisfies

$$\frac{\varepsilon_1}{\sqrt{k_{GSP}^2 - \varepsilon_1 k_0^2}} + \frac{\varepsilon_2}{\sqrt{k_{GSP}^2 - \varepsilon_2 k_0^2}} = -\frac{i\sigma_s}{\omega\varepsilon_0} \tag{2.11}$$

where k_{GSP} is the wavevector for the plasmon and ε_0 is the permittivity of vacuum. Figure 2.5 shows a schematic of graphene SPs. In the mid- and far-infrared region, the intraband transitions dominate and the conductivity can be approximately expressed in a Drude-like model [117]

$$\sigma_s = \frac{e^2\mu}{\pi\hbar^2}\frac{\tau}{1 - i\omega\tau} \tag{2.12}$$

In this wavelength region, if graphene is surrounded by vacuum, i.e. $\varepsilon_1 = \varepsilon_2 = 1$, the dispersion can be simplified as [70]

$$k_{GSP} = \frac{\omega}{c_0}\sqrt{\varepsilon_1 - \frac{4\varepsilon_0}{\sigma_s^2\mu_0}} \approx \frac{2i\omega\varepsilon_0}{\sigma_s} \tag{2.13}$$

where μ_0 is the vacuum permeability.

As a material that has a similar lattice structure with graphene, hBN has been used as an ideal dielectric substrate (bandgap ~5.9 eV) supporting high-quality graphene [118,119]. While 2D plasmonic materials and semiconductors have been studied extensively because of their potential applications in microelectronic, optoelectronic, and

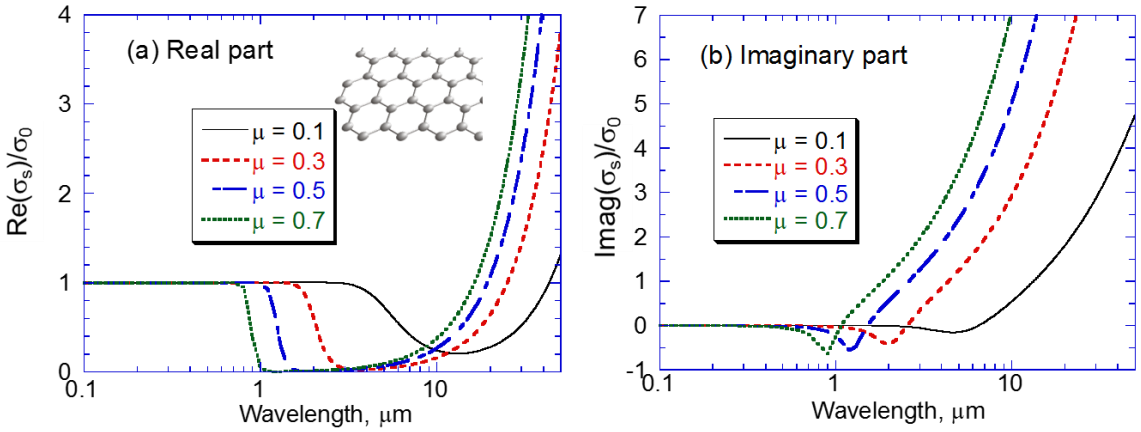

Figure 2.4 Sheet conductivity of graphene at different μ based on Eq. (2.9) and (2.10).

photonic devices [83], few studies have yet explored the radiative properties anisotropic phononic materials, especially for materials like hBN that is a hyperbolic material.

Hyperbolic materials refer to uniaxial materials whose axial and tangential permittivities have opposite signs. The isofrequency surfaces obey a hyperbolic shape instead of a closed sphere for common isotropic materials. Subsequently, these materials can support propagating modes with very large tangential wavevectors that possess unique applications in sub-wavelength imaging [120-122] and heat transfer [43,123-125]. The hyperbolic response of hBN is mainly caused by its optical phonon vibrations. The real

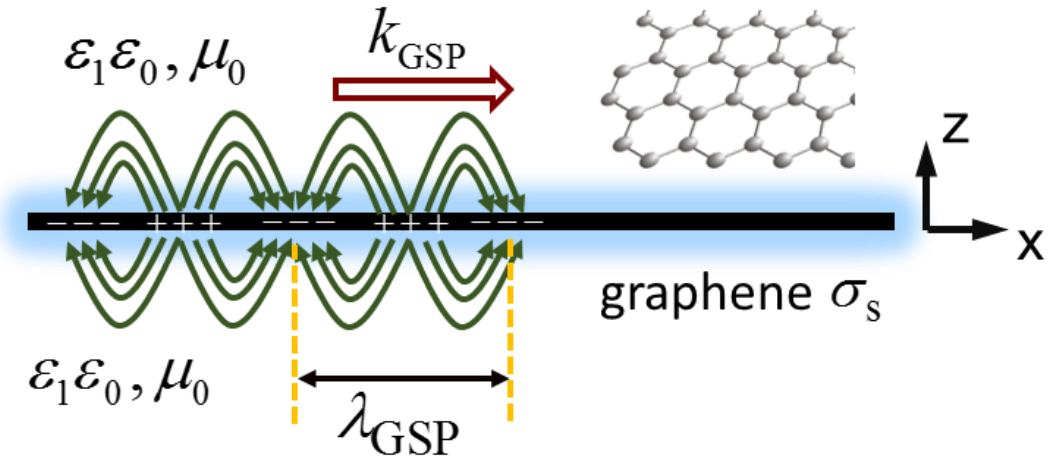

Figure 2.5 Schematic of graphene surface plasmon (GSP).

part of the dielectric function of hBN is shown in Figure 2.6. The two mid-infrared Reststrahlen bands due to the optical phonon modes are evident. The in-plane phonon modes ($\omega_{\mathrm{TO},\perp}$ = 1370 cm^{-1} and $\omega_{\mathrm{LO},\perp}$ = 1610 cm^{-1}) and out-of-plane phonon modes ($\omega_{\mathrm{TO},\|}$ = 780 cm^{-1} and $\omega_{\mathrm{LO},\|}$ = 830 cm^{-1}) contribute to the in-plane (**E** lies in the *x*-*y* plane, denoted by $\perp$) and out-of-plane (**E** parallel to the optical axis or the *z*-direction, denoted by $\|$) dielectric functions, respectively [82]:

$$\varepsilon_{\xi} = \varepsilon_{\infty,\xi}\left(1+\frac{\omega_{\mathrm{LO},\xi}^2-\omega_{\mathrm{TO},\xi}^2}{\omega_{\mathrm{TO},\xi}^2-i\gamma_{\xi}\omega-\omega^2}\right) \tag{2.14}$$

where ξ = $\|$, $\perp$. The other parameters used are $\varepsilon_{\infty,\|}=2.95$, $\gamma_{\|}=4$ cm^{-1}, $\varepsilon_{\infty,\perp}=4.87$, and $\gamma_{\perp}=5$ cm^{-1}. Since the damping coefficients γ are rather small, the dielectric function becomes negative between the TO and LO phonon modes, making the in-plane and out-of-plane dielectric functions of hBN possess opposite signs in either Reststrahlen band. In the lower Reststrahlen band, $\varepsilon_{\|}'=\varepsilon_z'<0$ and $\varepsilon_{\perp}'=\varepsilon_x'=\varepsilon_y'>0$, hBN has Type-I hyperbolicity, while in the upper Reststrahlen band, $\varepsilon_x'=\varepsilon_y'<0$ and $\varepsilon_z'>0$, hBN holds Type-II hyperbolicity [126]. Meanwhile, in the two regions with hyperbolicity, loss is negligibly small.

The hyperbolic regions allow propagating waves with unbounded wavevectors as can be seen from the isofrequency surface for an uniaxial medium with the optical axis in the *z*-direction [43]:

$$\frac{k_x^2+k_y^2}{\varepsilon_{\|}}+\frac{k_z^2}{\varepsilon_{\perp}}=\frac{\omega^2}{c_0^2} \tag{2.15}$$

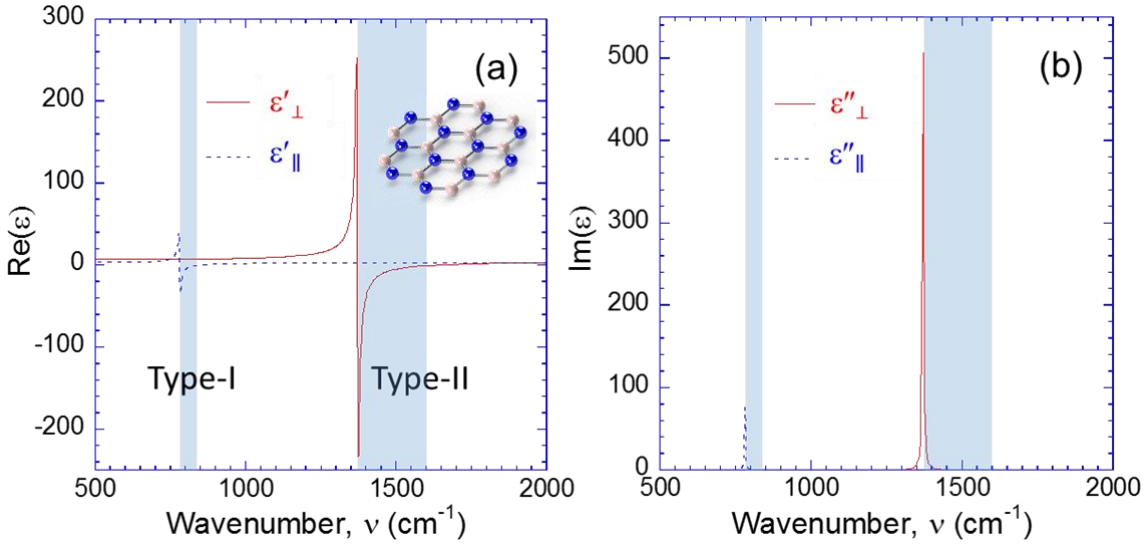

Figure 2.6 In-plane and out-of-plane dielectric function of hBN: (a) the real part and (b) the imaginary part. The two hyperbolic regions are shaded and marked with the corresponding type of hyperbolicity.

where $\mathbf{k} = \left(k_x, k_y, k_z\right)$ represents the allowed wavevector. If loss is neglected, in the frequency ranges that possess hyperbolicity, Eq. (2.15) becomes a hyperboloid and both k_x and k_z can theoretically be infinitely large. Note that Eq. (2.15) is for extraordinary waves or TM waves. For transverse electric or TE waves, the isofrequency surface becomes a sphere described by $|\mathbf{k}|^2 = \varepsilon_\perp \omega^2 / c_0^2$, thus hBN behaves the same as an isotropic material with the ordinary dielectric function.

2.4 Theory of Near-Field Radiative Heat Transfer

Based on the fluctuation-dissipation theorem, thermal emission is originated by the random motions of the charges inside a medium, which generates a fluctuating current. The correlation function of the thermally generated random currents for an anisotropic, local,

and nonmagnetic medium with time-reversal symmetry at local thermal equilibrium can be expressed as [3]

$$\left\langle J_i(\mathbf{r},\omega) J_k^*(\mathbf{r}',\omega') \right\rangle = \frac{4\omega\varepsilon_0}{\pi} \Theta(\omega,T) \varepsilon_{ik}''(\mathbf{r},\omega) \delta(\mathbf{r}-\mathbf{r}') \delta(\omega-\omega') \quad (2.16)$$

Here, subscript *i* and *k* denote vector components, ε_{ik}'' is the imaginary part of the dielectric tensor component. δ_{ik} is the Kronecker delta and $\delta(\mathbf{r}-\mathbf{r}')$ or $\delta(\omega-\omega')$ is the Dirac delta function indicating spatial or temporal incoherence, respectively. For an isotropic medium, $\varepsilon_{ik}'' = \varepsilon''\delta_{ik}$. The electric and magnetic field generated by the random currents can be obtained using the dyadic Green functions together with Eq. (2.16). The near-field radiative heat flux, which is the Poynting vector component perpendicular to the interface, between two media with temperature T_1 and T_2 is then given as [3]

$$q = \frac{1}{4\pi^2} \int_0^\infty \left[\Theta(\omega,T_1) - \Theta(\omega,T_2) \right] d\omega \int_0^\infty \xi(\omega,\beta)\, \beta d\beta \quad (2.17)$$

where $\Theta(\omega,T)$ is the average energy of Planck's oscillator, β designates the magnitude of the wavevector in the *x*-*y* plane, and $\xi(\omega,\beta)$ is the photon tunneling probability (also called energy transmission coefficient). ξ includes the contributions from both the transverse electric waves (TE wave or s-polarization) and transverse magnetic waves (TM wave or p-polarization) and can be expressed as [127]

$$\xi(\omega,\beta,\phi) = \begin{cases} \mathrm{Tr}\left[(\mathbf{I}-\mathbf{R}_2^\dagger\mathbf{R}_2)\mathbf{D}(\mathbf{I}-\mathbf{R}_1\mathbf{R}_1^\dagger)\mathbf{D}^\dagger \right], & \beta < k_0 \\ \mathrm{Tr}\left[(\mathbf{R}_2^\dagger-\mathbf{R}_2)\mathbf{D}(\mathbf{R}_1-\mathbf{R}_1^\dagger)\mathbf{D}^\dagger \right] e^{-2|k_{z0}|d}, & \beta > k_0 \end{cases} \quad (2.18)$$

Here k_{z0} is its z-component of wavevector in vacuum. $\mathbf{D} = \left(\mathbf{I} - \mathbf{R}_1 \mathbf{R}_2 e^{2ik_{z0}d} \right)^{-1}$ is a Fabry-Pérot type denominator representing the multiple reflections inside the vacuum cavity, and $\mathbf{R}_1$ and $\mathbf{R}_2$ are the 2 × 2 reflection coefficient matrices:

$$\mathbf{R}_{1,2} = \begin{bmatrix} r_{ss}^{(1,2)} & r_{sp}^{(1,2)} \\ r_{ps}^{(1,2)} & r_{pp}^{(1,2)} \end{bmatrix} \tag{2.19}$$

including both the co-polarization (r_{ss} and r_{pp}) and cross-polarization (r_{sp} and r_{ps}) components.

CHAPTER 3

TWO-DIMENSIONAL ANISOTROPIC RIGOROUS COUPLED-WAVE ANALYSIS

In this Chapter, a two-dimensional rigorous coupled-wave analysis is presented that can calculate radiative properties of multilayer periodic structures made of anisotropic materials. The core equations are presented with the steps of matrix manipulations that are used to solve the radiative properties and field distributions. The methodology to calculate the local power dissipation density are discussed. This chapter ends with a discussion on the convergence of the program.

Maxwell's equations describe the way electromagnetic waves propagate in a certain medium. Together with the constitutive relations from which the permittivity and permeability of the medium can be obtained, radiative properties can be attained by studying how light interacts with the medium. Numerical methods are usually used to simulate the radiative properties of periodic structures since analytical solutions are seldom available due to the complex geometries [98]. The most popular modeling methods may include the finite-difference time-domain (FDTD) or Yee's method [128,129], the finite element method (FEM) [130], and the rigorous-coupled wave analysis (RCWA) method [131].

FDTD is a time domain method that uses wideband sources and computes a wideband response in one run, whereas RCWA is a frequency domain method that has to calculate the system response for each frequency point. If a very narrow band response is of the interest, a very large number of timesteps may be required [130]. Meanwhile, the properties of the material, i.e. the permittivity and permeability, can be expediently

expressed as a function of the frequency in the frequency domain, but in the time domain it is more challenging since a convolution is implied [98]. FEM can be used in both time and frequency domain. All three methods are widely used. Commercial software such as Remcom's XFDTD and Lumerical's FDTD solutions, as well as a free-software package [132], are based on FDTD. COMSOL's RF Module and Ansoft's HFSS are examples that use FEM, while RCWA programs are also accessible online free of charge [133,134].

FDTD and FEM methods discretize the structure or computation domain with mesh or grid and numerically solve the quantity of interest associated with each element or cell. For structures with small dimensions like 2D materials, accrete simulation using FEM and FDTD may become very challenging and time-consuming since the dimension of the mesh needs to be very small in the out-of-plane direction, especially when structures with small characteristic lengths coexist with large structures, like the hybrid structures with 2D materials and micro/nanostructures. On the contrary, RCWA is a semi-analytical method that does not require a discretization of the structure. Instead, the electric or magnetic field in the structure are expressed as a Fourier series with the coefficients to be solved using boundary conditions. Since mesh is not needed, RCWA has advantages in modeling the structures that contain extremely small geometries.

RCWA has been widely used in modeling the radiative properties of periodic structures. However, most available RCWA algorithms are for isotropic materials only. Anisotropic RCWA has been studied by different researchers starting from the 1990s after the widely-used isotropic RCWA for one-dimensional (1D) grating was proposed in 1981 [131]. Glytsis and Gaylord [135] formulated RCWA for 1D anisotropic gratings, but the algorithm may have convergence issues for highly conducting metal gratings because of

the way that Fourier factorizations were calculated. Later, Li [136,137] reformulated the algorithm with the correct Fourier factorization rules. Continuous effort has been devoted and more general algorithms have been formulated to consider 2D arbitrary lattice configurations and permittivity tensor [138-140]. However, most of these works are intended to solve impressively general problems and thus are very complex and formidable to be implemented. The present study provides an easy-to-implement algorithm that allows the modeling of a 2D multilayered periodic structure made of biaxial materials with a diagonal permittivity tensor. In the following, an easy-to-implement algorithm to model a 2D multilayered periodic structure made of biaxial materials with a diagonal permittivity tensor are summarized. This algorithm is an extension of the public available RCWA code [134], which has been presented in other work [14,141-143]. It also serves as a theoretical background of the later sections since the resonance mechanisms are easier to be understood in the frequency domain.

The 2D anisotropic multilayered periodic structure is schematically shown in Figure 3.1. The periodicity is characterized by Λ_x and Λ_y, which are the periods in the *x*- and *y*-directions, respectively. Each layer in the structure can be either a grating or a continuous film by adjusting the lateral dimensions l_x and l_y, and its thickness is d_j. In the schematic, the first layer is a 2D grating and the rest are films. The medium where the wave is incident, the intermediate layers (total *N* layers), and the semi-infinite substrate can be categorized as Region I, II, and III, respectively, as indicated in the schematic. The incident medium with a dielectric function ε_{I} (refractive index n_{I}) is usually vacuum or lossless dielectric and set to be isotropic. The incident wave with an electric field $\mathbf{E}_{\mathrm{inc}}$ is assumed to be linearly polarized and with a unit magnitude. The plane of incidence

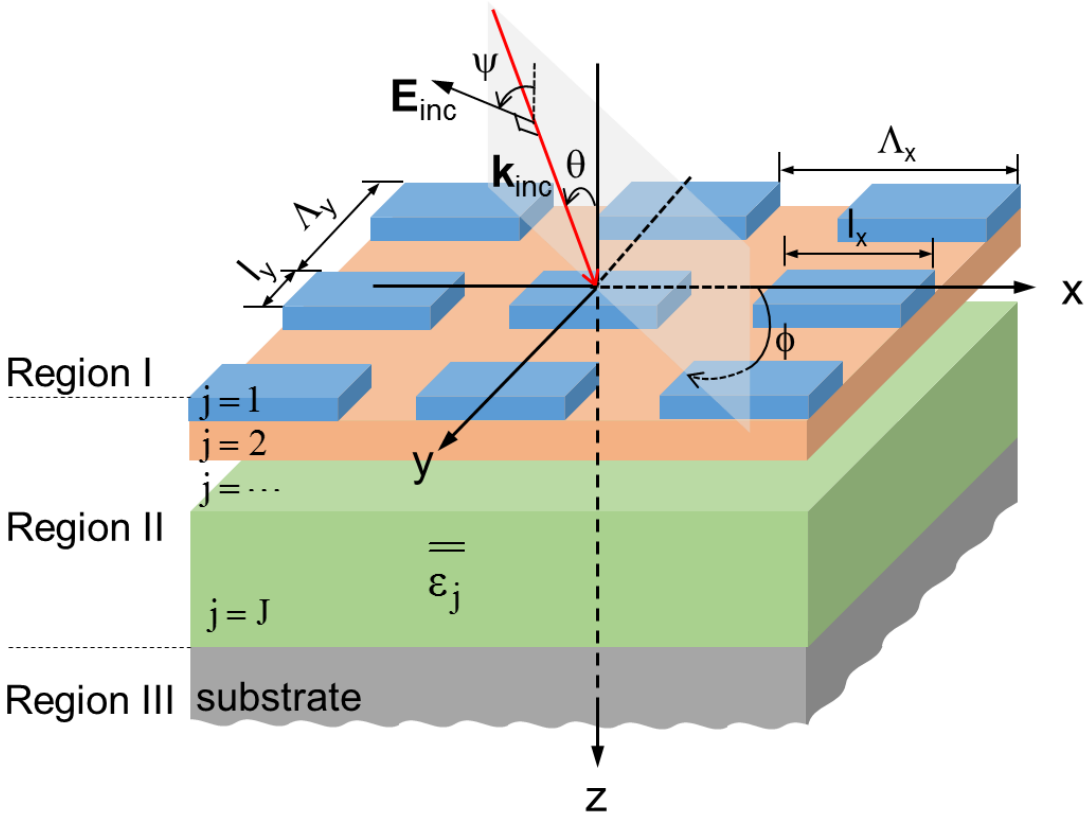

Figure 3.1 Illustration of the numerical model for general 2D periodic multilayer structures consisting of anisotropic materials.

indicated in transparent gray color is the plane determined by the *z*-axis and the incident wavevector $\mathbf{k}_{\text{inc}} = \left(k_{x,\text{inc}}, k_{y,\text{inc}}, k_{z,\text{inc}}\right)$. A polar angle θ (the angle between $\mathbf{k}_{\text{inc}}$ and the *z*-axis) and azimuthal angle ϕ (the angle between the *x*-axis and the plane of incidence) are used to depict the direction of $\mathbf{k}_{\text{inc}}$:

$$\begin{aligned} k_{x,\text{inc}} &= k_0 n_{\text{I}} \sin\theta\cos\phi \\ k_{y,\text{inc}} &= k_0 n_{\text{I}} \sin\theta\sin\phi \\ k_{z,\text{inc}} &= k_0 n_{\text{I}} \cos\theta \end{aligned} \tag{3.1}$$

where $k_0 = \omega/c_0$ is the wavevector (magnitude) in vacuum with c_0 being the speed of light in vacuum and ω being the angular frequency. Polarization angle ψ is defined as the angle

between the electric field and the plane of incidence. With these definition, $\mathbf{E}_{\text{inc}}$ can be written as

$$\begin{aligned}\mathbf{E}_{\text{inc}} = &\left(\cos\psi\cos\theta\cos\phi - \sin\psi\sin\phi\right)x \\ &+\left(\cos\psi\cos\theta\sin\phi + \sin\psi\cos\phi\right)y - \left(\cos\psi\sin\theta\right)\hat{z}\end{aligned} \tag{3.2}$$

Thus, a TE wave means $\psi = 90°$ and a TM wave means $\psi = 0°$. Since all the radiative properties concerned in this dissertation are spectral properties, the word "spectral" is omitted in the description of the radiative properties. According to Kirchhoff's law [3], the directional emittance is equal to the directional absorptance, which is one minus the directional-hemispherical reflectance if the substrate can be treated as opaque. This will be true for all the senarios considered in this dissertation. Therefore, $\varepsilon'_\lambda = \alpha'_\lambda = 1 - R$ for either TE- or TM-wave incidence [29]. The problem becomes how to numerically calculate the reflectance of the emitter structure for any given wavelength, angle of incidence, and polarization status.

In Region I, the electric field contains the incident and reflected fields and the expression is the same as the isotropic RCWA [144]:

$$\mathbf{E}_{\text{I}} = \mathbf{E}_{\text{inc}} \exp\left(ik_{x,\text{inc}}x + ik_{y,\text{inc}}y + ik_{z,\text{inc}}z\right) + \sum_m \sum_n \mathbf{E}^{\text{r}}_{mn} \exp\left(ik_{x,m}x + ik_{y,n}y - ik^{r}_{z,mn}z\right) \tag{3.3}$$

The time-harmonic term, $\exp(-i\omega t)$, is omitted hereafter. The second term on the right-hand side is the reflected wave. $\mathbf{E}^{\text{r}}_{mn}$ is the complex amplitude of the (m, n) order reflected wave and its transverse wavevector components are determined by the Bloch-Floquet condition [135]:

$$k_{x,m} = k_{x,\text{inc}} + m\frac{2\pi}{\Lambda_x}$$
$$k_{y,n} = k_{y,\text{inc}} + n\frac{2\pi}{\Lambda_y} \tag{3.4}$$

where m and n denote the diffraction orders in the x- and y-directions, respectively, and they can take both positive and negative numbers. The z-components of the wavevector is

$$k_{z,mn}^{r} = \begin{cases} \sqrt{k_{\text{I}}^2 - k_{x,m}^2 - k_{y,n}^2} & , \quad \varepsilon_{\text{I}} k_0^2 \geq k_{x,m}^2 + k_{y,n}^2 \\ i\sqrt{k_{x,m}^2 + k_{y,n}^2 - k_{\text{I}}^2} & , \quad \varepsilon_{\text{I}} k_0^2 < k_{x,m}^2 + k_{y,n}^2 \end{cases} \tag{3.5}$$

In each layer of Region II, both the electromagnetic field and the dielectric function are expressed as Fourier series based on the periods in the x- and y-directions. The materials of each layer are assumed to be nonmagnetic and thus the dielectric function of the layer can be described by a location-dependent permittivity tensor

$$\overline{\overline{\varepsilon}}_j(x,y) = \begin{pmatrix} \varepsilon_{j,x} & 0 & 0 \\ 0 & \varepsilon_{j,y} & 0 \\ 0 & 0 & \varepsilon_{j,z} \end{pmatrix} \tag{3.6}$$

where j is the number of the layer in the structure ranging from 1 to J. Generally, $\varepsilon = \varepsilon' + i\varepsilon''$ is a complex number with ε' and ε'' being its real and imaginary part, respectively. The electric and magnetic field can be expressed as

$$\mathbf{E}_{\text{II}} = \sum_m \sum_n \boldsymbol{\chi}_{mn}(z) \exp\left(ik_{x,m}x + ik_{y,n}y\right)$$
$$\mathbf{H}_{\text{II}} = i\sqrt{\frac{\varepsilon_0}{\mu_0}} \sum_m \sum_n \boldsymbol{\gamma}_{mn}(z) \exp\left(ik_{x,m}x + ik_{y,n}y\right) \tag{3.7}$$

The unknowns $\boldsymbol{\chi}_{mn}(z)$ and $\boldsymbol{\gamma}_{mn}(z)$ can be related by the following equations based on the Maxwell's equations, $\nabla\times\mathbf{E}_{\mathrm{II}}-i\omega\mu_0\mathbf{H}_{\mathrm{II}}=0$ and $\nabla\times\mathbf{H}_{\mathrm{II}}+i\omega\varepsilon_0\overline{\overline{\varepsilon}}\mathbf{E}_{\mathrm{II}}=0$, where μ_0 and ε_0 are the permeability and permittivity of vacuum, respectively:

$$\begin{aligned}
\frac{\partial\chi_{y,mn}}{\partial z}&=\frac{k_{y,n}}{k_0}\sum_p\sum_q\left(\frac{k_{x,p}\gamma_{y,pq}-k_{y,q}\gamma_{x,pq}}{\varepsilon^{\mathrm{ord}}_{z,m-p,n-q}}\right)+k_0\gamma_{x,mn}\\
\frac{\partial\chi_{x,mn}}{\partial z}&=\frac{k_{x,m}}{k_0}\sum_p\sum_q\frac{\left(k_{x,p}\gamma_{y,pq}-k_{y,q}\gamma_{x,pq}\right)}{\varepsilon^{\mathrm{ord}}_{z,m-p,n-q}}-k_0\gamma_{y,mn}\\
\frac{\partial\gamma_{y,mn}}{\partial z}&=\frac{k_{y,n}}{k_0}\left(k_{x,m}\chi_{y,mn}-k_{y,n}\chi_{x,mn}\right)-\sum_p\sum_q\frac{k_0\chi_{x,pq}}{\varepsilon^{\mathrm{inv}}_{x,m\text{-}p,n\text{-}q}}\\
\frac{\partial\gamma_{x,mn}}{\partial z}&=\frac{k_{x,m}}{k_0}\left(k_{x,m}\chi_{y,mn}-k_{y,n}\chi_{x,mn}\right)-\sum_p\sum_q\frac{k_0\chi_{y,pq}}{\varepsilon^{\mathrm{inv}}_{y,m-p,n-q}}
\end{aligned}\tag{3.8}$$

where p and q are two integers. The superscripts ord and inv indicate the coefficients of the Fourier series for the component of $\overline{\overline{\varepsilon}}$ and its inverse, respectively [142]:

$$\varepsilon^{\mathrm{ord}}_{m,n}=\frac{1}{\Lambda_x}\frac{1}{\Lambda_y}\int_0^{\Lambda_x}\int_0^{\Lambda_y}\varepsilon(x,y)\exp\left[-i\left(\frac{2m\pi}{\Lambda_x}x+\frac{2n\pi}{\Lambda_y}y\right)\right]\mathrm{d}x\mathrm{d}y \tag{3.9}$$

and

$$\varepsilon^{\mathrm{inv}}_{m,n}=\frac{1}{\Lambda_x}\frac{1}{\Lambda_y}\int_0^{\Lambda_x}\int_0^{\Lambda_y}\frac{1}{\varepsilon(x,y)}\exp\left[-i\left(\frac{2m\pi}{\Lambda_x}x+\frac{2n\pi}{\Lambda_y}y\right)\right]\mathrm{d}x\mathrm{d}y \tag{3.10}$$

These formulas work for each directional component. The inverse of the dielectric function is used for the sake of fast convergence of the algorithm according to the Fourier factorization rule [136]. Note that different dielectric function components are used in Eq. (3.8) because of the anisotropy of the material. When all three components of the dielectric tensor are equal, Eq. (3.8) degenerates to the isotropic scenario presented in [142].

Equation (3.8) can be written in a matrix form

$$\frac{1}{k_0}\begin{bmatrix} \dfrac{\partial \mathbf{X}^Y}{\partial z} \\ \dfrac{\partial \mathbf{X}^X}{\partial z} \\ \dfrac{\partial \mathbf{\Gamma}^Y}{\partial z} \\ \dfrac{\partial \mathbf{\Gamma}^X}{\partial z} \end{bmatrix} = \begin{bmatrix} \mathbf{0} & \mathbf{P} \\ \mathbf{Q} & \mathbf{0} \end{bmatrix} \begin{bmatrix} \mathbf{X}^Y \\ \mathbf{X}^X \\ \mathbf{\Gamma}^Y \\ \mathbf{\Gamma}^X \end{bmatrix} \tag{3.11}$$

where

$$\mathbf{P} = \begin{bmatrix} \mathbf{K}^Y \mathbf{E}_z^{-1} \mathbf{K}^X & \mathbf{I} - \mathbf{K}^Y \mathbf{E}_z^{-1} \mathbf{K}^Y \\ \mathbf{K}^X \mathbf{E}_z^{-1} \mathbf{K}^X - \mathbf{I} & -\mathbf{K}^X \mathbf{E}_z^{-1} \mathbf{K}^Y \end{bmatrix} \tag{3.12}$$

and

$$\mathbf{Q} = \begin{bmatrix} \mathbf{K}^Y \mathbf{K}^X & \alpha \mathbf{M}_x^{-1} + (1-\alpha)\mathbf{E}_x - \mathbf{K}^Y \mathbf{K}^Y \\ \mathbf{K}^X \mathbf{K}^X - \alpha \mathbf{E}_y - (1-\alpha)\mathbf{M}_y^{-1} & -\mathbf{K}^X \mathbf{K}^Y \end{bmatrix} \tag{3.13}$$

and α is a real positive number between 0 and 1 used for fast convergence in 2D structure calculations. 1 or 0 is used respectively for structures with a periodicity only in the *x* or *y*-direction. $\mathbf{K}^X$ and $\mathbf{K}^Y$ are diagonal matrices. The equations can be further simplified as

$$\frac{1}{k_0^2}\begin{bmatrix} \dfrac{\partial^2 \mathbf{X}^Y}{\partial z^2} \\ \dfrac{\partial^2 \mathbf{X}^X}{\partial z^2} \end{bmatrix} = \mathbf{\Omega} \begin{bmatrix} \mathbf{X}^Y \\ \mathbf{X}^X \end{bmatrix} \tag{3.14}$$

where

$$\mathbf{\Omega}=\begin{bmatrix} \mathbf{K}^X\mathbf{K}^X & \mathbf{K}^Y\left\{\mathbf{E}_z^{-1}\mathbf{K}^X\begin{bmatrix}\alpha\mathbf{M}_x^{-1}\\ +(1-\alpha)\mathbf{E}_x\end{bmatrix}\right\} \\ +\mathbf{D}\left[\alpha\mathbf{E}_y+(1-\alpha)\mathbf{M}_y^{-1}\right] & \begin{bmatrix}\\ -\mathbf{K}^X\end{bmatrix} \\ \mathbf{K}^X\left\{\mathbf{E}_z^{-1}\mathbf{K}^Y\begin{bmatrix}\alpha\mathbf{E}_y\\ +(1-\alpha)\mathbf{M}_y^{-1}\end{bmatrix}\right\} & \mathbf{K}^Y\mathbf{K}^Y+\mathbf{B}\left[\alpha\mathbf{M}_x^{-1}+(1-\alpha)\mathbf{E}_x\right] \\ \begin{bmatrix}\\ -\mathbf{K}^Y\end{bmatrix} & \end{bmatrix} \tag{3.15}$$

with two matrices defined as $\mathbf{D}=\mathbf{K}^Y\mathbf{E}_z^{-1}\mathbf{K}^Y-\mathbf{I}$ and $\mathbf{B}=\mathbf{K}^X\mathbf{E}_z^{-1}\mathbf{K}^X-\mathbf{I}$. The coupled-wave equations of above-mentioned equation are solved by finding the eigenvalues and eigenvectors of $\mathbf{\Omega}$:

$$\chi_{y,mn}(z)=\sum_{l=1}^{2MN}W_{mn,1}^{j}\left[C_l^{j+}\mathrm{e}^{k_0\xi_l(z-d)}+C_l^{j-}\mathrm{e}^{-k_0\xi_l z}\right] \tag{3.16}$$

$$\chi_{x,mn}(z)=\sum_{l=1}^{2MN}W_{mn,2}^{j}\left[C_l^{j+}\mathrm{e}^{k_0\xi_l(z-d)}+C_l^{j-}\mathrm{e}^{-k_0\xi_l z}\right] \tag{3.17}$$

where $M = 2m_{\max}+1$ and $N = 2n_{\max}+1$ are the total number of diffraction orders with $m_{\max}$ and $n_{\max}$ being the maximum diffraction order in the x and y directions, respectively. $\mathbf{W}$ is the eigenvector matrix of $\mathbf{\Omega}$, and ξ's are the corresponding eigenvalues. Meanwhile,

$$\gamma_{y,mn}(z)=\sum_{l=1}^{2MN}V_{mn,1}^{j}\left[C_l^{j+}\mathrm{e}^{k_0\xi_l(z-d)}-C_l^{j-}\mathrm{e}^{-k_0\xi_l z}\right] \tag{3.18}$$

$$\gamma_{x,mn}(z)=\sum_{l=1}^{2MN}V_{mn,2}^{j}\left[C_l^{j+}\mathrm{e}^{k_0\xi_l(z-d)}-C_l^{j-}\mathrm{e}^{-k_0\xi_l z}\right] \tag{3.19}$$

where $\mathbf{V}_1=\left(\mathbf{Q}_{11}\mathbf{W}_1+\mathbf{Q}_{12}\mathbf{W}_2\right)\mathbf{\Xi}^{-1}$ and $\mathbf{V}_2=\left(\mathbf{Q}_{21}\mathbf{W}_1+\mathbf{Q}_{22}\mathbf{W}_2\right)\mathbf{\Xi}^{-1}$. $\mathbf{\Xi}$ is a diagonal matrix with ξ's being its diagonal terms. The subscript numbers associated with the matrices indicate submatrices that are used for convenience. The first number is associated with the division of rows while the second number, if present, is associated with the

division of columns.

The substrate (Region III) in general can be a biaxial medium. A transmitted plane wave (forward-propagating wave) in this region with an in-plane wavevector $\left(k_{x,m},\ k_{y,n}\right)$ can have two different $k_{z,mn}^{t}$. If the electric field is $\mathbf{E}_{mn}^{t}=\left(E_{x,mn}^{t},E_{y,mn}^{t},E_{z,mn}^{t}\right)$, then based on the Maxwell's equation [145], one obtains

$$\begin{pmatrix} \varepsilon_{\mathrm{III},x}k_0^2-k_{y,n}^2-\left(k_{z,mn}^{t}\right)^2 & k_{x,m}k_{y,n} & k_{x,m}k_{z,mn}^{t} \\ k_{x,m}k_{y,n} & \varepsilon_{\mathrm{III},y}k_0^2-k_{x,m}^2-\left(k_{z,mn}^{t}\right)^2 & k_{y,n}k_{z,mn}^{t} \\ k_{x,m}k_{z,mn}^{t} & k_{y,n}k_{z,mn}^{t} & \varepsilon_{\mathrm{III},z}k_0^2-k_{x,m}^2-k_{y,n}^2 \end{pmatrix}\begin{pmatrix} E_{x,mn}^{t} \\ E_{y,mn}^{t} \\ E_{z,mn}^{t} \end{pmatrix}=0 \tag{3.20}$$

To have nontrivial plane-wave solutions, the determination of the matrix has to be zero and four solutions can be obtained. Two solutions of $k_{z,mn}^{t}$ that correspond to the two forward propagating waves [137] are used to express the electric field in Region III as

$$\mathbf{E}_{\mathrm{III}}=\sum_{m}\sum_{n}\sum_{\sigma=\mathrm{o},e}E_{\sigma,mn}^{t}\mathbf{p}_{\sigma,mn}\exp\left(ik_{x,m}x+ik_{y,n}y+ik_{\sigma,z,mn}^{t}z\right) \tag{3.21}$$

in which

$$\mathbf{p}_{\sigma,mn}=N_{\sigma,mn}\begin{pmatrix} \left(\varepsilon_{\mathrm{III},y}k_0^2-k_{x,m}^2-\left(k_{\sigma,z,mn}^{t}\right)^2\right)\left(k_0^2\varepsilon_{\mathrm{III},z}-k_{x,m}^2-k_{y,n}^2\right)-k_{y,n}^2\left(k_{\sigma,z,mn}^{t}\right)^2 \\ k_{x,m}k_{y,n}\left(k_{\sigma,z,mn}^{t}\right)^2-k_{x,m}k_{y,n}\left(\varepsilon_{\mathrm{III},z}k_0^2-k_{x,m}^2-k_{y,n}^2\right) \\ k_{x,m}k_{y,n}^2k_{\sigma,z,mn}^{t}-k_{x,m}k_{\sigma,z,mn}^{t}\left(\varepsilon_{\mathrm{III},y}k_0^2-k_{x,m}^2-\left(k_{\sigma,z,mn}^{t}\right)^2\right) \end{pmatrix} \tag{3.22}$$

is the polarization vector for the electric field with diffraction order (m, n) and σ is the index for the two forward propagating waves. For uniaxial medium, o and e correspond to the ordinary and extraordinary waves, respectively. Note that $N_{\sigma,mn}$ is a coefficient that normalizes $\mathbf{p}_{\sigma,mn}$. The magnetic field can be obtained based on Maxwell's equations.

The boundary conditions require that the tangential components of the electric and magnetic field are equal. At $z = 0$, one obtains

$$\delta_{m0}\delta_{n0}(\cos\psi\cos\theta\sin\phi+\sin\psi\cos\phi)+R_{mn,y}=\sum_{l=1}^{2MN}W_{mn,1}^{1}(C_l^{1+}e^{-k_0\xi_l d_1}+C_l^{1-}) \tag{3.23}$$

$$\delta_{m0}\delta_{n0}(\cos\psi\cos\theta\cos\phi-\sin\psi\sin\phi)+R_{mn,x}=\sum_{l=1}^{2MN}W_{mn,2}^{1}(C_l^{1+}e^{-k_0\xi_l d_1}+C_l^{1-}) \tag{3.24}$$

$$\begin{aligned}&\frac{k_{\mathrm{z,inc}}}{k_0}\delta_{m0}\delta_{n0}(\cos\psi\cos\theta\cos\phi-\sin\psi\sin\phi)+\frac{k_{x,\mathrm{inc}}}{k_0}\delta_{m0}\delta_{n0}(\cos\psi\sin\theta)\\&-\frac{k^r_{z,mn}}{k_0}R_{mn,x}-\frac{k_{x,m}}{k_0}\left(\frac{R_{mn,x}k_{x,m}+R_{mn,y}k_{y,n}}{k^r_{z,mn}}\right)=i\sum_{l=1}^{2MN}V_{mn,1}^{1}(C_l^{1+}e^{-k_0\xi_l d_1}-C_l^{1-})\end{aligned} \tag{3.25}$$

and

$$\begin{aligned}&-\frac{k_{y,\mathrm{inc}}}{k_0}\delta_{m0}\delta_{n0}(\cos\psi\sin\theta)-\frac{k_{z,\mathrm{inc}}}{k_0}\delta_{m0}\delta_{n0}(\cos\psi\cos\theta\sin\phi+\sin\psi\cos\phi)\\&+\frac{k_{y,n}}{k_0}\left(\frac{R_{mn,x}k_{x,m}+R_{mn,y}k_{y,n}}{k^r_{z,mn}}\right)+\frac{k^r_{z,mn}}{k_0}R_{mn,y}=i\sum_{l=1}^{2MN}V_{mn,2}^{1}(C_l^{1+}e^{-k_0\xi_l d_1}-C_l^{1-})\end{aligned} \tag{3.26}$$

They correspond to $E_{\mathrm{I},y}=E_{1,y}$, $E_{\mathrm{I},x}=E_{1,x}$, $H_{\mathrm{I},y}=H_{1,y}$, and $H_{\mathrm{I},x}=H_{1,x}$, respectively, and δ_{mn} is the Kronecker delta. They can be written in matrix form

$$\begin{bmatrix} \boldsymbol{\delta}_{\mathbf{m0}}\boldsymbol{\delta}_{\mathbf{n0}}(\cos\psi\cos\theta\sin\phi+\sin\psi\cos\phi) \\ \boldsymbol{\delta}_{\mathbf{m0}}\boldsymbol{\delta}_{\mathbf{n0}}(\cos\psi\cos\theta\cos\phi-\sin\psi\sin\phi) \\ \boldsymbol{\delta}_{\mathbf{m0}}\boldsymbol{\delta}_{\mathbf{n0}}[\frac{k_{z,\mathrm{inc}}}{k}(\cos\psi\cos\theta\cos\phi-\sin\psi\sin\phi)+\frac{k_{x,\mathrm{inc}}}{k}(\cos\psi\sin\theta)] \\ \boldsymbol{\delta}_{\mathbf{m0}}\boldsymbol{\delta}_{\mathbf{n0}}[-\frac{k_{y,\mathrm{inc}}}{k}(\cos\psi\sin\theta)-\frac{k_{z,\mathrm{inc}}}{k}(\cos\psi\cos\theta\sin\phi+\sin\psi\cos\phi)] \end{bmatrix}+$$

$$\begin{bmatrix} \mathbf{I} & \mathbf{0} \\ \mathbf{0} & \mathbf{I} \\ -\dfrac{\mathbf{K_x K_y}}{\mathbf{K_{Iz}}} & -\dfrac{\mathbf{K_x^2+K_{Iz}^2}}{\mathbf{K_{Iz}}} \\ \dfrac{\mathbf{K_y^2+K_{Iz}^2}}{\mathbf{K_{Iz}}} & \dfrac{\mathbf{K_x K_y}}{\mathbf{K_{Iz}}} \end{bmatrix}\begin{bmatrix} \mathbf{R_y} \\ \mathbf{R_x} \end{bmatrix}=\begin{bmatrix} \mathbf{W}_{1,1}\mathbf{X}_1 & \mathbf{W}_{1,1} \\ \mathbf{W}_{1,2}\mathbf{X}_1 & \mathbf{W}_{1,2} \\ i\mathbf{V}_{1,1}\mathbf{X}_1 & -i\mathbf{V}_{1,1} \\ i\mathbf{V}_{1,2}\mathbf{X}_1 & -i\mathbf{V}_{1,2} \end{bmatrix}\begin{bmatrix} \mathbf{C}_1^+ \\ \mathbf{C}_1^- \end{bmatrix} \tag{3.27}$$

where $\mathbf{X}_j$ is a diagonal matrix with diagonal elements equal to $\exp\left(-k_0\xi_l d_j\right)$. Similarly, we can match the boundary conditions at the interfaces between j and j +1 layer, with j varying between 1 to J – 1. In matrix form, we obtain

$$\begin{bmatrix} \mathbf{W}_{j,1} & \mathbf{W}_{j,1}\mathbf{X}_j \\ \mathbf{W}_{j,2} & \mathbf{W}_{j,2}\mathbf{X}_j \\ i\mathbf{V}_{j,1} & -i\mathbf{V}_{j,1}\mathbf{X}_j \\ i\mathbf{V}_{j,2} & -i\mathbf{V}_{j,2}\mathbf{X}_j \end{bmatrix}\begin{bmatrix} \mathbf{C}_j^+ \\ \mathbf{C}_j^- \end{bmatrix}=\begin{bmatrix} \mathbf{W}_{j+1,1}\mathbf{X}_{j+1} & \mathbf{W}_{j+1,1} \\ \mathbf{W}_{j+1,2}\mathbf{X}_{j+1} & \mathbf{W}_{j+1,2} \\ i\mathbf{V}_{j+1,1}\mathbf{X}_{j+1} & -i\mathbf{V}_{j+1,1} \\ i\mathbf{V}_{j+1,2}\mathbf{X}_{j+1} & -i\mathbf{V}_{j+1,2} \end{bmatrix}\begin{bmatrix} \mathbf{C}_{j+1}^+ \\ \mathbf{C}_{j+1}^- \end{bmatrix} \tag{3.28}$$

At $z = \sum_{j=1}^{J} d_j$, one obtains

$$\begin{bmatrix} \mathbf{W}_{J,1} & \mathbf{W}_{J,1}\mathbf{X}_J \\ \mathbf{W}_{J,2} & \mathbf{W}_{J,2}\mathbf{X}_J \\ i\mathbf{V}_{J,1} & -i\mathbf{V}_{J,1}\mathbf{X}_J \\ i\mathbf{V}_{J,2} & -i\mathbf{V}_{J,2}\mathbf{X}_J \end{bmatrix}\begin{bmatrix} \mathbf{C}_J^+ \\ \mathbf{C}_J^- \end{bmatrix}=\begin{bmatrix} \mathbf{p_{o,y}} & \mathbf{p_{e,y}} \\ \mathbf{p_{o,x}} & \mathbf{p_{e,x}} \\ \mathbf{K_{III,z}^o p_{o,x}}-\mathbf{K_x p_{o,z}} & \mathbf{K_{III,z}^e p_{e,x}}-\mathbf{K_x p_{e,z}} \\ \mathbf{K_y p_{o,z}}-\mathbf{K_{III,z}^o p_{o,y}} & \mathbf{K_y p_{e,z}}-\mathbf{K_{III,z}^e p_{e,y}} \end{bmatrix}\begin{bmatrix} \mathbf{T}_o \\ \mathbf{T}_e \end{bmatrix} \tag{3.29}$$

Using these equations, the unknowns can be solve through matrix manipulations. If we define

$$\begin{bmatrix}\mathbf{f}_{J+1}\\ \mathbf{g}_{J+1}\end{bmatrix}=\begin{bmatrix}\mathbf{p_{o,y}} & \mathbf{p_{e,y}}\\ \mathbf{p_{o,x}} & \mathbf{p_{e,x}}\\ \mathbf{K^{o}_{IIIz}p_{o,x}-K_{x}p_{o,z}} & \mathbf{K^{e}_{IIIz}p_{e,x}-K_{x}p_{e,z}}\\ \mathbf{K_{y}p_{o,z}-K^{o}_{IIIz}p_{o,y}} & \mathbf{K_{y}p_{e,z}-K^{e}_{IIIz}p_{e,y}}\end{bmatrix} \tag{3.30}$$

and

$$\mathbf{O}_J=\begin{bmatrix}\mathbf{W}_{J,1} & \mathbf{W}_{J,1}\\ \mathbf{W}_{J,2} & \mathbf{W}_{J,2}\\ i\mathbf{V}_{J,1} & -i\mathbf{V}_{J,1}\\ i\mathbf{V}_{J,2} & -i\mathbf{V}_{J,2}\end{bmatrix} \tag{3.31}$$

so that

$$\begin{bmatrix}\mathbf{W}_{J,1} & \mathbf{W}_{J,1}\mathbf{X}_J\\ \mathbf{W}_{J,2} & \mathbf{W}_{J,2}\mathbf{X}_J\\ i\mathbf{V}_{J,1} & -i\mathbf{V}_{J,1}\mathbf{X}_J\\ i\mathbf{V}_{J,2} & -i\mathbf{V}_{J,2}\mathbf{X}_J\end{bmatrix}=\mathbf{O}_J\begin{bmatrix}\mathbf{I} & \mathbf{0}\\ \mathbf{0} & \mathbf{X}_J\end{bmatrix} \tag{3.32}$$

Thus,

$$\begin{bmatrix}\mathbf{C}_J^{+}\\ \mathbf{C}_J^{-}\end{bmatrix}=\begin{bmatrix}\mathbf{W}_{J,1} & \mathbf{W}_{J,1}\mathbf{X}_J\\ \mathbf{W}_{J,2} & \mathbf{W}_{J,2}\mathbf{X}_J\\ i\mathbf{V}_{J,1} & -i\mathbf{V}_{J,1}\mathbf{X}_J\\ i\mathbf{V}_{J,2} & -i\mathbf{V}_{J,2}\mathbf{X}_J\end{bmatrix}^{-1}\begin{bmatrix}\mathbf{f}_{J+1}\\ \mathbf{g}_{J+1}\end{bmatrix}\begin{bmatrix}\mathbf{T}_o\\ \mathbf{T}_e\end{bmatrix}=\begin{bmatrix}\mathbf{I} & \mathbf{0}\\ \mathbf{0} & \mathbf{X}_J\end{bmatrix}^{-1}\mathbf{O}_J^{-1}\begin{bmatrix}\mathbf{f}_{J+1}\\ \mathbf{g}_{J+1}\end{bmatrix}\mathbf{T} \tag{3.33}$$

where $\mathbf{T}=\begin{bmatrix}\mathbf{T}_o & \mathbf{T}_e\end{bmatrix}^{\mathrm{T}}$. If we define

$$\begin{bmatrix}\mathbf{a}_J\\ \mathbf{b}_J\end{bmatrix}=\mathbf{O}_J^{-1}\begin{bmatrix}\mathbf{f}_{J+1}\\ \mathbf{g}_{J+1}\end{bmatrix} \tag{3.34}$$

and

$$\mathbf{T}=\mathbf{b}_J^{-1}\mathbf{X}_J\mathbf{T}_J \tag{3.35}$$

then we can obtain

$$\begin{bmatrix}\mathbf{C}_J^+\\ \mathbf{C}_J^-\end{bmatrix}=\begin{bmatrix}\mathbf{I} & \mathbf{0}\\ \mathbf{0} & \mathbf{X}_J\end{bmatrix}^{-1}\begin{bmatrix}\mathbf{a}_J\\ \mathbf{b}_J\end{bmatrix}\mathbf{b}_J^{-1}\mathbf{X}_J\mathbf{T}_J=\begin{bmatrix}\mathbf{a}_J\mathbf{b}_J^{-1}\mathbf{X}_\mathbf{A}\\ \mathbf{I}\end{bmatrix}\mathbf{T}_J \tag{3.36}$$

Substitute this matrix equation to the right-hand-side of Eq. (3.28), we have

$$\begin{bmatrix}\mathbf{W}_{J,1}\mathbf{X}_J & \mathbf{W}_{J,1}\\ \mathbf{W}_{J,2}\mathbf{X}_J & \mathbf{W}_{J,2}\\ i\mathbf{V}_{J,1}\mathbf{X}_J & -i\mathbf{V}_{J,1}\\ i\mathbf{V}_{J,2}\mathbf{X}_J & -i\mathbf{V}_{J,2}\end{bmatrix}\begin{bmatrix}\mathbf{C}_J^+\\ \mathbf{C}_J^-\end{bmatrix}=\begin{bmatrix}\mathbf{W}_{J,1}\mathbf{X}_J & \mathbf{W}_{J,1}\\ \mathbf{W}_{J,2}\mathbf{X}_J & \mathbf{W}_{J,2}\\ i\mathbf{V}_{J,1}\mathbf{X}_J & -i\mathbf{V}_{J,1}\\ i\mathbf{V}_{J,2}\mathbf{X}_J & -i\mathbf{V}_{J,2}\end{bmatrix}\begin{bmatrix}\mathbf{a}_J\mathbf{b}_J^{-1}\mathbf{X}_J\\ \mathbf{I}\end{bmatrix}\mathbf{T}_J=\begin{bmatrix}\mathbf{f}_J\\ \mathbf{g}_J\end{bmatrix}\mathbf{T}_J \tag{3.37}$$

Therefore,

$$\begin{bmatrix}\mathbf{W}_{J-1,1} & \mathbf{W}_{J-1,1}\mathbf{X}_{J-1}\\ \mathbf{W}_{J-1,2} & \mathbf{W}_{J-1,2}\mathbf{X}_{J-1}\\ i\mathbf{V}_{J-1,1} & -i\mathbf{V}_{J-1,1}\mathbf{X}_{J-1}\\ i\mathbf{V}_{J-1,2} & -i\mathbf{V}_{J-1,2}\mathbf{X}_{J-1}\end{bmatrix}\begin{bmatrix}\mathbf{C}_{J-1}^+\\ \mathbf{C}_{J-1}^-\end{bmatrix}=\begin{bmatrix}\mathbf{f}_J\\ \mathbf{g}_J\end{bmatrix}\mathbf{T}_J \tag{3.38}$$

where

$$\begin{bmatrix}\mathbf{f}_J\\ \mathbf{g}_J\end{bmatrix}=\begin{bmatrix}\mathbf{W}_{J,1}\mathbf{X}_J & \mathbf{W}_{J,1}\\ \mathbf{W}_{J,2}\mathbf{X}_J & \mathbf{W}_{J,2}\\ i\mathbf{V}_{J,1}\mathbf{X}_J & -i\mathbf{V}_{J,1}\\ i\mathbf{V}_{J,2}\mathbf{X}_J & -i\mathbf{V}_{J,2}\end{bmatrix}\begin{bmatrix}\mathbf{a}_J\mathbf{b}_J^{-1}\mathbf{X}_J\\ \mathbf{I}\end{bmatrix}=\begin{bmatrix}\mathbf{W}_{J,1}(\mathbf{I}+\mathbf{X}_J\mathbf{a}_J\mathbf{b}_J^{-1}\mathbf{X}_J)\\ \mathbf{W}_{J,2}(\mathbf{I}+\mathbf{X}_J\mathbf{a}_J\mathbf{b}_J^{-1}\mathbf{X}_J)\\ i\mathbf{V}_{J,1}(-\mathbf{I}+\mathbf{X}_J\mathbf{a}_J\mathbf{b}_J^{-1}\mathbf{X}_J)\\ i\mathbf{V}_{J,2}(-\mathbf{I}+\mathbf{X}_J\mathbf{a}_J\mathbf{b}_J^{-1}\mathbf{X}_J)\end{bmatrix} \tag{3.39}$$

This matrix equation has the same form with the last set matrix of equation; therefore we can follow the same procedure and finally get a matrix equation for **R** and $\mathbf{T}_1$:

$$\begin{bmatrix} \boldsymbol{\delta_{m0}\delta_{n0}}(\cos\psi\cos\theta\sin\phi+\sin\psi\cos\phi) \\ \boldsymbol{\delta_{m0}\delta_{n0}}(\cos\psi\cos\theta\cos\phi-\sin\psi\sin\phi) \\ \boldsymbol{\delta_{m0}\delta_{n0}}[\frac{k_{z,\mathrm{inc}}}{k}(\cos\psi\cos\theta\cos\phi-\sin\psi\sin\phi)+\frac{k_{x,\mathrm{inc}}}{k}(\cos\psi\sin\theta)] \\ \boldsymbol{\delta_{m0}\delta_{n0}}[-\frac{k_{y,\mathrm{inc}}}{k}(\cos\psi\sin\theta)-\frac{k_{z,\mathrm{inc}}}{k}(\cos\psi\cos\theta\sin\phi+\sin\psi\cos\phi)] \end{bmatrix} + \begin{bmatrix} \mathbf{I} & \mathbf{0} \\ \mathbf{0} & \mathbf{I} \\ -\frac{\mathbf{K_x K_y}}{\mathbf{K_{Iz}}} & -\frac{\mathbf{K_x^2+K_{Iz}^2}}{\mathbf{K_{Iz}}} \\ \frac{\mathbf{K_y^2+K_{Iz}^2}}{\mathbf{K_{Iz}}} & \frac{\mathbf{K_x K_y}}{\mathbf{K_{Iz}}} \end{bmatrix} \begin{bmatrix} \mathbf{R_y} \\ \mathbf{R_x} \end{bmatrix} = \begin{bmatrix} \mathbf{f_1} \\ \mathbf{g_1} \end{bmatrix} \mathbf{T_1} \tag{3.40}$$

We can rewrite this equation in a simpler form:

$$\begin{bmatrix} \mathbf{A_1} \\ \mathbf{A_2} \end{bmatrix} + \begin{bmatrix} \mathbf{B_1} \\ \mathbf{B_2} \end{bmatrix} [\mathbf{R}] = \begin{bmatrix} \mathbf{f_1} \\ \mathbf{g_1} \end{bmatrix} \mathbf{T_1} \tag{3.41}$$

Thus

$$\mathbf{T_1} = \left[\mathbf{g_1} - \mathbf{B_2 B_1^{-1} f_1} \right]^{-1} \left[\mathbf{A_2} - \mathbf{B_2 B_1^{-1} A_1} \right] \tag{3.42}$$

and

$$\mathbf{R} = \mathbf{B_1^{-1}} \left[\mathbf{f_1 T_1} - \mathbf{A_1} \right] \tag{3.43}$$

Note that **a**, **b**, and **O** can also be defined in each layer. Matrix T can be obtained by using Eq. (3.35)

$$\mathbf{T} = \mathbf{b}_J^{-1} \mathbf{X}_J \mathbf{b}_{J-1}^{-1} \mathbf{X}_{J-1} \cdots \mathbf{b}_1^{-1} \mathbf{X}_1 \mathbf{T}_1 \tag{3.44}$$

If the substrate is isotropic, which is true for the cases discussed in this work, the diffraction efficiency for each order of the reflected and transmitted waves can be expressed as

$$DE_{\mathrm{R},mn} = \left|r_{\mathrm{s},mn}\right|^2 \mathrm{Re}\left(\frac{k_{z,mn}^{r}}{k_{\mathrm{I}}\cos\theta}\right) + \left|r_{\mathrm{p},mn}\right|^2 \mathrm{Re}\left(\frac{k_{z,mn}^{r}}{k_{\mathrm{I}}\cos\theta}\right) \tag{3.45}$$

$$DE_{\mathrm{T},mn} = \left|t_{\mathrm{s},mn}\right|^2 \mathrm{Re}\left(\frac{k_{z,mn}^{t}}{k_{\mathrm{I}}\cos\theta}\right) + \left|t_{\mathrm{p},mn}\right|^2 \mathrm{Re}\left(\frac{k_{z,mn}^{t}\varepsilon_{\mathrm{I}}}{k_{\mathrm{I}}\varepsilon_{\mathrm{IV}}\cos\theta}\right) \tag{3.46}$$

where subscripts p and s represent the components for TM and TE waves with respect to the output plan known as the plane of diffraction [146]. It should be noted that since the beam output plane is different from the plane of incidence, in general the polarization status of the diffracted waves will be different from the incident wave. The directional-hemispherical reflectance and transmittance can be obtained by summing up the diffraction efficiencies for all orders:

$$R = \sum DE_{\mathrm{R},mn} \quad \text{and} \quad T = \sum DE_{\mathrm{T},mn} \tag{3.47}$$

The field distributions can be obtained as well.

To illustrate the local absorption profile inside the structure, the local power dissipation density in W/m^3 can be calculated based on [147]

$$w(x,y,z) = \frac{1}{2}\mathrm{Re}\left\{-i\omega\varepsilon_0 \overline{\overline{\varepsilon}}\mathbf{E}\bullet\mathbf{E}^*\right\} = \frac{1}{2}\varepsilon_0\omega\left(\varepsilon_x''\left|E_x\right|^2 + \varepsilon_y''\left|E_y\right|^2 + \varepsilon_z''\left|E_z\right|^2\right) \tag{3.48}$$

in which **E** is the complex electric field obtained from RCWA. The absorptance of a certain volume or layer can be calculated by the ratio of the absorption inside the volume over the incident power [148,149]:

$$\alpha = \frac{\iiint \omega(x,y,z)\,dV}{0.5c_0\varepsilon_0\left|\mathbf{E}_{\mathrm{inc}}\right|^2 A\cos\theta} \tag{3.49}$$

The denominator is the incident power on area A at a polar angle θ. Using Eq.(3.49), the absorptance inside a certain volume can be retrieved. The integration over the whole

structure yield the same absorptance with $1-R-T$.

The numerical accuracy of RCWA is dependent on the number of the diffraction orders and the Fourier expansion terms to synthesize the profile of the grating and they are related with each other. Referring m_{max} and n_{max} to the highest diffraction orders in the x and y directions, respectively, since $-m_{max} \le m \le +m_{max}$ and $-n_{max} \le n \le +n_{max}$, the total number of diffraction orders used in the calculation is $MN = (2m_{max} + 1)\times(2n_{max} + 1)$ and the Fourier expansion terms will be $(4m_{max} + 1)\times(4n_{max} + 1)$ in total. Thus, one can simply investigate the effects of the number of diffraction orders on the accuracy. As more orders are used, the accuracy improves, however, both the memory required and the processing time consumed in the calculation increase dramatically. Thus, a convergence check was conducted to determine the number of diffraction orders needed to yield accurate results using reasonable computational time and resource.

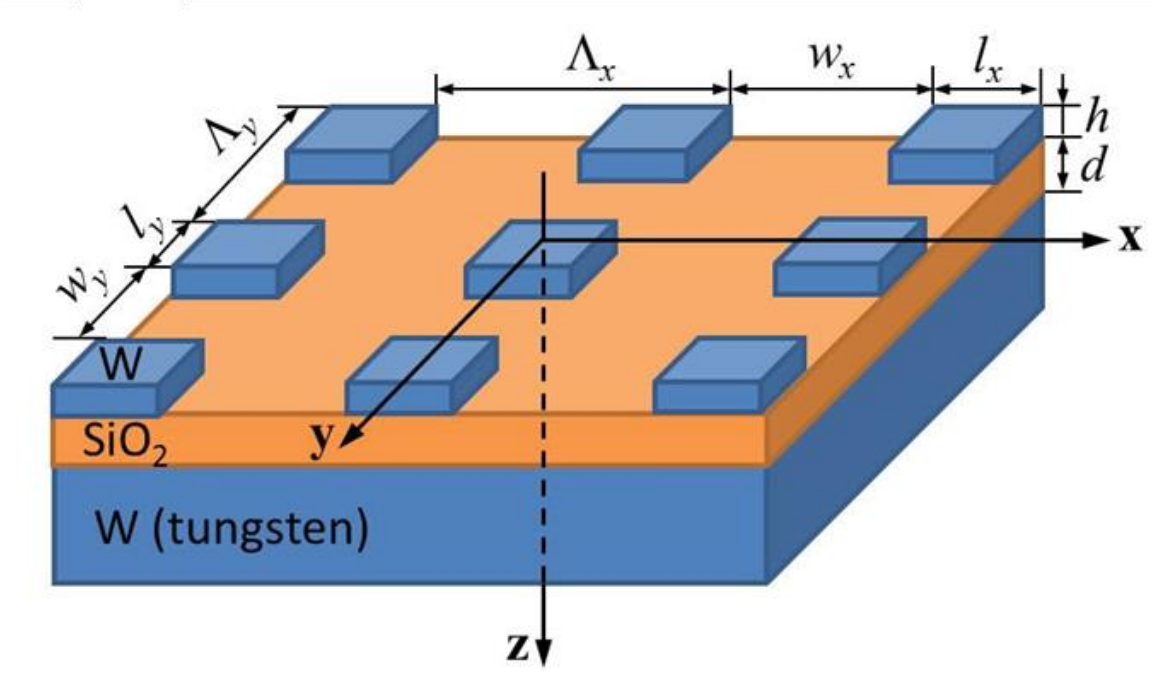

Figure 3.2 Schematic of the structure for the 2D grating/thin-film nanostructure.

In order to test the convergence and evaluate the computational cost, a test run is conducted. Figure 3.2 is a schematic of the 2D grating/thin-film structure considered. The grating is made of rectangular tungsten (W) patches whose lateral dimensions are l_x and l_y with a height h and periods Λ_x and Λ_y. The periodic arrays of patches are on a thin dielectric film SiO_2 of thickness d that is deposited on a tungsten substrate. In the test, the geometric parameters are fixed as follows: $\Lambda_x = \Lambda_y = 600$ nm , $l_x = l_y = 300$ nm , and $h = d = 60$ nm . The groove widths (i.e., the lateral distances between patches) are $w_x = w_y = 300$ nm . All the materials are isotropic and the dielectric functions are from [150].

Figure 3.3(a) shows the calculated normal emittance with different numbers of diffraction orders. In the calculation, $m_{\max}$ and $n_{\max}$ are set to be the same because same patterns are used along the x and y directions. It can be seen that, in the spectral region 0.3 μm $\leq \lambda \leq$ 2.0 μm, the emittance barely changes when the value of $m_{\max}$ is increased from

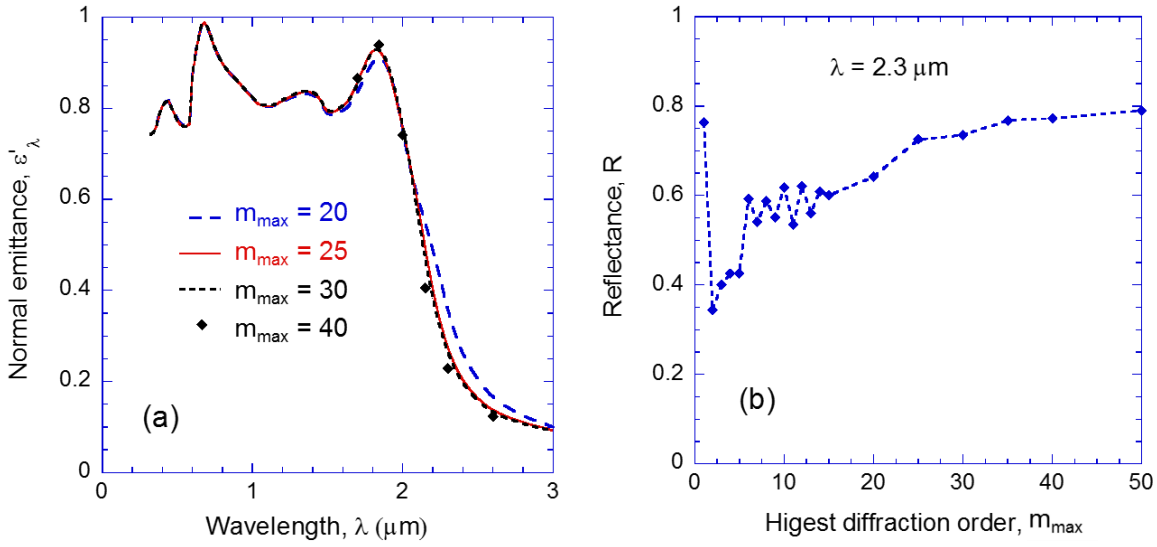

Figure 3.3 Convergence test results: (a) normal emittance spectra calculated with different orders; (b) reflectance at λ = 2.3 μm calculated with different orders.

25 to 30. Hence, m_{max} = 25 can be used for this structrue. However, for 2.0 μm < $\lambda \leq$ 3.0 μm, the calculated emittance is lower for m_{max} = 40 than m_{max} = 30, especially around λ = 2.3 μm. The reflectance at λ = 2.3 μm is shown in Figure 3.3(b) as a function of m_{max} to further study the numerical convergence. The reflectance changes within 3% when m_{max} is increased from 35 to 50. The processing time scales with m_{max} to the sixth power (m_{max}^6), and it takes 140 min to calculate each single point for m_{max} = 35 using a dual eight core XEON E5-2687W workstation. Hence, m_{max} = 35 may be used for 2.0 μm < $\lambda \leq$ 3.0 μm considering the time consumption. FDTD method is also used to verify the calculated results. For 1D structures, the computation time is much more less and on the order of seconds for each data point and m_{max} = 50 to 100 is typically sufficient. However, for highly conductive materials, more orders may be needed. Convergence test is conducted for all the structures studied in this dissertation.

CHAPTER 4

RADIATIVE PROPERTIES OF MICRO/NANOSTRUCTURED PLASMONIC METAMATERIALS

This chapter covers the radiative properties of micro/nanostructured plasmonic metamaterials. Section 4.1 focuses on a 2D grating/thin-film periodic nanostructure that can thermally excite MPs, SPPs, and Wood's Anomaly to create polarization-independent and wavelength-selective emittance for thermophotovoltaic applications. Section 4.2 studies the MPs in deep metal gratings. The role of kinetic inductance, the scalability of MPs, and the relationship between cavity modes and MPs are discussed. In the end, Section 4.3 investigates the polarization dependence of anisotropic periodic metamaterials. An L-shape structure is used as an example, where the excitation of MPs dependents on the polarization of the incidence.

4.1 Two-Dimensional Grating/Thin-Film Periodic Nanostructure

Thermophotovoltaic (TPV) systems convert thermal energy directly into electricity and hold promise in waste heat recovery, solar energy harvesting, and space applications [28,151,152]. A TPV system is environmentally-friendly and requires two key components: an emitter that gives out radiation by receiving thermal energy from various heating sources, and a TPV cell that can generate electricity by absorbing incident photons from the emitter. The main challenges for such a technique are low conversion efficiency and power generation. Near-field thermal radiation has been proposed for the enhancement of TPV power generation by bringing the emitter and receiver in close proximity [153,154]. However, there exist technological barriers for utilizing nanoscale TPV systems in the near

future. To improve efficiency of TPV systems, a more appealing way is to use a selective TPV emitter, which emits photons in a certain spectral range that matches with a specific TPV cell, because only when the photon energies are higher than the bandgap of the semiconductor material used in the TPV cell, the absorbed radiant energy can produce electron-hole pairs and thus generate electricity [3,28]. On the other hand, if the photon energies are too high, the conversion efficiency becomes too low. Usually, the emitter radiates energies in a broad spectral region and much of the energies are at longer wavelength with insufficient photon energies to produce electron-hole pairs. While band-pass filters may be used to improve the overall efficiency, this method is cumbersome and overheating of the filter may become problematic [155-157]. Therefore, wavelength-selective emitter is crucial to improve the conversion efficiency and power generation of TPV systems [32,158].

Micro/nanostructures of wide profile diversity are able to tailor thermal radiation by utilizing different physical mechanisms. Not only one-dimensional (1D) gratings [159,160], V-groove gratings [161], and photonic crystals [162-164], but also various two-dimensional (2D) micro/nanostructures have been investigated as promising selective TPV emitters. Heinzel et al. [165] manufactured 2D wavelength-selective emitters for the near-infrared spectral range, but the emittance exhibited directional dependence. Pralle et al. [166] fabricated 2D gold gratings that can emit over selected wavelengths in the mid-infrared. Similarly, Sai et al. [167-169] experimentally demonstrated the potentials of 2D concave tungsten surface gratings as TPV emitters whose emittance is enhanced by exciting cavity resonances. Chen and Tan [142] designed a 2D convex tungsten grating structures as TPV emitters. Multilayer micro/nanostructures have also been proposed to

control thermal radiation [170-178]. Recently, Wang and Zhang [29] used a 1D tungsten trilayer grating/thin-film nanostructure as a selective TPV emitter by taking advantage of MPs, which are resonant responses based on the excitation of induced current loops in the structure by incident electromagnetic waves [5,45,50,52,109,179]. The emittance can be enhanced in the desired spectral range by exciting MPs and SPPs [40,53,180-182].

An ideal TPV emitter should not only be wavelength-selective, but also desired to be polarization-insensitive so that high emittance for both polarizations can be achieved. However, since only TM waves can excite MPs and SPPs in the 1D grating/thin-film configuration, application of the emitter is somewhat limited. Here, a 2D trilayer structure is proposed as a wavelength-selective and polarization-insensitive TPV emitter. The structure is the same as the one shown in Figure 3.2. The grating is made of rectangular tungsten (W) patches whose lateral dimensions are l_x and l_y with a height h and periods Λ_x and Λ_y. The periodic arrays of patches are on a thin dielectric film SiO_2 of thickness d that is deposited on a tungsten substrate. The geometric parameters are fixed as follows: $\Lambda_x = \Lambda_y = 600$ nm, $l_x = l_y = 300$ nm, and $h = d = 60$ nm.

Figure 4.1 compares the normal emittance spectra calculated for the 2D structure and for the 1D grating/thin-film structure discussed in Ref. [29] for both TE and TM waves. The radiative properties are calculated by RCWA and the orders are chosen based on the previous convergence test. The emittance spectrum for plain tungsten is also shown to help explain some of the peaks observed in the nanostructures. The emittance spectrum matches well with the $In_{0.2}Ga_{0.8}Sb$ p-n junction TPV cell, which has a bandgap λ_g around 2.1 μm [28]. As mentioned previously, a higher emittance at $\lambda < \lambda_g$ and lower emittance

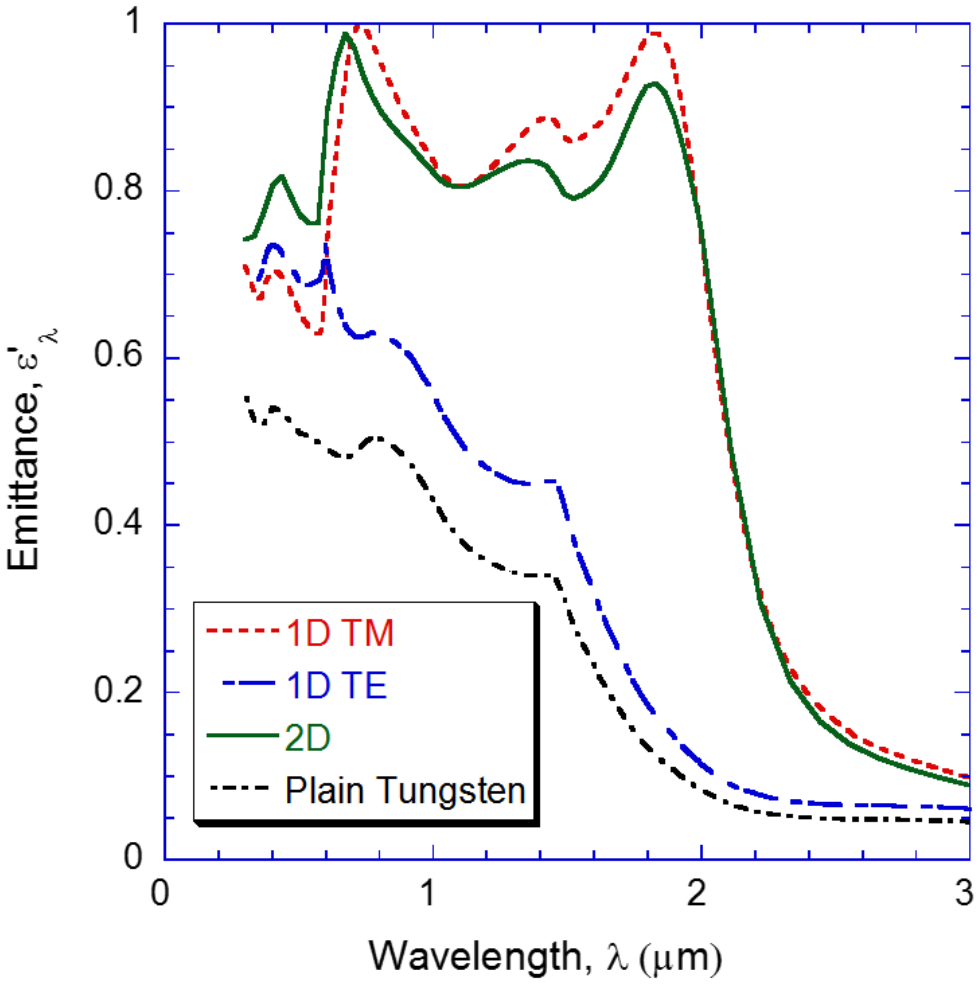

Figure 4.1 Normal emittance spectra of the 2D structure and a 1D structure for both TE and TM waves, along with that of plain tungsten.

at $\lambda > \lambda_g$ is desired to improve the conversion efficiency. Since the TPV emitter temperature usually is less than 2000 K, the effect of emittance at wavelengths shorter than 0.5 μm on the conversion efficiency is much weaker according to Planck's blackbody spectral distribution. Therefore, it is desired to enhance the emittance in the wavelength region from 0.5 to 2.1 μm. Note that the geometric parameters, such as the grating period and patch dimensions, can be adjusted to enhance emittance spectrum for use with other TPV cells with different bandgaps [28,183].

The normal emittance is independent of polarization for the 2D structure due to symmetry. The emittance spectrum of the 1D grating/thin-film structure for TE waves is similar to that of plain tungsten except for the peak at 0.6 μm, which is due to Wood's anomaly [142]. Several small peaks located near 0.4, 0.6, and 1.4 μm are associated with the interband transitions of tungsten [45, 46]. The peak near 0.6 μm does not appear in the spectra for the 2D structure or the 1D structure with TM waves. The emittance spectrum for the 1D structure with TM waves and that for the 2D structures are very similar, both contain two major emission peaks (near 0.7 and 1.8 μm) that do not exist in the spectra for the TE wave or plain tungsten. The overall emittance at normal direction is the average of those for TE and TM waves. As an example, the normal emittance λ = 1.7 μm for the 2D structure is 0.85 and the emittance averaged over the two polarizations for the 1D structure is only 0.58. Therefore, the throughput and efficiency of the TPV system can be significantly improved with the 2D grating/thin-film structure. The underlying mechanisms for the two highest emittance peaks, which elevate the whole emittance spectra, will be explored in the following section.

The emittance peaks at λ = 1.83 μm is due to the coupling of the magnetic resonance inside a micro/nanostructure with the external electromagnetic waves or magnetic plasmon polariton. When the MP is excited, the magnetic field is strongly enhanced in the dielectric layer inserted between the tungsten grating and tungsten substrate, as shown in Figure 4.2. The electric field and current density vectors, denoted by the arrows, are the instantaneous values at t = 0, while the magnetic field, represented by the color contour, is the square of relative amplitude. The maximum value of $\left|H_y / H_{\text{inc}}\right|^2$ is 26.0 as compared to 25.8 for the 1D structure (not shown here), suggesting that the magnitude of enhancement is about the

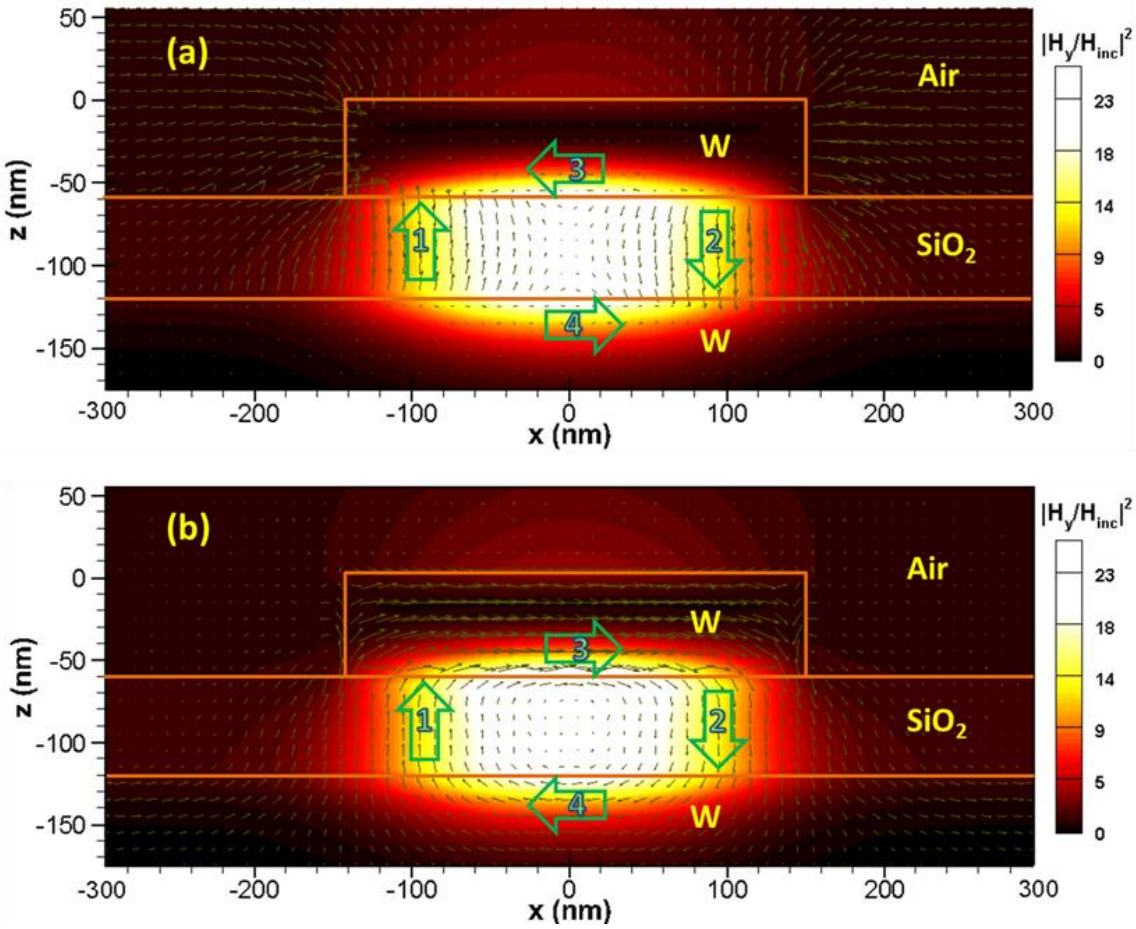

Figure 4.2 The electromagnetic fields and current density distribution in the 2D structure for TM waves at normal incidence and λ = 1.83 μm. The fields are calculated at y = 0 in the x-z plane. The color shows the relative magnitude of the y component of the magnetic field. The vectors show the direction and magnitude of (a) the electric field and (b) current density. Note that $m_{max} = n_{max} = 40$ was used in the calculation.

same in both 1D and 2D structures. Also, the coupling between the metal patch and the substrate becomes weaker and the enhancement decrease as the slide parallel to the x-z plane is moved towards the patch edges. The emittance peak is higher for the 1D structure (TM waves) than for the 2D structure. It is interesting to note that even though the area under the tungsten grating for the 2D structure is only half of that for the 1D structure, the emittance can still be significantly enhanced with a peak near 0.93 when MP is excited.

An inductor-capacitor (LC) model, where the dielectric is regarded as a capacitor and the metal is treated as an inductor, was used by Wang and Zhang [29] to predict the MP resonance frequency. Since the resistance elements will not affect the resonance frequency, they are usually neglected for simplicity. The 2D structure has the same cross section as the 1D structure in the *x*-*z* plane. The same LC model can be used to predict the MP resonance frequency for the 2D structure, because the length in the *y* direction merely cancels out. The MP resonance wavelength can be obtained to be 1.87 μm by zeroing the impedance of the circuit, which is in good agreement with the RCWA calculation. The electric field vectors were used to illustrate the antiparallel currents in the metal above and below the dielectric spacer [29,115]. However, the electric field vectors do not form a closed loop [47]. As shown in Figure 4.2(a), the directions of the electric fields in the metal and dielectric layer are against each other. According to Lenz's law, the induced current should form a loop that will create a diamagnetism effect. In the following, the local current density vector is analyzed to illustrate that the current indeed forms a loop.

The electrical conductivity of a material is frequency dependent and is related to the dielectric function as [3]

$$\sigma = \sigma' + i\sigma'' = -i\omega\varepsilon\varepsilon_0 \tag{4.1}$$

where σ' and σ'' are the real and imaginary parts of the conductivity, ω is the angular frequency, and ε_0 is the vacuum permittivity. The current density vector is related to the electric field vector by $\mathbf{J} = \sigma\mathbf{E}$. Complex vector variables are used in the RCWA computational algorithm. However, only Re(**E**) represents the actual electric field. Similarly, only Re(**J**) represents the actual current density, which can be expressed as the sum of the conduction current and displacement current. Therefore,

$$\mathrm{Re}(\mathbf{J}) = \mathbf{J}_{\mathrm{cond}} + \mathbf{J}_{\mathrm{disp}} = \sigma' \mathrm{Re}(\mathbf{E}) - \sigma'' \mathrm{Im}(\mathbf{E}) \qquad (4.2)$$

The sign of the current density depends on the relative magnitude of these two terms. Figure 4.2(b) shows the current density vectors Re(**J**), which do form a closed loop, in a unit cell of the 2D nanostructure. While the induced current always forms a closed loop, the directions of the current flow and electric field may or may not be the same.

The electric fields and current densities at four locations are calculated to illustrate how their signs vary in the metal and dielectric regions in the particular case studied here. The results are shown in Table 4.1, where locations 1 and 2 are on the left and right, respectively, of the dielectric layer and locations 3 and 4 are in the metal grating and substrate, respectively. For locations 1 and 2, $|\sigma''| >> \sigma'$ and displacement current is the dominant contribution to the current density. Since σ'' is negative, $\mathbf{J}_{\mathrm{disp}}$ will be in the same direction as the imaginary part of **E.** Additionally, the *x* component of **E** is negligibly small in these locations. Because the real and imaginary parts of E_z have the same sign, it

Table 4.1 Numerical values of the electric field and current density at $t = 0$ for the four locations in Figure 4.2. For locations 1 and 2, the *z* components of the current density and electric field vectors are given; while for locations 3 and 4, their *x* components are given.

No.	*x* (nm)	*z* (nm)	Re(*E*) (V/m)	Im(*E*) (V/m)	σ' (S/m)	σ'' (S/m)	J_{cond} (A/m^2)	J_{disp} (A/m^2)	Re(*J*) (A/m^2)
1	-95	-85	3.1	2.42	0.12	-1.9×10^4	0.38	4.6×10^4	4.6×10^4
2	95	-85	–3.1	–2.42	0.12	-1.9×10^4	–0.38	-4.6×10^4	-4.6×10^4
3	5	-45	–0.24	–0.81	1.8×10^5	3.6×10^5	-4.3×10^4	2.9×10^5	2.5×10^5
4	5	–135	0.39	0.36	1.8×10^5	3.6×10^5	6.9×10^4	-1.3×10^5	-6.2×10^4

can be inferred that the displacement current is in the same direction as the electric field. For locations 3 and 4, the electric field is almost parallel to x and only E_x needs to be considered. For tungsten at this wavelength, σ' and σ'' are both positive and on the same order of magnitude. From the RCWA calculation, the real and imaginary parts of E_x share the same sign. According to Eq. (4.2), the conduction and displacement current densities must have opposite signs. Since the magnitude of the displacement current density is greater than the conduction current density, the full current density follows the direction of the displacement current density, which is opposite to the electric field in the x direction. In general, the real and imaginary parts of the electric field may not have the same sign. Thus, it is possible for the current density and electric field in the dielectric layer to have different signs. Similarly, depending on the signs of the electric field and conductivity, the current density and electric field in the metal region can have the same or different signs. Nevertheless, the current flow always forms a closed loop. Since the instantaneous electric field vectors oscillate with time, the direction of the arrows may reverse but should always be antiparallel.

Figure 4.3 shows the emittance spectra of the 2D structure at different polar angles for both TM and TE waves for $\phi = 0°$. It can be seen that the location of the emittance peak near 1.83 μm changes little with θ for both TE and TM waves, because the resonance frequency of MPs only depends on the geometric structure and materials involved. For TE waves, MPs are excited by the x component of the magnetic field. The patterns are the same in both the x and y directions; thus, it is expected that the MP resonance frequency does not change. Furthermore, the peak emittance remains nearly the same even though θ is increased to 60° for TM waves similar to what has been observed previously for 1D

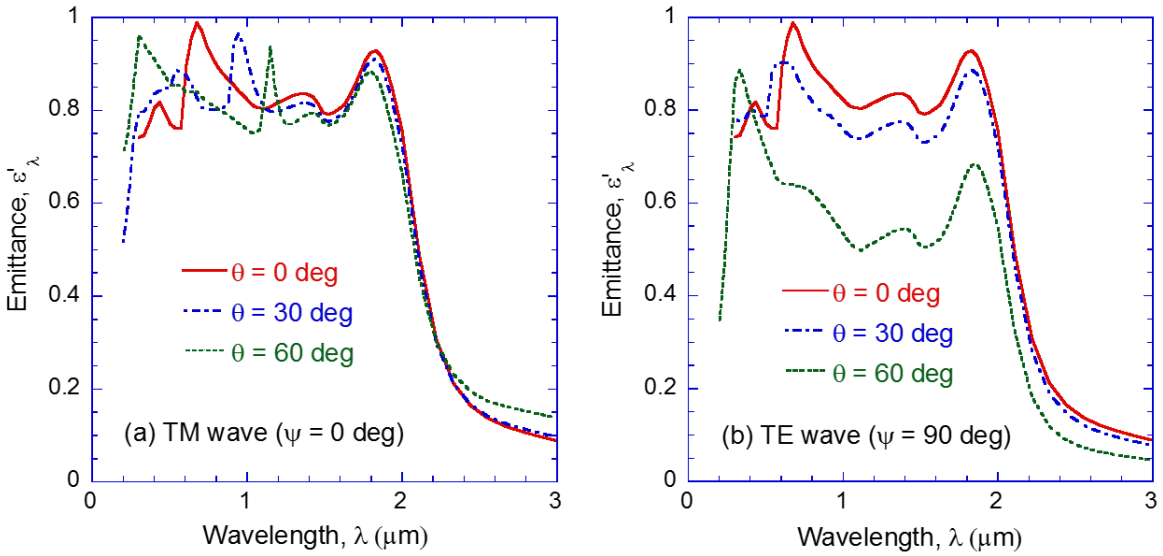

Figure 4.3 Emittance spectra of the 2D structure at different polar angles for: (a) TM waves; (b) TE waves.

structure. For TE waves, however, since the x component of the magnetic field is decreasing as θ increases, the field enhancement becomes weaker at larger polar angles. Hence, the emittance peak associated with the MP decreases as θ increases, as shown in Figure 4.3(b). The location of the emittance peak near λ = 0.7 μm at ϕ = 0° shifts in wavelength as θ changes.

The emittance peak around λ = 0.7 μm of the 2D structure emittance spectrum on Figure 4.1 is because of the excitation of Wood's anomaly or WA. Only TM waves can cause a high Wood's anomaly emittance peak for 1D gratings, but it can be accomplished for both TE and TM waves for 2D gratings. This peak is not due to SPP since the dielectric function of tungsten has a positive real part between 0.24 to 0.92 μm [150]. At longer wavelengths, however, the real part can go negative and SPPs can be excited. Following the Bloch-Floquet condition shown in Eq. (3.4), the tangential component of the wavevector of the (m, n) order of the diffracted waves can be expressed as

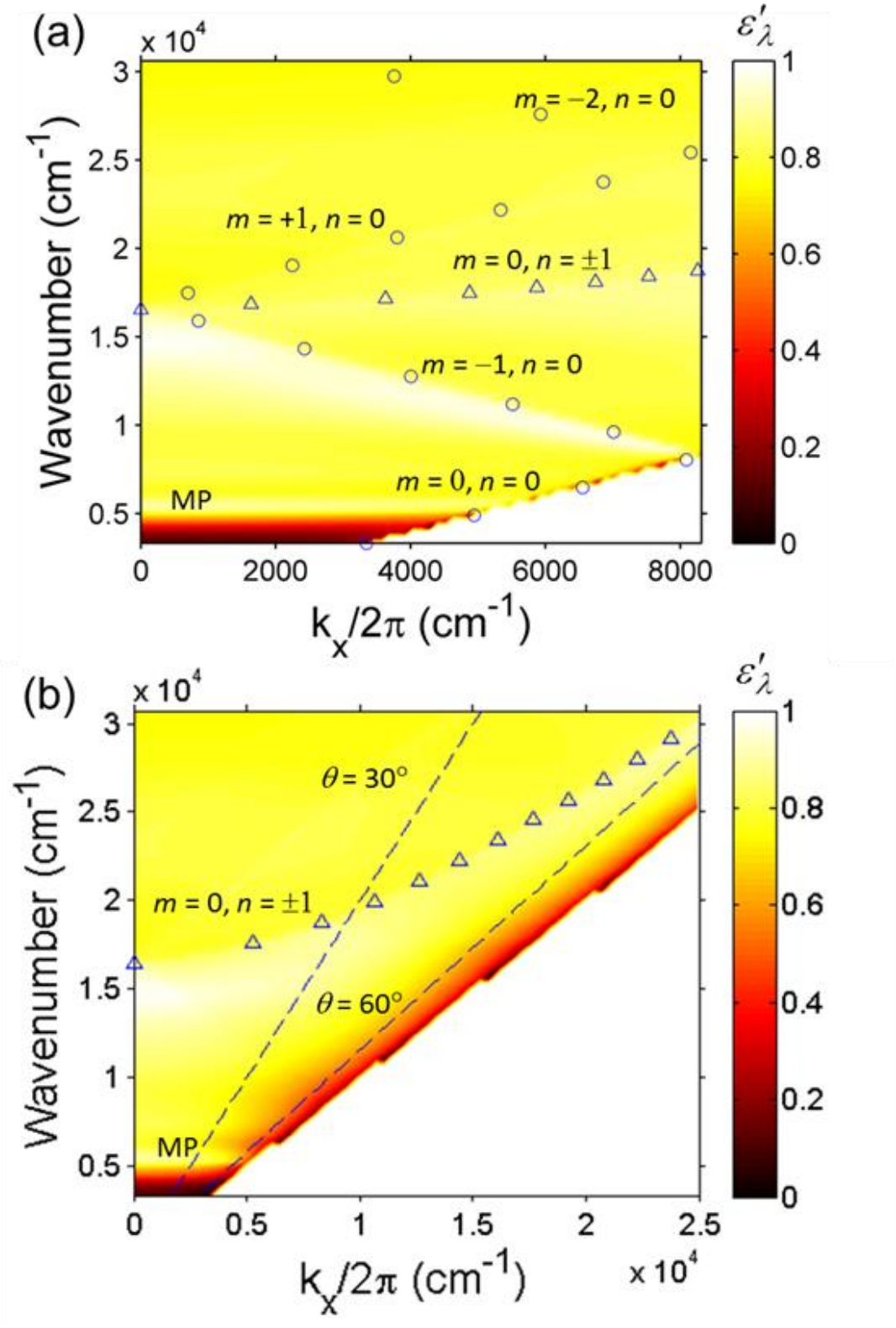

Figure 4.4 Emittance contour plots of the 2D grating/thin-film structure from RCWA calculations along with the SPP dispersion relations: (a) TM waves; (b) TE waves.

$$\mathbf{k}_{\|,mn} = \left(k_{x,\text{inc}} + \frac{2\pi m}{\Lambda_x} \right) \hat{\mathbf{x}} + \left(k_{y,\text{inc}} + \frac{2\pi n}{\Lambda_y} \right) \hat{\mathbf{y}} \tag{4.3}$$

where the subscript ‖ denotes the component in the *x*-*y* plane. To excite WA or SPPs, the diffracted wavevector must be equal to that of the surface wave.

Figure 4.4 shows the contour plot of the emittance for the 2D structure at TM waves in terms of wavenumber and the *x* component of the free-space wavevector, calculated by the 2D RCWA. The oblique bright bands indicate the emittance enhancement due to SPPs or WAs, while the flat bright band around 5400 cm^{-1} is due to the excitation of MP as discussed previously. It can be seen that the SPPs and WAs have strong directional dependence, but the MP resonance frequency is insensitive to the polar angle. The lower-right corner beyond the light line is simply left blank. The contour plots are calculated with $m_{\max} = n_{\max} = 15$ here with the 2D RCWA to save the computation time. The results are sufficiently accurate at wavenumbers higher than approximately 7000 cm^{-1}, which is the major region of interest for surface waves. Relatively larger errors (but still within 5%) exist at wavenumbers below 7000 cm^{-1} when compared to the results calculated with $m_{\max} = n_{\max} = 25$ at normal incidence. Finite-difference time-domain (FDTD) method is also used to verify the contour plots obtained from the 2D RCWA at $\theta \leq 60°$ and the results compare well with each other. At polar angles exceeding $60°$, the computational time required for the FDTD to calculate the emittance spectra increases significantly. Thus, RCWA with fewer orders should be considered to be both reasonable and practical for generating the contour plots.

The effect of the periodicity in the *x* direction can be analyzed by considering n = 0 in Eq. (4.3). In this case, surface waves (can be SPPs or Wood's anomaly) can be excited along the *x* direction once the following dispersion relation is satisfied:

$$k_{\mathrm{sw}} = \left| k_{\mathrm{inc}} \sin\theta + \frac{2\pi m}{\Lambda_x} \right| \tag{4.4}$$

This dispersion relation is solved with different m values (−2, −1, 0, and +1) for surface waves excited between air and tungsten, and the resonance frequencies are marked as circles on Figure 4.4(a). These circles follow well the bright emittance band obtained from the 2D RCWA calculation. Since SPPs are quite close the light line, the solutions are essentially the dispersion for Wood's anomaly. Losses in tungsten can broaden the emittance peak, which has been verified by using a simple 1D tungsten grating without SiO_2 film, although the results are not shown here.

For 2D periodic grating structures, the periodicity (Λ_y) in the *y* direction can affect surface waves as well. Take m = 0 and $n \neq 0$ for simplicity. The incident wave will be diffracted into the *y* direction. The electric field of the reflected waves will have a component along the *y* axis even though the incident wave does not carry an electric field in the *y* direction. When m = 0, the dispersion relation of the surface waves becomes

$$k_{\mathrm{sw}} = \sqrt{\left(k_{\mathrm{inc}} \sin\theta\right)^2 + \left(\frac{2\pi n}{\Lambda_y}\right)^2} \tag{4.5}$$

The solutions of this equation are marked on Figure 4.4(a) with triangles and they agree well with the emittance band obtained from the 2D RCWA. Within the considered ranges of frequency and wavevector, only the surface waves associated with n = ±1 shows up when m = 0. This branch will fold with the grating period Λ_x in the *x* direction and show

up as $m = \pm 1,\ \pm 2$ orders. However, these higher orders also do not show up in the contour plot due to the intrinsic losses of tungsten. At wavelengths shorter than the grating period of 0.6 μm, the peaks become complicated because higher-order SPPs, Wood's anomaly, and higher-order MPs can couple with each other [105], and losses in tungsten make it difficult to identify the peaks.

For TE incident waves, the periodicity in the *y* direction plays a crucial role to excite surface waves. Figure 4.4(b) shows the emittance contour of the 2D structure for TE waves. The plot is extended beyond the first Brillouin zone (i.e., $k_x > \pi / \Lambda$) and lines with polar angles $\theta = 30°$ and $60°$ are identified. The lower-right region beyond the light line is left blank. For TE wave incidence with $\phi = 0°$, the order *n* must not be zero since k_y must have a nonzero real part for SPPs to propagate in the *y* direction. As can be seen from Figure 4.4(b), besides the flat MP resonance, a resonance band is also observed whose resonance frequency increases with k_x. This branch is identified as the surface waves with $m = 0$ and $n = \pm 1$ and can be calculated from Eq. (4.5) as shown by the triangles. Higher-

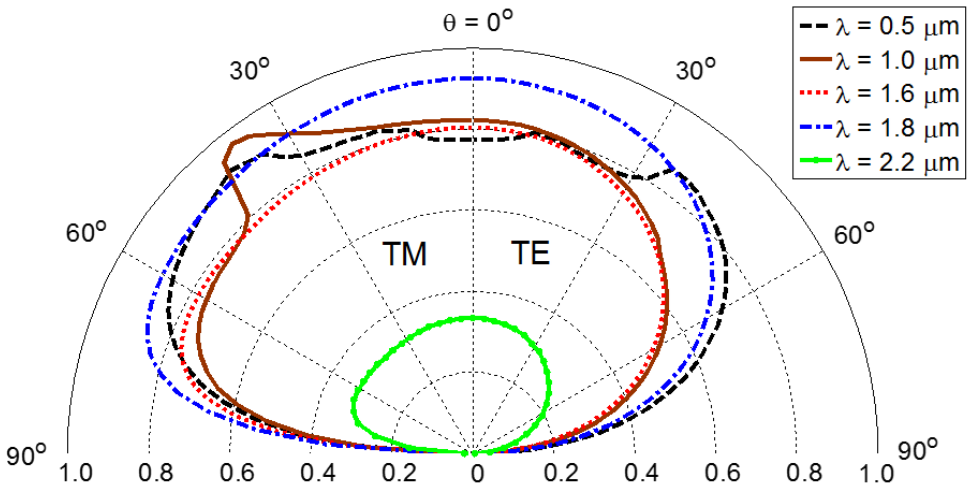

Figure 4.5 Polar plots of the emittance at ϕ = 0°, 90°, 180° or 270° for several given wavelengths. The left half is for TM waves and the right half is for TE waves.

order SPP branches can also be predicted but cannot be discerned from the contour plot. Moreover, Wood's anomaly may exist especially for the $m = 1$ and $n = 0$ order, although it is not clear. The above discussions explain the shift of the surface wave peaks shown in Figure 4.3. the Emittance peak shifts toward longer wavelength as the polar angle increases for TM waves while for TE waves, the peak location shifts toward shorter wavelengths with increasing polar angles.

The effect of the polar angle and azimuthal angle on the emittance of the 2D structure is also investigated at $\lambda = 0.5$, 1.0, 1.6, 1.8 and 2.2 μm. The first four wavelengths fall in the wavelength range for TPV cells that high emittance is desirable. However, low emittance is desired at $\lambda = 2.2$ μm and beyond. Figure 4.5 is a polar plot of the emittance with respect to θ at the azimuthal angle $\phi = 0°$. The left and right sides of the plot show the emittance for TM and TE waves, respectively, since θ can only vary from 0° to 90°. This plot is also valid for $\phi = 90°$, 180°, or 270°, due to the symmetry of the structure. The

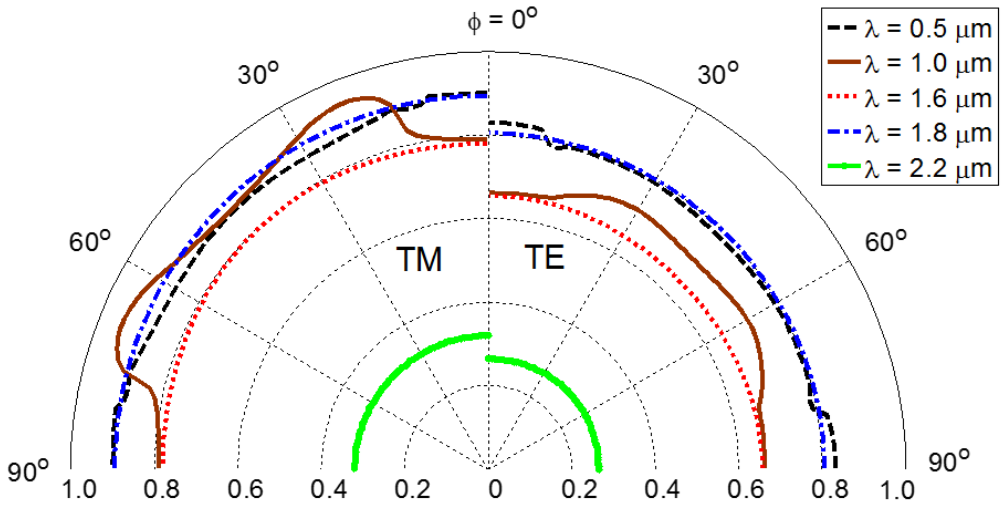

Figure 4.6 Polar plots of emittance at $\theta = 45°$ for several given wavelengths. The left half is for TM waves and the right half is for TE waves. Only the results for $0° \le \phi \le 90°$ is shown since the emittance has an eight-fold symmetry with respect to ϕ.

emittance is above 0.7 for polar angles less than 40° for both TM and TE waves in the desired wavelength range. For λ = 2.2 μm, the maximum emittance is about 0.3, which will further decrease at longer wavelengths. Based on the previous analysis, the emittance peak around θ = 38° at λ = 1 μm for TM waves and that around θ = 35° at λ = 0.5 μm for TE waves are due to the excitation of surface waves. The MP excitation results in high emittance at λ = 1.8 μm for a large range of polar angles, especially for TM waves.

The effect of ϕ on the emittance is studied by fixing θ = 45°, and the results are shown in Figure 4.6. The azimuthal angle ϕ can vary from 0° to 360°. However, due to the symmetry of the 2D structure, the emittance polar plots for both TE and TM waves have an eight-fold symmetry. Hence, only the emittance for 0° < ϕ < 90° is shown. Again, the left side displays the emittance for TM waves (ψ = 0°) and the right side displays the emittance for TE waves (ψ = 90°). For the wavelengths in the desired range, the emittance is higher than 0.78 and 0.64 for TM and TE waves, respectively. For λ = 2.2 μm, the emittance is lower than 0.35 for both polarizations at all azimuthal angles, which again shows the wavelength selectivity and angle independence of the emittance of the nanostructure. As mentioned previously, the geometric parameters can be tuned to fit TPV cell materials with different bandgaps. Surface waves depend on the grating period. For MP resonances, a larger lateral dimension of patches can result in the red shift of the emittance peak. Also, increasing the thickness of the dielectric layer will decrease the MP resonance wavelength. These properties can be used in the design of practical TPV emitters once the TPV cell materials and properties are known.

In conclusion, this work theoretically demonstrates the advantages of using a 2D periodic array of tungsten patches over a thin dielectric film coated on a tungsten substrate

as a high-performance TPV emitter. The normal emittance of this 2D nanostructure is wavelength-selective and polarization-independent. The mechanisms of excitations of MPs and surface waves in the 2D structure are elucidated. The current density vectors are analyzed to show that when MP is excited, the induced current indeed forms a loop. Furthermore, it is shown that high emittance can be achieved in the desired spectral region for both polarizations with the 2D nanostructure in a large range of polar and azimuthal angles. The detailed analysis and findings from this study not only will help understand the mechanisms that can be used to tailor the emittance for the proposed 2D structure, but also will facilitate the design and optimization for plasmonic nanostructures for applications in TPV systems and solar cells.

4.2 Deep Metal Grating Structures

As mentioned before, since thermal radiation is generated by the thermal motion of charged particles in matter, it is usually incoherent. Researchers have put significant effort towards controlling thermal radiation for applications such as solar cells [161,184-186] and thermophotovoltaic (TPV) systems [28,29,142,160,167], in which it is desired to have a receiver (or emitter) that can absorb (or emanate) radiation only in certain wavelength regions. The work done in the previous chapter is a good example. One-, two-, or three-dimensional (1D, 2D, or 3D) micro/nano periodic structures of wide profile diversity and dimensionality can enable tailoring the radiative properties for developing spectral selective absorbers and emitters [141]. As a matter of fact, 1D and 2D gratings have been extensively investigated both theoretically and experimentally.

Hesketh et al. [1,187] experimentally demonstrated the resonance in the emission spectra with 1D doped-Si deep gratings, and explained them with an acoustic analog of the organ pipe mode. Later, Maruyama et al. [188] used the cavity resonance modes to explain the resonance conditions in 2D-microcavity gratings. Sai et al. [167] and Kusunoki et al. [189] also experimentally demonstrated resonances in similar structures as cavity modes. Though the cavity resonance theory has successfully explained the resonances in the certainty periodic structures [190], it cannot predict the maximum (or cutoff) resonance wavelength in a grating with narrow slits or trenches. As an example, the resonance wavelength can be about ten times the grating depth (or height) [107] while the cavity resonance formulation yields a maximum resonance wavelength four times the grating depth. Finite inductance [191,192], coupled SPPs [193,194], and trapped modes theory have been used to explain the mechanisms of resonances and the increase of the cutoff wavelength in gratings [195], grating/thin-film structures [47], holes [191], and slits [192]. Mattiucci et al. [107] evaluated the impedance of the grating using coupled SPP modes and successfully predicted the emittance of grating structures with the metamaterial effective media approach. However, the resonance peaks could not be obtained explicitly. Pardo et al. [108] explained the funneling of light into narrow grooves etched on a metal surface as a result of magnetoelectric interference, but did not quantify the resonance condition. To guide the engineering design of the nanostructures [159], it is desirable to develop simple models to the predict resonance wavelength for certain kind of structures.

The theory of MPs has successfully been used to predict the resonances in metallic grating/thin-film structures [29,144] and narrow slit arrays [50]. Wang and Zhang [52] also used the excitation of MPs to explain the phonon-mediated resonances in SiC deep

gratings. In addition, MP resonance has been used to explain the responses in the structures mentioned in [107,108]. Since the resonance in deep gratings shows different geometry dependence in different wavelength ranges, it is worthwhile to explore the possibility of using MPs to explain the anomalous maximum wavelength in deep gratings for various materials and spectral regions. In this work, the inductor-capacitor (LC) circuit model [114,115] is used to predict the fundamental MP resonance mode in deep gratings.

The 1D metallic grating structure considered in this work is the same as illustrated in Figure 2.1. The region below the grating is made of the same material and thick enough to be treated opaque. Consider radiation incident from air (medium above the grating) to the grating. Due to the high reflectivity of the metallic material, the reflectivity of the grating is generally high except when resonance occurs that can cause a sudden reduction of the reflectance (i.e., increase of the absorptance or emittance). The cavity resonance model has often been used to explain the emittance peaks for 2D grating or cavity structures [167,188,189]:

$$\lambda_{lmn} = \frac{2}{\sqrt{\left(\frac{l}{L_x}\right)^2 + \left(\frac{m}{L_y}\right)^2 + \left(\frac{n+\frac{1}{2}}{L_z}\right)^2}} \tag{4.6}$$

where l, m, and n are integers (0, 1, 2, …), and L_x, L_y, and L_z define the cavity dimensions. For a 1D grating, L_y is infinitely long such that only L_x and L_z (which are referred as b and h in Figure 2.1 can affect the resonance wavelengths. The maximum

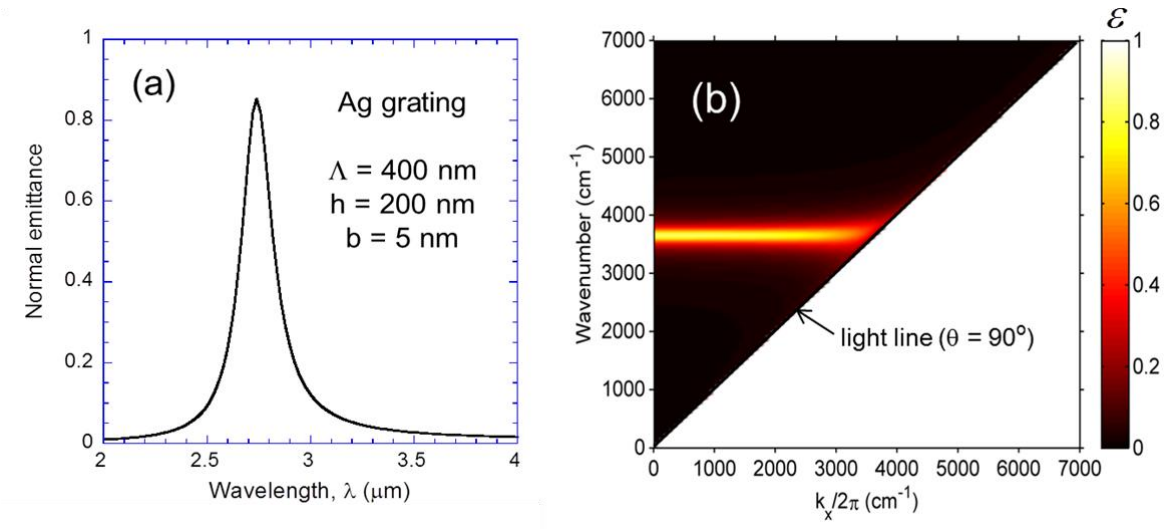

Figure 4.7 Emittance for Ag deep gratings with Λ = 400 nm, h = 200 nm, and b = 5 nm: (a) Normal spectral emittance; (b) Contour plot of the emittance in terms of the wavenumber and parallel component of the wavevector. The vertical line with k_x = 0 represents normal direction and the diagonal represents grazing angle or light line.

value of λ_{lmn} is called the cutoff wavelength and can be determined by setting $l = n = 0$ in Eq. (4.6), resulting in a resonance wavelength (λ_R) that is four times the grating height ($4h$). However, this value may be much smaller than the resonance wavelength in a deep grating with a high aspect ratio (h/d), as shown in the example below.

Figure 4.7(a) shows the normal emittance spectrum TM waves for a Ag grating with Λ = 400 nm, h = 200 nm, and b = 5 nm. The emittance spectrum is characterized by a peak as high as 0.85 at the wavelength of 2.74 μm . The emittance enhancement is remarkable since the emittance is less than 0.005 for a smooth Ag surface at this wavelength. Note that λ_R for this mode is nearly 14 times the grating height. This resonance cannot be explained by SPP or Wood's anomaly since both of which would occur at much short wavelengths on the order of period. Furthermore, the high emittance is almost omnidirectional as seen from the contour plot displayed in Figure 4.7(b), which

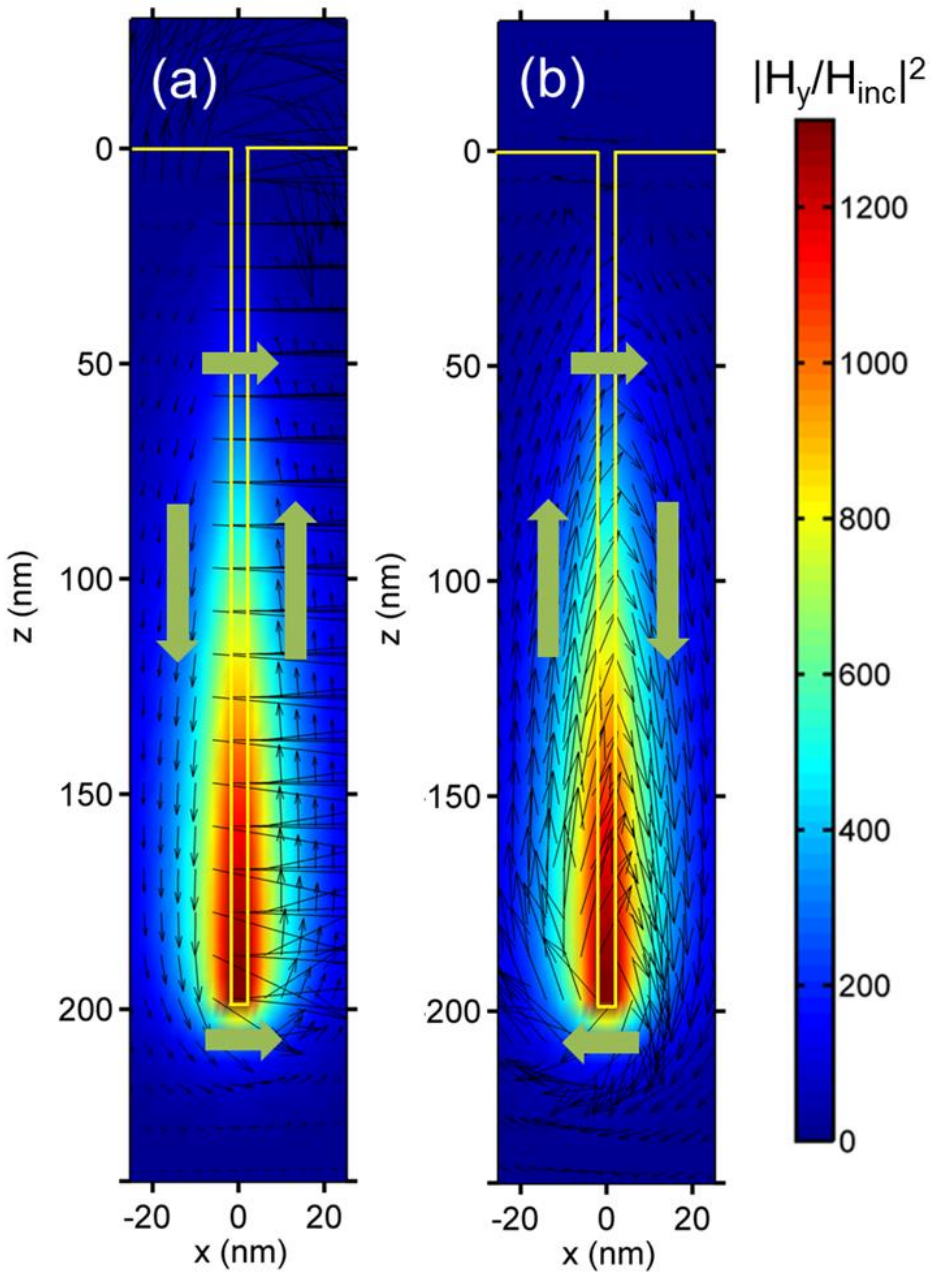

Figure 4.8 (a) The electromagnetic field and (b) current-density distribution in the Ag grating with the same parameters as for Figure 4.7 at $\lambda = \lambda_R = 2.74$ μm. The color contour shows the relative magnitude of the *y* component of the magnetic field. The vectors show the direction and magnitude of the electric field in (a) and current density in (b). Note that positive *z*-direction is downward.

shows the directional spectral emittance in terms of the wavenumber and parallel wavevector $k_x = k_{\text{inc}} \sin\theta$. Emittance values at $k_x = 0$ (i.e., along the ordinate) correspond to normal incidence with an emittance peak located at 3650 cm^{-1}. A quantitative explanation is given below using the MP model that takes account of the geometry and materials properties.

Under a time-varying magnetic field parallel to the *y*-direction, an oscillating current is produced around the grooves in the *x*-*z* plane, forming a MP. Figure 4.8(a) and (b) show the electromagnetic and current-density field when the resonance occurs in the aforementioned Ag grating. The *x*-*y* plane is at the interface between the grating and air; besides, $x = 0$ is located at the center of a trench. The electric field and current-density vectors, denoted by the arrows, are the instantaneous values at time $t = 0$, while the magnetic field, represented by the color contour, is the square of the relative amplitude. Since the instantaneous electric and current-density field vectors oscillate with time, the direction of the arrows may reverse. The big arrows show the general direction of the vectors. The electric field at the opening is greatly enhanced and decays nearly linearly towards the bottom.

The current-density vectors are obtained from $\mathbf{J} = \sigma\mathbf{E}$ where σ is the complex electrical conductivity of the material at the given location [3], and they form a closed loop around the trench. The electric current consists of two parts: displacement current and conduction current. The conduction current is directly related to the real part of **E**, which is the instantaneous electric field. However, the displacement current is related to the imaginary part of **E**. As it turned out, the signs of the current and field differ in the Ag wall, as indicated by the big arrows. Therefore, the current forms a closed loop while the electric

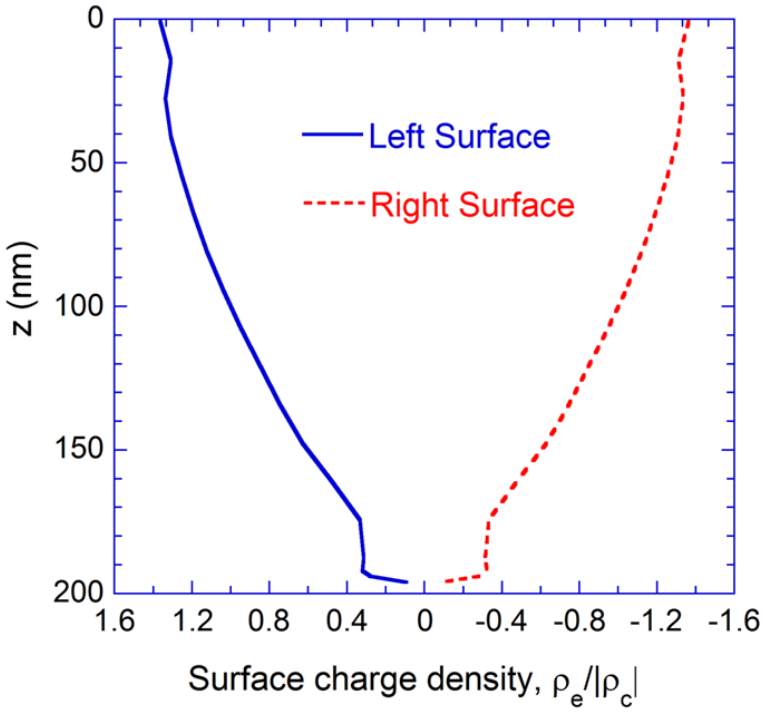

Figure 4.9 Relative charge density distribution along the side walls of the trench for the grating. Note that $z = 0$ is the opening and $z = 200$ nm is the bottom of the grooves.

field does not, as has been discussed in the previous work. The strongest magnetic enhancement corresponding to the closed current loop is at the bottom of the trench, where the magnitude of magnetic field is more than 30 times that of the incident waves, showing a strong diamagnetic effect. The magnetic fields oscillate and the current loop varies from clockwise to counterclockwise and vice versa. Figure 4.9 shows the relative surface charge density distribution on the left and right surfaces of the trench at $t = 0$ calculated by

$$\rho_e = \varepsilon_0 \mathbf{n} \cdot (\mathbf{E}_1 - \mathbf{E}_2) \tag{4.7}$$

where ε_0 is the electric permittivity of vacuum; $\mathbf{E}_1$ and $\mathbf{E}_2$ are the electric fields on either side of the surface, and $\mathbf{n}$ is a unit normal vector to the surface from side 1 to side 2. The charge density is normalized by ρ_c which is the charge density at the center of the surface ($z = 100$ nm). The sign and magnitude of the charge density also change with time.

Corresponding to the electric field in Figure 4.8(a), when the resonance happens, charges tend to accumulate at the upper corner of the grating and this in turn creates a strong electric field.

Based on the closed current loop, an equivalent LC circuit model [29,50,52,114] shown in Figure 2.1 is used to predict the magnetic resonance condition. The numerical factor c' in Eq. (2.6) is between 0 and 1 accounting for the nonuniform charge distribution between the ridges of the grating [52,115]. If the charges are uniformly distributed on the surfaces around the trench, c' would be 1 and Eq. (2.6) would degenerate to the capacitance between two infinitely long parallel plates. The actual charge distribution is complicated as shown in Figure 4.9 and the non-uniform charge density distribution suggests the existence of fringe effect [196]. If the charge were linearly distributed along the surfaces on both sides of the grooves and the charge density increases from zero at the bottom to a maximum at the opening of the grating, then c' would be 0.5. Without using a full-wave model, c' can be taken as an adjustable parameter that is about 0.5. As an example, if $c' = 0.5$ is used, the LC model yields a resonance at $\lambda_{\mathrm{R}} = 2.78\ \mu\mathrm{m}$, which agrees well with the RCWA simulation. By using an effective parameter c', one could still evaluate the capacitance of the cavity by a simple formula and thus make it possible to capture the fundamental physics with a simple model. Note that *l* does not show up in the Eq. (2.8). This may also explain why the resonance wavelength predicted for a 1D grating is similar for a 2D grating with the same geometry in the *x*-*z* plane. Since the thickness of the plates is much greater than δ, each groove can be considered as an isolated unit.

The emittance contour shown in Figure 4.10 demonstrates the effect of the trench width on the resonance frequency of the Ag grating with Λ = 400 nm and *h* = 200 nm. The

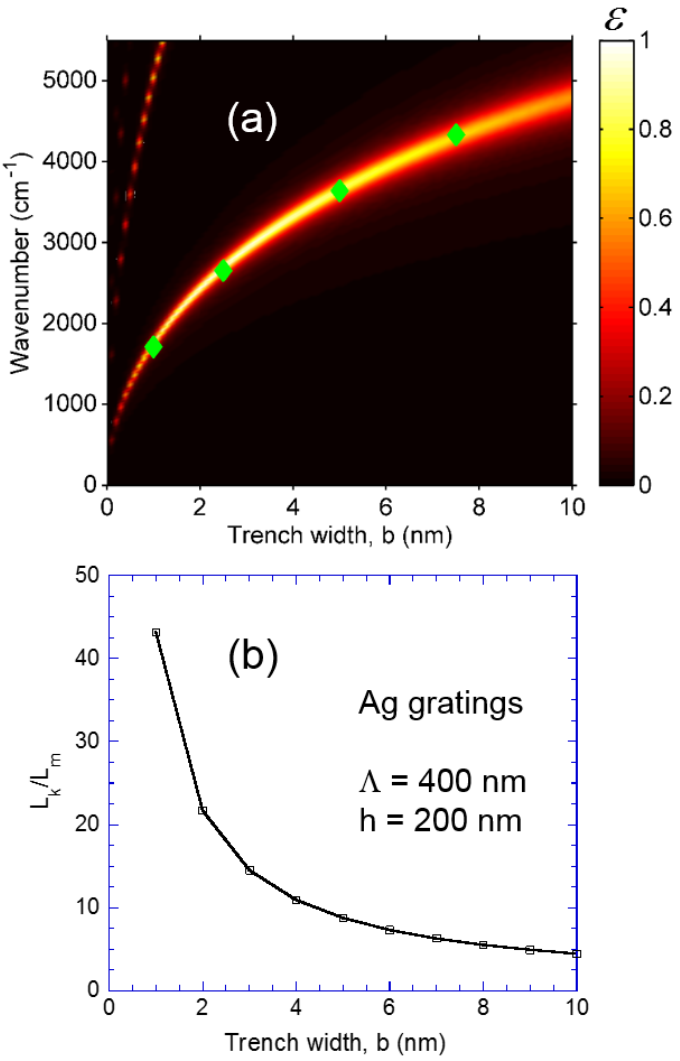

Figure 4.10 (a) Emittance contour of Ag gratings with Λ = 400 nm and h = 200 nm calculated by RCWA, where the diamond marks indicate the resonance conditions predicted by the LC model; (b) Ratio of the kinetic inductance to the magnetic inductance (L_k/L_m) calculated at the MP resonance.

major bright band is attributed to the fundamental MP mode that is the focus of the present study and the other bands are higher-order MP modes. At sufficiently large trench width, the dispersion curve tends to become flat (not shown in the figure), but bends toward lower wavenumbers when the trench width decreases, suggesting a significant dependence of the resonance frequency on the trench width in deep gratings. The green diamond marks

indicate those predicted from the LC model in this and the rest contour plots. It can be seen that the LC model agrees very well with the dispersion curve determined from the full-wave RCWA calculation. When the trench width is narrow, the resonance wavelength increases significantly with decreasing trench width, resulting in a cutoff wavelength that can be more than 10 times the grating height. This effect is further explained by comparing the magnitude of the inductances in the LC model as discussed in the following.

According to Eqs. (2.3) and (2.5), for a 1D deep grating with fixed period and height, L_{m} depend linearly on the trench width b but is independent of the frequency. However, L_{k} depends little on b due to the fact that $2h >> b$, but depends strongly on the frequency or wavelength. On the other hand, the capacitance is inversely proportional to b based on Eq. (2.6). According to Eq. (2.8), if L_{k} is negligible compared with L_{m}, the resonance wavelength depends on the product of $L_{\mathrm{m}}C$, which is independent of b. The ratio $L_{\mathrm{k}}/L_{\mathrm{m}}$ at the MP resonance is plotted in Figure 4.10(b) as a function of b under the condition showing in Figure 4.10(a). In this case, L_{k} is much greater than L_{m}. A large kinetic inductance shifts the resonance to longer wavelengths according to Eq. (2.8). As the trench width increases, L_{m} increases and the ratio $L_{\mathrm{k}}/L_{\mathrm{m}}$ becomes smaller and subsequently the resonance frequency increases and eventually reaches a constant that is independent of b.

The effects of the kinetic inductance on the resonance wavelength can be better understood if we consider similar MP resonances in different frequency ranges. Figure 4.11 shows MPs in three deep gratings with the same aspect ratio but the dimensions are increased by a scaling factor (*SF*) of 10, 100, and 1000 compared with those for

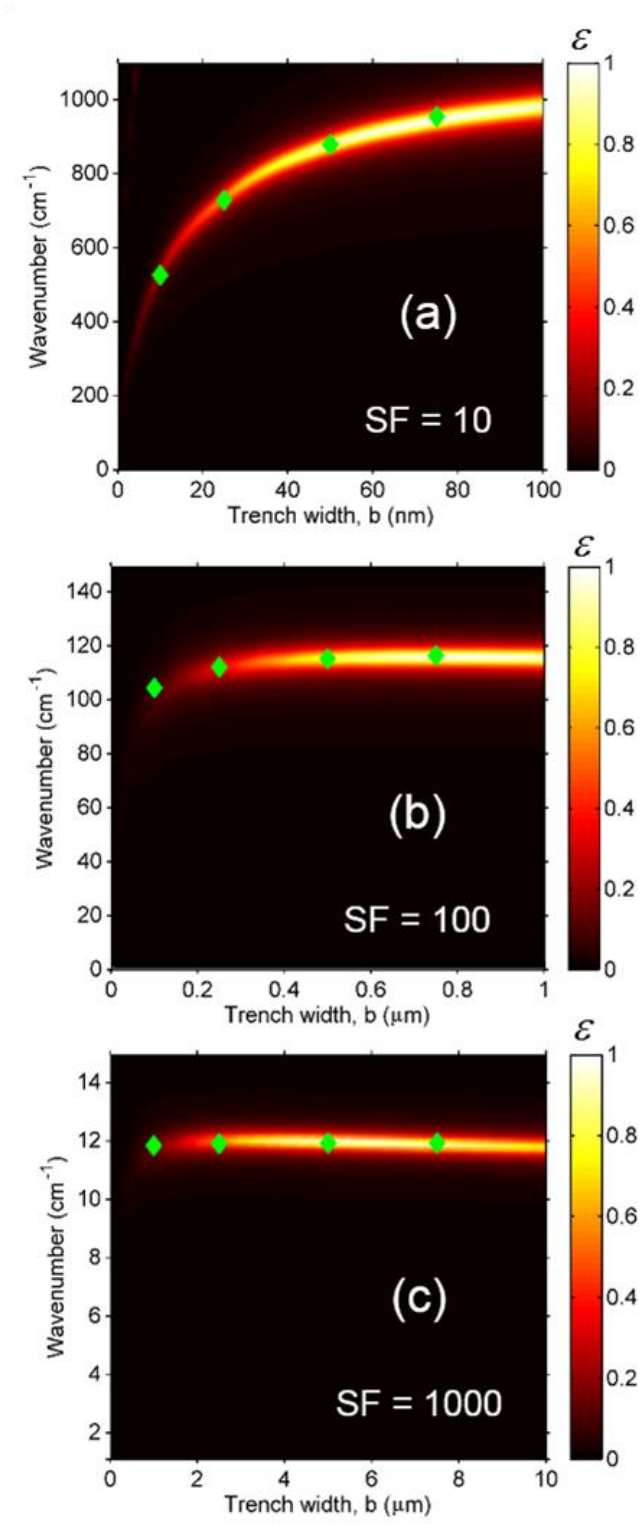

Figure 4.11 Emittance contours and LC model predictions (shown as diamonds) of Ag gratings when the geometric dimensions are scaled up compared with the based case in Figure 4.10(a): (a) *SF* = 10; (b) *SF* = 100; and (c) *SF* = 1000.

Figure 4.10. The different shapes of the dispersion curves are due to the different frequency dependence of the dielectric function of Ag. For metals in the long-wavelength region, $\varepsilon' \ll \varepsilon''$, resulting in a decrease of L_k / L_m as the dimensions (and wavelength) are scaled up. With large *SF* values, resonances are very weak and cannot exist toward the left end of the emittance contour. As shown in (b) and (c), the resonance frequency is essentially independent of the trench width. In the low frequency limit, L_k is negligible and Eq. (2.8) yields an asymptotic value for the resonance wavelength:

$$\lambda_A = 2\pi c_0 \sqrt{L_m C} = 2\pi h \sqrt{c'} \tag{9}$$

which gives $\lambda_A \approx 4.4h$ for $c' = 0.5$ and is close to that predicted from the cavity mode.

The values of the physical properties corresponding to the resonances are listed in Table 4.2 for the MP modes different wavelength ranges. The value of c' listed in the table is treated as an adjustable parameter to match with the MP resonance peaks for each scaling factor, but is assumed to be independent of the trench width. It can be seen that c' is very close to 0.5 and the LC model agrees with the RCWA calculation well as demonstrated in

Table 4.2 Physical properties for MP resonances in Ag gratings with different scaling factors. The base case for *SF* = 1 is the same as for Figure 4.10.

SF	Wavenumber (cm^{-1})	Wavelength (μm)	L_k (Wb/A)	L_m (Wb/A)	C (C/V)	c'	*Q*-factor
1	3650	2.74	1.10×10^{-20}	1.26×10^{-21}	1.72×10^{-10}	0.49	14.9
10	877.4	11.4	1.09×10^{-19}	1.26×10^{-19}	1.56×10^{-10}	0.44	16.3
100	115.2	86.8	7.83×10^{-19}	1.26×10^{-17}	1.59×10^{-10}	0.45	19.2
1000	11.92	838.9	4.65×10^{-18}	1.26×10^{-15}	1.57×10^{-10}	0.44	25.4

Figure 4.10(a) and Figure 4.11. The last column of the table shows the Q-factor, which is the ratio of the resonance frequency over the full width at half maximum of the emittance peak for MP resonance. A large Q-factor indicates a relative sharp peak or more coherent thermal emission. It can be seen that the Q-factor increases with the scaling factor or resonance wavelength. The reason needs further exploration.

Since for the aforementioned deep gratings with the aspect ratio more than 20, even though the Bosch process [197] and nanoimprint lithography [198] could be used, the fabrication of the structure is still very challenging. For a practical structure for thermal emission control, structures with a somewhat larger trench width is certainly designed if high emittance can still be achieved. For Ag gratings with Λ = 4 μm and h = 2 μm, when b > 0.5 μm, the resonance becomes very weak as shown in Figure 4.12. For example, for b = 0.8 μm, the peak emittance is only 0.07, which is too small for use as a thermal emitter. Note that Ag has a very high extinction coefficient and the electromagnetic field can only penetrate inside by a very short distance. Strong field coupling between the two sides of

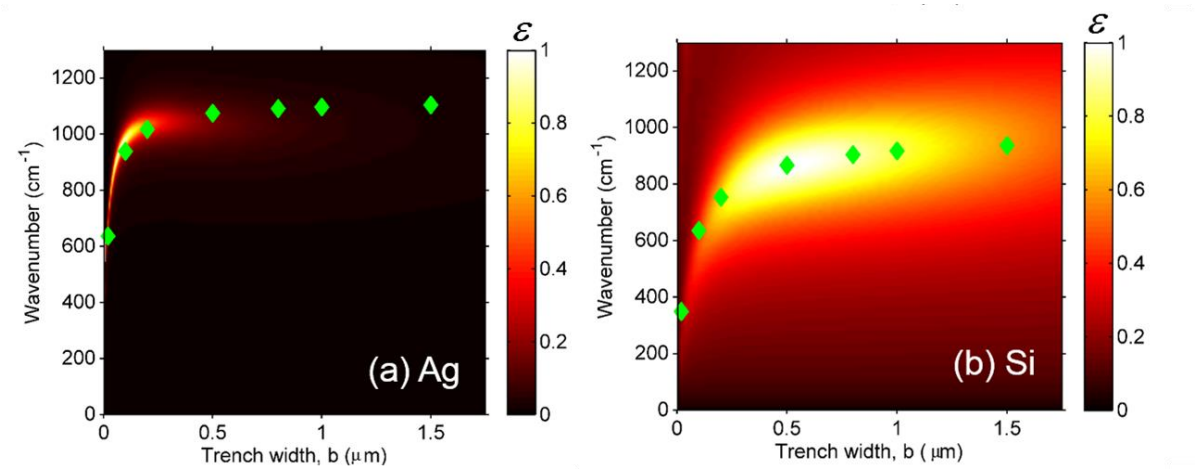

Figure 4.12 Emittance contours with LC model predictions marked as diamonds of (a) Ag gratings with Λ = 4 μm and h = 2 μm; (b) doped Si gratings with the same period and height.

the trench happens only when the trench is very narrow. Additionally, since the relative penetration depth (δ / λ) decreases as λ increases, it is even more difficult for the field to couple and create MP resonance at longer wavelengths.

The aforementioned problem can be alleviated by using heavily-doped Si because of its smaller plasma frequency and relatively small extinction coefficient as compared to Ag. Since the field can penetrate deeper into doped Si, it may be easier for the two surfaces in the trench to couple at a relatively large distance. The dielectric function for p-type doped Si is taken from [199], assuming the temperature is at 300 K with a doping concentration 10^{21} cm^{-3}. Figure 4.12(b) shows the emittance contour for doped Si with the same geometries as for (a). The resonance is much stronger and broader for 0.25 μm < b < 1 μm with doped Si than with Ag. The broadening effect is due to the large scattering rate or resistance of doped Si compared to Ag. The MP resonance becomes weaker if b is increased to beyond 1 μm.

Figure 4.13 shows the emittance spectra for doped Si gratings with different scaling factors so that the MPs are excited in different wavelength ranges. The grating with parameters Λ = 400 nm, h = 200 nm, and b = 80 nm is not included, because doped-Si does not exhibit metallic behavior in the near-infrared. The physical properties at the MP modes are listed in Table 4.3. Due to the effect of the kinetic inductance, the resonance wavelength is shifted to 5.6 times the grating height in Figure 4.13(a) and the ratio drops to 4.7 in (d). Note that the resonance wavelength in (d) is about 1 cm, indicating the scalability of MPs up to the microwave region. One could also argue that the MP model merely predicts the cavity modes when the kinetic inductance is negligible. It appears that the kinetic inductance is the key for the coupled SPPs between the two sides of the grooves.

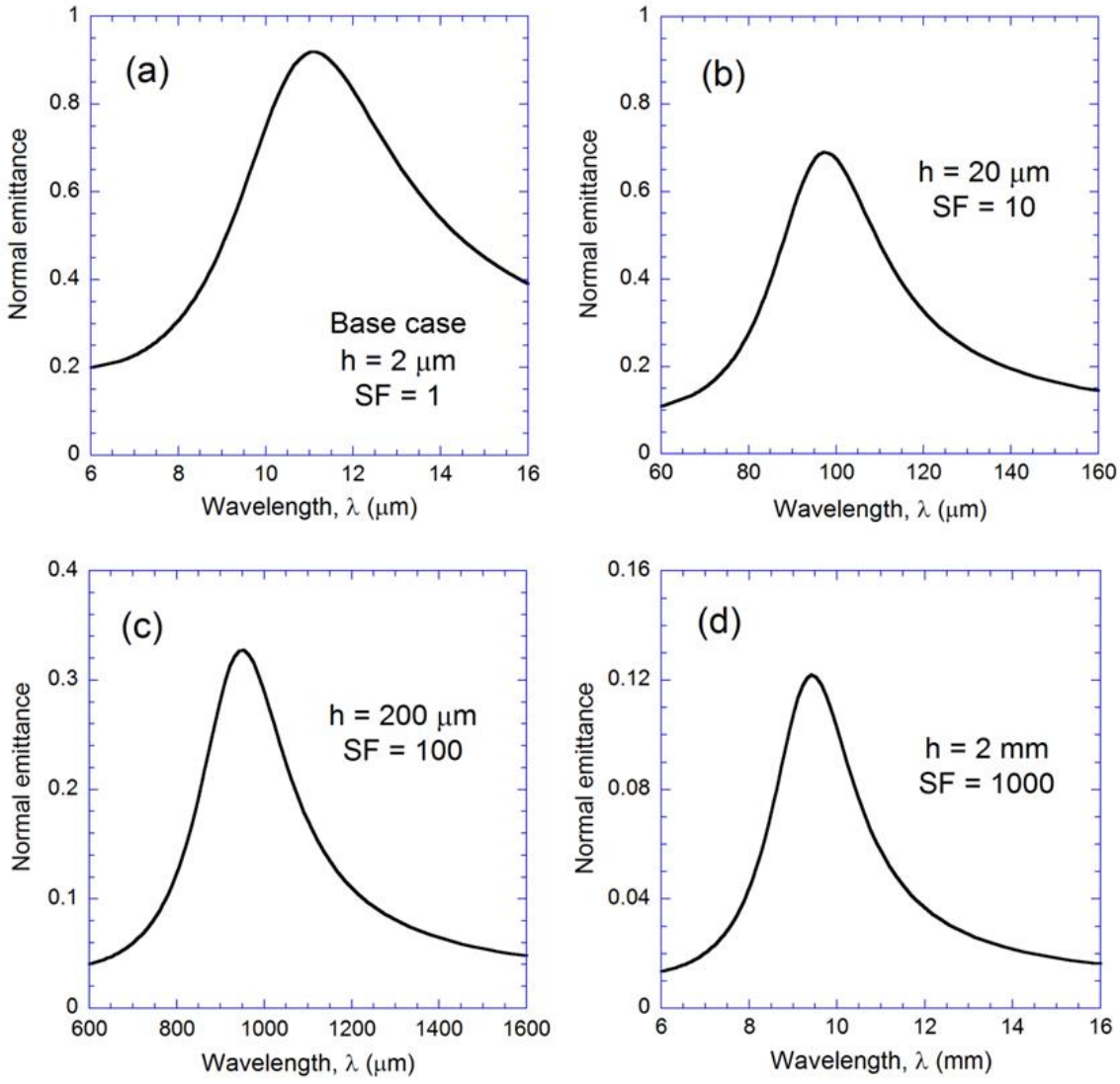

Figure 4.13 Emittance spectra for doped Si deep gratings with the base geometry (*SF* = 1) of Λ = 4 μm, *h* = 2 μm, and *b* = 0.8 μm and for different scaling factors: (a) *SF* = 1; (b) *SF* = 10; (c) *SF* = 100; and (d) *SF* = 1000.

Furthermore, one could use the waveguide mode to explain the guided wave nature for deep gratings. All the explanations appear to be consistent but are from different aspects. The advantage of using the LC model is due to its simplicity and ability to explain the resonance behavior with scalability and for different materials. Relatively lower Q-factors

Table 4.3 Physical properties for MP resonances in doped Si gratings with different scaling factors. The base case corresponding to $\Lambda = 4$ μm, $h = 2$ μm, and $b = 0.8$ μm.

SF	Wavenumber (cm^{-1})	Wavelength (μm)	L_k (Wb/A)	L_m (Wb/A)	C (C/V)	c'	Q-factor
1	908	11.1	4.27×10^{-19}	2.01×10^{-18}	1.42×10^{-11}	0.64	2.0
10	103	97.2	1.34×10^{-18}	2.01×10^{-16}	1.32×10^{-11}	0.59	2.9
100	10.5	952	4.12×10^{-18}	2.01×10^{-14}	1.27×10^{-11}	0.57	3.5
1000	1.06	9420	1.30×10^{-17}	2.01×10^{-12}	1.24×10^{-11}	0.56	3.8

listed in Table 4.3 indicate the broadening effect of doped Si due to its high electrical resistance, showing a difference of MP resonances with doped Si gratings with those in Ag deep gratings.

The adjustable c' values listed in Table 4.3 are very close for the four cases. The value 0.64 is also used for the LC model prediction in Figure 4.12(b), which agrees well with the full-wave simulation. It should be mentioned that $c' = 0.5$ is used in the predictions in Figure 4.12(a). Since trench width covers a wide range, the LC model predictions with a fixed c' value may deviate somewhat from the full-wave simulation when b is greater than 1 μm [200]. Also, the value of c' is related to the choice of the penetration depth used in Eq. (2.5) to evaluate the kinetic inductance. Even the field penetration depth works well in previous discussions, the penetration depth is only an approximation and, for some lossy materials, the power penetration depth might be more reasonable. Take the 2D tungsten grating thermal emitter in [142] as an example, the normal emittance spectrum is very similar for the 1D grating with the same geometric parameters in the x direction and extended to infinite in the y direction, as shown in Figure

4.14 . The optical properties of tungsten are obtained from [150] and linear interpolation is used between adjacent data points. The advantage of using a 2D nanostructure over 1D nanostructure is that it allows high emittance, particularly near 1.5 μm, for both polarizations [144]. The emittance peak at $\lambda = 1.55$ μm is direction independent for TM waves and the resonance wavelength is 7.6 times of the grating height. From the charge density and field distribution (not shown here), it can be convinced that MP resonance is responsible for this peak. Furthermore, one can use $c' = 0.58$ to well predict this MP resonance wavelength by using the power penetration depth (which is half of the electric field penetration depth) to evaluate the kinetic inductance. In addition, if one uses the power penetration depth to evaluate the kinetic inductance for doped Si gratings, the c' listed in Table 4.3 for SF = 1 would be 0.55 and closer to 0.5. On the other hand, the c' values for other cases listed in Table 2 change little since L_k/L_m is very small.

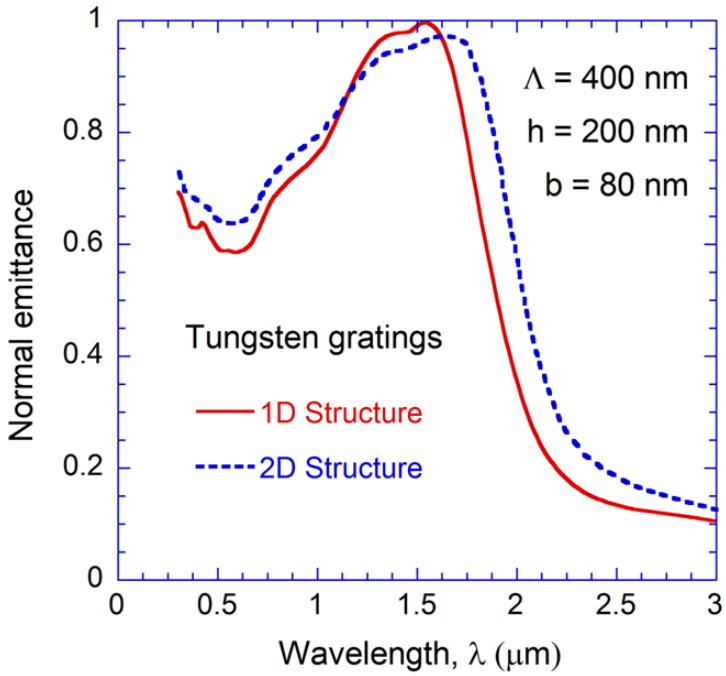

Figure 4.14 Emittance spectra for 1D and 2D tungsten gratings with Λ = 400 nm, h = 200 nm, and b = 80 nm. The 2D grating has the same geometries in both x and y directions.

Deep cavity gratings can also be used to create high broadband emittance. Unlike the coupling between non-periodic grating and waveguide mode [201] or some other symmetric-braking structures [202], MPs are highly localized and insensitive to the grating period. However, since MPs are sensitive to the height and width of the cavity, one may achieve broadband emittance by distribute cavities with different geometries within one period that can excite MPs at different frequencies. Similar structures have been investigated by researchers previously [160,185,203]. For those structures, the effective medium theory cannot be applied to calculate the emittance due to the complex geometric structures and full-wave simulation would be required.

One should note that the MP resonance does not exist for TE waves in 1D deep gratings. Even though the cavity mode explained by Eq. (4.6) is supposed to work for both TE and TM waves [159], the resonances associated with the height dimension do not show up for TE waves. This is because tangential component of electric field has to be continuous across the boundary of the trench, at least the first order resonance associated with the later dimension of the trench should exist (that is, l cannot be zero) for TE waves. Take the case in Figure 4.12(a) with b = 0.8 μm as an example, the normal emittance of spectrum for TE waves only show a cutoff wavelength around 1.6 μm, which is due to the resonance in the x direction associated with the trench width [159]. Similar results were obtained for slit array gratings [14], where the cavity modes or trapped modes can enhance the transmittance [204-206].

In conclusion, this study demonstrates that MPs can provide a convincing explanation of the fundamental resonance in deep gratings. By employing a simple LC model, the resonance wavelength can be quantitatively predicted. Due to the effect of the

kinetic inductance, the cutoff wavelength can be extended to more than ten times the grating height for very narrow grooves. The cutoff wavelength predicted by the conventional cavity resonance model agrees with the prediction of MPs only when the kinetic inductance is negligibly small compared with the mutual inductance. Ag and doped Si are considered and the resonance frequency can be scaled from near-infrared to microwave region by scaling the grating geometries. The MP model can also explain the thermal emission peak in 2D tungsten grating emitters. Caution should be taken when choosing the penetration depth and the constant c' for high-loss materials. This study further clarifies one of the underlying mechanisms of optical resonance in deep gratings, which can benefit the future design of thermal emitters based on 1D and 2D grating structures.

4.3 Anisotropic Metamaterials

Periodic micro/nanostructures of varies shapes have been used in metamaterial design [144,207-225] to manipulate light propagation. For metamaterial absorbers designed for energy harvesting purpose, patterns with polarization-independent radiative properties may be preferred [159,207,211,218,226]. However, some shapes can induce polarization-dependent response and can be used to design metamaterials with polarization control ability. These structures have recently attracted a lot of attention for their potential applications in plasmon-enhanced solar cells [216], nonlinear optics [227], holography [228], chemical sensing [229], one-way transmission [230,231], anomalous refraction [20], and Fano resonances [232]. Polarization-dependent emissivity can also be achieved using anisotropic metamaterials since the emissivity is equal to the absorptivity following

Kirchhoff's law [233]. Knowledge of thermal radiative properties are critical for applications such as material processing and spacecraft thermal insulation. Since the absorptivity can be obtained from the reflectance and transmittance by energy balance, the emissivity as a function of polarization angle can be calculated once the polarization-dependent reflectance and transmittance are known. To determine their radiative properties of metamaterials with anisotropic shapes, it is important to understand the polarization-dependent reflectance and transmittance.

The reflectance and transmittance exhibit an extreme when eigenmodes are excited [234,235], and for other polarizations, the reflectance and transmittance can be decomposed to that of the eigenmodes. Thus, it is critical to identify the eigenmodes associated with those shapes. To excite the eigenmodes, the incident wave should not only

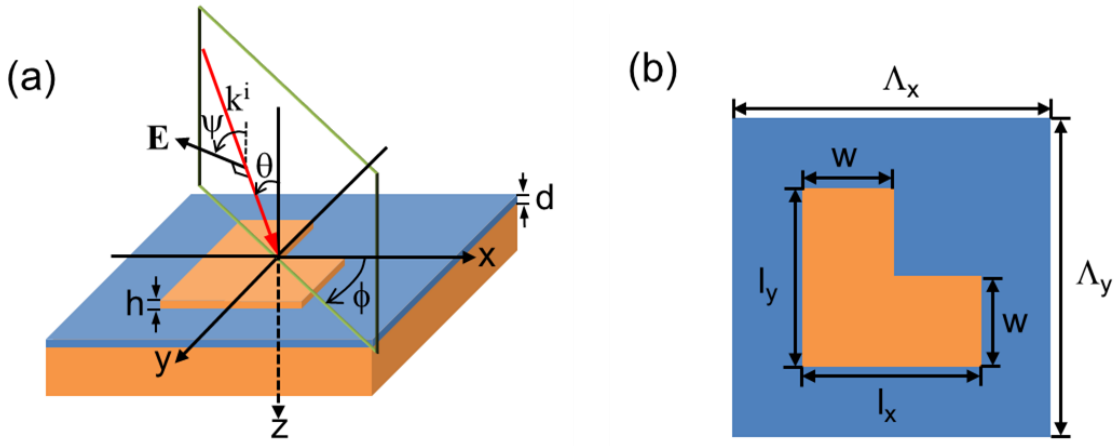

Figure 4.15 Illustration of the L-shape metal/dielectric/metal metamaterial: (a) Schematic of the plane of incidence, incident wavevector, electric field vector, polar angle θ, azimuthal angle ϕ, and polarization angle ψ; (b) the *x*-*y* plane view of the structure. Here, Λ_x and Λ_y are the period in the *x* and *y* directions, respectively, l_x and l_y are the length in the *x* and *y* directions, *w* is the width of the L shape, *h* is the thickness of the gold pattern, and *d* is the thickness of the Al_2O_3 dielectric film. The ground plane is assumed to be gold and semi-infinity.

at the eigenfrequency but also with the right polarization status. For the perfect metallic rod, the two eigenmodes can be excited at two eigenfrequencies when the electric field of incident wave is along the long and short axis, respectively, and those two polarizations status are the two eigenpolarizations. However, identifying the eigenpolarization can be very difficult when the shapes are asymmetrical.

Consider the film-coupled metamaterial structure shown in Figure 4.15 under illumination of a linearly polarized plane wave. If the L shape is symmetric in the *x* and *y* direction (i.e., with respect to the diagonals), the reflectance of the TE and TM waves is equal for normal incidence. However, when the polarization angle ψ, which is the angle between the plane of incidence (POI) and the electric field of the incident wave, is rotated, the reflectance extrema appear at 45° and 135° [236], which are the eigenpolarizations of the symmetric structure. On the other hand, if the arms of the L shape are not equal ($l_x \neq l_y$), the dependence on polarization angle becomes more complicated and it becomes difficult to identify the eigenpolarizations. Though the matrix method for anisotropic medium [237,238] may be applied for metamaterials analysis, obtaining the matrix can be difficult and it is more convenient if the reflectance and transmittance can be directly used to identify the eigenpolarizations. Thus, it is important to explore the relationship between the reflectance (transmittance) and the polarization angle for general anisotropic metamaterials.

For isotropic nonmagnetic materials, the reflectance of a linearly polarized wave with a polarization angle ψ can be related to the reflectance of TE wave and TM wave by $R_\psi = R_{\mathrm{TE}} \sin^2 \psi + R_{\mathrm{TM}} \cos^2 \psi$, and the relation $R_{\mathrm{TM}} \leq R_\psi \leq R_{\mathrm{TE}}$ holds according to the Fresnel's coefficients [3]. However, these rules are not applicable for anisotropic

metamaterials. The polarization-dependent reflectance or transmittance of anisotropic metamaterials has been observed by a number of researches [208,209,213-216,223,234]. Chen et al. [213] investigated plasmonic switching and electromagnetically induced transparency (EIT) with complex patterns. Cao et al. [214] studied the hybridized modes in a tri-rod nanostructure and polarization-dependent transmission. Husu et al. [234] discussed the eigenmodes in symmetric L-shape metamaterials based on the field distributions, but the way to identify the eigenmodes from reflectance (or transmittance) for asymmetric shapes has not been addressed. Sung et al. [223] experimentally demonstrated polarization dependence and birefringence effects of a symmetric L-shape metamaterial. Nevertheless, the relationship between the reflectance (or transmittance) and the polarization angle for general anisotropic metamaterials is still unclear.

In the present work, analytical expression of the reflectance or transmittance of a linearly polarized incident plane wave is derived as a function of the polarization angle. The reflectance or transmittance extrema are presented. A three-polarization-angle method is proposed to obtain the reflectance or transmittance for any polarization angle using the reflectance or transmittance of TE, TM, and another polarization status.

For reflection analysis, as shown in Figure 4.15(a), the direction of a linearly polarized incidence is characterized by the incident wavevector $\mathbf{k}^{\mathrm{i}}$ with polar angle θ and azimuthal angle ϕ, while polarization angle ψ $\left(-\pi < \psi \le \pi\right)$ describes the polarization status based on the angle between the POI and the electric field. Thus, TE and TM incident waves correspond to $\psi = 90°$ and $0°$, respectively. Due to the near-field coupling effect, the reflected wave generally has a different polarization status with the incident wave [146,239] and is generally elliptically polarized. Note that the focus of this study is on the

reflection or transmission not the polarization status. For a plane wave with arbitrary polarization incident from vacuum to a medium, the incident and reflected electric fields can be expressed as [237,240]:

$$\mathbf{E}^{\mathrm{i}} = \left(A_s \hat{\mathbf{s}}^{\mathrm{i}} + A_p \hat{\mathbf{p}}^{\mathrm{i}}\right) \exp\left(i\mathbf{k}^{\mathrm{i}} \bullet \mathbf{r} - i\omega t\right) \tag{4.8}$$

$$\mathbf{E}^{\mathrm{r}} = \left(B_s \hat{\mathbf{s}}^{\mathrm{r}} + B_p \hat{\mathbf{p}}^{\mathrm{r}}\right) \exp\left(i\mathbf{k}^{\mathrm{r}} \bullet \mathbf{r} - i\omega t\right) \tag{4.9}$$

where superscripts i and r denote incidence and reflection, respectively, $\hat{\mathbf{s}}$ and $\hat{\mathbf{p}}$ are the unit vectors in the electric field direction for TE (*s*-polarized) and TM (*p*-polarized) waves, respectively. It can be shown that

$$\hat{\mathbf{s}} = \frac{\mathbf{k} \times \hat{\mathbf{z}}}{\left|\mathbf{k} \times \hat{\mathbf{z}}\right|} \quad \text{and} \quad \hat{\mathbf{p}} = \frac{\hat{\mathbf{s}} \times \mathbf{k}}{\left|\hat{\mathbf{s}} \times \mathbf{k}\right|} \tag{4.10}$$

for either incident or reflected waves. Those two vectors can be used to describe the polarization status of incident and reflected waves, no matter they are linearly polarized or elliptically polarized. The general Fresnel's coefficients are defined by

$$r_{\alpha\beta} = B_\beta / A_\alpha \tag{4.11}$$

where $\alpha = s,p$ and $\beta = s,p$. The co-polarized reflection coefficients are r_{ss} and r_{pp}, while the cross-polarized reflection coefficients are r_{sp} and r_{ps}. The first and second subscripts describe the polarization status of the incident and reflected waves, respectively. For isotropic medium, no cross polarization can occur thus $r_{sp} = r_{ps} = 0$. Due to the anisotropy of the medium, in general, the reflected wave contains both *s* and *p* components though the incident wave is either purely *s*- or *p*-polarized. Therefore, the reflectance consists of contributions from both TE and TM waves. For incidence with polarization angle ψ and unit field amplitude, one obtains (by omitting the exponents)

$$\mathbf{E}_{\psi}^{\mathrm{i}} = \sin\psi\hat{\mathbf{s}}^{\mathrm{i}} + \cos\psi\hat{\mathbf{p}}^{\mathrm{i}} \tag{4.12}$$

$$\mathbf{E}_{\psi}^{\mathrm{r}} = \left(r_{ss}\sin\psi + r_{ps}\cos\psi\right)\hat{\mathbf{s}}^{\mathrm{r}} + \left(r_{sp}\sin\psi + r_{pp}\cos\psi\right)\hat{\mathbf{p}}^{\mathrm{r}} \tag{4.13}$$

Thus, the power reflectance is

$$\begin{aligned} R_{\psi} &= \left|r_{ss}\sin\psi + r_{ps}\cos\psi\right|^2 + \left|r_{sp}\sin\psi + r_{pp}\cos\psi\right|^2 \\ &= R_{\mathrm{TE}}\sin^2\psi + R_{\mathrm{TM}}\cos^2\psi + R_{\mathrm{C}}\sin\left(2\psi\right) \end{aligned} \tag{4.14}$$

Here, $R_{\mathrm{TE}} = \left|r_{sp}\right|^2 + \left|r_{ss}\right|^2$ and $R_{\mathrm{TM}} = \left|r_{pp}\right|^2 + \left|r_{ps}\right|^2$ are the reflectance for TE and TM waves, respectively, and $R_{\mathrm{C}} = \mathrm{Re}\left(r_{ss}r_{ps}^{*}\right) + \mathrm{Re}\left(r_{pp}r_{sp}^{*}\right)$, which is generally nonzero but can be either positive or negative due to cross polarization. Note that the incidence medium discussed here is assumed lossless and all the materials are nonmagnetic. Equation (4.14) can be recast as

$$R_{\psi} = A\sin\left(2\psi + \chi\right) + \bar{R} \tag{4.15}$$

where $A = \sqrt{\left(R_{\mathrm{TM}} - R_{\mathrm{TE}}\right)^2/4 + R_{\mathrm{C}}{}^2}$ is the amplitude and $\bar{R} = \left(R_{\mathrm{TE}} + R_{\mathrm{TM}}\right)/2$ is the average reflectance for TE and TM waves. The phase $\chi \in \left(-\pi,\ \pi\right]$ is determined by

$$\sin\chi = \frac{R_{\mathrm{TM}} - R_{\mathrm{TE}}}{2A} \quad \text{and} \quad \cos\chi = \frac{R_{\mathrm{C}}}{A} \tag{4.16}$$

Thus, the reflectance is a periodic function of the polarization angle with a period of π. This is expected since the response of the structure under an illumination polarized at $\psi + \pi$ can be obtained by that of ψ with a phase delay of π. Thus the reflectance (or transmittance to be shown later) is the same. The reflectance averaged over all polarization angles is the same as the reflectance for an unpolarized (or randomly polarized) incident wave, viz.

$$R_{\text{unpolarized}} = \frac{1}{2\pi}\int_{-\pi}^{\pi} R_\psi \, d\psi = \bar{R} \tag{4.17}$$

Thus, the reflectance of an unpolarized wave is equal to the average reflectance of TE and TM waves. In fact, for any two linearly polarized incident waves with orthogonal polarizations, their reflectance average is equal to the reflectance of an unpolarized wave.

Another interesting conclusion is that, due to the phase χ, the reflection extrema do not necessary occur at TE or TM polarization incidence. Based on Eq. (4.15), the reflection maximum and minimum actually occur at $\psi_1 = \pi/4 - \chi/2$ and $\psi_2 = \psi_1 + \pi/2$, respectively. After identifying the polarization status of the reflectance extrema, the reflectance for any polarizations can then be simply decomposed into the two reflection extrema as

$$R_\psi = R_{\max}\cos^2(\psi - \psi_1) + R_{\min}\sin^2(\psi - \psi_1) \tag{4.18}$$

where $R_{\max} = \bar{R} + A$ and $R_{\min} = \bar{R} - A$ are the reflection maximum and minimum, respectively. R_ψ follows an ellipse with a major axis of $2R_{\max}$ and a minor axis of $2R_{\min}$. Equation (4.18) is similar to decomposing the electromagnetic field, and thus offers a handy method for the calculation of the reflectance of an arbitrary polarization. Also, it can be seen that the difference of the polarization angles of the two reflection extrema is always 90°. If the reflectance of TE and TM waves are identical, i.e., $R_{\text{TE}} = R_{\text{TM}}$, then $\chi = 0$ or π, so that the two reflection extrema occur at $\psi = 45°$ and 135°, respectively. However, it cannot be identified that which one corresponds to the maxima because χ can be either 0 or π depending on the sign of R_{C}. If R_{C} is positive, then $\chi = 0$ and the maxima occurs at $\psi_1 = 45°$; if R_{C} is negative, then $\chi = \pi$ and the maxima occurs at $\psi_1 = -45°$ or 135°.

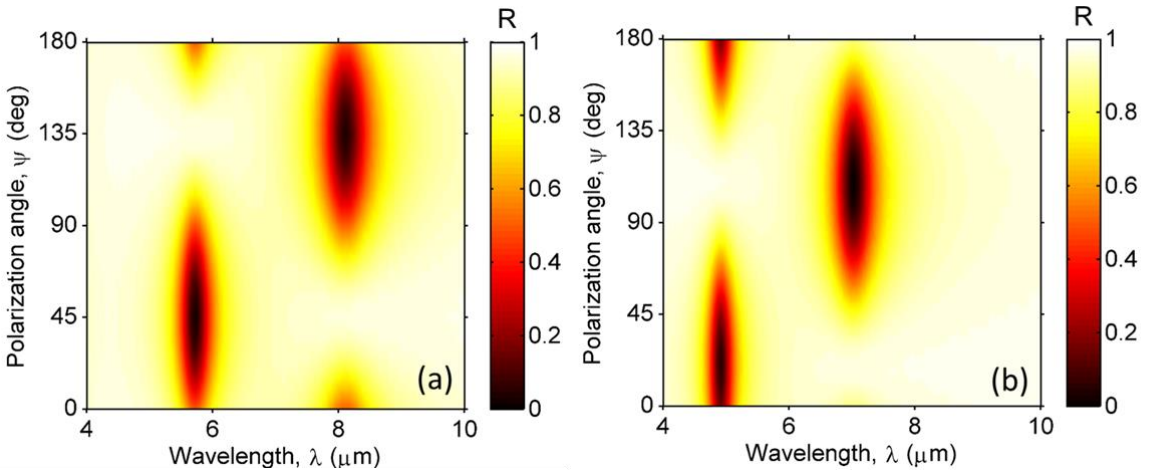

Figure 4.16 Normal reflectance (i.e. $\theta = 0°$ and $\phi = 0°$) contours obtained from FDTD simulations for the two metamaterials as shown in Figure 4.15 with the following parameters: d = 140 nm, h = 100 nm, $\Lambda_x = \Lambda_y = 3.2$ μm, $l_y = 1.7$ μm, and $w = 0.85$ μm. The two metamaterials have different x-direction lengths as follows: (a) the metamaterial with $l_x = 1.7$ μm; (b) the metamaterial with $l_x = 1.275$ μm.

As an example, Figure 4.16 plots the normal reflectance contours for the two structures as a function of the wavelength and polarization angle. The geometric structure is based on Figure 4.15 and the parameters are as follows. Both of the metamaterial structures consist a dielectric layer (Al_2O_3) of thickness d = 140 nm, sandwiched between an L-shape patterned 100-nm-thick gold layer and a gold ground plane that is opaque. The top metallic pattern repeats periodically in the x and y directions with the same period $\Lambda_x = \Lambda_y = 3.2$ μm. Also, the width w = 0.85 μm and y-direction length l_y = 1.7 μm for both structures. The only difference of the two structures lies in the x-direction length: l_x = 1.7 μm for Figure 4.16(a) and l_x = 1.275 μm for Figure 4.16(b). This difference results in different polarization dependence between the two structures. The dielectric function of gold is obtained from [150] and the refractive index of Al_2O_3 is set to 1.6, which is a good approximation of sapphire in the spectral range of interest. For the normal incidence in the

considered wavelength range, only zero-order diffraction (specular reflection) contributes to the reflectance, since all high-order terms are evanescent modes that are confined to the near-field regime of the subwavelength structure. The commercial Lumerical Solutions FDTD software was used to compute the reflectance of the metamaterial structures. Figure 4.16 shows the strong polarization dependence of the reflectance, especially at the wavelengths when the two resonances are excited. Details of the MPs that are responsible for the resonance absorption will be discussed later. For Figure 4.16(a), the first and second resonances are at 5.7 and 8.1 μm, respectively, and they shift to 4.9 and 7.0 μm in (b) for the asymmetric L-shape structure due to the effect of a shorter arm length in the *x* direction. The polarization-dependent reflectance at the resonance wavelength is shown in the following as illustration of the previous analysis and the three-polarization-angle method.

The structure with $l_x = l_y$ is symmetric along the diagonals; thus, the reflection extrema occur at $\psi = 45°$ and $135°$ as mentioned before. Furthermore, the reflectance of TE and TM waves is expected to be identical at normal incidence. This can be seen from Figure 4.16(a) at $\psi = 0°$ and 90°. For wavelengths 5.7 and 8.1 μm, the value of R_{TE}, R_{TM}, and R_C can be obtained based on the reflection coefficients. For both wavelengths, R_{TE} is equal to R_{TM}, however, $R_C = -0.470$ for $\lambda = 5.7$ μm and $R_C = 0.457$ for $\lambda = 8.1$ μm. Thus, based on the previous discussion, the reflection maximum is at $\psi = 135°$ for $\lambda = 5.7$ μm but 45° for $\lambda = 8.1$ μm. For the second structure, since the symmetry is broken, the reflectance of TE and TM are not equal any more as shown in Figure 4.16(b). Thus, the reflection extrema occur at other polarization angles other than 45° or 135°. Using the Fresnel's reflection coefficients from the simulation, one can calculate and show that the

reflection maxima $R_{\max}$ occurs at 110° for $\lambda = 4.9$ μm and 18.6° for $\lambda = 7.0$ μm, as shown by the reflection contour in Figure 4.16(b).

Moreover, the polarization dependence of reflectance can be determined from the reflectance of three different polarization angles in the range $0 \le \psi < \pi$. For example, if R_{TE}, R_{TM} and $R_{\psi'}$ are known, where ψ' is a polarization angle between 0° and 90°, the term R_{C} can be solved from Eq. (4.14). Furthermore, since the phase χ can also be determined, one can easily identify the polarization status of the reflectance extrema and then determine the eigenpolarizations. For instance, the reflectance for the second structure at $\lambda = 7.0$ μm and $\psi = 45°$ is 0.774. Using this value together with R_{TE} and R_{TM}, one can obtain $R_{\mathrm{C}} = 0.289$, which is the same as obtained from Fresnel's reflection coefficients. Furthermore, $R_{\max} = 0.964$, $R_{\min} = 0.006$, and $\psi_1 = 18.6°$ can also be determined. Then the reflectance as a function of polarization angle can be accurately obtained using either Eq. (4.14), (4.15) or (4.18), as shown in Figure 4.17 with markers. If the reflection spectra for TE, TM, and another polarization can be obtained from simulations or experiments, then the same calculation can be repeated for each wavelength and thus the reflection contours shown in Figure 4.16 can be reproduced based on the three-polarization-angle method.

For a semitransparent subwavelength periodic structure, under the same incident wave as described by Eq. (4.8) and illustrated in Figure 4.15(a), the transmitted electric field can be expressed as

$$\mathbf{E}^{\mathrm{t}} = \left(C_s \hat{\mathbf{s}}^{\mathrm{t}} + C_p \hat{\mathbf{p}}^{\mathrm{t}}\right) \exp\left(i\mathbf{k}^{\mathrm{t}} \bullet \mathbf{r} - i\omega t\right) \tag{4.19}$$

where the superscript t denotes transmission, and $\hat{\mathbf{s}}$ and $\hat{\mathbf{p}}$ are defined in terms of the

wavevector of the transmitted wave similar to the reflected wave. The general Fresnel's transmission coefficients are defined by $t_{\alpha\beta} = C_\beta / A_\alpha$, where α = *s,p* and β = *s,p*. For incidence with polarization angle ψ and unit field amplitude as expressed in Eq. (4.12), one obtains

$$\mathbf{E}_\psi^{\mathrm{t}} = \left(t_{ss}\sin\psi + t_{ps}\cos\psi\right)\hat{\mathbf{s}}^{\mathrm{t}} + \left(t_{sp}\sin\psi + t_{pp}\cos\psi\right)\hat{\mathbf{p}}^{\mathrm{t}} \tag{4.20}$$

Thus, the power transmittance is [3,146]

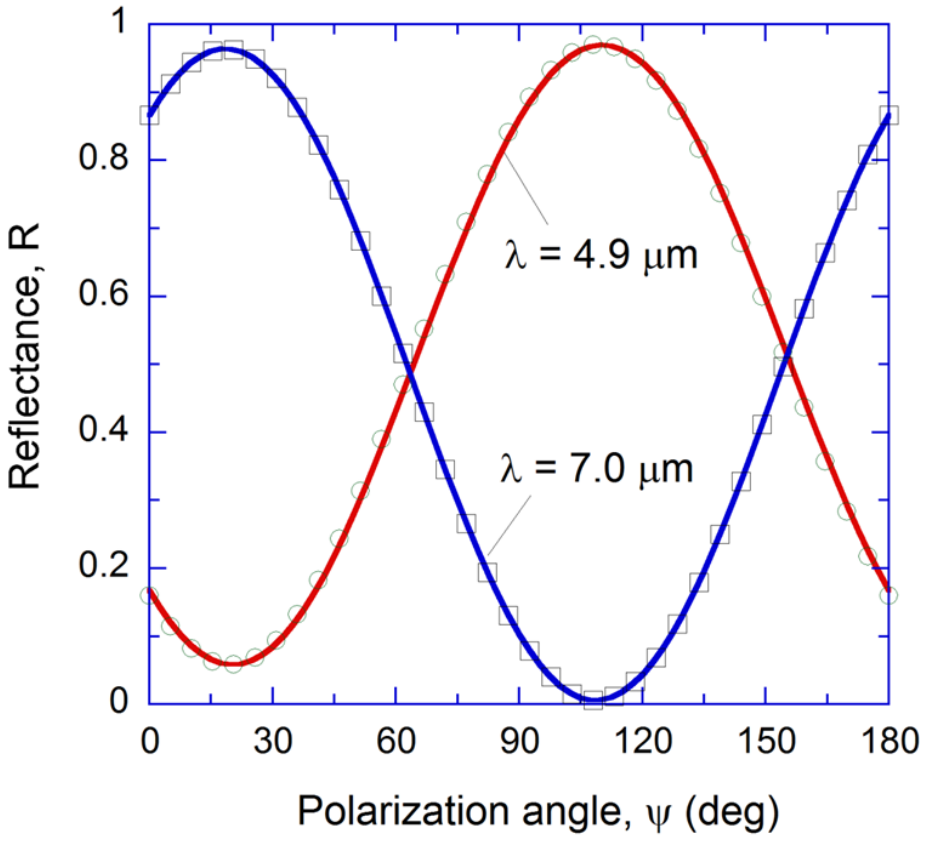

Figure 4.17 Simulated normal reflectance as a function of the polarization angle at the resonance wavelengths $\lambda = 4.9$ and 7.0 μm for the metamaterial associated with Figure 4.16b. Reproduced reflectance from the simulated reflectance for $\psi = 0°$, $\psi = 90°$, and $\psi = 45°$ using the three-polarization-angle method are shown with markers.

$$T_\psi = \left|t_{ss}\sin\psi + t_{ps}\cos\psi\right|^2 \mathrm{Re}\left(\frac{k_z^{\mathrm{t}}}{k_z^{\mathrm{i}}}\right) + \left|t_{sp}\sin\psi + t_{pp}\cos\psi\right|^2 \mathrm{Re}\left(\frac{\varepsilon^{\mathrm{i}}k_z^{\mathrm{t}}}{\varepsilon^{\mathrm{t}}k_z^{\mathrm{i}}}\right) \quad (4.21)$$

where ε is the dielectric function and k_z is the z component of the wavevector. By defining

$$T_{\mathrm{TE}} = \mathrm{Re}\left(\frac{\varepsilon^{\mathrm{i}}k_z^{\mathrm{t}}}{\varepsilon^{\mathrm{t}}k_z^{\mathrm{i}}}\right)\left|t_{sp}\right|^2 + \mathrm{Re}\left(\frac{k_z^{\mathrm{t}}}{k_z^{\mathrm{i}}}\right)\left|t_{ss}\right|^2 , \quad (4.22)$$

$$T_{\mathrm{TM}} = \mathrm{Re}\left(\frac{\varepsilon^{\mathrm{i}}k_z^{\mathrm{t}}}{\varepsilon^{\mathrm{t}}k_z^{\mathrm{i}}}\right)\left|t_{pp}\right|^2 + \mathrm{Re}\left(\frac{k_z^{\mathrm{t}}}{k_z^{\mathrm{i}}}\right)\left|t_{ps}\right|^2 , \quad (4.23)$$

and

$$T_{\mathrm{C}} = \mathrm{Re}\left(\frac{\varepsilon^{\mathrm{i}}k_z^{\mathrm{t}}}{\varepsilon^{\mathrm{t}}k_z^{\mathrm{i}}}\right)\mathrm{Re}\left(t_{pp}t_{sp}^*\right) + \mathrm{Re}\left(\frac{k_z^{\mathrm{t}}}{k_z^{\mathrm{i}}}\right)\mathrm{Re}\left(t_{ss}t_{ps}^*\right), \quad (4.24)$$

Equation (4.21) can be written as

$$T_\psi = T_{\mathrm{TE}}\sin^2\psi + T_{\mathrm{TM}}\cos^2\psi + T_{\mathrm{C}}\sin\left(2\psi\right) \quad (4.25)$$

Here, T_{TE} and T_{TM} are the transmittance for TE and TM waves, respectively. Since Eq. (4.25) has the same form as Eq. (4.14), all the previous discussion for reflection can be repeated for the transmittance. Hence, the transmittance is also a sinusoidal function of the polarization angle.

Two metamaterial surfaces in vacuum environment made of L shapes are used to demonstrate the transmittance as a function of the polarization angle in the same coordinate as with the reflectance analysis. Those metamaterial surfaces are made of the same L shape gold patterns as shown in Figure 4.15, without the dielectric layer and the ground plane. The normal transmittance contours are shown in Figure 4.18(a) and (b) for l_x = 1.7 μm and 1.275 μm, respectively, keeping the period, thickness, and *y*-directional length the same as for Figure 4.16. The resonance at $\lambda = 3.2$ μm is due to SPPs [144], and the other two

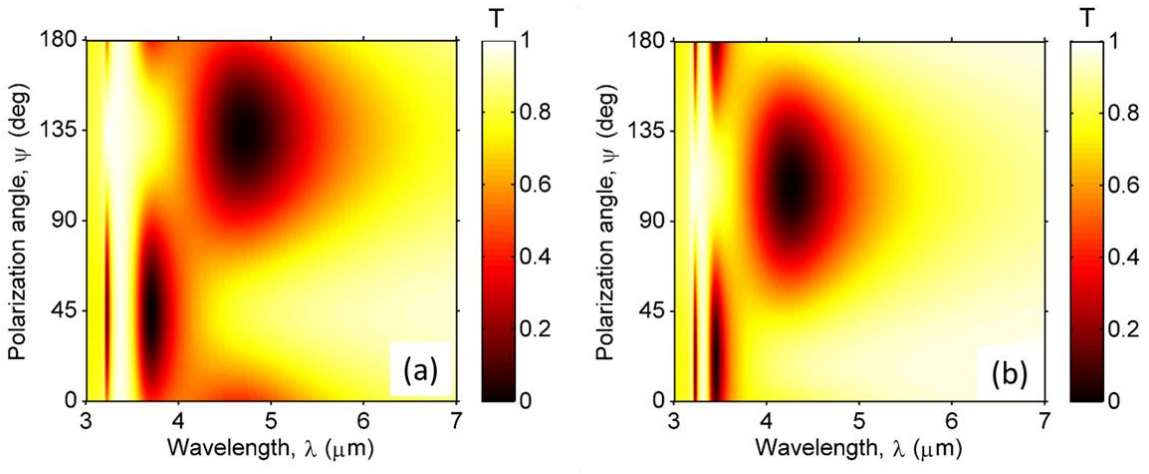

Figure 4.18 Normal transmission contours obtained from FDTD simulations for the two L-shape metamaterial surfaces. The two structures are made of the same L-shape gold patterns as shown in Figure 4.15, without the dielectric layer and the ground plane: (a) The metamaterial surface with $l_x = 1.7$ μm; (b) The metamaterial surface with $l_x = 1.275$ μm.

resonances can be attributed to the localized plasmonic resonances associated with the L shape [234]. Due to the relatively short arm in the *x* direction, the two localized resonances shift toward shorter wavelengths in Figure 4.18(b) compared with Figure 4.18(a). Due to symmetry, the transmittance extrema in Figure 4.18(a) occur at $\psi = 45°$ and 135°, but they are at about $\psi = 110°$ and 20° for Figure 4.18(b) at $\lambda = 3.2$ μm. These results can be also obtained with three-polarization-angle method from the transmittance of TE, TM, and another polarization. The contour plots can thus be reproduced if the transmittance at three different polarization angles is known at each wavelength. The procedure is similar to that for the reflectance and will not be repeated here. Note that the above analysis is valid for all incident directions, not just the normal direction, even though the reflectance and transmittance contours shown here are for normal incidence.

The above discussion assumes that only the zero-order (specular) diffracted wave is propagating wave, while all high orders are evanescent waves that do not carry energy

in the far field. As discussed next, this assumption is not necessary and the diffraction efficiency for each order as well as the directional-hemispherical reflectance for diffracted waves also follow similar trend. This still holds for practical fabricated structures as long as scattering due to surface roughness, inhomogeneity, and other irregularities is negligibly small.

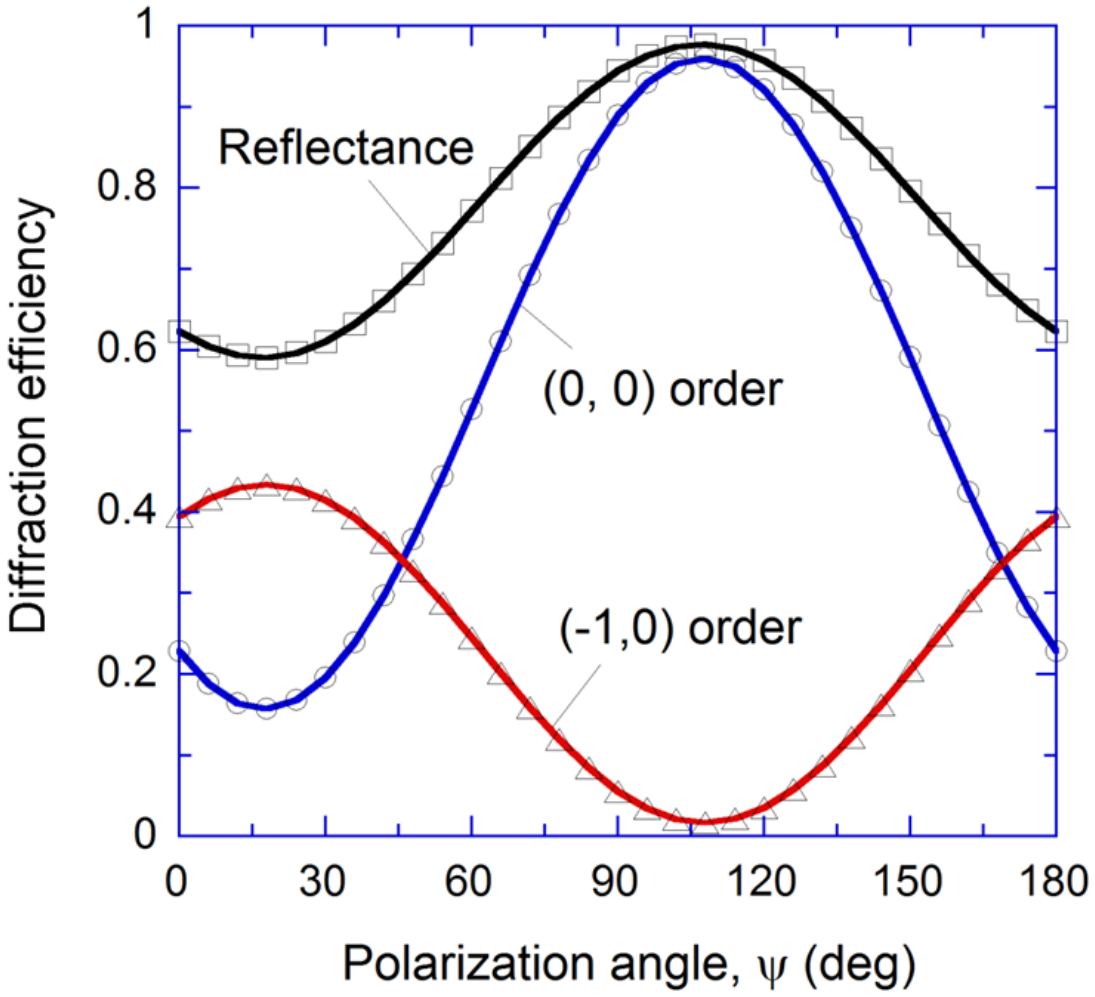

Figure 4.19 Polarization-dependent reflectance and DEs of the propagating orders at incident direction $\theta = 45°$ and $\phi = 0°$ for the metamaterial corresponding to Figure 4.16b at $\lambda = 4.9$ μm. Markers are reproduced by the three-polarization-angle method using the simulated DEs and reflectance at $\psi = 0°$, 45°, and 90°.

At large incident angles, the two-dimensional periodic metamaterial structure shown in Figure 4.15 can reflect multiple propagating waves that are not necessarily in the POI, but in the planes of diffraction [144,146]. These diffraction orders may be denoted as *m* and *n* in the *x* and *y* directions, respectively. If the incident wave is described by Eq. (4.12), then the electric field of the *mn*-th reflected order can be expressed as

$$\mathbf{E}^{\mathrm{r}}_{\psi,mn} = \left(r_{ss,mn}\sin\psi + r_{ps,mn}\cos\psi\right)\hat{\mathbf{s}}^{\mathrm{r}}_{mn} + \left(r_{sp,mn}\sin\psi + r_{pp,mn}\cos\psi\right)\hat{\mathbf{p}}^{\mathrm{r}}_{mn} \quad (4.26)$$

where $\hat{\mathbf{s}}_{mn}$ and $\hat{\mathbf{p}}_{mn}$ are defined similar to $\hat{\mathbf{s}}$ and $\hat{\mathbf{p}}$ but are in terms of the wavevector of the *mn*-th reflected order. Thus the diffraction efficiency (DE) can be obtained as [146]

$$DE^{\mathrm{r}}_{\psi,mn} = R_{\mathrm{TE},mn}\sin^2\psi + R_{\mathrm{TM},mn}\cos^2\psi + R_{\mathrm{C},mn}\sin(2\psi) \quad (4.27)$$

where
$$R_{\mathrm{TE},mn} = \mathrm{Re}\left(\frac{k^{\mathrm{r}}_{z,mn}}{k^{\mathrm{i}}_{z}}\right)\left(\left|r_{sp,mn}\right|^2 + \left|r_{ss,mn}\right|^2\right),$$

$$R_{\mathrm{TM},mn} = \mathrm{Re}\left(\frac{k^{\mathrm{r}}_{z,mn}}{k^{\mathrm{i}}_{z}}\right)\left(\left|r_{pp,mn}\right|^2 + \left|r_{ps,mn}\right|^2\right),$$

and
$$R_{\mathrm{C},mn} = \mathrm{Re}\left(\frac{k^{\mathrm{r}}_{z,mn}}{k^{\mathrm{i}}_{z}}\right)\left[\mathrm{Re}\left(r_{ss,mn}r^{*}_{ps,mn}\right) + \mathrm{Re}\left(r_{pp,mn}r^{*}_{sp,mn}\right)\right].$$

Equation (4.27) has the same form as Eq. (4.14) and therefore, the DE for each order is a sinusoidal function of the polarization angle with a period of π. However, the phase and diffraction efficiency extrema would in general be different for different orders, though the diffraction efficiency extrema still occur at a pair of orthogonal polarization status for different orders. For example, Figure 4.19 illustrates the DE as a function of polarization angle for the second structure with $\phi = 0°$ and $\theta = 45°$. In this direction, the (0, 0) and (–1, 0) order of the reflected wave are propagating and they have different phases as the figure

shows. The directional-hemispherical reflectance (DHR), or simply reflectance, can be obtained by adding the DE of each order:

$$R_\psi = \sum_{m,n} DE^{\mathrm{r}}_{\psi,mn} = R_{\mathrm{TE}} \sin^2\psi + R_{\mathrm{TM}} \cos^2\psi + R_{\mathrm{C}} \sin(2\psi) \qquad (4.28)$$

where R_{TE}, R_{TM}, and R_{C} are the summation of $R_{\mathrm{TE},mn}$, $R_{\mathrm{TM},mn}$, and $R_{\mathrm{C},mn}$ of all orders. Therefore, R_{TE} and R_{TM} are the reflectance of TE and TM waves, respectively. Equation (4.28) is similar to the case where only one order is propagating and thus the DHR is always a sinusoidal function. Similarly, the DHR and DE can be reproduced by using three-polarization-angle method from the DHR and DEs of three different polarizations. For instance, the makers in Figure 4.19 show the reproduced results by using the reflectance and DEs for TE, TM, and $\psi = 45°$. The results obtained from the three-polarization-angle method match the results of direct simulations exactly.

For semitransparent metamaterials that have multiple transmission orders, if the incident wave is expressed as Eq. (4.12), the transmitted electric field for the *mn*-th order can be obtained by

$$\mathbf{E}^{\mathrm{t}}_{\psi,mn} = \left(t_{ss,mn}\sin\psi + t_{ps,mn}\cos\psi\right)\hat{\mathbf{s}}^{\mathrm{t}}_{mn} + \left(t_{sp,mn}\sin\psi + t_{pp,mn}\cos\psi\right)\hat{\mathbf{p}}^{\mathrm{t}}_{mn} \qquad (4.29)$$

where $\hat{\mathbf{s}}_{mn}$ and $\hat{\mathbf{p}}_{mn}$ are defined similar to $\hat{\mathbf{s}}$ and $\hat{\mathbf{p}}$ but are in terms of the wavevector of the *mn*-th transmission order. Thus, the DE for transmitted waves is [146]

$$DE^{\mathrm{t}}_{\psi,mn} = T_{\mathrm{TE},mn} \sin^2\psi + T_{\mathrm{TM},mn} \cos^2\psi + T_{\mathrm{C},mn} \sin(2\psi) \qquad (4.30)$$

where $$T_{\mathrm{TE},mn} = \mathrm{Re}\left(\frac{\varepsilon^{\mathrm{i}} k^{\mathrm{t}}_{z,mn}}{\varepsilon^{\mathrm{t}} k^{\mathrm{i}}_{z}}\right)\left|t_{sp,mn}\right|^2 + \mathrm{Re}\left(\frac{k^{\mathrm{t}}_{z,mn}}{k^{\mathrm{i}}_{z}}\right)\left|t_{ss,mn}\right|^2,$$

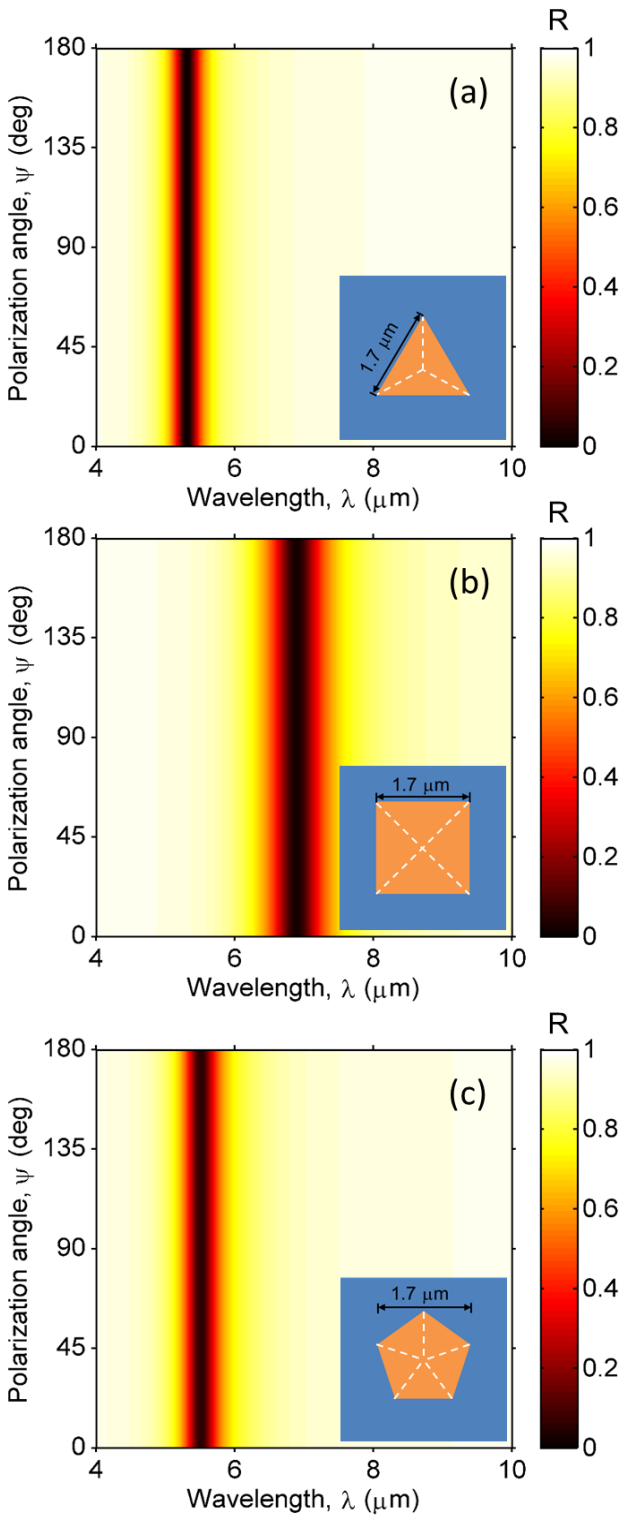

Figure 4.20 Normal reflectance contours for some metamaterials made by replacing the L shapes in Figure 4.15 with a different pattern: (a) equilateral triangles; (b) squares; (c) regular pentagons.

$$T_{\mathrm{TM},mn} = \mathrm{Re}\left(\frac{\varepsilon^{\mathrm{i}} k_{z,mn}^{\mathrm{t}}}{\varepsilon^{\mathrm{t}} k_z^{\mathrm{i}}} \right) \left| t_{pp,mn} \right|^2 + \mathrm{Re}\left(\frac{k_{z,mn}^{\mathrm{t}}}{k_z^{\mathrm{i}}} \right) \left| t_{ps,mn} \right|^2,$$

and $$T_{\mathrm{C},mn} = \mathrm{Re}\left(\frac{\varepsilon^{\mathrm{i}} k_{z,mn}^{\mathrm{t}}}{\varepsilon^{\mathrm{t}} k_z^{\mathrm{i}}} \right) \mathrm{Re}\left(t_{pp,mn} t_{sp,mn}^{*} \right) + \mathrm{Re}\left(\frac{k_{z,mn}^{\mathrm{t}}}{k_z^{\mathrm{i}}} \right) \mathrm{Re}\left(t_{ss,mn} t_{ps,mn}^{*} \right).$$

Equation (4.30) has the same form as Eq. (4.27) and thus the conclusions for reflection DEs also hold for transmission DEs.

Furthermore, since the reflectance is a sinusoidal function of the polarization angle, if three different polarization angles that have the same reflectance can be found in the range $0 \le \psi < \pi$, then $R_{\mathrm{TE}} = R_{\mathrm{TM}}$ and $R_{\mathrm{C}} = 0$. Thus the reflectance becomes independent of polarization angle. For instance, the L-shape pattern in Figure 4.15 is replaced by regular polygon patterns as shown in the insets of Figure 4.20(a) to (c), where an equilateral triangle, a square, and a regular pentagon pattern are used, respectively. Due to the symmetry, the reflectance at normal incidence is expected to be equal when the electric field of the incident wave is along the directions of 45° and 135°. A third polarization angle, e.g., 90°, can be used to check the polarization dependence. As it turned out, the normal reflectance is polarization independent; this is also confirmed by the contour plots shown in Figure 4.20 obtained from the FDTD simulations. Other symmetrically patterned structures like crosses [217] and fishnet [226] also exhibit polarization independence. Similar rules also hold for semitransparent anisotropic metamaterials whose transmission is of interest. In the next, we will explore the mechanism of the two resonances in Figure 4.16(a).

As Figure 4.16(a) shows, the first and second resonances are at λ = 5.70 μm and 8.13 μm, respectively. The instantaneous electromagnetic field distributions are shown in Figure 4.21. These electromagnetic field profiles are for the plane in the middle of dielectric

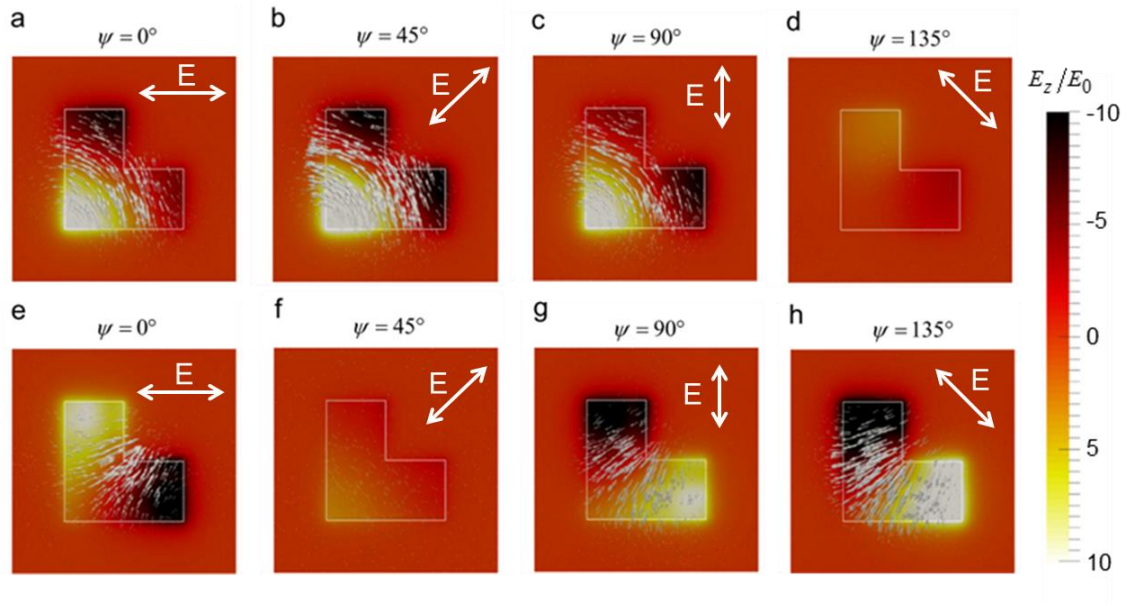

Figure 4.21 Electric field contour at each resonant wavelength in the middle plane of the dielectric spacer with varying polarization angles. The contour shows the relative magnitude of the *z* component of the electric field. (a-d) λ = 5.7 μm and (e-h) λ = 8.13 μm.

spacer at the resonant wavelength under illuminations of different incidence with varying polarization angles. The magnitudes of incident electric wave are all unit. The contour shows the *z* component of the electric field normalized by the magnitude of the incident electric field and the vectors show the direction and magnitude of the magnetic field. Also, the length of the arrows indicates the magnitude of the instantaneous magnetic field and the scale bar for the magnetic fields is the same for all plots. The wavelengths of incidence are λ = 5.70 μm and 8.13 μm in a-d and e-h, respectively. Also, the polarization angles are $0°, 45°, 90°,$ and $135°$. Although it does not show here, the case for polarization angle $\psi = 180°$ was calculated, and the fields are pointing to the opposite direction at each space point for both the electric and magnetic field as compared with the case for $\psi = 0°$, since $\psi = 180°$ can be treated as $\psi = 0°$ with an additional π phase delay.

Since the electromagnetic field at $\psi = 45°$ can be obtained by linearly adding the field shown in Figure 4.21(a) and (c) with an amplitude modulation of $\sqrt{2}/2$, the resonance in (b) is enhanced. Similarly, the field at $\psi = 135°$ can be obtained by linearly adding the field shown in (c) with an amplitude modulation of $\sqrt{2}/2$ and the field for $\psi = 180°$ with the same amplitude modulation. Since the field for $\psi = 180°$ is pointing to the opposite direction compared with (a), the magnetic fields cancel out with each other and resonance effect is suppressed at $\psi = 135°$ as shown in (d). This is the reason why at λ = 5.70 μm the emittance peak is maximized at $\psi = 45°$. Similar explanation can be applied to understand the polarization dependence at λ = 8.13 μm. However, at this wavelength, the magnetic field in (e) and (g), are generally pointing to opposite directions. Also, the magnetic field in (g) and the case for $\psi = 180°$, respectively, are pointing to the same direction, resulting in that the resonance is enhanced in (h) but annihilated in (f). Therefore, the emittance peak is maximized at $\psi = 135°$ for λ = 8.13 μm. Therefore, $\psi = 45°$ and 135° are the eigenpolarizations of the resonance at λ = 5.70 μm and 8.13 μm, respectively.

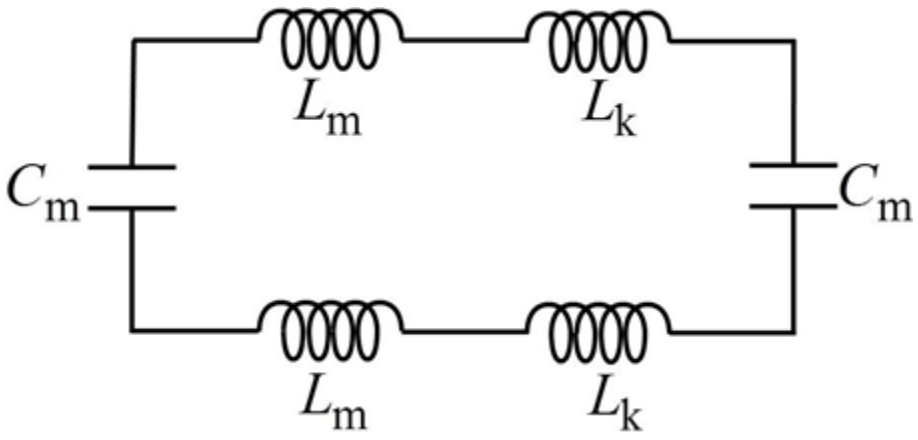

Figure 4.22 Schematic of the equivalent LC circuit.

The two resonances at λ = 5.70 μm and 8.13 μm can be explained using a LC circuit shown in Figure 4.22. For wavelength λ = 5.70 μm, the eigenpolarization suggests that the current is oscillating at $\psi = 45°$, while for λ = 8.13 μm, the current is along $\psi = 135°$. The parameters used in the LC model are evaluated based on the field distribution at resonances. For the resonant wavelength λ = 5.70 μm, the mutual and kinetic inductance and capacitance can be evaluated as

$$L_{\mathrm{m}} = \frac{1}{2}\mu_0 \frac{\frac{\sqrt{2}}{2} l_x d}{\frac{\pi}{4} l_x} = \frac{\sqrt{2}}{\pi}\mu_0 d \tag{4.31}$$

$$L_{\mathrm{k}} = -\frac{\frac{\sqrt{2}}{2} l_x}{\varepsilon_0 \omega^2 \frac{\pi}{4} l_x \delta \left(\varepsilon'^2_{\mathrm{Au}} + \varepsilon''^2_{\mathrm{Au}}\right)} \frac{\varepsilon'_{\mathrm{Au}}}{} = -\frac{2\sqrt{2}}{\pi\varepsilon_0 \omega^2 \delta} \frac{\varepsilon'}{\left(\varepsilon'^2_{\mathrm{Au}} + \varepsilon''^2_{\mathrm{Au}}\right)} \tag{4.32}$$

$$C_{\mathrm{m}} = c' \varepsilon_{\mathrm{Al_2O_3}} \varepsilon_0 \frac{3 l_x^2}{4d} \tag{4.33}$$

For the inductance calculation, the length *l* is assumed to be curved along the diagonal, and also the characteristic length is defined along the diagonal. For the capacitance, the area of L-shape pattern used. For the resonant wavelength λ = 8.13 μm, the parameters can be expressed as

$$L_{\mathrm{m}} = \frac{1}{2}\mu_0 \frac{\sqrt{2} l_x d}{\frac{\sqrt{2}}{2} l_x} = \mu_0 d \tag{4.34}$$

$$L_{\mathrm{k}} = -\frac{\sqrt{2} l_x}{\varepsilon_0 \omega^2 \frac{\sqrt{2}}{2} l_x \delta \left(\varepsilon'^2_{\mathrm{Au}} + \varepsilon''^2_{\mathrm{Au}}\right)} \frac{\varepsilon'_{\mathrm{Au}}}{} = -\frac{2}{\varepsilon_0 \omega^2 \delta} \frac{\varepsilon'_{\mathrm{Au}}}{\left(\varepsilon'^2_{\mathrm{Au}} + \varepsilon''^2_{\mathrm{Au}}\right)} \tag{4.35}$$

$$C_{\mathrm{m}} = c'\varepsilon_{\mathrm{Al_2O_3}}\varepsilon_0 \frac{3l_x^2}{4d} \tag{4.36}$$

The optimized parameters *c'* for the L-shape pattern metamaterial can be obtained as 0.25 and 0.23 for fitting the resonant wavelengths λ = 5.70 μm and 8.13 μm, respectively. Consequently, this explanation with the LC circuit model is valid for the L-shape metamaterial. Thus, the two emittance peaks are due to two eigenmodes of the structure, which are MPs.

In conclusion, the reflectance and transmittance of a linearly polarized wave are shown to be sinusoidal functions of the polarization angle. The two reflectance (or transmittance) extrema occur at a pair of orthogonal polarization status called eigenpolarizations. For an arbitrary polarization status, the reflectance, transmittance as well as diffraction efficiency of each diffracted order can be determined using the three-polarization-angle method. The two eigenmodes in the L-shape structure is due to MPs with different eigenpolarizations. This work helps the understanding of the polarization dependence of reflectance or transmittance of anisotropic nanostructures and facilitates the investigation of the eigenmodes in metamaterial structures and their potential applications for polarization control.

CHAPTER 5

RADIATIVE PROPERTIES OF 2D MATERIALS AND THE COUPLING WITH METAMATERIALS

In this chapter, the micro/nanostructured 2D materials and their coupling with plasmonic metamaterials are investigated regarding their radiative properties. Section 5.1 studies a hybrid structure constructed with a monolayer graphene on a deep grating. Primary focus is in the visible and near-infrared range, where graphene shows a wavelength-independent real conductivity. Section 5.2 investigates a metal grating covered by a graphene ribbon array, where MPs and graphene plasmons in ribbons couple significantly to create unique radiative properties. Section 5.3 demonstrates another hybrid structure constructed with hyperbolic material, hBN, with metal gratings. The coupling between hyperbolic phonon polaritons and MPs are investigated. In Section 5.4, a trapezoidal grating made of hBN is studied to take advantage of its hyperbolic response that can enable broadband perfect absorption. This Chapter ends with Section 5.5, where the resonance effect of the directional hyperbolic phonon polaritons are scrutinized in hBN resonators with different shapes.

5.1. Graphene-covered Metal Gratings in the Visible and Near-infrared

As a layered 2D material with carbon atoms arranged in a honeycomb lattice, graphene has unique electrical, mechanical, and optical properties [61,70]. Unlike conventional metals, the electrons in graphene are massless quasiparticles (Dirac fermions), which exhibit a linear energy-momentum dispersion. Its linear energy dispersion relation implies a vanishing of the effective mass of the carriers, and a remarkably high carrier

mobility reaching 200,000 $cm^2 V^{-1}s^{-1}$ at room temperature for both electrons and holes.[59] This high mobility makes graphene a great candidate for ultrafast optoelectronic devices such as transistors [241] and photodetectors [242-245] in the visible and near-infrared (NIR) range. In the visible and near-infrared (NIR) region, interband transitions can happen in doped graphene and photons absorbed generate electron-hole pairs, creating electrical signals for photodetection. This makes graphene a potential material for the construction of an ultrafast photodetector, considering its high carrier mobility. However, because of its atomically thin thickness, the absorptance of graphene is only about 0.023 in this spectral region, and is related to the fine structure constant [67]. High absorption is also preferred for graphene-based optical antennas [73] and solar cells [75]. This minimal absorptance substantially hinders these applications; therefore, enhancing the absorption of graphene has drawn much attention recently.

The chemical potential of graphene can be changed through electrical gating or chemical doping and the optical properties of highly doped graphene resemble those of Drude-type materials in mid- to far-infrared region [246]. In this case, the graphene absorption can be improved by taking advantage of its plasmonic response and can also be tuned by changing its chemical potentials [61,247]. One can make patterned graphene resonator and excite plasmons associated with them. For example, Thongrattanasiri et al. [68] demonstrated total light absorption by critical-coupling in a single round-patterned sheet. Fang et al. [248] showed tunable enhanced absorption in graphene nano-disk array from 0.03 to 0.30 by exciting local plasmonic resonances. Graphene can also be shaped to ribbons [94,249] to enhance its absorption since graphene surface plasmons can be excited in ribbons [250-252]. Graphene patch arrays of cross shapes [253] and square shapes [254]

have also been demonstrated for absorption enhancement. In addition, graphene can be used together with other structures such as gratings and photonic crystals to enhance its absorption [255-262]. For example, Gao et al. [263] and Zhan et al. [264] utilized a dielectric surface-relief grating to excite the surface plasmon wave in graphene, which also enhanced graphene absorption.

The above-mentioned plasmonic responses, however, cannot be excited in the visible and NIR region to enhance graphene absorption because the optical property of graphene is dominated by the interband transition. One way to enhance graphene absorption in this frequency region is to employ a microcavity that enables light to pass through the graphene sheet multiple times to improve the absorption of graphene [244]. Another way is to utilize the plasmonic oscillations associated with optical nanoantennas that can create a localized strong electric field [73,74,245,265-267]. While the attenuated total reflection configuration setup can also be employed to enhance absorption near the critical angle [268], the enhancement is generally not very significant. It should be noted that guided resonances in dielectric gratings [269,270] can create an enhanced electric field to boost graphene absorption, through critical coupling using photonic crystals [271], and may achieve total absorption. However, the enhancement achieved by this mechanism is usually narrowband and highly directionally sensitive.

In this work, a method of enhancing the absorptance of graphene is presented by using a deep metallic grating, which can enable a strong localized electric field at the MPs and SPPs. Figure 5.1 illustrates the structure of the graphene-covered deep gratings. The one-dimensional (1D) grating is made of silver (Ag) and the geometric parameters are period Λ, height h, and trench width b. When the plane of incidence is the x-z plane, the

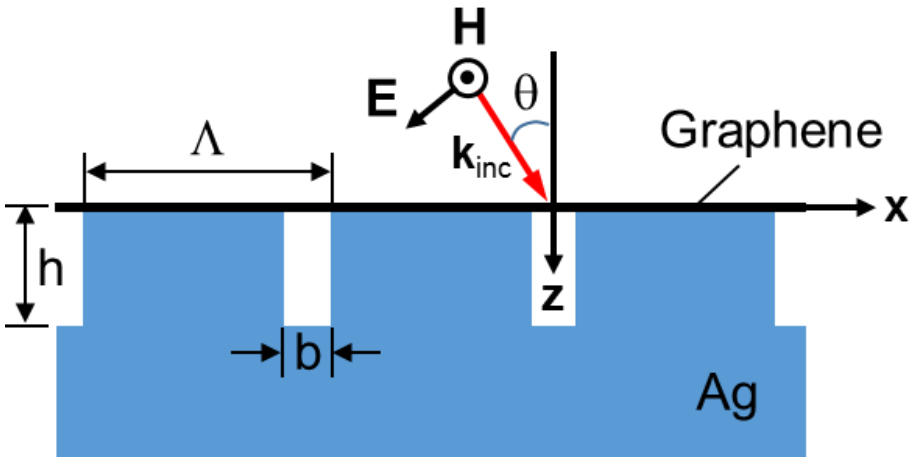

Figure 5.1 Schematic of the graphene-covered 1D grating nanostructure for a plane TM wave incident at an angle of θ. The top medium and the trench region are assumed to be vacuum or air, and the bottom Ag region is assumed to be opaque or semi-infinite.

wavevector of an incident plane wave does not have a *y*-component and can be expressed as $\mathbf{k}_{\text{inc}} = k_x\,\hat{\mathbf{x}} + k_z\,\hat{\mathbf{z}} = k_0 \sin\theta\,\hat{\mathbf{x}} + k_0 \cos\theta\,\hat{\mathbf{z}}$, where θ is the incidence angle and k_0 is the wavevector in vacuum. For the 1D grating considered here, since the wavevectors of all the diffracted waves lie in the *x*-*z* plane, the electromagnetic field is independent of *y* and no resonance excitation occurs in the *y*-direction. Here, the incident medium is assumed to be vacuum or air (but with the same dielectric property as that of vacuum). The graphene monoatomic layer lies at the top surface of the gratings at $z = 0$. Only TM waves are considered in this study, since MPs and SPPs can only be excited when the magnetic field is in the *y*-direction for the 1D grating. The metal under the grating region is assumed to be sufficiently thick for it to be opaque. Therefore, the incoming radiation will be either reflected or absorbed, and the absorptance can be indirectly calculated from one minus the reflectivity.

RCWA is used to calculate the reflectivity of the structure as well as the field distribution, with sufficient Fourier expansion orders to ensure convergence. In the

simulation, the dielectric function of Ag, $\varepsilon_{\mathrm{Ag}}$, is modeled with the Drude model mentioned before, while graphene is modeled as a ultrathin layer with a thickness Δ according to an equivalent dielectric function [70]:

$$\varepsilon(\omega) = 1 + i\frac{\sigma_{\mathrm{s}}}{\varepsilon_0 \omega \Delta} \tag{5.1}$$

where σ_{s}, ε_0, and ω are the sheet conductivity, the vacuum permittivity, and the angular frequency, respectively. Another method is to model graphene as a 2D conductive film with a sheet conductivity σ_{s}, which induces a surface current along graphene and thus modifying the boundary conditions for the magnetic field. Those two methods yield identical results as long as Δ is chosen to be sufficiently small to ensure convergence [271,272]. In this study, graphene is treated as a thin film with an isotropic dielectric function so that the above presented RCWA algorithm can be directly employed without modifying the boundary conditions. In the calculation, Δ = 0.3 nm is chosen to ensure convergence. The following parameters are used in all the calculations presented in this work: chemical potential μ = 0.3 eV, relaxation time $\tau = 10^{-13}$ s, and temperature T = 300 K. With these parameters, $k_{\mathrm{B}}T \ll \mu$ is satisfied, the interband contribution is manifested by a step function feature and the conductivity at photon energies above the threshold at $\hbar\omega \approx 2\mu$ is dominated by interband transitions [116]. This yields a purely real conductivity $\sigma_{\mathrm{s}} = \sigma_{\mathrm{I}} = e^2/4\hbar$ when photon energy is greater than 0.6 eV, which corresponds to a wavenumber of 4762 cm^{-1} (or wavelength of 2.1 μm). Since the frequency region of interest in the present work is in the visible and near-infrared region, the conductivity of graphene is essentially a constant equal to $e^2/4\hbar$.

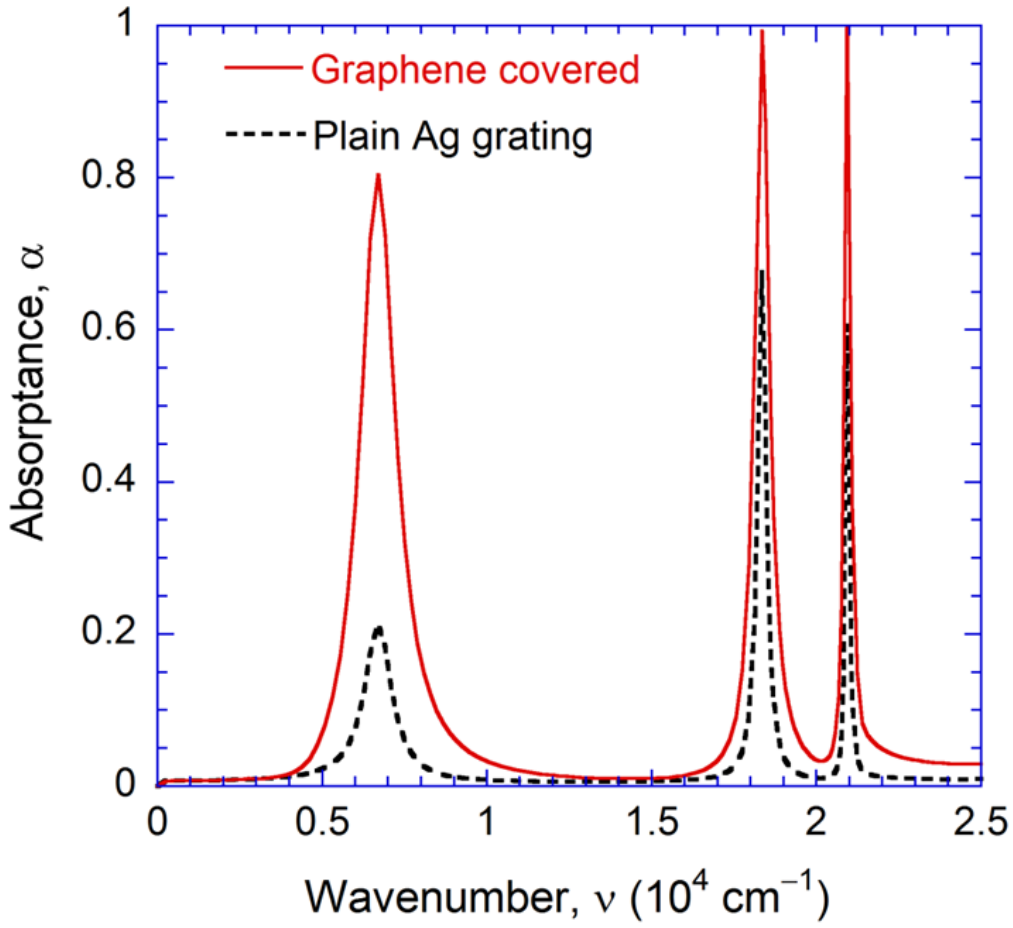

Figure 5.2 Comparison of the absorptance of the graphene-covered and plain Ag grating with h = 200 nm, Λ = 400 nm, and b = 30 nm at incidence angle θ = 10° for TM waves.

The absorptance spectra for the plain and graphene-covered structure are shown in for TM waves at incidence angle θ = 10° in terms of the wavenumber. The absorptance is for the whole structure and calculated from one minus the reflectance that is predicted by RCWA. In the simulation, the geometric parameters of the Ag grating are set to Λ = 400 nm, b = 30 nm, and h = 200 nm. These are the default values used in the present study unless otherwise specified. To realize a structure with such geometries, one could separately fabricate graphene using chemical vapor deposition on a copper foil and the grating structure by e-beam lithography with a lift-off process. Then, graphene could be

transferred onto the grating to form the desired structure. There exist three distinct peaks in the absorptance spectra located at wavenumber ν = 6700 cm^{-1} (1.49 μm), 18350 cm^{-1} (545 nm), and 20930 cm^{-1} (478 nm). The value in parentheses indicates the corresponding wavelength. As will be explained later, these peaks are associated respectively with the excitation of the fundamental MP (MP1), the second-order MP (MP2), and an SPP. Clearly, adding graphene can increase the peak absorptance significantly without shifting the peak locations. For a plain grating, the absorptance is only 0.21 at MP1, because of the weak coupling between the two side walls of in the trench as noted previously [46,148]. Higher absorptance of 0.66 and 0.57 can be obtained with the MP2 and SPP modes, respectively. With graphene coverage, the absorptance at the resonance wavenumbers is raised to 0.81, 0.99, and 1.0 for MP1, MP2, and SPP, respectively. However, the fraction of energy absorbed by the graphene monolayer itself is not the same as the difference between the absorptance of the whole structure before and after the graphene is added, since the absorption is redistributed due to the coupling effect to be discussed.

The absorptance contours for the plain grating and graphene-covered grating are shown in Figure 5.3(a) and (b), respectively, in the reduce zone scheme for $0 \le k_x \le \pi/\Lambda$. The lower-right corner beyond the light line is left blank since no propagating waves exist in vacuum. The dispersion relations for different resonances, such as SPP or MPs with different orders, are manifested by the bright bands. The incidence angle is related to the parallel wavevector component k_x by $k_x = 2\pi\nu \sin\theta$, and the inclined solid and dashed white lines represent $\theta = 10°$ and $\theta = 40°$, respectively. The contrast between the two figures clearly shows that graphene enhances the absorption when resonances are excited for all the spectral region and incidence angles. The fundamental order, the second order,

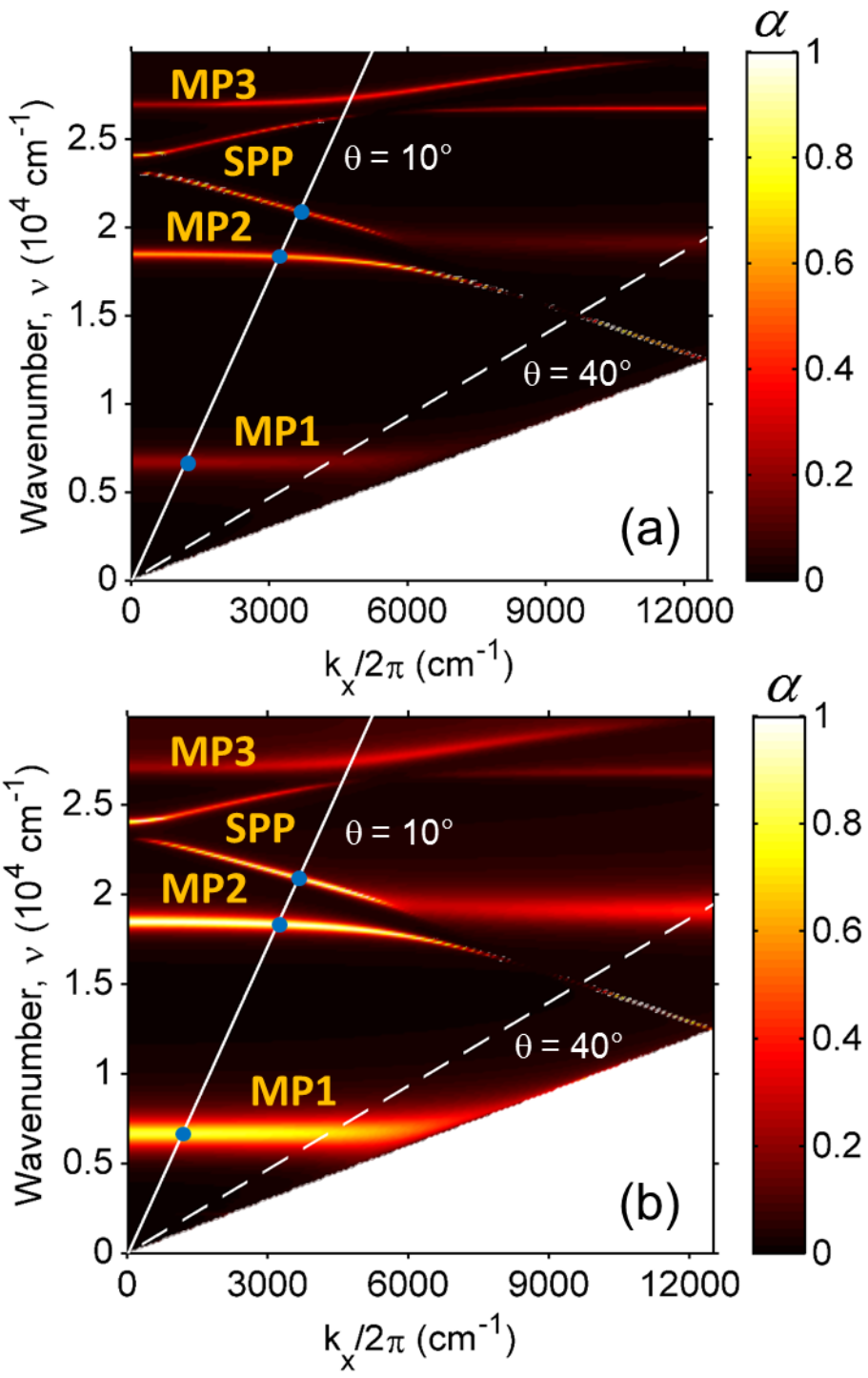

Figure 5.3 Absorptance contours for (a) plain Ag grating and (b) graphene-covered grating. The white solid and dashed lines indicate the incidence at $\theta = 10°$ and $\theta = 40°$, respectively, and the intersections indicated by the dot markers correspond to the three absorption peaks shown in Figure 5.2.

and the third order of MPs are excited in the considered spectral region as indicated by MP1, MP2, and MP3, respectively. MPs usually show up as nearly flat lines because the excitation is insensitive to the incidence angle as has been discussed before. Note that these modes are conventionallycalled waveguide modes, while MP is used here to stress the magnetic response of these resonances. SPP resonances and their effects on the radiative properties of gratings have been extensively investigated by many researchers [12,104,144,159,273,274]. The lower and upper branches can be identified as –1 and +1 orders of the SPP in the grating structures (as indicated in the contour above and below the sign "SPP"). The dots at the intersection of $\theta = 10°$ line and MP1, MP2, and SPP (–1 order) correspond to the three peaks in Figure 5.2. Note that the anti-crossing between SPP and MPs can break the continuous bright bands [275] and thus neutralize the absorption peak. The anti-crossing effects also cause some hybridization between MP and SPP. The SPP bands show a discontinuity at $k_x = 0$, because two standing-wave solutions with different energies can be obtained, resulting in a bandgap [99,276].

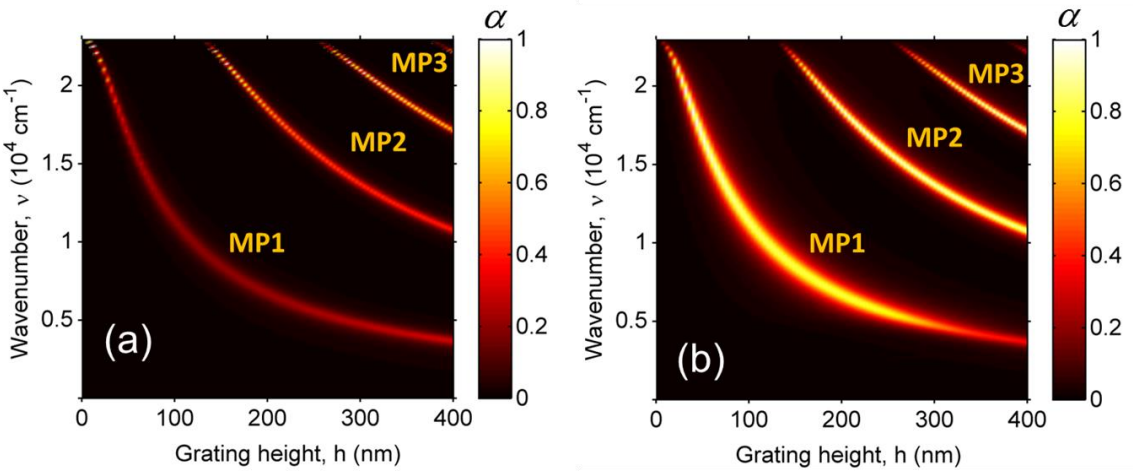

Figure 5.4 Absorptance contours at normal incidence for the (a) plain and (b) graphene-covered Ag gratings in terms of the wavenumber and the grating height *h*.

In addition, the enhanced absorption can be tuned by the geometry of the grating. Figure 5.4(a) and (b) illustrate the grating height effect on the MP resonances for plain gratings and graphene-covered gratings, respectively. The MP excitation wavenumber decreases as *h* increases, and graphene enhances absorption without changing the resonance frequencies. While these figures are for normal incidence, similar results can be obtained for other incident directions. The MP resonance frequency can also be tuned by changing the slit width and graphene also give rise to the absorptance without affecting the resonance frequency as demonstrated in Figure 5.5 [148]. When the period increases (with fixed *h* and *b*), the MP resonance condition will not change much due to their localized resonance nature, whereas the SPP resonance will shift to low frequencies [50]. Therefore, it is possible to tailor the grating geometries to enhance the absorption at the frequency of interest. Next, we focus on the mechanism of the enhanced absorptance.

The enhanced absorption at the MP excitation is directly related with the electromagnetic field at the resonance. The time-varying magnetic field parallel to the *y*-direction creates an oscillating closed current loop around the trench in the *x*-*z* plane, which

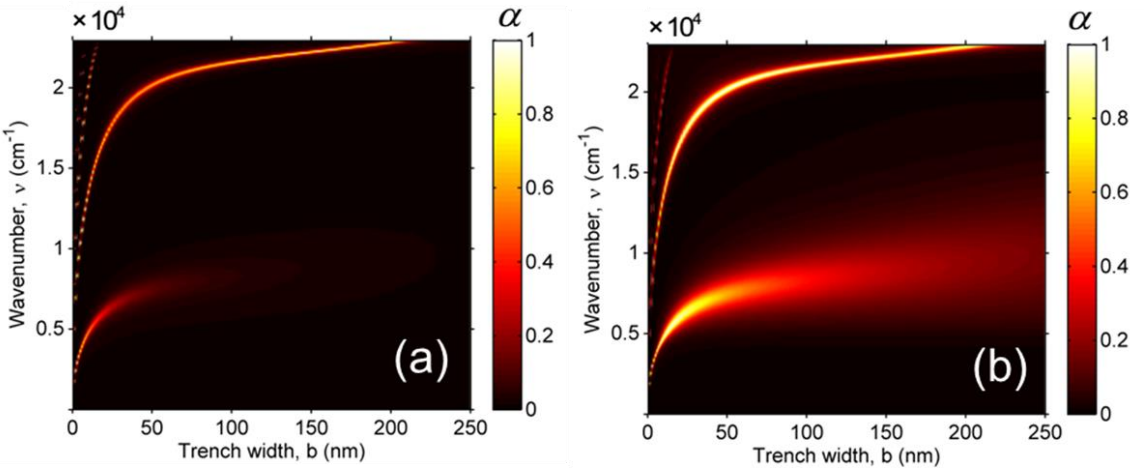

Figure 5.5 Absorptance contour for the two structures with *h* = 200 nm and Λ = 400 nm for varying *b*: (a) plain Ag grating; (b) graphene-covered Ag grating.

generates a highly localized magnetic field inside the trench according to Lenz's law [144]. Figure 5.6(a) and (b) show electromagnetic fields for the MP1 and MP2 resonances, respectively, at $\theta = 10°$. The arrows show the electric field while the contour indicates the magnitude of the magnetic field, and the same pattern is followed in later field plots. The magnetic field inside the trench in (a) is enhanced by more than twelve times compared with the incident, indicating the excitation of the fundamental mode of MP and showing the localization feature of the MP resonances [46].

Not only the magnetic field is enhanced, but the electric field is also greatly enhanced at MP1 and MP2 resonances. The electric field is minimal in the Ag grating, except along the interface between Ag and vacuum, but is extremely strong in the trench

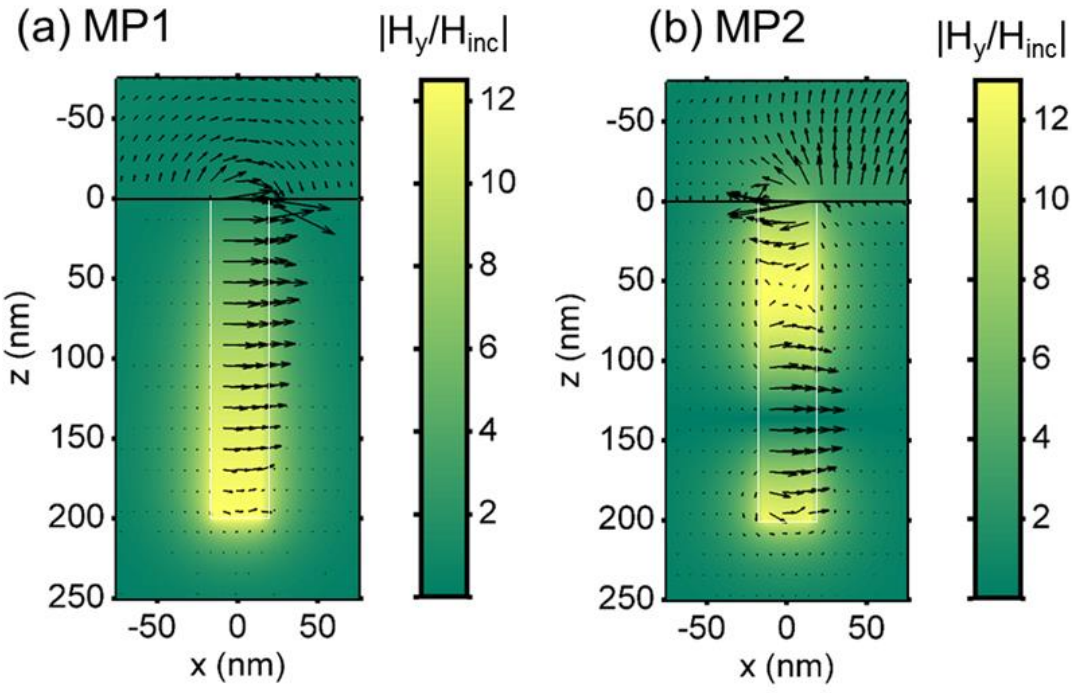

Figure 5.6 The electromagnetic fields for (a) MP1 ($\nu = 6700\ \mathrm{cm}^{-1}$) and (b) MP2 ($\nu = 18350\ \mathrm{cm}^{-1}$) at $\theta = 10°$. The contour shows the normalized magnitude of the magnetic field while the arrows indicate the direction and relative magnitude of the electric field.

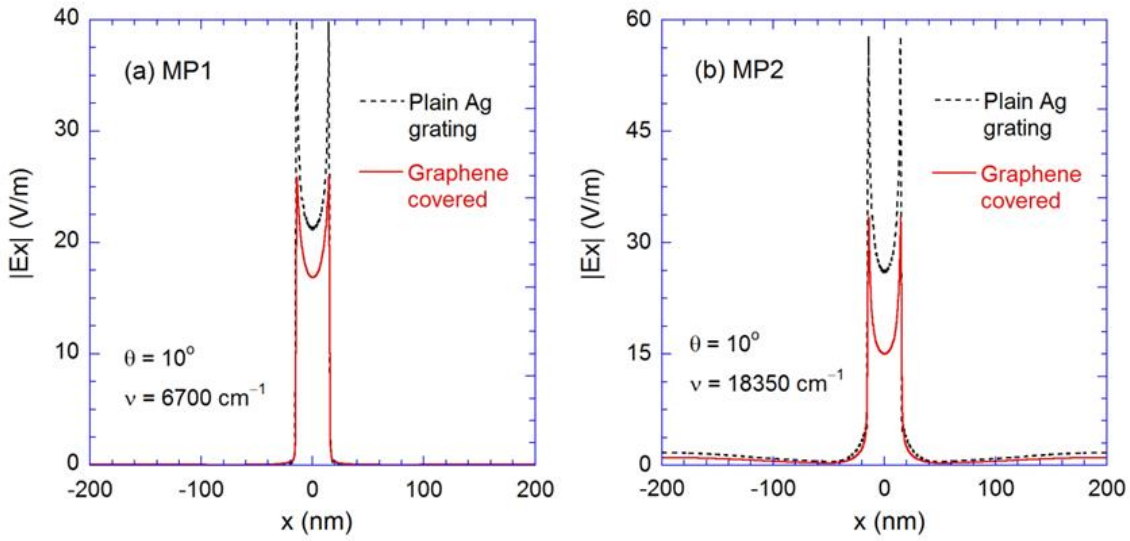

Figure 5.7 The magnitude of the *x*-component of the electric field at $z = \Delta / 2$ for plain and graphene-covered gratings at (a) MP1 ($\nu = 6700$ cm^{-1}) and (b) MP2 ($\nu = 18350$ cm^{-1}) resonances for $\theta = 10°$.

especially at the trench opening as shown in Figure 5.6(a) and (b). At the opening, the *x*-component of the electric field E_x dominates since the *z*-component is negligibly small. Figure 5.7(a) and (b) show E_x in the middle of graphene monolayer for MP1 and MP2, respectively. Note that the magnitude of the incident electric field is set to 1 V/m in the simulation. It can be seen that, for plain gratings, the electric field at the trench opening is enhanced by more than 20 times of the incident for MP1 and even higher for MP2. After covering graphene, the electric field is attenuated in both cases, and it can be inferred that adding graphene weakens the electric field. The result for normal incidence is almost identical. Note that for MP1, the electric field is negligibly small beyond the trench opening at –15 nm < *x* < 15 nm. The same cannot be said for MP2 for which the electric field is nontrivial beyond this range. This difference results in a different absorption profile in graphene as discussed in the following.

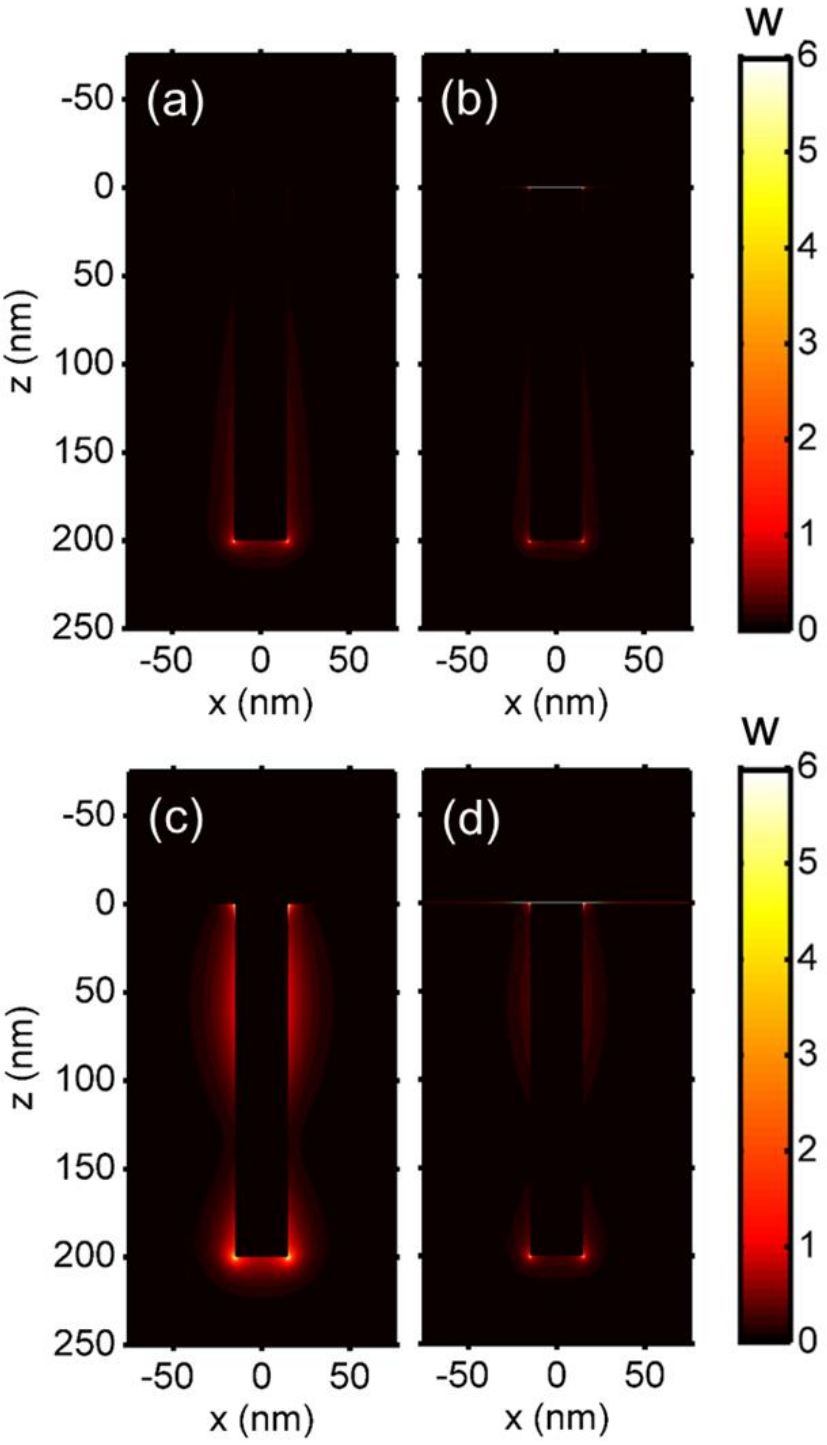

Figure 5.8 Power dissipation profiles for the two structures when θ = 10°: (a,b) MP1 resonance (ν = 6700 cm^{-1}) and (c,d) MP2 resonance (ν = 18350 cm^{-1}). The left (a,c) are for the plain Ag grating and the right (b,d) are for the graphene-covered grating. The unit of w is 10^5 W/m^3 and the scale bar is not linear beyond 6×10^5 W/m^3.

Figure 5.8(a) and (b) illustrate the power dissipation profiles calculated from Eq. (3.48) at MP1 resonance with $\theta = 10°$ for the plain grating and graphene-covered structure, respectively. For comparison, Figure 5.8(c) and (d) show the power dissipation at MP2 resonance for the two structures. The contour describes the value of the power dissipation density and the same scalar bar is used for all four figures. The scale bar is not linear beyond 6×10^5 W/m^3 to better show the absorption in grating. As shown in Figure 5.8(a) and (c), the incoming radiation is mainly absorbed near the surfaces of the trench walls especially at the corners. While displacement currents exist in vacuum, it does not contribute to absorption since there is no dissipation. For MP2, the enhanced electric field induces extremely high power dissipation up to 10^6 W/m^3 at the four corners of the trench. After covering with graphene, however, the absorption by the grating is weakened for both resonance modes. It should be noted that the power dissipation inside graphene is extremely strong reaching 10^8 W/m^3 for both MP1 and MP2. The shape of the power dissipation profile in graphene is similar to the electric field profile shown in Figure 5.7, i.e., high in the trench opening with two spikes at the grating edges. A distinction between MP1 and MP2 is that the graphene absorption is negligibly small beyond -15 nm $< x <$ 15 nm for MP1, while absorption beyond this range may not be neglected for MP2.

The absorptance of graphene can be obtained exactly by evaluating Eq. (3.49). For 1D gratings, a unit length in the *y* direction can be used such that Eq. (3.49) is evaluated in the *x*-*z* plane. Moreover, the integration in the *x* direction needs to be performed only in one period. It can be seen from Eq. (5.1) that the imaginary part of the dielectric function of graphene can be expressed as $\varepsilon''(x,z) = \sigma_s/(\varepsilon_0\omega\Delta)$ since σ_s is purely real in this region. Meanwhile, the electric field inside the graphene layer is essentially independent

of *z*. Therefore, the absorbed power in graphene can be expressed using its conductivity as follows:

$$\langle P_{\text{abs}} \rangle = \int_{\text{G}} w(x,z)\, dV = \frac{\sigma_{\text{s}}}{2} \int_{-\Lambda/2}^{\Lambda/2} \left| E_x(x) \right|^2 dx \tag{5.2}$$

Note that G indicates that the volume integration is carried out in graphene. The absorptance can be calculated by dividing Eq. (5.2) by the incident power.

One can apply the Cauchy-Schwarz inequality to Eq. (5.2):

$$\langle P_{\text{abs}} \rangle \geq \frac{\sigma_{\text{s}}}{2\Lambda} \left| \int_{-\Lambda/2}^{\Lambda/2} E_x(x)\, dx \right|^2 \tag{5.3}$$

The right-hand side (RHS) gives the lower bound of the power dissipated in graphene. If the electric field in graphene is independent of *x*, the RHS of Eq. (5.3) will be equal to the exact expression of $\langle P_{\text{abs}} \rangle$. In this case, the electric field forms an alternating voltage across the graphene and the power dissipation directly resembles the macroscopic form, V_{RMS}^2 / R. As to be shown in the next section, for MP resonances, the dissipation is concentrated only at the trench opening and the electric field across the trench can be approximated as uniform. The power dissipation can then be estimated by replacing the period Λ in the RHS of Eq. (5.3) with the trench width *b* [148].

For MP1, the dissipation of graphene is mainly confined in the range -15 nm $< x <$ 15 nm. Furthermore, the lower bound absorptance of graphene can be obtained from the RHS of Eq. (5.3) by replacing the period Λ with the trench width *b*, which gives 0.66. The lower bound value agrees well with the exact value 0.68 for MP1. The integration of E_x from $-b/2$ to $b/2$ in the RHS of Eq. (5.3) can be viewed as the alternating voltage drop

across the graphene, and b/σ_s is the resistance of graphene at the trench opening [148]. The graphene layer behaves like a resistor that dissipates power, resulting in a good agreement between the exact absorptance and the lower bound. Though the graphene layer is very thin, it carries an intense current that can induce a significant dissipation or loss. For MP2, the absorptance for the whole graphene is 0.77, among which 0.65 is in the trench opening and 0.12 is due to the dissipation beyond the opening region due to the nontrivial electric field.

Table 5.1 compares the absorptance for plain gratings and graphene-covered gratings at different resonances. For graphene-covered gratings, the absorptance of graphene and grating is also listed separately. The absorptance of the grating is evaluated directly from Eq. (3.49) by performing the integration in the grating and the substrate. At

Table 5.1 Absorptance calculated from RCWA at the wavenumber corresponding to the resonance of different modes for incidence angle $\theta = 0°$ (normal) and 10° with TM waves. The last two rows list the individual absorptance of the graphene sheet and the grating in the graphene-covered structure.

	$\theta = 0°$			$\theta = 10°$		
	MP1	MP2	SPP	MP1	MP2	SPP
Resonance wavenumber ν (cm^{-1})	6700	18490	24050	6700	18350	20930
Plain grating	0.22	0.63	0.67	0.21	0.66	0.57
Graphene-covered structure	0.81	0.99	1.0	0.81	0.99	1.0
Graphene only	0.68	0.78	0.69	0.68	0.77	0.80
Grating only	0.13	0.21	0.31	0.13	0.22	0.20

MP2 resonance and $\theta = 10°$, the absorptance of the grating is 0.22 with graphene coverage. This is a significant reduction from that of 0.66 for a plain grating. On the other hand, the absorptance of graphene itself is boosted to 0.77, more than 33 times than 0.023 for a suspended graphene. Graphene can absorb more power than the Ag grating mainly because of two reasons. The first is that graphene is very lossy due to the interband transition. By assuming a thickness of 0.3 nm, the imaginary part of the effective dielectric function (ε'') for graphene is 6.6 at MP2 resonance, while $\varepsilon'' = 0.1$ for Ag at the same frequency. The second reason is that MP resonances create a strong electric field at the trench opening that is about 15 times of that of the incidence waves, as shown previously. Interestingly, the electric field strength remains the same through graphene in the *z*-direction. Although the electric field strength is comparable to that in graphene at the surface of the grating, it decays exponentially into the grating with a penetration depth of approximately 12 nm. Therefore, even though the thickness of graphene is thousand times smaller than that of the grating, the absorptance of graphene can be greater than that of the grating.

The graphene absorptance is nearly independent of θ for MP1 when θ is smaller than 20°, but will decrease at large angles closer to the light line. For example, at $\theta = 45°$, graphene absorptance decreases to 0.58, though not shown in the table. Moreover, the graphene absorptance at MP2 shows a decreasing trend as the incident angle increases, especially beyond 15° where the effect of anti-crossing between MP2 and SPP (–1 order) occurs.

The MP resonance in deep gratings can be described by an inductor-capacitor (LC) circuit model as shown before. The metal grating severs as an inductor with an inductance L_{Ag} and the trench acts like a capacitor with a capacitance *C*. One can obtain the

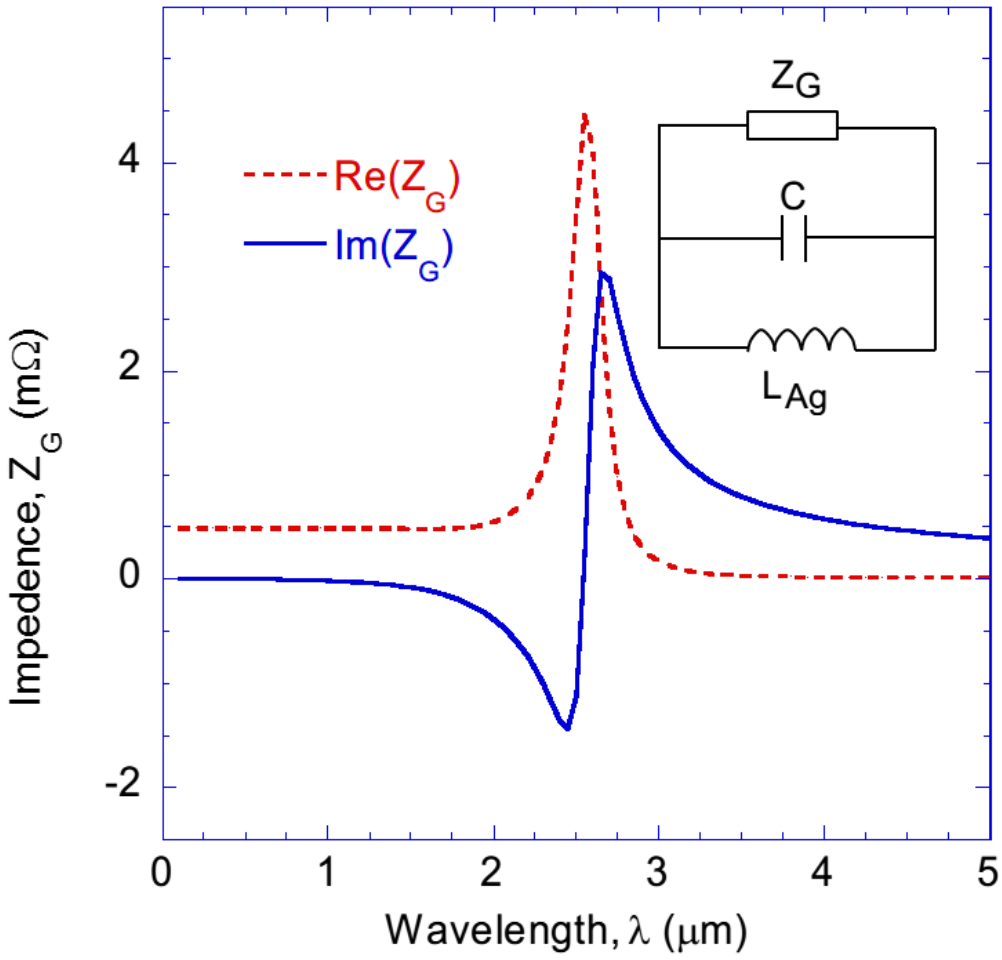

Figure 5.9 The impedance of graphene in the LC circuit model versus wavelength.

fundamental resonance wavelength for the uncovered grating as $\lambda_{\mathrm{MP}} = 2\pi c_0 \sqrt{CL_{\mathrm{Ag}}}$. To consider the effect of graphene on the resonance, additional impedance should be added into the LC circuit. Figure 5.8(b) suggests that only the graphene across the trench opening may be involved in the effective circuit. The additional impedance introduced by the graphene layer can be evaluated by

$$Z_{\mathrm{G}} = R_{\mathrm{G}} + i\omega L_{\mathrm{G}} = b/\sigma_{\mathrm{s}} \tag{5.4}$$

Figure 5.9 shows the real and imaginary part of the impedance of the graphene sheet, where the inset shows the modified LC circuit for the graphene-covered grating. Note that σ_{s} is

dominated by the interband contribution σ_I, when the photon energy is greater than the interband threshold 2μ [277]. Taking $\mu = 0.3$ eV, this corresponds to a wavelength of about 2.1 μm. Therefore, at the MP1 resonance wavelength 1.49 μm, the impedance becomes a pure resistance $R_G = 4.9\times10^{-4}\,\Omega$. This makes the graphene layer behave like a pure resistor across the trench, where a strongly enhanced local electric field exists when MPs are excited. Since R_G is large, the imaginary part of the total impedance of the circuit shown in Figure 5.9 does not change with the graphene overlay. Therefore, the resonance wavelength can still be expressed as $\lambda_{MP} = 2\pi c_0\sqrt{CL_{Ag}}$ even with the presence of graphene. However, the graphene layer does add resistance to the circuit, making the resonance peaks broader (lower *Q* factor). The same argument holds for higher-order MPs and SPPs.

As can be seen from Table 5.1, SPP results in nearly complete absorption by the graphene-covered grating structure, while both the resonance wavenumber and graphene absorptance are strongly angular dependent. The angular dependence of the resonance frequency can be understood by the negative slope of the −1 order SPP dispersion curve shown in Figure 5.3. SPPs produce a longitudinal surface wave that propagates along the interface between the dielectric and the metal. Figure 5.10(a) shows the electromagnetic field for the plain grating at the SPP resonance at $\nu = 24050$ cm^{-1} and for normal incidence. Note that graphene-covered structure exhibits similar field distribution (not shown), except that the magnitude of the magnetic field is about half of that for the plain grating. Strong electric field along the surface of the grating is generated as indicated by the arrows. It can be seen that the field strength exponentially decays away from the interface; this is a

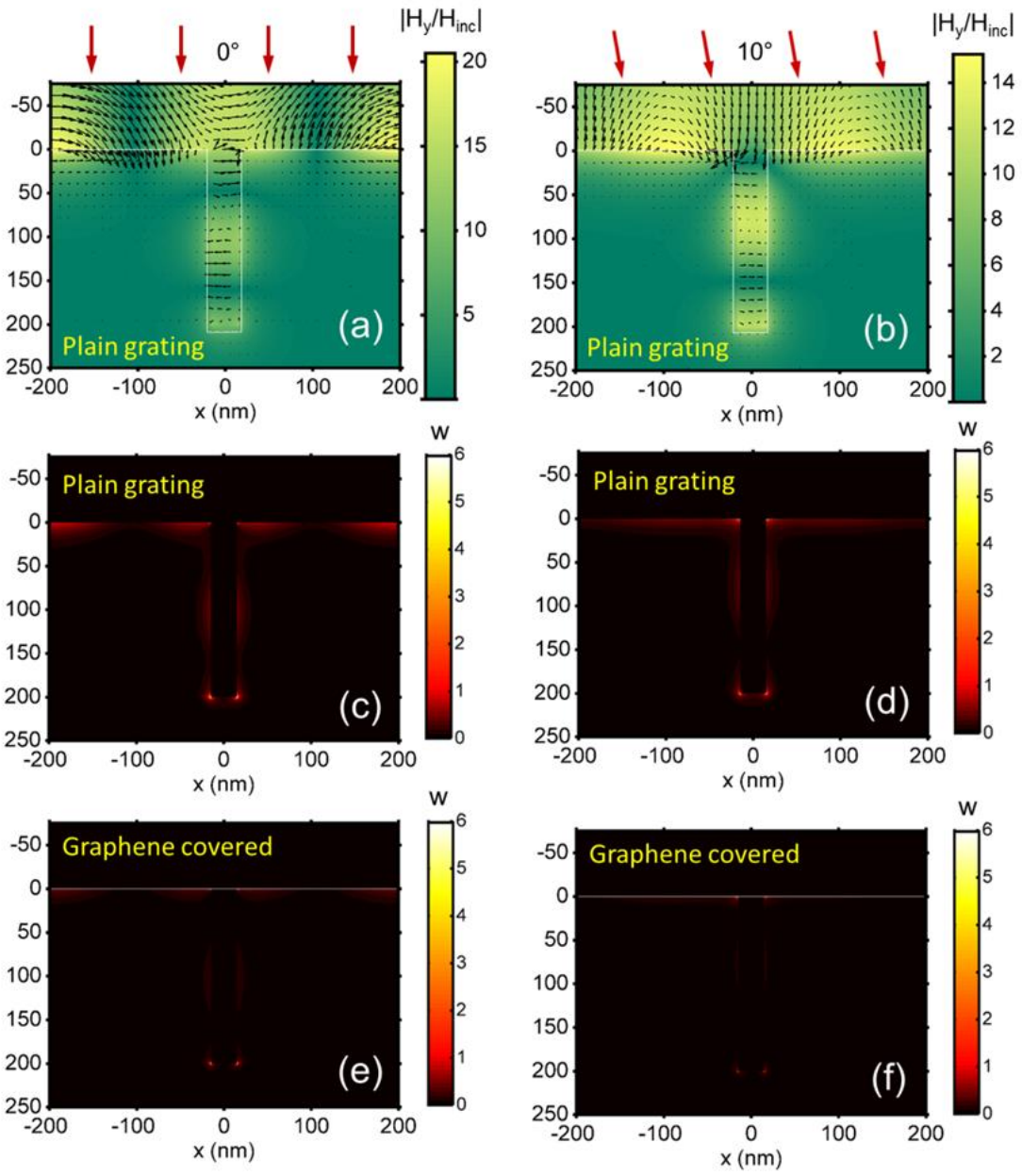

Figure 5.10 (a,b) Electromagnetic field of the plain grating; (c,d) power dissipation contours of plain grating; (e,f) power dissipation contours of graphene-covered grating. The left figures (a,c,e) are for normal incidence at the SPP resonance $\nu = 24050$ cm^{-1} and the right figures (b,d,f) are for $\theta = 10°$ at the SPP resonance $\nu = 20930$ cm^{-1}. The unit of w is 10^5 W/m^3, and the scale is not linear beyond 6×10^5 W/m^3.

distinguished feature of SPPs. Meanwhile, the field along the surface of the grating shows a standing wave pattern with clear nodes and antinodes. At normal incidence, the incident photon can couple with two surface plasmons: one is the +1 order with a wavevector $k_{sp} = 2\pi/\Lambda$ (right traveling) and the other is the −1 order branch with $k_{sp} = -2\pi/\Lambda$ (left traveling). The two surface waves form a standing wave [276], whose wavelength is nearly equal to the period of the grating. Interestingly, there are some waveguide or MP features inside the deep trench or optical cavity when SPP is excited. It can be seen from Figure 5.10(a) that the field distribution inside the trench is similar to that of MP2 shown in Figure 5.6(b). This implies the SPP resonance is not a pure SPP mode, but a hybridization of a standing surface wave and a localized resonance mode; which has been addressed in the literature for similar structures [273].

Figure 5.10(b) shows the field distribution of the plain grating at the SPP resonance and θ = 10°, where the −1 order SPP is excited at $\nu = 24050\ \text{cm}^{-1}$. This resonance is actually a hybridization of a propagating surface wave (SPP) and a localized resonance (MP2). The magnetic field displays two antinodes in the trench, while standing waves appear along the grating surface. Furthermore, the left side of has stronger field enhancement than the right side. Figure 5.10(c) and (d) show the power dissipation contours for the plain deep grating at normal and 10° incidence, respectively. The absorption along the surface of the grating in (c) shows a standing wave pattern with clear nodes and antinodes, which correspond to the magnetic field shown in (a). However, the standing wave feature does not present in (d). Meanwhile, on the two walls of the trench, the absorption contour is similar with that of MP2 shown in Figure 5.9(c) for both normal and oblique incidence case due to the hybrid nature of the resonance.

Figure 5.10(e) and (f) depict the power dissipation contour for structures covered by graphene. They are similar to (c) and (d) but the absorption of the grating is attenuated. Unlike in the case with MPs, the absorption of graphene for SPPs is significant not only in the trench opening but also along the surface of the grating (indicated by the bright white line). This is the reason why the absorptance distribution between graphene and grating is very sensitive to the incidence angle. For example, graphene has an absorptance of 0.69 at normal incidence and this value increases to 0.80 at $\theta = 10°$. It can be further boosted to 0.82 at $\theta = 14°$. The directional dependence can be attributed to the stronger electromagnetic field near the trench opening for oblique angles. The absorption at the grating surface beyond the trench appears not as strong in Figure 5.10(d) as in Figure 5.10(c), but is higher at the corners of the trench opening as indicated by the two brighter spots at the corners. Therefore, a stronger electric field is generated near the trench opening and the graphene is able to absorb more at oblique incidence than at normal incidence. However, when the incidence angle is greater than 20°, the absorption peak of SPP becomes trivial due to anti-crossing, and thus, the graphene absorption due to SPP becomes much weaker or may disappear at large angles.

To further understand graphene absorption at SPPs, the power dissipation along the center line of graphene at $z = \Delta / 2$ is shown in Figure 5.11. At normal incidence, the standing wave feature is clearly shown beyond the trench and the dissipation in the trench opening resembles the feature of MP2. Detailed calculation shows that the absorptance of graphene at the trench opening is 0.2, whereas the left portion ($-200\ \text{nm} < x < -15\ \text{nm}$) and right portion ($15\ \text{nm} < x < 200\ \text{nm}$) of graphene have the same absorptance of 0.245. Thus, the standing surface wave dominates the graphene absorption enhancement. At $\theta =$

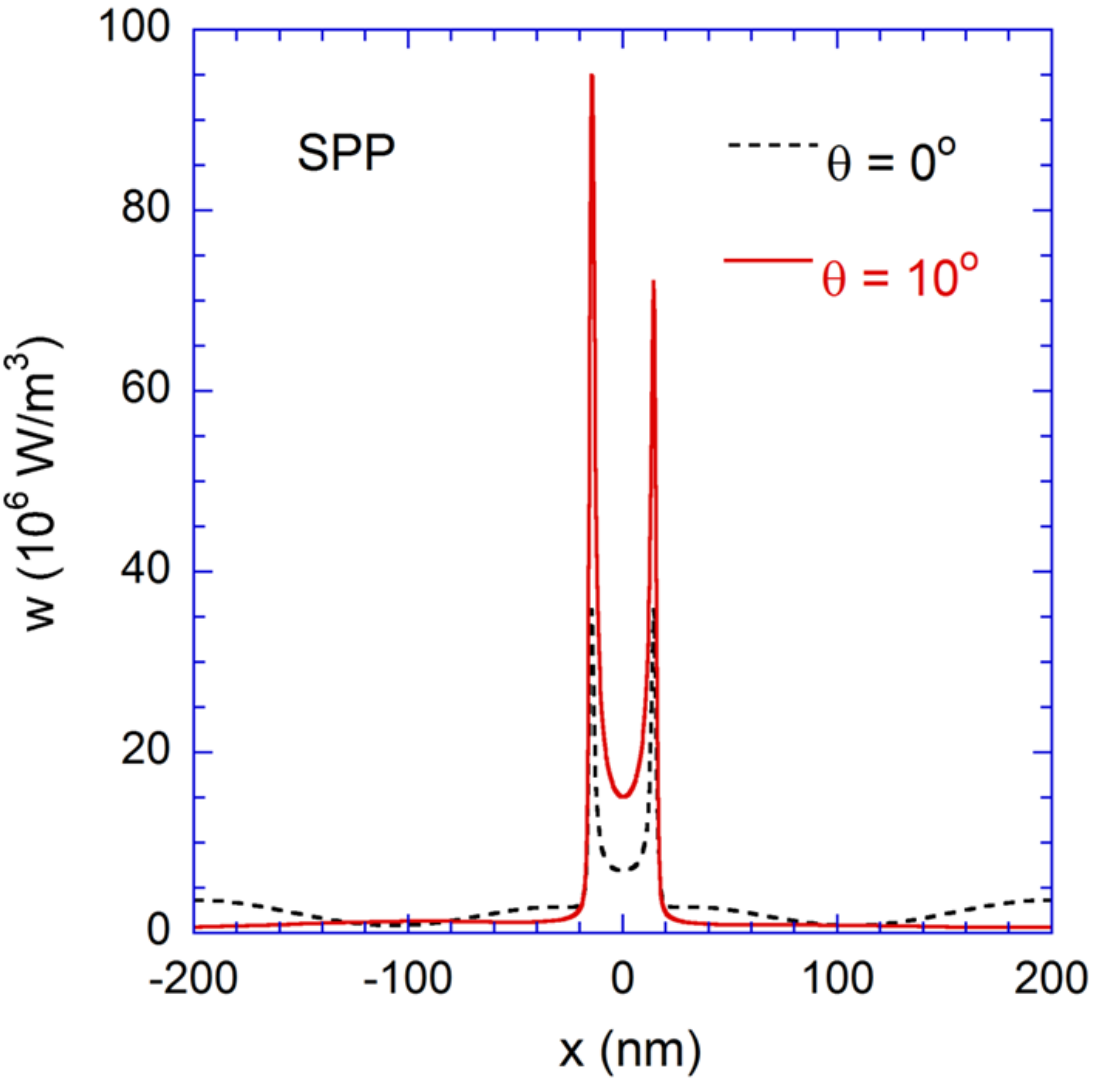

Figure 5.11 Power dissipation density profile across the middle of the graphene layer when the SPP resonance is excited at normal incidence and $\theta = 10°$.

10°, the absorption profile is no longer symmetric. The graphene at the trench opening absorbs 0.49 of the incoming power, while the left and right portion contributes to the absorptance by 0.18 and 0.13, respectively. Therefore, the enhanced field near the trench opening is indeed the major contribution of the enhanced graphene absorption. Therefore,

SPP resonance at oblique incidence can greatly enhance graphene absorption, even better than MPs, due to its hybrid nature.

In conclusion, this work theoretically demonstrates enhancement of graphene absorption by metal gratings. The excitation of MPs and SPP resonances can enhance the absorptance of graphene up to 0.80, without affecting the resonance frequency or dispersion in gratings. Due to the different nature of MP and SPP in the nanostructures, the enhanced graphene absorption is insensitive to the incidence angle for MPs when it is not close to the SPP dispersion line. On the contrary, the SPP-enhanced graphene absorption depends strongly on the direction of incidence. The enhanced graphene absorption at MP resonances is localized at the trench opening. At the SPP resonance, however, surface waves contribute more to the enhancement at the normal incidence while the localized field near the trench opening contributes more at oblique angles. The understanding gained from this work may facilitate the development of graphene-based photodetecting, energy harvesting, as well as plasmonic devices.

5.2 Graphene-covered Metal Gratings in the Mid- and Far-infrared

The previous work focuses on the visible and near-infrared range. The following discusses the plasmonic coupling in mid- and far-infrared range. Plasmons are collective oscillations of charge carriers and they play a critical role in optoelectronics and metamaterials applications. Graphene can support highly-confined surface plasmons in the infrared region with relatively low loss compared to traditional plasmonic materials [61,117,278,279]. The strong coupling between the incident photon and the plasmons in graphene results in a polariton, which creates coherent absorption or transmission desired

in applications such as energy harvesting and optical detection [94,251,261,271,280]. To excite polaritons with the photons incident from vacuum, graphene can be patterned into different periodic resonators such as ribbons [250,281-283], disks [248,284-286], and cross shapes [253]. In particular, graphene ribbon arrays [250,282,283] have attracted extensive attention recently. The electrons in the ribbons can be driven by external electromagnetic waves and oscillate inside the ribbon, forming surface plasmons that can induce a resonance absorption. Meanwhile, the optical properties of graphene ribbons can be tuned by controlling its chemical potential, resulting in tunable plasmonic resonances in the infrared region [252,287,288].

In spite of these advantages, high resonance absorptance that is desired in the above-mentioned applications is difficult to achieve solely with graphene ribbon array due to its atomically thin thickness, especially for high-order resonances [250]. Thus, there is a need to explore novel ways that can enhance the plasmonic resonances in graphene structures like periodic ribbons. In the visible and near-infrared region, graphene has no plasmonic responses but has very high loss. Thanks to this lossy property, the absorptance of graphene can be enhanced by placing graphene into an environment with strong electric fields to enhance its absorption, as has been demonstrated in the previous work. However, in the mid- and far-infrared, plasmons in graphene can strongly couple with the nanostructures and gratings to form a new hybrid plasmonic system [289-291]. For example, the plasmons in graphene can be launched and controlled by the plasmonic dipole resonance of metal nanoantennas [292]. This coupling phenomenon offers a novel route for the enhancement of plasmonic resonances in graphene and its nanostructures.

This work demonstrates that the localized polaritons, i.e., MPs, in deep metal

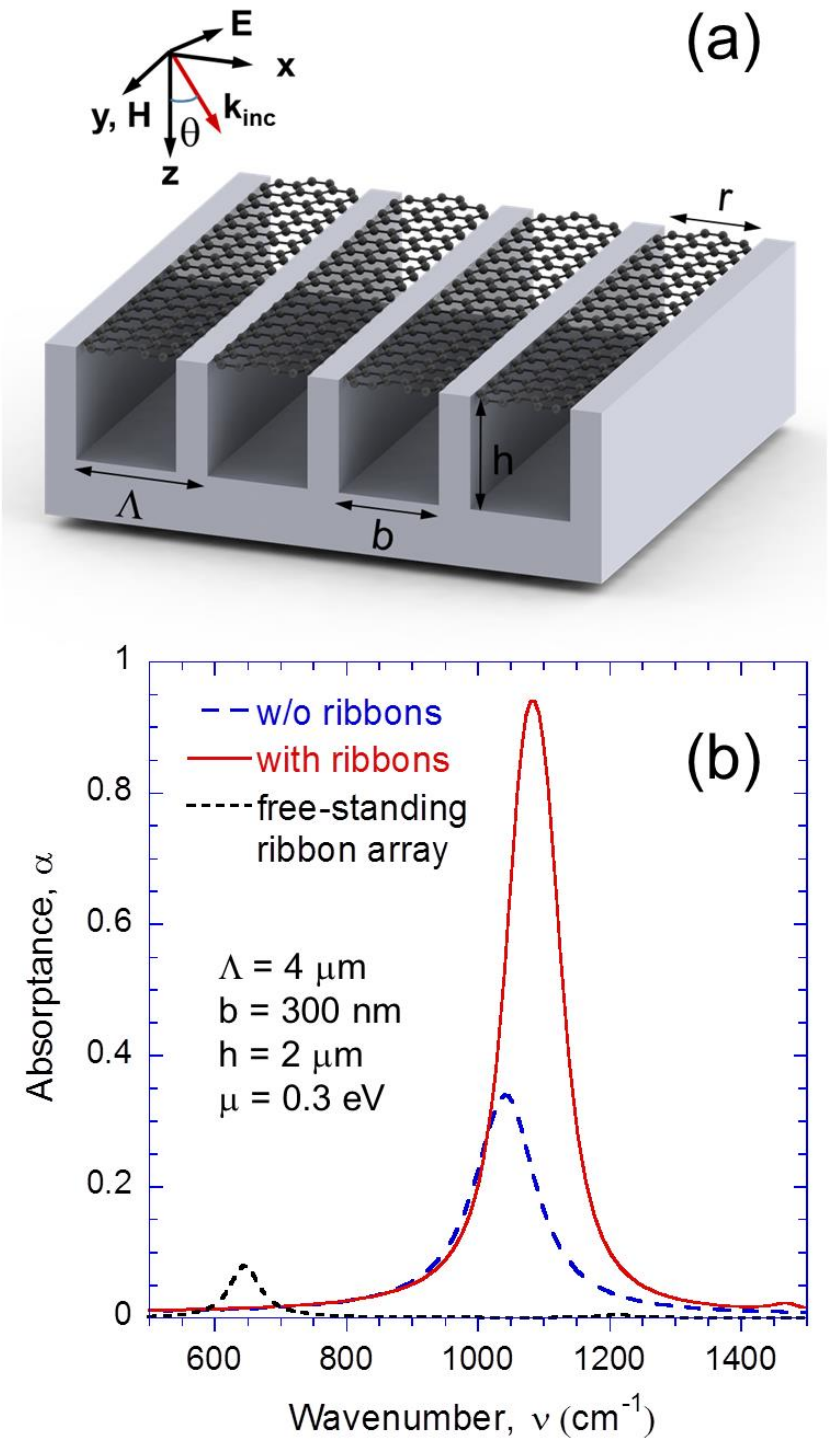

Figure 5.12 (a) Schematic of the hybrid grating-graphene ribbon plasmonic structure. (b) The absorptance spectrum for a plain Ag grating, a free-standing ribbon array, and a ribbon-covered grating ($r = b$). The geometries for the grating are given in the figure.

gratings, can strongly couple with the surface plasmons in graphene sheets and ribbons. The geometric arrangement of the graphene ribbon-grating hybrid structure is illustrated in Figure 5.12(a). The grating is periodic in the *x*-direction and extended infinitely in the *y*-direction. It has a period Λ, trench width *b*, and grating height *h*. Unless specified, the geometries are fixed as $\Lambda = 4\ \mu\text{m}$, $b = 300\ \text{nm}$, and $h = 2\ \mu\text{m}$. The width of the ribbons is *r* ($r \le b$); noting that when *r* = *b*, the edges of ribbons will be in physical contact with the grating as shown in the schematic. The cases where they are not in contact will be discussed later. The ground plane is assumed to be thick enough to be treated as opaque. The grating and ground plane are chosen to be silver (Ag). The optical properties of graphene include the contributions from the interband and intraband transitions [116]. In the mid- and far-infrared region, the intraband transitions dominate and the conductivity can be approximately expressed in a Drude-like model as expressed in Eq. (2.12). The chemical potential can be tuned by electrical gating or chemical doping, and thus offering an active way to control the optical properties of graphene ribbons. In this study, otherwise specified, μ = 0.3 eV and $\tau = 10^{-13}$ s are used. For TM waves, as discussed before, the oscillating magnetic field in the *y*-direction induces a current loop around the trench of the

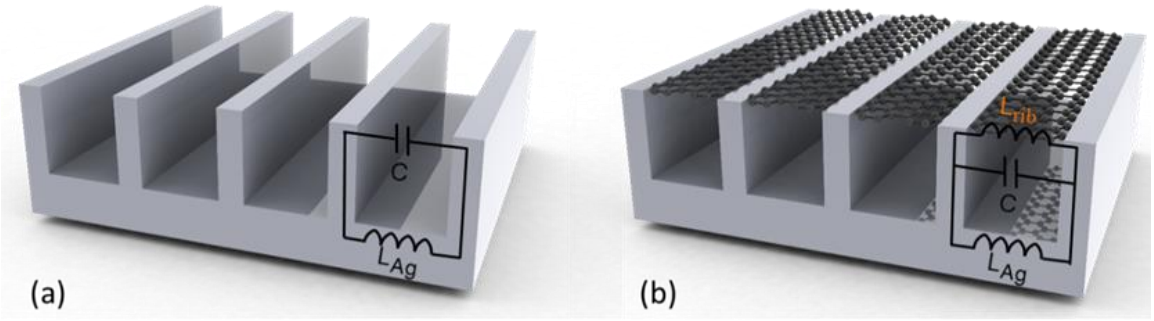

Figure 5.13 (a) Plain Ag grating and (b) graphene ribbon covered Ag grating and their corresponding LC circuit models.

grating, which generates a highly localized magnetic field inside the trench and forms an MP. The absorptance spectra of the plain and ribbon-covered structure are shown in Figure 5.12(b). For the plain grating, the MP resonance is at 1041 cm^{-1} with an absorptance of 0.35. After coving ribbons on the grating, the absorptance is boosted to 0.94 and the resonance shifts to 1086 cm^{-1}, indicating a strong coupling between graphene and the grating. The spectrum of the free-standing ribbon array without the grating is also given for comparison. In this case, the ribbon plasmon gives rise to a small absorption peak around 650 cm^{-1}. It will be discussed later that the grating can alter the dispersion of the graphene plasmons by changing the phase shift of the plasmon waves at the edges of the ribbons.

The resonances with and without graphene can be modeled using the equivalent circuit method. Similar as before, metal and dielectric are treated as inductors and capacitors, respectively, as shown in Figure 5.13. The impedance of the graphene ribbon can be obtained as

$$Z_{\text{rib}} = R_{\text{rib}} - i\omega L_{\text{rib}} = \text{Re}\left(\frac{r}{l\sigma_{\text{s}}}\right) + i\,\text{Im}\left(\frac{r}{l\sigma_{\text{s}}}\right) \tag{5.5}$$

Thus,

$$L_{\text{rib}} = -\text{Im}\left(\frac{r}{\omega l\sigma_{\text{s}}}\right) \tag{5.6}$$

Im means taking the imaginary part. Note that near the coupled resonance frequencies, the impedance of graphene and Ag is dominated by its inductance term, thus, in the LC circuit, only the inductance is kept. The inductance L is L_{Ag} for plain gratings and equals to $L_{\text{Ag}}L_{\text{rib}}/\left(L_{\text{Ag}} + L_{\text{rib}}\right)$ for the ribbon-covered structure since the two inductors are in

parallel. The factor in the capacitance formular, c', is taken as 0.5. By solving the natural frequency of the LC circuit, the model yields a resonance frequency of 1047 cm^{-1} without the graphene ribbon and 1093 cm^{-1} with the graphene ribbon. The red shift caused by graphene is because graphene ribbons serves as an inductor across the trench that lowers the total inductance in the circuit. However, the reason for the absorptance enhancement cannot be explained by the LC model that does not consider loss. To further elucidate the enhanced absorption, the ribbon plasmon is discussed next.

As discussed before, surface plasmons for TM waves can propagate along the *x*-direction with low loss in a continuous, free-standing graphene layer. The plasmons in ribbons, however, cannot propagate freely but are reflected back on the ribbon edges with a phase shift $\Delta\varphi$. The reflection of plasmon waves in various graphene nanostructures has been previously studied [293,294]. Recently, it is found that this phase shift is $\pi/4$ for free-standing ribbons in vacuum [295,296]. Once the reflection phase shift is known, the resonance in suspended graphene ribbons can be described by a Fabry-Pérot model:

$$\Delta\varphi + \mathrm{Re}\left(k_{\mathrm{GSP}}\right) r = m\pi \tag{5.7}$$

where integer *m* denotes the resonance order and Re takes the real part of the complex quantity. By substituting Eq. (2.13) into Eq. (5.7), the resonance condition of suspended ribbons in vacuum ($\varepsilon_1 = \varepsilon_2 = 1$) can be expressed explicitly as [296]

$$\omega = \sqrt{\frac{e^2 \mu \left(m - \Delta\varphi/\pi\right)}{2\varepsilon_0 \hbar^2 r}} \tag{5.8}$$

At normal incidence, the plasmon initiated from the two edges of the ribbon are out of phase, and thus only the plasmons associated with odd *m*'s can show up. The plasmons

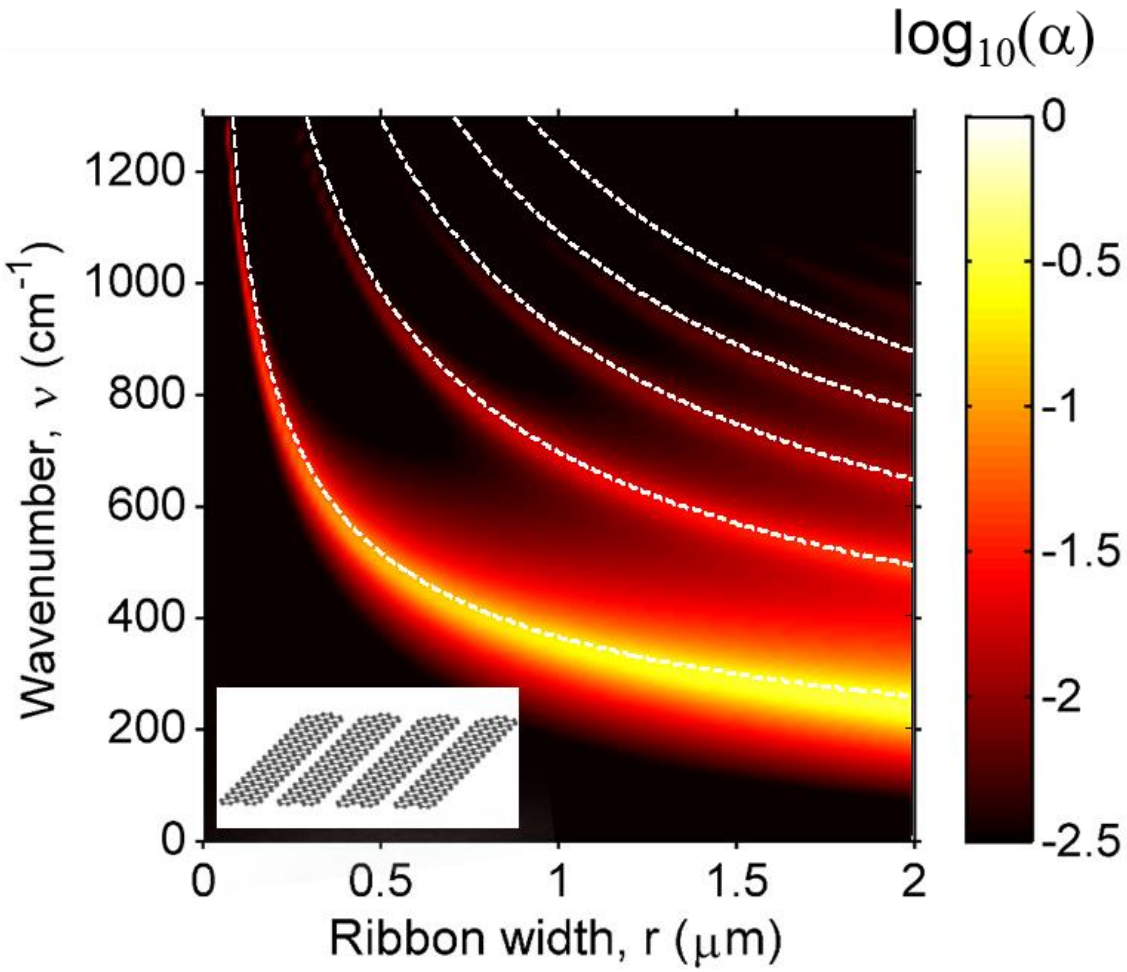

Figure 5.14 The absorptance contour of a free-standing graphene ribbon array with $\Lambda = 4$ μm and $\mu = 0.3$ eV, where the dashed lines are the predictions of Eq. (5.8) with $\Delta\varphi = \pi/4$.

with even *m*'s can only occur at oblique incidence since in-phase plasmons can be excited from the two edges [296].

Figure 5.14 shows the absorptance (α) contour of a suspended graphene ribbon arrays at normal incidence obtained by using RCWA. Continuous graphene sheet can be simulated as a thin isotropic layer with an effective dielectric function that is related to its conductivity as discussed before. However, graphene ribbons are difficult to be modeled in a similar way due to convergence issues [297]. Here, an approximate boundary condition

is used [297], in which the graphene ribbons is treated as a period surface conductivity pattern that modifies the boundary conditions of the magnetic field. The dashed lines, from bottom to top, are the predictions from Eq. (5.8) with m = 1, 3, 5, and 7, respectively. The frequency of the resonance is inversely proportional to $\sqrt{r}$. Note that the highest absorptance occurs for m = 1 at $r \approx 2$ μm with a value near 0.35. For the other branches with higher orders, the absorption by graphene ribbons is rather small. As will be shown next, metal gratings can significantly enhance these ribbon resonances.

Figure 5.15 compares the absorptance contours at normal incidence for four different configurations versus the trench width. The plain gratings support MP resonances in the considered frequency range as shown in (a). The frequency of the MP increases with b and reaches an asymptotic value when $b > 0.25$ μm. The absorptance diminishes at large trench widths due to the poor coupling of the evanescent waves between the two side walls in the trench, as has been discussed before. The dot markers are the predictions of the LC model. The absorptance contour stays the same if the graphene ribbon is covered only on the ridges of the grating, as shown in (b). The graphene ribbons appear to have no effect on the resonance since they are in contact with the metal on one side. On the contrary, if the ribbons are suspended above the trench openings, as the case in the inset of (c), the plasmonic resonances of the ribbons show up and the absorptance becomes more plentiful. The bright bands that exhibit a dependence on $1/\sqrt{b}$ are caused by the plasmons in ribbons. Note that when the grating trench is changing, r changes accordingly so that the edges of the ribbons are always in touch with Ag. Although the shape of these bands is similar to those in Figure 5.14, the ribbon resonances in Figure 5.15(c) cannot be predicted with Eq. (5.8) using the reflection phase shift $\pi/4$. In fact, since the edge is touched with Ag instead

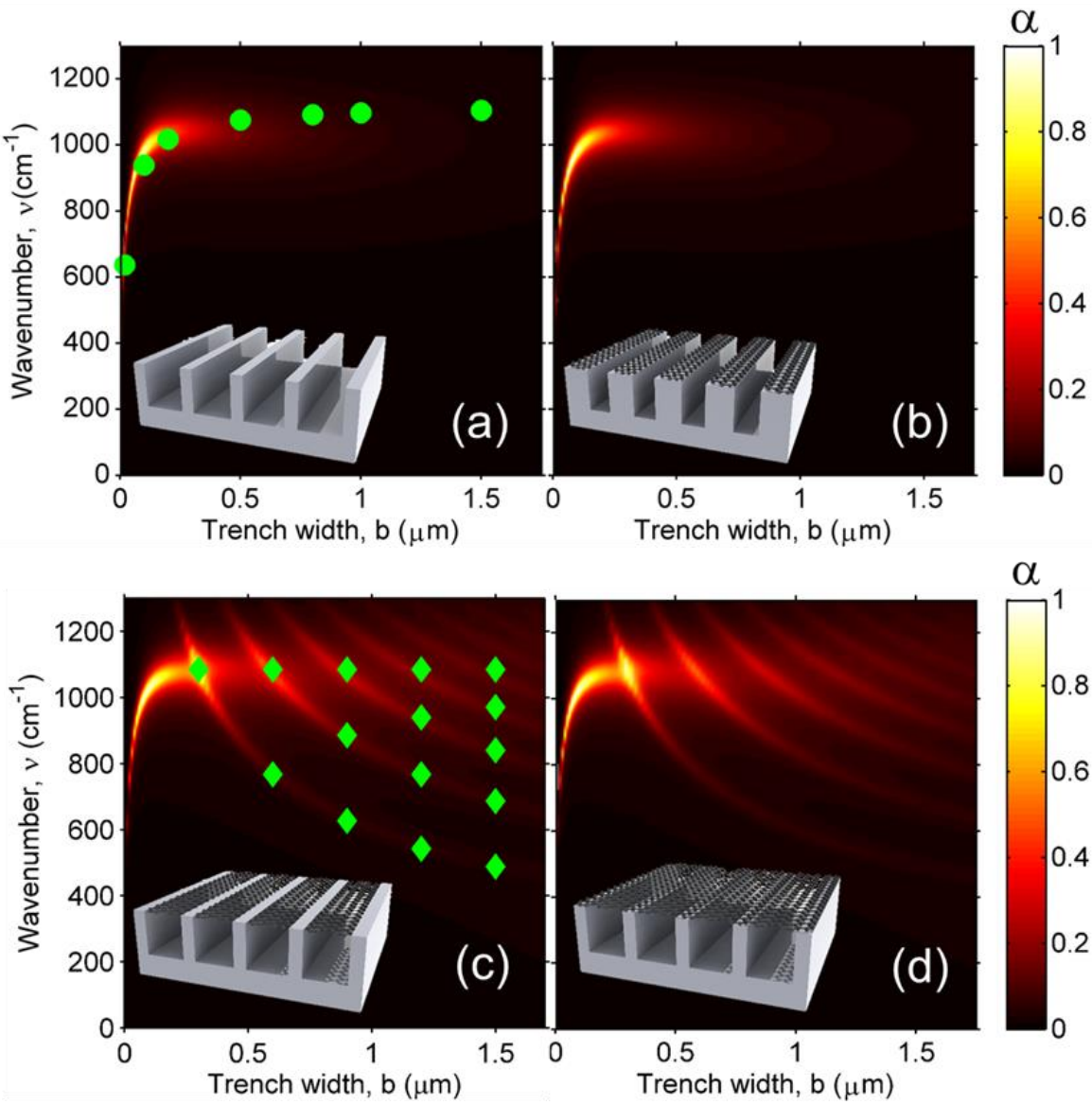

Figure 5.15 Compilation of the absorptance contours for four different structures when $\Lambda = 4$ μm , $h = 2$ μm , and μ = 0.3 eV fixed and b changes: (a) Plain Ag grating; (b) Graphene ribbons covering the Ag grating ridges; (c) Graphene ribbons covering the trench opening ($r = b$); and (d) Continuous graphene sheet covering the whole grating. The round markers are the predictions of the LC model and the diamond markers are the predictions of Eq. (5.8).

of vacuum, the tangential component of the electric field (E_z) at the edges need to vanish at the boundary due to the high conductivity of Ag, resulting in a phase shift of $-\pi$ for the

plasmon waves. This can be further justified by the excellent agreement between the simulation and the prediction results of Eq. (5.8) with $\Delta\varphi = -\pi$, which is demonstrated in Figure 5.15(c). Note that the plasmons are all associated with odd *m*'s since the incidence is normal.

Covering the grating by a continuous graphene, as illustrated in Figure 5.15(d), yields the same absorptance contour as Figure 5.15(c). Again, the portion of the graphene on the ridges has little contribution on the resonance. Thus, in terms of absorptance, continuous graphene is equivalent to a periodic ribbon array suspended over the grating trenches. Since

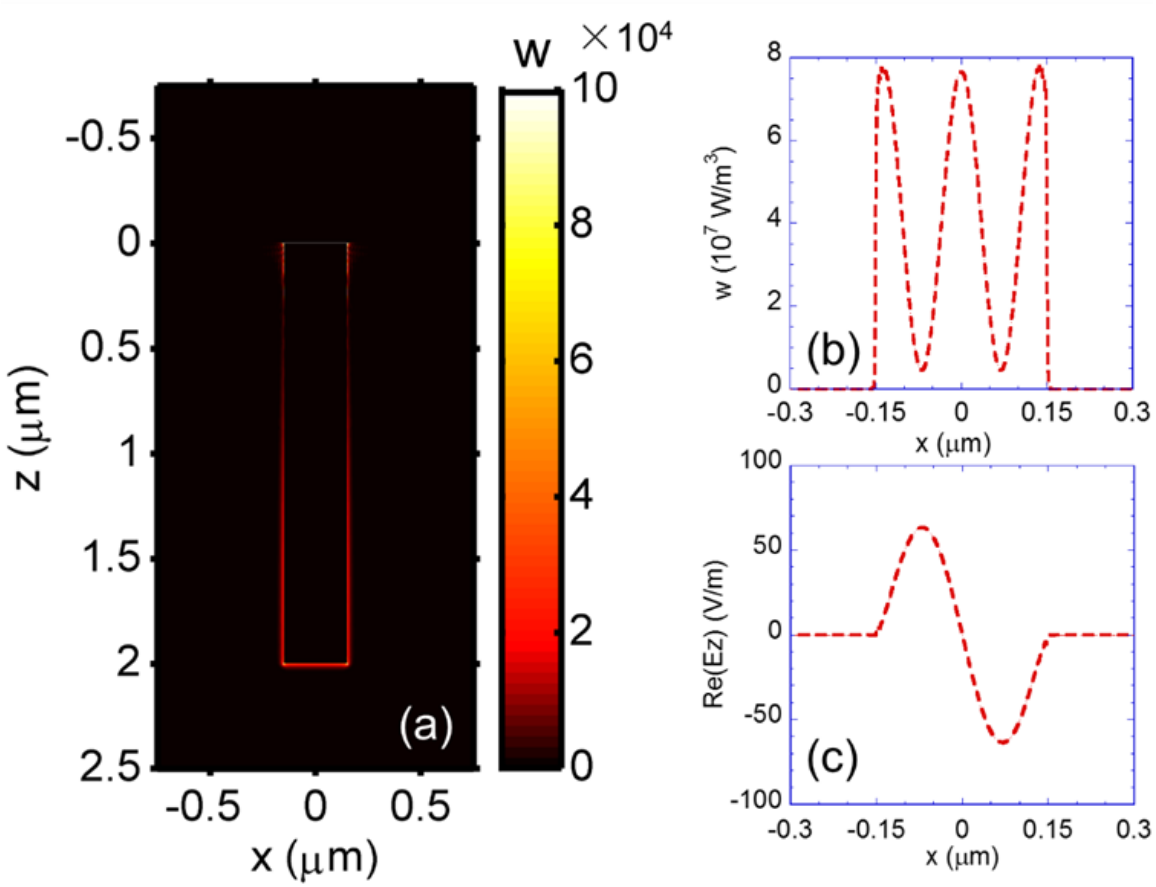

Figure 5.16 The power dissipation density at the coupled resonance when b = 0.3 μm: (a) for the whole structure and (b) across the middle of the graphene. (c) The modulus of E_z at the location beneath the graphene inside the trench.

the fabrication of the structure with continuous graphene on grating can be realized with the existing fabrication technique [289], it provides a realistic way to experimentally achieve the coupling between MP and plasmons in ribbon array. The branches for ribbon plasmons are intersected with the MP and the absorptance at the intersection points are enhanced significantly, indicating a strong coupling between the MP and the ribbon plasmons. The spectrum at $b = 0.3$ μm contains a strongly coupled resonance at $\nu = 1086$ cm^{-1} and has been shown in Figure 5.12(b). The absorption by the graphene ribbons, to be shown next, can be significantly enhanced at this resonance.

Figure 5.16 illustrates the power dissipation profile at the coupled resonance when $b = 0.3$ μm. The grating is covered with a continuous graphene. The absorption in grating at the coupled resonance, as demonstrated in Figure 5.16(a), is mainly confined at the surface of the trench. This is due to the short penetration depth of electric field in the metal that is only about 10 nm. The absorption in the graphene, however, is concentrated in the portion that is on the trench opening. This further justifies that the graphene in contact with the grating ridges plays little role on the resonance. Note that the scale bar is chosen in a way such that the absorption of the grating can be clearly seen. The detailed absorption distribution in graphene is shown in (b) according to the dissipation density along the middle of the graphene layer. Due to the interference effect of the plasmonic waves, the dissipation exhibits a standing-wave pattern at the trench opening and is symmetric with respect to the $x = 0$ plane. Note that the electric field is dominated by its x-component in the graphene. The portion of energy absorbed by the graphene is calculated to be 72%, which is greatly boosted from 8% for a free-standing graphene ribbon with $r = 0.3$ μm when the first-order plasmon is excited at normal incidence, as shown in Figure 5.14. The

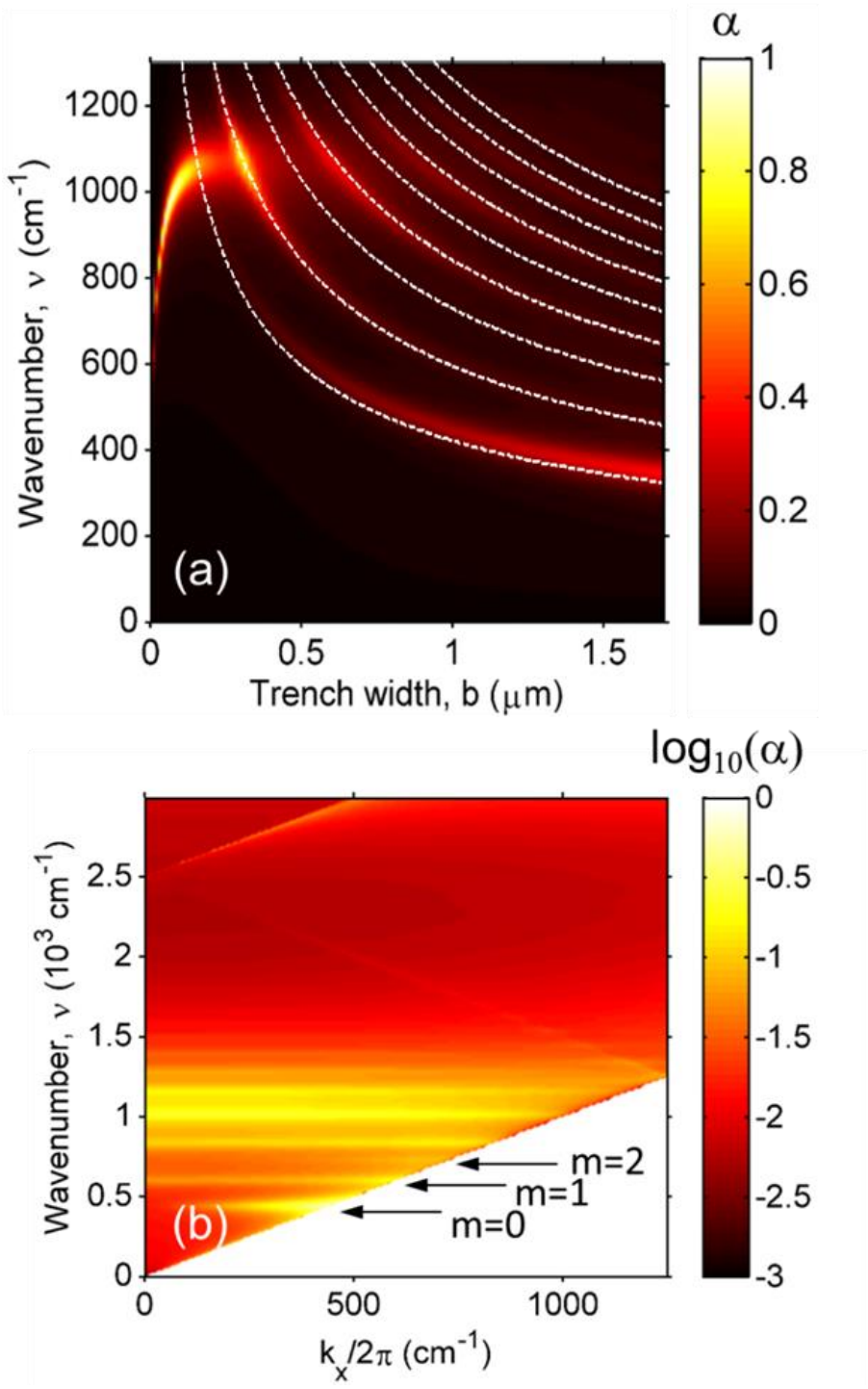

Figure 5.17 (a) The absorptance contour at $\theta = 50°$ for the structure with ribbons covered at the trench opening ($r = b$), where the dashed lines are the predictions from Eq. (5.8). (b) The absorptance contour for a grating with $b = 1$ μm showing dependence on the transverse wavevector.

last figure is the real part of E_z close to the lower surface of graphene layer at the coupled resonance. Note that E_z vanishes at the edges. The phase shift across the trench, $\mathrm{Re}\left(k_{\mathrm{GSP}}\right)r$, equals 2π, in agreement with Eq. (5.7) when $m = 1$.

Figure 5.17(a) illustrates the contour plot of the absorptance when the incidence angle is fixed at 50° with varying trench width while the ribbon width remains the same as the trench width ($r = b$). Compared with Figure 5.15(c), Figure 5.17(a) exhibits additional bright bands corresponding to the even-order plasmons. The predictions from Eq. (5.8) are shown as dashed lines, which agree well with the direct simulation. Moreover, the resonance frequencies of the MPs and the ribbon plasmons, compared to the normal incidence case, change little at $\theta = 50°$ due to their localized resonance feature. Figure 5.17(b) illustrates the absorptance contour of a grating with $b = 1$ μm when the x-component of the wavevector of the incidence, $k_x = \sin\theta\left(\omega/c_0\right)$, changes. The folded bright bands are the SPPs between the interface of silver grating and the vacuum [144]. The ribbon plasmons associated with odd m's can be excited at all incident angles while the even ones show up only at the oblique incidence. However, the absorptance bands are all flat, indicating that they are insensitive to the incidence angle. The MP resonance at around 1000 cm^{-1} is also insensitive [46] to k_x so that it can omnidirectionally couple with the plasmons in the ribbons that are around the same frequency.

The previous discussions are for the scenarios where the graphene ribbons are in contact with the top surface of the Ag grating, i.e., the elevation between graphene ribbons and the grating (t) is zero. In the applications where the chemical potential of graphene

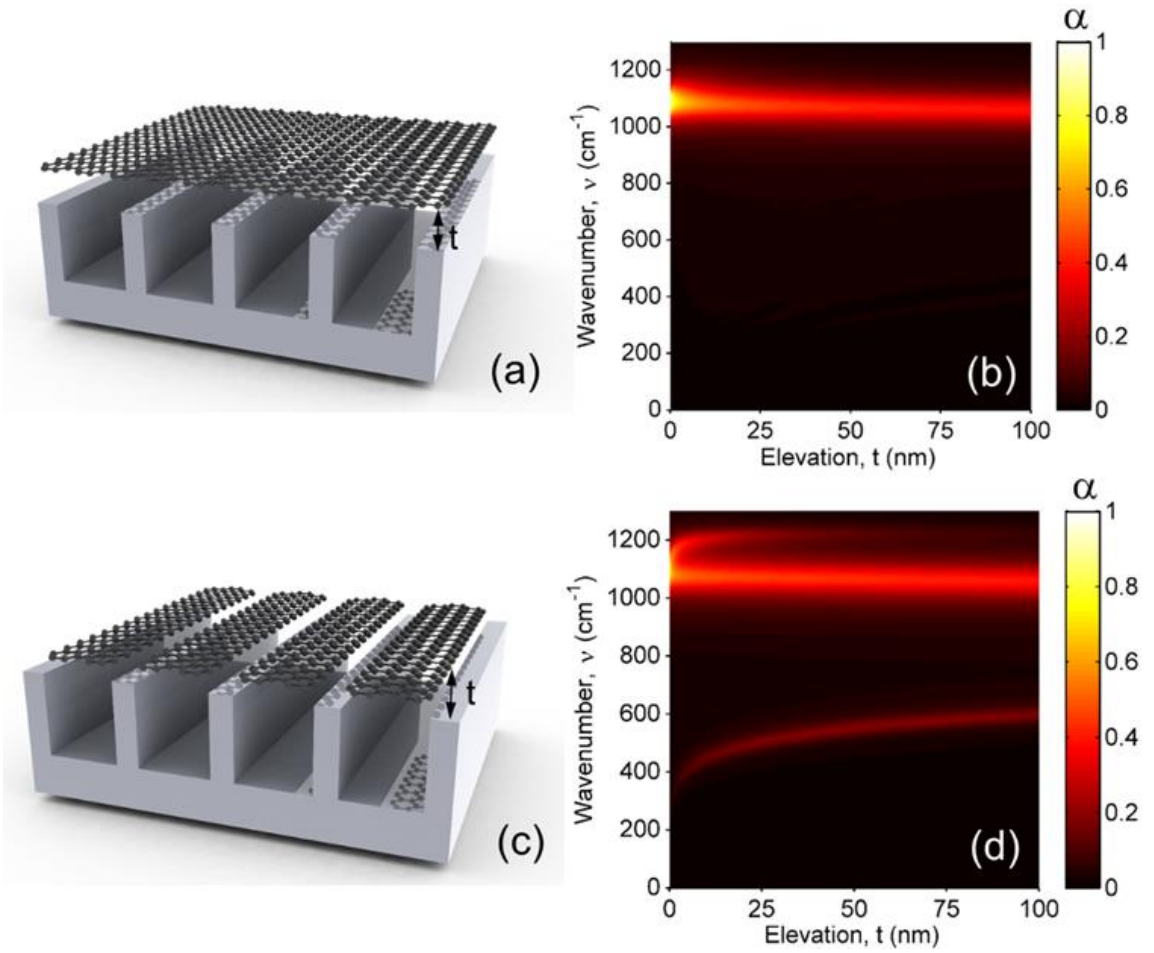

Figure 5.18 (a) Graphene above Ag grating with an elevation *t*. (b) The absorptance contour for the structure shown in (a) when *t* changes. (c) Graphene ribbons above Ag grating with an elevation *t*. (d) The absorptance contour for the structure shown in (c) when *t* changes.

need to be tuned by electrical gating, a dielectric layer may be inserted between the grating and graphene to prevent the flow of electrons between them [287]. It is expected that the coupling strength may deteriorate or even vanish when *t* increases. Figure 5.18 demonstrates this transition for normal incidence with $b = 0.3$ μm, where the graphene is lifted in vacuum with respect to the ridges of the grating (without using a dielectric layer). For continuous graphene shown in Figure 5.18(a), the coupling strength deteriorates once the graphene sheet detaches from the grating as shown in Figure 5.18(b). The resonance

frequency shifts slightly to lower frequencies when *t* increases. When *t* exceeds about 1.5 μm, the asymptotic value is reached at 1041 cm^{-1}, which is the frequency of the MP resonance for a plain grating, though not shown here.

The scenario becomes more complicated for the ribbon covered grating shown in Figure 5.18(c). Three resonance branches are identified on Figure 5.18(d). The coupled resonance, which is the middle branch, degenerates to the MP resonance of the plain grating at 1041 cm^{-1} when *t* increases, similar to the previous continuous graphene case. The upper and lower branches are associated with the plasmons in the ribbon array. When the ribbons are in contact with the grating, the strong resonance at 1086 cm^{-1} is due to the coupling of the MP in grating and the plasmon in ribbons with $m = 1$ and $\Delta\varphi = -\pi$. Once the ribbon array is detached, the phase shift of the plasmon upon reflection at the edges is no longer $-\pi$. Due to the sudden change of $\Delta\varphi$, the plasmon in ribbons associated with $m = 1$ shifts to lower frequencies and create the lower branch and the plasmon associated with $m = 3$ generates the upper branch. This also explains why the lower branch disappears at small *t* values. The graphene ribbon plasmons recover the case of a free-standing ribbon array when *t* is very large. The asymptotic resonance frequencies for the upper and lower branches are 1272 cm^{-1} and 664 cm^{-1}, respectively, which are obtained from Eq. (5.8) using $\Delta\varphi = \pi / 4$. Thus, the phase shift is dependent on *t*. Due to the effect of grating, the two branches gradually approach the asymptotic values as the elevation increases.

When the ribbons are moved down into the grating trench, the magnitude of the absorptance and the resonance condition will change. Figure 5.19 demonstrates this trend in which *p* is used to describe the elevation difference between the ribbon and the surface of the grating. The geometries of the grating are $\Lambda = 4$ μm, $b = 300$ nm, $h = 2$ μm, and

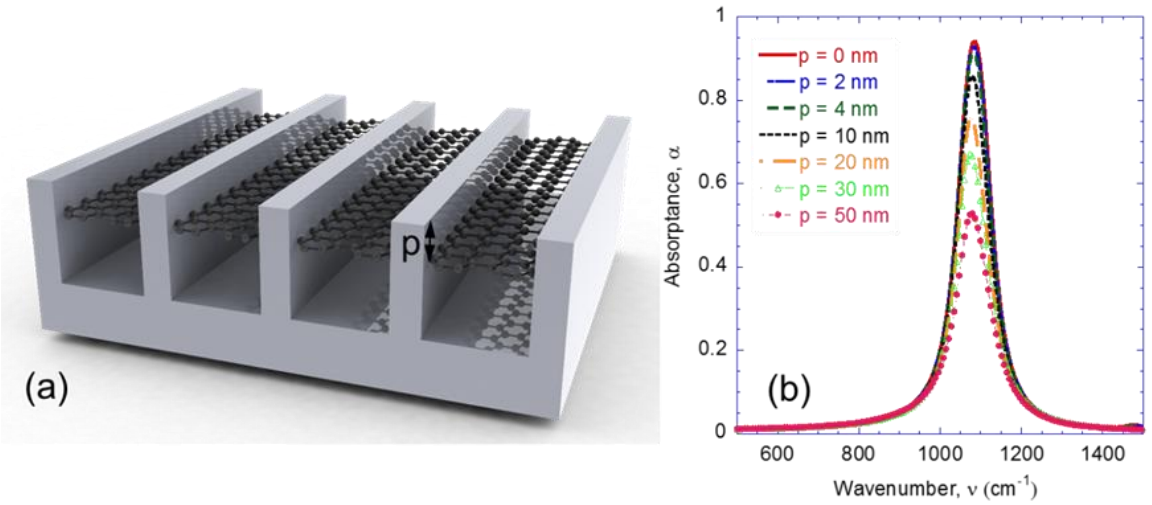

Figure 5.19 (a) Schematic of graphene ribbon-covered grating with $\Lambda = 4$ μm, b = 300 nm, $h = 2$ μm, and $\mu = 0.3$ eV. (b) Absorptance spectra for different p.

$\mu = 0.3$ eV. When p increases, the resonance frequency shifts to lower frequencies. Besides, the magnitude of the absorptance decreases as p increases, since the electric field is weaker away from the opening of the grating, resulting in less power dissipation and absorption.

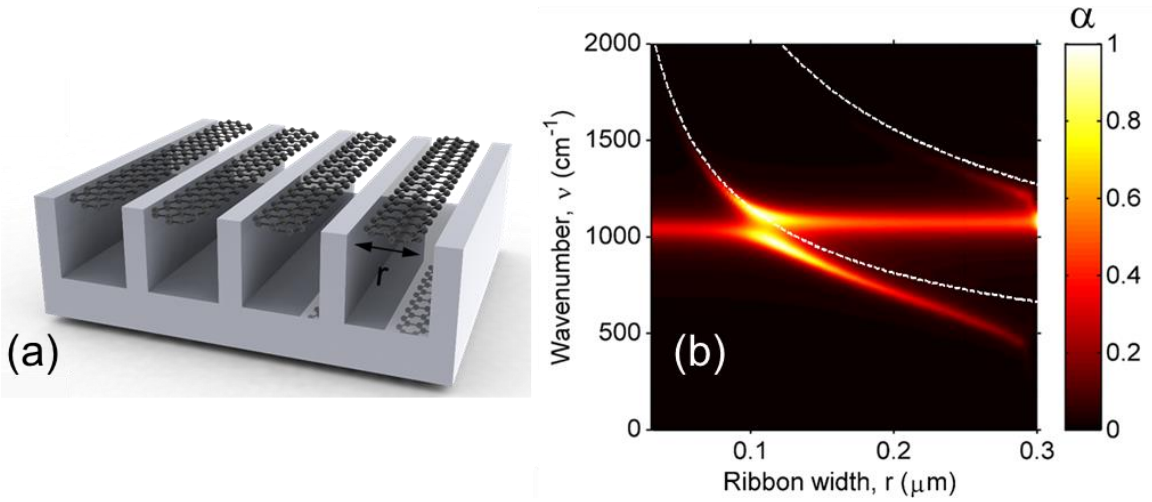

Figure 5.20 (a) Graphene ribbons covered Ag grating with ribbon width $r < b$. (b) The absorptance contour for the structure shown in (a) when r changes.

The coupling phenomena can also be significantly modified by the width of the ribbon. Figure 5.20(a) illustrates the structure where r is narrower than the trench width, which is fixed at 0.3 μm. The graphene ribbons are centered at the trench openings with t = 0. The continuous absorption branch for the graphene plasmon associated with m = 1 splits when crossed with the MP branch, as shown in Figure 5.20(b). There appears to be mode splitting or anti-crossing between the MP and ribbon plasmon branches near r = 0.11 μm, when the ribbon edges are not in contact with the grating. There exists an upper branch that corresponds to m = 3, as shown in Figure 5.20(b). The dashed lines represent the predictions of Eq. (5.8) with $\Delta\varphi = \pi/4$ for m = 1 (lower branch) and 3 (upper branch, respectively. It can be seen that the predicted ribbon plasmon dispersions agree well with the simulation for a small r but deviate when r gets larger. This deviation may be caused by the change of reflection phase shift, which is $\pi/4$ at small r and varies when the edges of the ribbons get closer to the silver trench walls. The m =1 branch disappears at $r \approx 0.3$ μm since $\Delta\varphi$ approaches $-\pi$, and similar reason holds for t = 0 in Figure 5.18(d).

Besides the geometry factors, the chemical potential of graphene can also modify the coupling picture by changing the dispersion of the graphene plasmons. For example, Figure 5.21 shows the absorptance spectra for the structure shown in Figure 5.12(a) with various μ. The case when μ = 0.3 eV corresponds to the solid spectrum in Figure 5.12(b). If μ changes to 0.28 eV or 0.32 eV, the ribbon plasmon shifts to a slightly lower or higher frequency, respectively, and the coupling strength decreases as the peak absorptance becomes lower. When μ further decreases to μ = 0.2 eV, two bumps at 871 cm^{-1} and 1164 cm^{-1} occur that are due to the plasmons associated with m = 1 and 3, respectively.

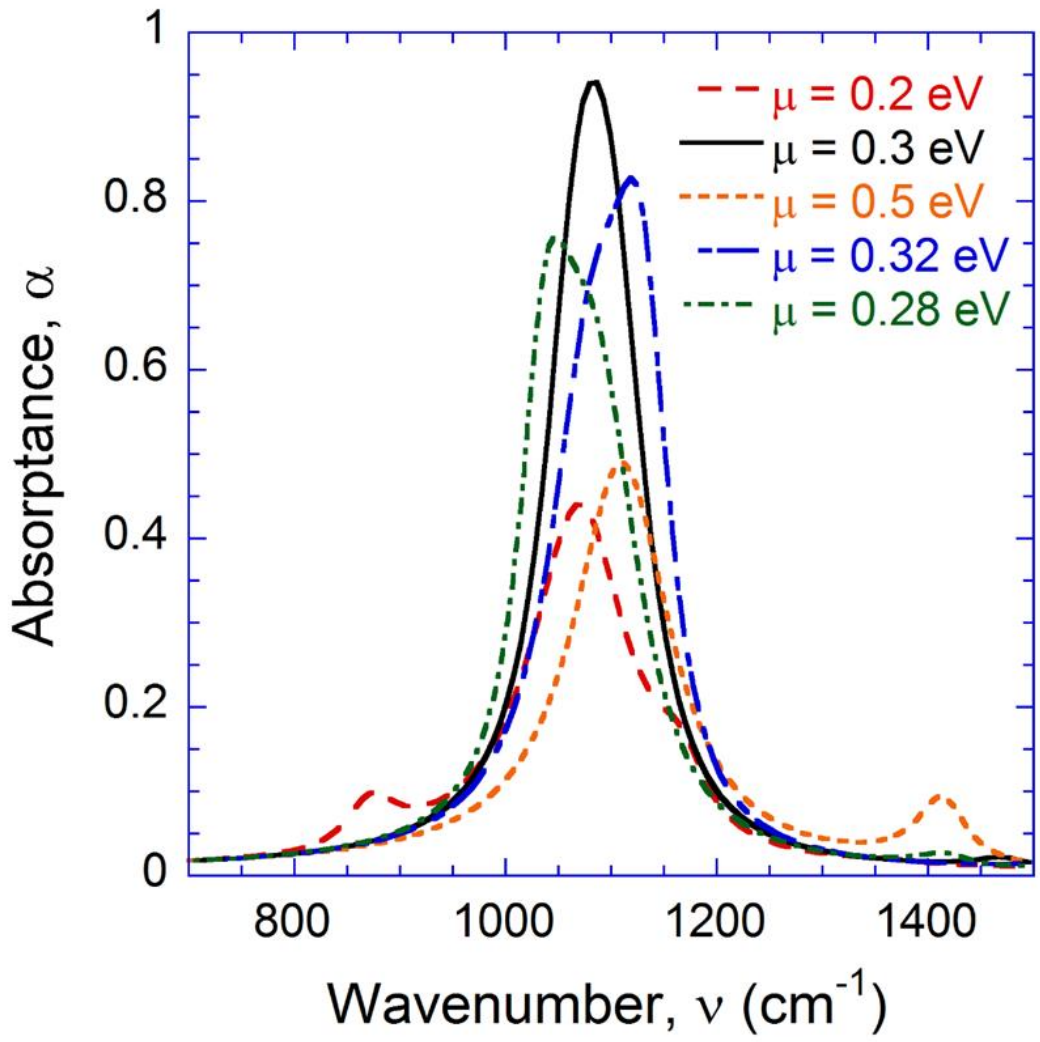

Figure 5.21 The absorptance spectra of the structure shown in Figure 5.12(a) with different graphene chemical potentials.

However, neither of them can couple with the MP, whose absorptance drops down to about 0.4. Similarly, at μ = 0.5 eV, the plasmon in ribbons associated with m = 1 moves to 1412cm^{-1} and totally decouples with the MP. Note that there is a slight shift of MP resonance at different μ and this can be understood with the equivalent LC model [298]. Therefore, the chemical potential can be tuned to control plasmons in the ribbons to couple or decouple with the MP resonance in the grating. If the interband transitions dominate the

conductivity of graphene, the ribbon will couple with MPs in grating without affecting the resonance frequency of the MPs, as has been discussed before.

In conclusion, this work demonstrates that the MPs in Ag grating can couple with the plasmons in ribbon arrays, resulting in greatly enhanced absorption of ribbons. The graphene ribbon acts as an inductor in the equivalent LC circuit and shifts the MP resonance to higher frequencies. In contrast to the free-standing ribbon arrays, the reflection phase shift becomes $-\pi$ when the ribbon edges are in contact with silver. The coupling effect deteriorates when the ribbons are elevated above the gratings. The width of the ribbon can be adjusted to create two coupled resonances at the same time. Furthermore, the chemical potential of graphene may be tuned to control the coupling between the two resonances. It is noted that graphene covered ridges has negligible effect and the resulting absorptance spectrum for a continuous sheet of graphene covered gratings is essentially the same as graphene ribbon arrays at the trench openings. Findings from this study shed light on the plasmonic coupling between graphene ribbons and metal gratings and may facilitate the design of next-generation optoelectronic systems based on graphene nanostructures.

5.3 Metal Gratings Covered by Hyperbolic Materials

Not only graphene but also hyperbolic 2D materials can be used together with plasmonic structures to create unusual properties such as perfect absorption. Perfect absorption is of critical importance in applications such as energy harvesting, radiative cooling, and photodetection applications [10,28,33,34,36,38,175,299]. Different kinds of metamaterials and micro/nanostructures have been proposed to achieve perfect absorption by utilizing various resonance modes. Among them are gratings that can support SPPs

[41,144] or surface phonon polaritons (SPhPs) [2], metal/dielectric/metal structures and deep metal gratings that can enable MPs [45-47,211,300-303], nanoparticles and nanoantennas that can create localized surface plasmon polaritons (LSPPs) [232], and hyperbolic metamaterials that can empower hyperbolic modes and epsilon-near-zero modes [42,44,304]. These resonances or modes can couple with incident light and capture the energy of the incident waves efficiently [31]. Besides these metamaterials and nanostructures, 2D materials such as graphene and black phosphors offer enormous novel ways to create electromagnetic resonances because of their unique plasmonic properties [58,285]. Various nanostructured resonators and ribbons using 2D materials have been demonstrated to support localized surface plasmon resonances [94,305,306]. However, with an atomically thin thickness and relatively short light-matter interaction path, it is difficult to achieve perfect absorption in standalone 2D material nanostructures.

A promising way is to combine 2D materials with nano/microstructures. The previous works in this chapter demonstrate that 2D materials covered micro/nanostructures and metamaterials can provide a new route to achieve perfect absorption. Moreover, Piper and Fan [271] utilized critical coupling in graphene/photonic crystals hybrid structures to achieve perfect absorption. Zhu et al. [307] used a similar mechanism to construct angle-selective perfect absorbers consisting of graphene and a chalcogenide layer atop a mirror. Plasmonic optical nanoantennas with different shapes can also be hybridized with 2D materials to capture light efficiently [74,265]. While 2D plasmonic materials and semiconductors have been studied extensively because of their potential applications in microelectronic, optoelectronic, and photonic devices [83], few studies have yet explored the potentials of using phononic 2D materials to achieve perfect absorption through

coupling with nano/microstructures, especially for hBN that is a hyperbolic material. Considering that hBN can endure a temperature of 1500 °C in air [308], accomplishing strong absorption or emission bands in the infrared region with hBN films holds great significance for high-temperature energy harvesting applications [36].

As explained previously, hyperbolic materials refer to uniaxial materials whose axial (extraordinary) and tangential (ordinary) permittivities have opposite signs. Owning to its optical phonon vibrations, hBN naturally possesses two mid-infrared Reststrahlen bands that have hyperbolic response [64,126]. Because of the hyperbolicity, hBN films support multiple orders of low-loss hyperbolic phonon-polariton (HPP) waveguide modes [81,82] that can potentially be utilized to achieve perfect absorption. However, since the lateral wavevectors of these modes are much larger than the magnitude of the wavevector in vacuum, HPPs cannot be excited directly by the incident waves from vacuum. Thus, hybridizing hBN with periodic structures can possibly match the wavevectors required by HPPs and achieve strong absorption induced by phonons. Furthermore, hBN exhibits inverted hyperbolic response since the phonon vibrations are in perpendicular crystallographic directions [126], making it an ideal material to explore the basic coupling phenomena between hyperbolic materials and other resonances such as plasmonic polaritons in nano/microstructures.

This work reports a numerical investigation of the possibility to achieve perfect and near-perfect absorption in a hybrid structure consisting of an hBN film and a metal grating. The geometric arrangement of the hBN/metal grating hybrid structure is illustrated in Figure 5.22. The 1D grating is made of silver (Ag) with a period Λ in the *x*-direction and extends infinitely in the *y*-direction. Its trench width is *b* and height is *h*. The thickness of

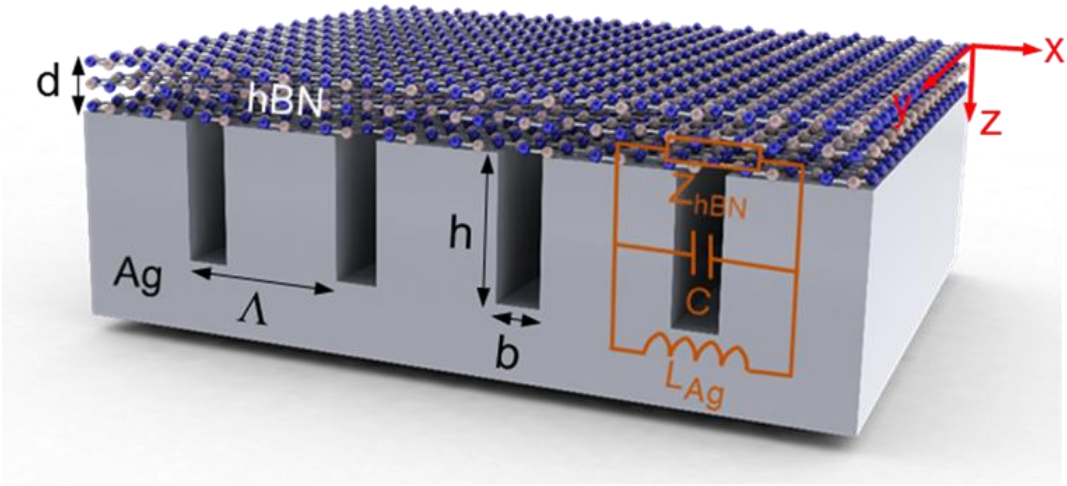

Figure 5.22 Schematic of the hBN/metal grating hybrid structure, where the Ag grating period, height, and trench width are Λ, *h*, and *d*, and the thickness of the hBN is *d*. The LC circuit model is overlaid on the hybrid structure.

the covered hBN film is denoted as *d*. The substrate of the grating structure is also Ag and assumed to be semi-infinite. In reality, a Ag film whose thickness is much greater than the photon penetration depth can be deposited on another supporting substrate. Thus, the directional (spectral) absorptance of the structure, α, can be calculated by $\alpha = 1 - R$, where *R* is the directional-hemispherical reflectance of the whole structure that can be calculated using RCWA.

The hyperbolic regions allow waves with unbounded wavevectors to propagate as can be seen from the isofrequency surface in Eq. (2.15). For k_y = 0, the isofrequency surface can be drawn in k_x-k_z plane as shown in Figure 5.23. For both Type-I and Type-II regions, at very large $|\mathbf{k}|$, the allowed wavevectors approach the asymptotic lines described by $k_z = \pm k_x \sqrt{-\varepsilon_\perp / \varepsilon_{||}}$ (neglecting loss). In this case, the Poynting vector (*i.e.*, energy propagation direction of the polaritons) is orthogonal to the isofrequency curve. The

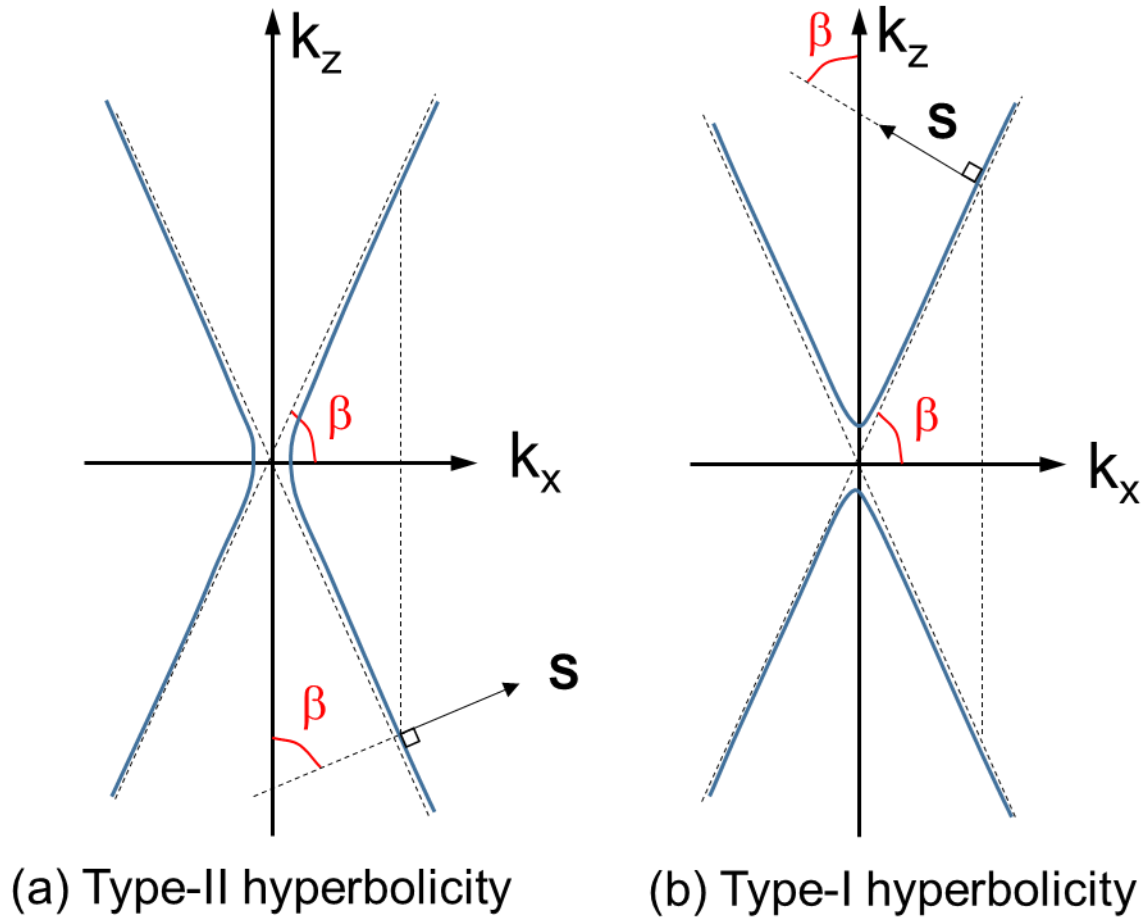

Figure 5.23 Isofrequency curves for (a) Type-II and (b) Type-I hyperbolic regions. **S** represents the Poynting vector and β is the angle between **S** and the *z*-axis.

polariton propagating angle is defined as the angle between the Poynting vector and the *z*-axis and is approximately equal to [120-122]

$$\beta(\omega) = \arctan\left(\sqrt{-\frac{\varepsilon_{\perp}}{\varepsilon_{\parallel}}}\right) \tag{5.9}$$

Equation (5.9) suggests that at a given frequency, there exists a unique propagation direction inside the hyperbolic material at sufficiently large lateral wavevectors.

For an hBN film, HPPs are supported in the two Reststrahlen bands or hyperbolic regions. Their dispersion can be obtained from the reflection coefficient of TM waves for an hBN film of a thickness *d* suspended in vacuum:

$$r = \frac{r_{12} + (1 - r_{12} - r_{21}) r_{23} \exp(2ik_{z,2}d)}{1 - r_{21} r_{23} \exp(2ik_{z,2}d)} \tag{5.10}$$

where indexes 1 and 3 are vacuum and 2 indicates the hBN film. The reflection coefficients between the vacuum and hBN or vice versa are given by

$$r_{ab} = \frac{\frac{\varepsilon_{\perp,b}}{k_{z,b}} - \frac{\varepsilon_{\perp,a}}{k_{z,a}}}{\frac{\varepsilon_{\perp,b}}{k_{z,b}} + \frac{\varepsilon_{\perp,a}}{k_{z,a}}} \tag{5.11}$$

where a = 1 or 2 and $k_{z,b} = \left(\varepsilon_{\perp,b} k_0^2 - \varepsilon_{\perp,b} \beta^2 / \varepsilon_{\parallel,b}\right)^{1/2}$ with b being 1, 2 or 3 is the z-component of the wavevector in hBN or vacuum. For vacuum, one can set $\varepsilon_\perp = \varepsilon_\parallel = 1$. The poles of Eq. (5.10) indicate the dispersion of HPPs in hBN films that can be seen by the bright bands from the contour plots of the imaginary part of r in k_x-ω space [82], as shown in Figure 5.24(a) and (b) for a 30 nm-thick hBN film in the frequency ranges near the higher and the lower hyperbolic regions, respectively. Multiple orders of HPPs exist in both hyperbolic regions and more orders are excited with thicker hBN films. Alternatively, when $k_x >> k_0$, the dispersion based on $1 - r_{21} r_{23} \exp(2ik_{z,2}d) = 0$ can be approximated by [81]

$$k_x(\omega) = \frac{1}{d} \sqrt{-\frac{\varepsilon_\parallel}{\varepsilon_\perp}} \left[p\pi \pm 2 \arctan\left(\frac{1}{\sqrt{-\varepsilon_\parallel \varepsilon_\perp}} \right) \right] \tag{5.12}$$

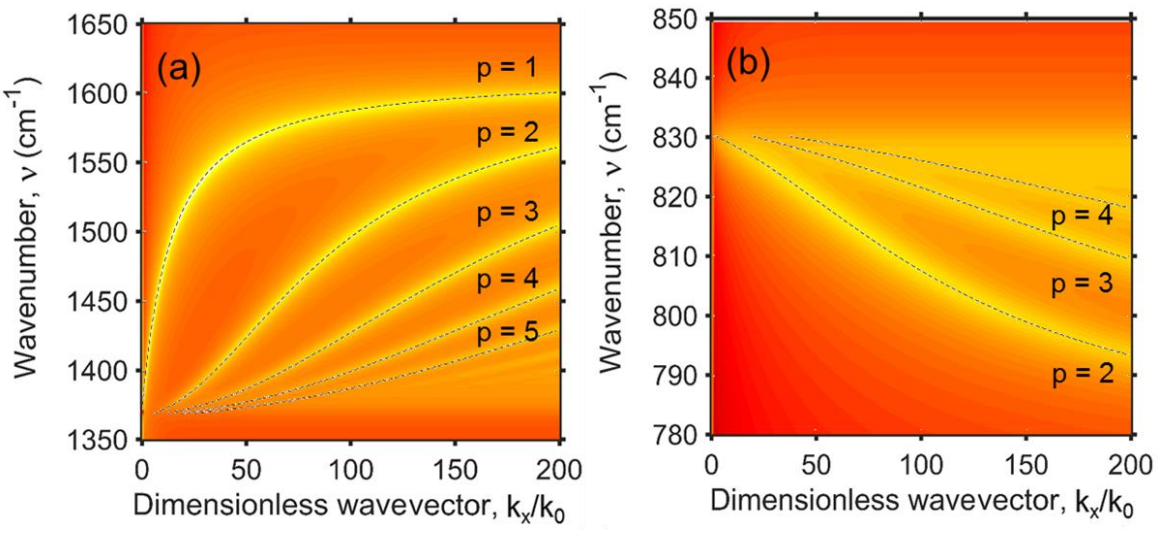

Figure 5.24 Contour plots showing Im(r) of a 30-nm-thick suspended hBN film in vacuum near (a) the upper (Type-II) hyperbolic region and (b) the lower (Type-I) hyperbolic region. The predictions from Eq. (5.12) are overlaid as dashed curves.

where integer p indicates the order of the HPPs. The plus and minus signs are chosen respectively for the higher and lower hyperbolic bands based on the shape of the dispersion curves [82]. The prediction from Eq. (5.12) is overlaid on the contour plot as broken lines in Figure 5.24 with the corresponding p. Note that $p = 1$ yields negative k_x in the lower hyperbolic region and thus is not shown. Clearly, Eq. (5.12) provides a convenient description of HPPs and will be referred to in later discussions. Since the HPPs have sufficient large wavevectors, Eq. (5.9) is valid and thus different orders of HPPs at the same frequency have the same energy flux propagation direction, as will be further demonstrated.

Figure 5.25 shows the absorptance spectra of plain gratings (dashed lines) and hBN-covered Ag gratings (solid lines) calculated based on the anisotropic RCWA algorithm for TM waves. Unless specified otherwise, the wave is incident normal to the x-y plane and the plane of incidence is set as the x-z plane. Since the considered structures

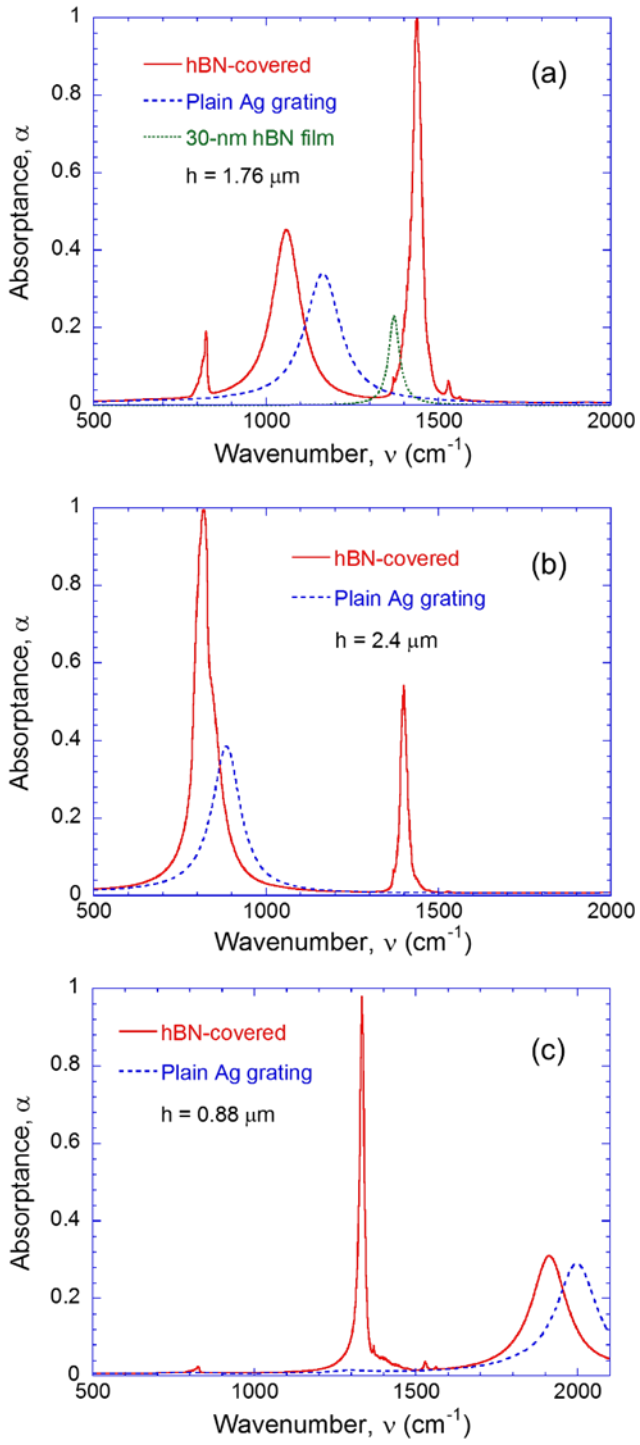

Figure 5.25 Absorptance spectra of plain Ag gratings (dashed lines) and hBN-covered Ag gratings (solid lines): (a) h = 1.76 μm, (b) h = 2.4 μm, and (c) h = 0.88 μm. The other parameters are $\Lambda = 4$ μm, $b = 300$ nm, and d = 30 nm. The absorptance spectrum of a suspended 30-nm hBN film in vacuum is also shown in (a).

are one-dimensional gratings and the electric field for TM waves is in the *x*-direction; therefore, $\theta = \psi = \phi = 0°$ and $k_y = 0$. The dielectric function of Ag is calculated using the introduced Drude model. Throughout the modeling, the parameters are set as $\Lambda = 4$ μm, $b = 300$ nm, and $d = 30$ nm, while h is allowed to change. Such grating geometries can create excitations of MPs in the infrared region as demonstrated before [46], but Λ and b can be other values to make MPs in the infrared. In Figure 5.25(a), (b), and (c), h is 1.76 μm, 2.4 μm, and 0.88 μm, respectively. One absorptance peak can be identified on each plain Ag grating spectrum, and this peak is caused by the excitation of MP resonances similar to the scenarios discussed before. Since in Ag gratings, a high absorptance peak due to MP relies on an efficient coupling between the surface waves on the trench walls that can be achieved only when the trench is very narrow, for trench width $b = 300$ nm, the absorptance peaks are far from unit in Figure 5.25. High absorptance is difficult to achieve with thin hBN films either, as demonstrated by the absorptance spectrum of a suspended 30-nm hBN film in Figure 5.25(a). Only a small absorptance peak at $\omega_{TO,\perp}$ is obtained, since no HPPs can be excited with propagating waves in air. However, after covering the hBN film on the Ag grating, perfect absorption ($\alpha = 1$) and near-perfect absorption ($\alpha = 0.99$) can be achieved at $\nu = 1436$ cm^{-1} and $\nu = 818.7$ cm^{-1} as shown in Figure 5.25(a) and (b), respectively. These two high absorptance peaks fall in the hyperbolic regions of hBN, while the absorption peak ($\alpha = 0.94$) at $\nu = 1333$ cm^{-1} shown in Figure 5.25(c), is slightly below the higher-frequency hyperbolic region. The origin of these high absorption peaks and other peaks on the spectra will be elucidated in the following.

Figure 5.26(a) and (b) exhibit the absorptance contours for plain and hBN-covered gratings, respectively, with respect to the wavenumber and grating height. Two bright

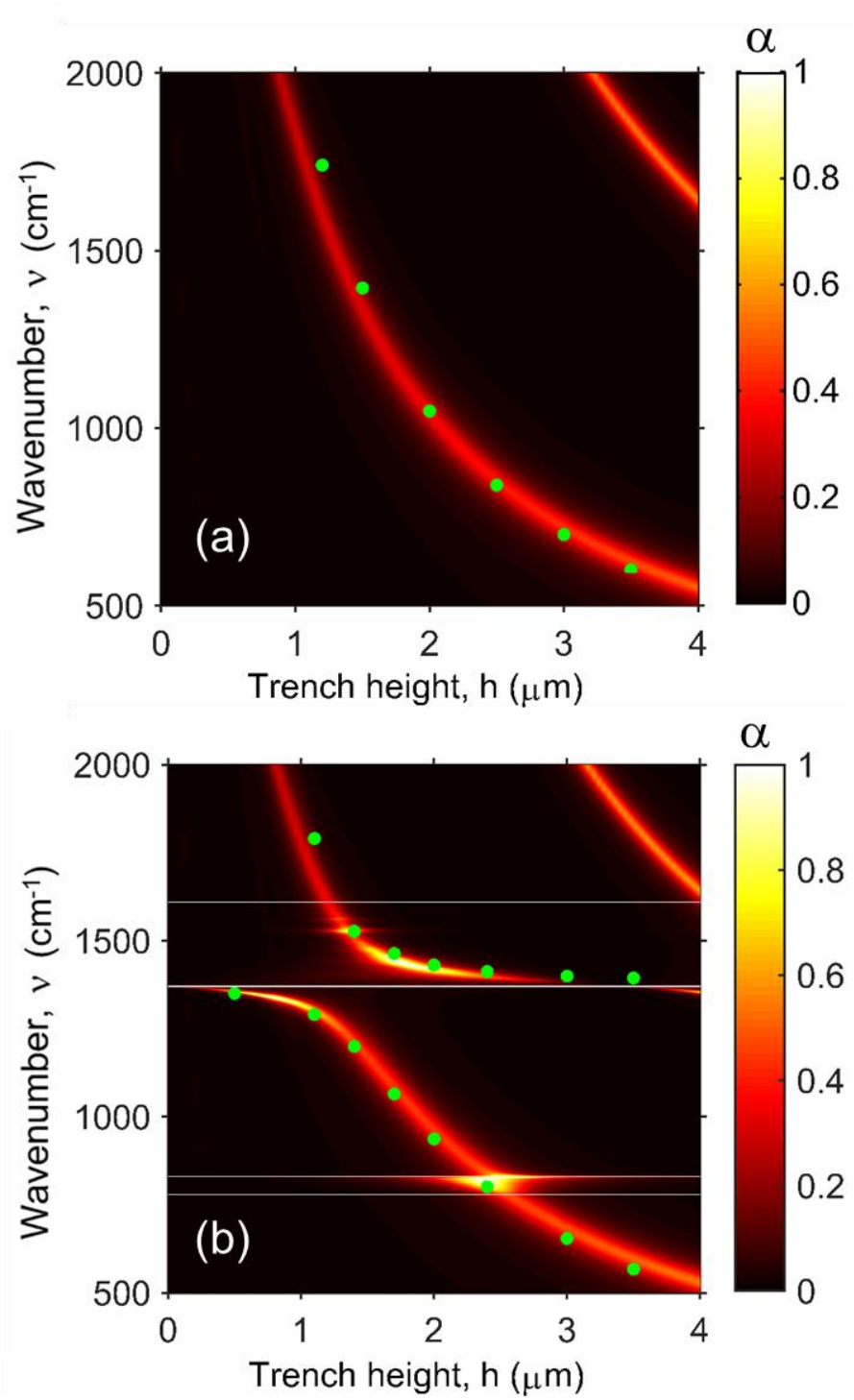

Figure 5.26 Absorptance contours of (a) plain Ag gratings and (b) hBN-covered Ag gratings in terms of frequency and the grating height. The parameters are $\Lambda = 4\ \mu\text{m}$, $b = 300\ \text{nm}$, and $d = 30\ \text{nm}$. The predictions from the LC circuit model are shown as round markers on both plots. The horizontal white lines in (b) show the two hyperbolic regions.

branches due to excitation of MPs show up in (a). The fundamental MP modes, corresponding to the lower branch, can be predicted using the LC circuit model as has been previously discussed. The predicted results are shown in (a) as round markers, giving a good agreement with RCWA calculation. The upper branch correspond to higher-order MP and will not be discussed further [50]. With the hBN, the fundamental resonance branch in (b) has a noticeably different shape compared to that in (a). A disconnection close to $\omega_{\mathrm{TO},\perp}$ occurs and high absorptance is achieved inside the two hyperbolic regions as well as at frequencies that are slightly lower than $\omega_{\mathrm{TO},\perp}$. The spectra presented in Figure 5.25 are representatives of the high absorptance in different frequency ranges achieved at specific grating heights. Note that the hyperbolic regions are indicated between two white horizontal lines. The fundamental modes can be predicted by adding Z_{hBN} in the LC circuit, as shown in Figure 5.22. However, Z_{hBN} takes different formula in different frequency ranges.

The frequency-dependent impedance of hBN can be obtained from $Z_{\mathrm{hBN}} = S/(\sigma A_{\mathrm{eff}})$, where S is the length along the current path, $\sigma = -i\omega\varepsilon\varepsilon_0$ is the electrical conductivity, and A_{eff} is the effective cross-section area [52]. Similar to the graphene-covered case discussed before, in the grating trench, the hybrid structure possess an electric field that is very similar to that of MPs in plain gratings. Thus, only the part of hBN that across the trench opening participates in the LC circuit, *i.e.*, $S = b$. The penetration depth of the electric field in hBN is much greater than d and thus $A_{\mathrm{eff}} = sd$, where s is the length in the y-direction that can be set to unity for one-dimensional gratings. The electric field near the trench opening in hBN is dominated by its x-component [148,149], indicating that the conductivity should be evaluated based $\varepsilon_\perp$ of hBN. The real part of Z_{hBN} is the

resistance and it is negligibly small in the frequency regions of interest. The imaginary part of Z_{hBN} can be positive or negative since $\varepsilon_{\perp}'$ takes different signs depending on frequency, meaning that hBN can serve as a capacitor or inductor [114,309]. In the upper hyperbolic region, $\varepsilon_{\perp}'$ is negative due to the in-plane phonon vibrations as shown in Figure 2.6, and hBN acts like an inductor across the trench opening with an inductance

$$L_{\mathrm{hBN}} = -\frac{\varepsilon_{\perp}' b}{\varepsilon_0 \left|\varepsilon_{\perp}\right|^2 \omega^2 sd} \tag{5.13}$$

On the other hand, outside the higher-frequency hyperbolic region, $\varepsilon_{\perp}'$ is positive and hBN provides a capacitance

$$C_{\mathrm{hBN}} = \frac{\varepsilon_0 sd \left|\varepsilon_{\perp}\right|^2}{\varepsilon_{\perp}' b} \tag{5.14}$$

Equations (5.13) and (5.14) can be obtained based on Z_{hBN}.

After all the elements in the circuit are known, the resonance frequency can be obtained as $\nu = \left(2\pi c_0 \sqrt{L_{\mathrm{tot}} C_{\mathrm{tot}}}\right)^{-1}$ [310]. In the upper hyperbolic region, L_{hBN} and L_{Ag} are in parallel, yielding $L_{\mathrm{tot}} = L_{\mathrm{Ag}} L_{\mathrm{hBN}} \big/ \left(L_{\mathrm{Ag}} + L_{\mathrm{hBN}}\right)$ and $C_{\mathrm{tot}} = C$. The total inductance is reduced by hBN compared to plain gratings and thus the fundamental resonance in the hybrid structure shifts to frequencies higher than those in plain gratings as shown in Figure 5.25(a). Outside the hyperbolic region, C_{hBN} and C are connected in parallel, yielding $L_{\mathrm{tot}} = L_{\mathrm{Ag}}$ and $C_{\mathrm{tot}} = C + C_{\mathrm{hBN}}$. This makes the total capacitance larger, shifting the MP resonance to lower frequencies, as demonstrated in Figure 5.25(b) and (c). The LC model (round markers) matches the RCWA simulation very well, as shown in Figure 5.26(b). The

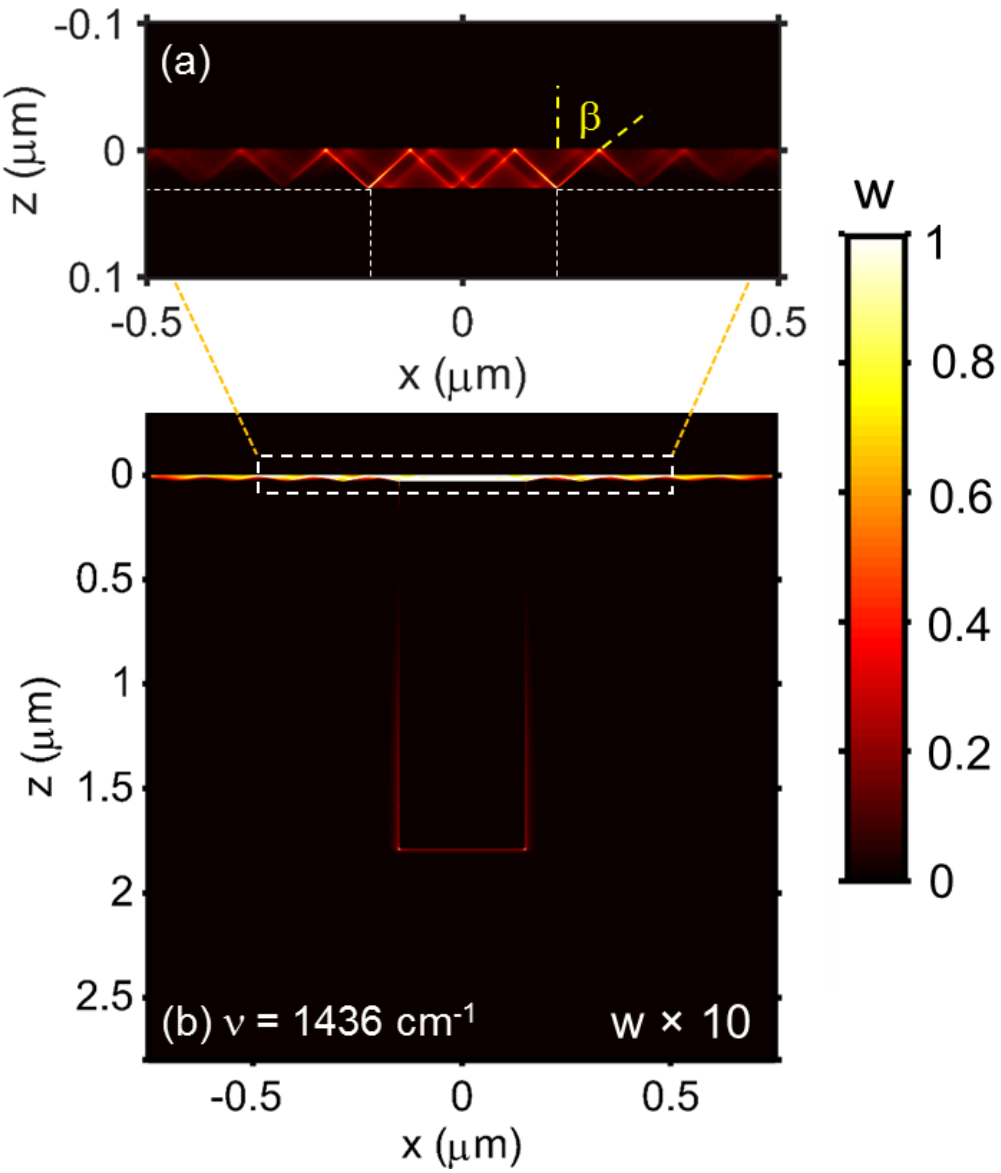

Figure 5.27 Local power dissipation density profile at $\nu = 1436$ cm^{-1} corresponding to the high-absorptance resonance in Figure 5.25(a): (a) Zoomed-in profile showing the details inside the hBN film, (b) The dissipation profile (enlarged by one order of magnitude) of the structure. The scale bar is in MW/m^3 with an upper limit 1 MW/m^3, beyond which w is displayed with white color. The propagation angle β is illustrated on (a). Note that the x and z scales are readjusted to show the profile clearly.

good agreement justifies that the fundamental resonance is a coupled resonance, which has some unique features depending on the frequency range.

Figure 5.27 shows the local power dissipation profile at the perfect-absorption peak shown in Figure 5.25(a), which lies in the high-frequency hyperbolic region, where Figure 5.27(a) displays a zoomed-in view of the hBN film and the unit of the contour scale for w is MW/m^3. For Figure 5.27(b), w is multiplied by a factor of 10 to show the dissipation near the surface of the Ag groove clearly. For example, at the trench bottom, the actual value is $w \approx 0.019$ MW/m^3 in Ag. In the calculation, the magnitude of the incident electric field is 1 V/m. It can be seen that dissipation is mainly at the surface of the grating, similar to previous observations of metal gratings at MP resonances. The absorption in the hBN film is much stronger than in the grating. The maximum w in hBN is 2.4 MW/m^3, which exceeds the upper limit of the scale bar. The absorptance of the hBN film can be obtained as 0.91 following Eq. (3.49), suggesting that most of the incident power is absorbed by the hBN film.

As can be seen from Figure 5.27(a), the dissipation profile follows a zigzag path in the hBN film that is symmetric about the middle of the trench, indicating that the power is nonuniformly absorbed in the film. This dissipation profile is a unique feature of the HPP waveguide modes [120-122]. Due to the diffraction of the grating, electric fields with large wavevectors are generated and they excite the hyperbolic polaritons in the hBN film. The polaritons predominantly initiate from the two corners of the grating because of the highly concentrated electric field therein that is about 50 times that of the incident waves. The polariton rays propagate inside the film with a fixed angle of $\beta = 65.7°$ as described by Eq. (5.9) and experience a total internal reflection on the top surface of the hBN film [121]. The predicted angle matches Figure 5.27(a) well, even though loss is neglected Eq. (14). Furthermore, the period of the zigzag pattern in the x-direction can be derived as $2d \tan \beta$

based on the wavevector of the polaritons. It should be noted that multiple orders of HPPs are excited simultaneously at the resonance frequency due to grating diffraction. For a specific frequency, according to Eq. (5.12), the wavevectors of the multiple HPPs form an arithmetic progression with a common difference $\Delta k_x = (\pi / d)\sqrt{-\varepsilon_{||}/\varepsilon_{\perp}}$. Thus, these HPPs produce an interference pattern with a spatial period $2\pi/\Delta k_x$ [121], which is the same as the above-obtained period in real space, providing a complementary way to understand the periodic zigzag pattern. Due to the weak loss of hBN, these HPPs dissipate power as they propagate inside the film and gradually vanish. The weak loss of hBN enables a long propagation length that is an advantage of hBN in subdiffractional focusing and imaging applications over other hyperbolic metamaterials constructed with metallic nanowires or metal/dielectric multilayers [120-122]. The unique directional propagation of the polaritons allows multiple reflections and long light-matter interaction distances, giving rise to the strong absorption in hBN.

Figure 5.28 illustrates a similar local power dissipation profile, which corresponds the high-absorptance resonance at $\nu = 818.7$ cm^{-1} (in the lower hyperbolic region) in Figure 5.25(b). The dissipation in hBN is again much stronger than in Ag, reaching 8 MW/m^3 at the two corners of the grating and 84% of the incident power is dissipated in hBN with a zigzag dissipation pattern with $\beta = 72.4°$. Due to higher loss at this resonance, the HPPs survive a relatively shorter propagation distance. Based on the above analysis, the dissipation profile at the perfect and near-perfect absorption in hyperbolic regions possesses both features of a MP and HPPs. Therefore, these resonances are hybrid hyperbolic phonon-plasmon polaritons formed by strong coupling between plasmonic MP in the metal grating and HPPs in the hBN film.

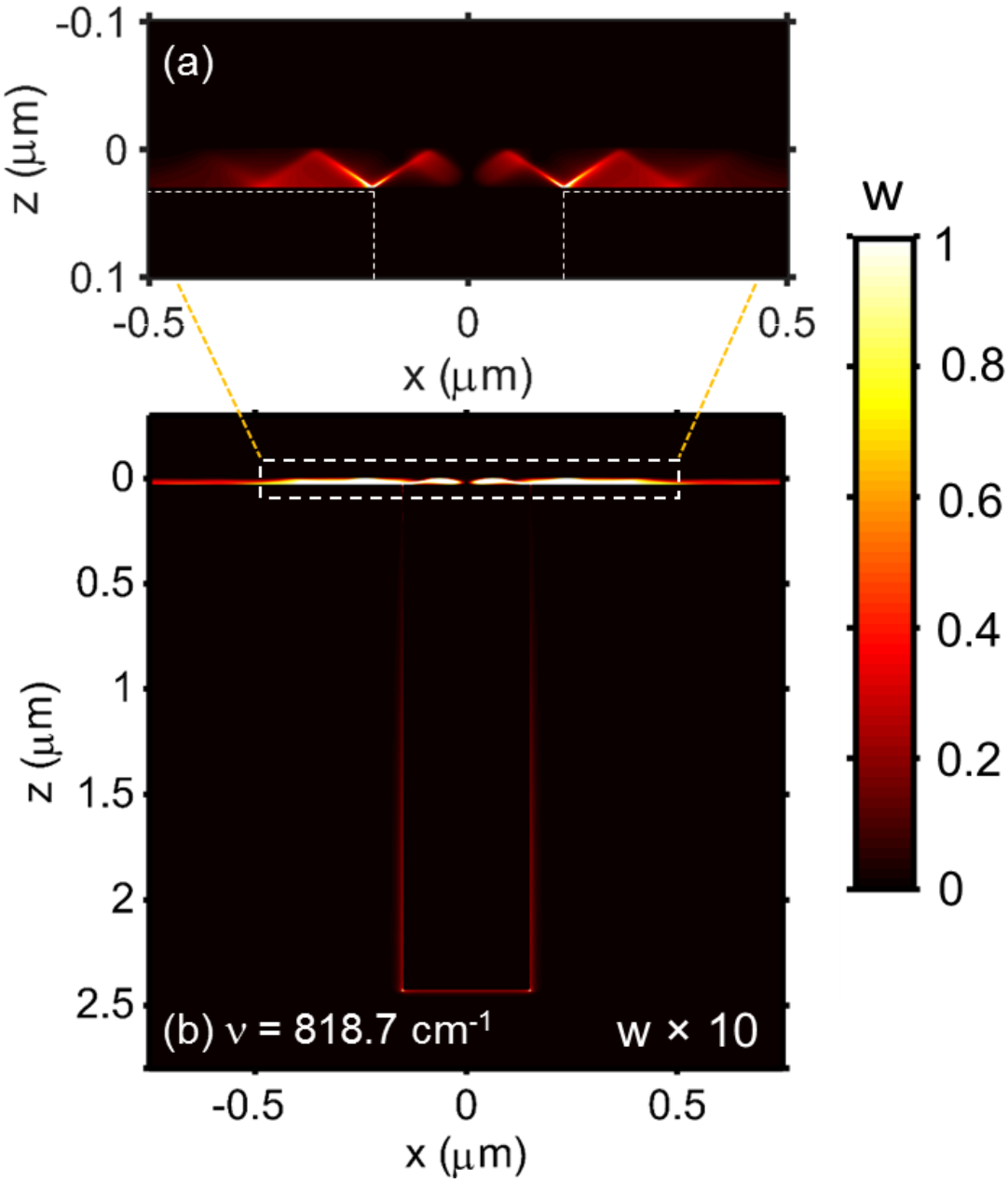

Figure 5.28 Local power dissipation density profile at $\nu = 818.7$ cm^{-1} corresponding to the high-absorptance resonance in Figure 5.25(b): (a) Zoomed-in profile, (b) The dissipation profile (enlarged by one order of magnitude) of the structure. The scale bar is in MW/m^3 with an upper limit 1 MW/m^3, beyond which w is displayed with white color.

The scenario of the near-perfect absorption at $\nu = 1333$ cm^{-1} shown in Figure 5.25(c) is different from the above discussion since it is not in the hyperbolic regions.

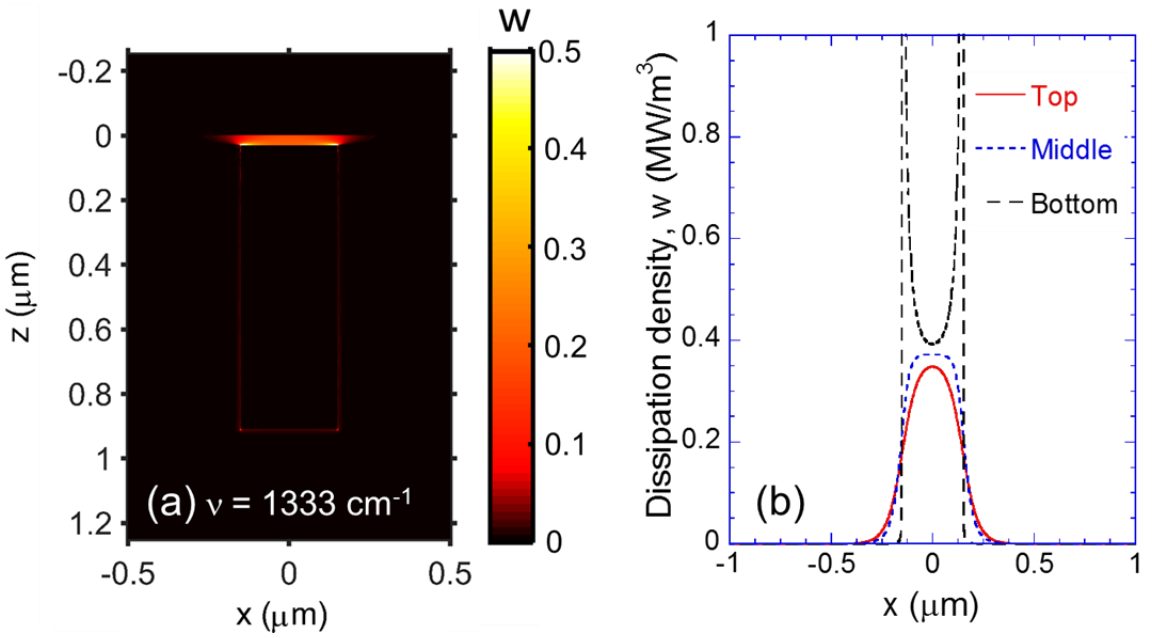

Figure 5.29 (a) Local power dissipation density contour at $\nu = 1333$ cm^{-1} corresponding to the near-perfect resonance in Figure 5.25(c). The scale bar is in MW/m^3 with an upper limit 0.5 MW/m^3, beyond which w is displayed with white color. (b) Local power dissipation density profiles of the top (z = 0 nm), the middle (z = 15 nm), and the bottom (z = 30 nm) of the hBN film.

Figure 5.29(a) shows the dissipation profile at this resonance. Here, the absorption in the hBN film is concentrated within the portion that is across the trench opening of the grating. The scale bar is nonlinear beyond 0.5 MW/m^3 to show the dissipation profile in the grating is again due to the excitation of MP [148,149]. One can obtain the absorptance of hBN to be 0.72, which is more than 3 times of the value in the Ag grating (*i.e.*, 0.22). The main reason for this high absorptance is an enhanced electric field near the trench opening when a MP is excited; this is very similar to the high absorptance in graphene-covered metal gratings discussed before [46,148,149]. Since the electric field strength decays gradually away from the trench opening, w becomes progressively smaller in hBN film as illustrated in Figure 5.29(b), showing the dissipation profiles at different height in the film. At the

bottom of the hBN film, *w* shows two spikes at the two corners of the grating due to the highly concentrated electric field therein. This strong electric field is also important to the zigzag dissipation profile of the hyperbolic phonon-plasmon polaritons as discussed before. Therefore, the strong absorption is a result of hybrid phonon-plasmon polaritons.

The general effect of the geometric parameters can be understood using the above-mentioned LC circuit model. For example, if *d* becomes larger, in the upper hyperbolic region, based on Eq. (5.13), the inductance of hBN decreases and pushes the coupled resonances to higher frequencies, and vice versa in frequency range that hBN is a capacitor. However, one may have noticed that, there exist some flat bright bands in the two hyperbolic regions in Figure 5.26(b) that cannot be explained by the LC circuit. In fact, they are HPPs excited by the electric field with large wavevectors due to grating diffraction. This can be seen more clearly if the hBN film becomes thicker, as demonstrated in Figure 5.30(a) and (b), in which *d* is 60 nm and 100 nm, respectively. The above-discussed perfect and near-perfect absorption appear again and the flat bright bands also become clearer. These flat bands are discrete and become sparser in frequency when the *d* becomes larger, indicating that the hyperbolic phonon polaritons are excited at specific frequencies instead of the whole hyperbolic region. This effect can be understood by the wavevectors of HPPs described in Eq. (5.12). Since multiple orders of HPPs are excited and the wavevectors are matched trough grating diffraction based on Eq.(3.4), the common difference of the wavevectors of the HPPs, Δk_x, must be a multiple of $2\pi/\Lambda$:

$$\frac{\pi}{d}\sqrt{-\frac{\varepsilon_{\parallel}}{\varepsilon_{\perp}}} = m\frac{2\pi}{\Lambda} \tag{5.15}$$

Thus, diffraction order *m* has to satisfy

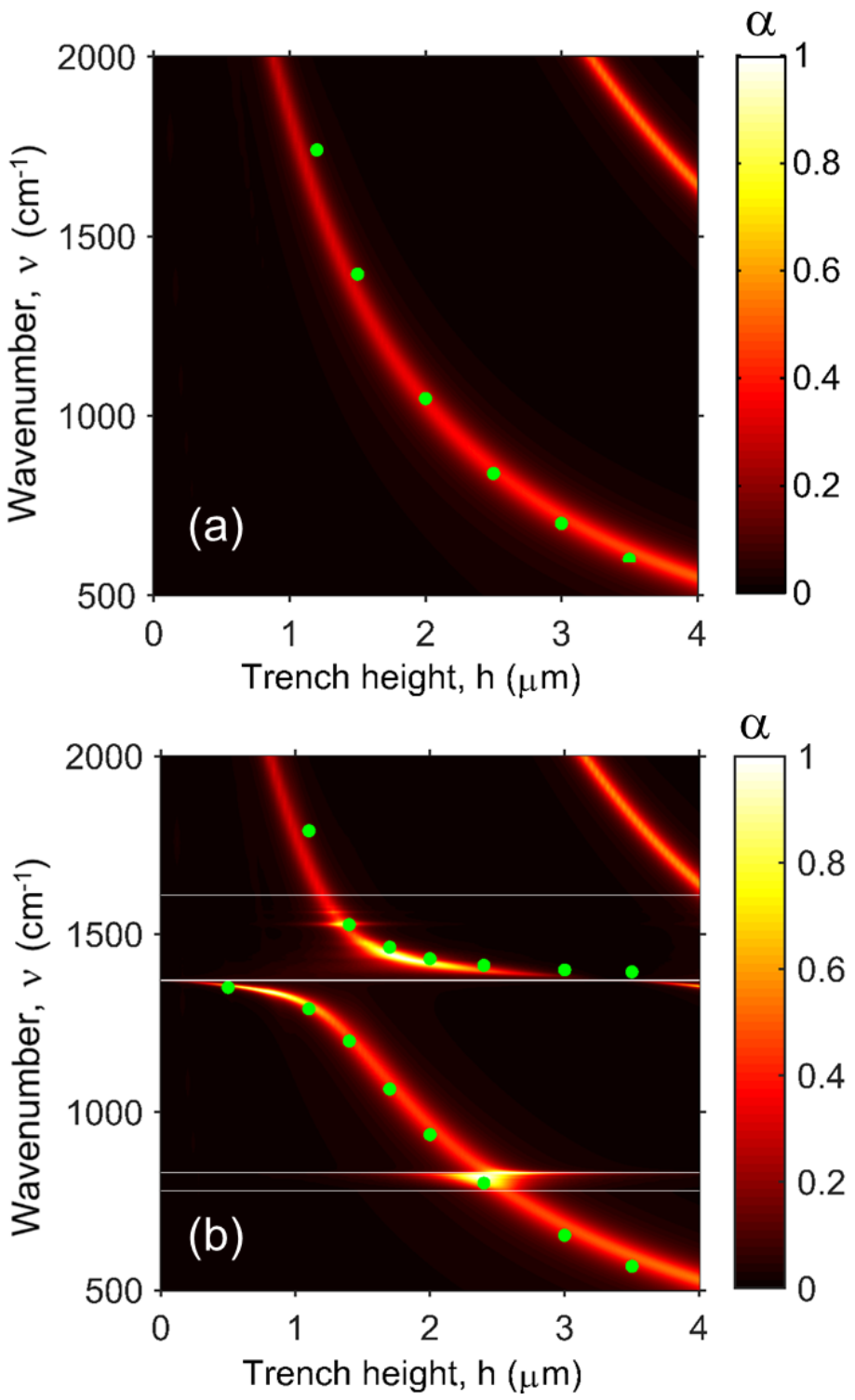

Figure 5.30 Absorptance contours of hBN-covered Ag gratings: (a) d = 60 nm and (b) d = 100 nm. The other parameters are $\Lambda = 4$ μm and $b = 300$ nm. The white lines show the two hyperbolic regions.

$$m = \frac{\Lambda}{2d}\sqrt{-\frac{\varepsilon_{\parallel}}{\varepsilon_{\perp}}} \tag{5.16}$$

Since $\sqrt{-\varepsilon_{\parallel}/\varepsilon_{\perp}}$ is frequency dependent, only at specific frequencies can *m* take integer numbers, yielding discretized frequency for the excitation of the hyperbolic polaritons. This is very different with the scenario where the structure is not periodic since continuous high wavevectors can be created [122]. Take the case in Figure 5.30(b) as an example, in the upper hyperbolic region, the first five excited polariton bands possess frequencies (from low to high) 1395, 1414, 1434, 1451, and 1468 cm^{-1}. Equation (5.16) yields 1396, 1415, 1436, 1457, and 1467 cm^{-1} at *m* = 5, 7, 9, 11, and 12, respectively, matching the simulation results well. The discrepancy may be caused by the metal grating that could affect the dispersion of the hyperbolic polaritons slightly.

Note that Eq. (5.16) is a necessary condition that has to be satisfied along with other requirements to fully predict the condition of the excitation of the hyperbolic polaritons. For example, the wavevector of a certain diffraction order should also match the needed wavevector descried by Eq. (5.12). However, Eq. (5.16) provides useful information to understand the observed hBN film thickness effect. Since *d* is in the denominator, a thicker film makes *m* smaller at a certain frequency and, thus, the frequency interval between satisfactory *m* becomes larger and the excited polariton bands tend to be more separated from each other in frequency as shown clearly in Figure 5.30. Similarly, Λ in the numerator can affect the excitation condition of hyperbolic polaritons in a reverse manner, though not shown here. Meanwhile, in the upper hyperbolic region, when the frequency increases and approaches $\omega_{LO,\perp}$, $\varepsilon_{\perp}$ becomes close to zero and thus $\sqrt{-\varepsilon_{\parallel}/\varepsilon_{\perp}}$ increases drastically. Therefore, many satisfactory *m*'s occur within a smaller frequency range, making the flat

bands denser in the upper hyperbolic region close to $\omega_{\mathrm{LO},\perp}$. Similar trend happens in the lower hyperbolic region when the frequency is closer to $\omega_{\mathrm{TO},\parallel}$, where $\left|\varepsilon_{\parallel}\right|$ increases drastically. When excited hyperbolic polaritons are coupled with the MP in grating at a certain grating height, the hybrid polaritons push the absorptance higher compared to that of uncoupled hyperbolic polaritons at other grating heights. Therefore, the hBN film thickness, the grating height, and period can all be used to control the excitation condition of the hybrid hyperbolic phonon-plasmon polaritons. Since the propagation angle of the HPPs depends on the frequency, these geometry parameters can be used to manipulate the location of the absorption in hBN films. Moreover, the excitation of hybrid polaritons is insensitive to the incident direction. For example, calculations show that when the incidence angle is changed to 30°, the high-absorptance peaks shown in Figure 5.25(a), (b), and (c) shift slightly to 1430 cm^{-1}, 819.7 cm^{-1}, and 1331 cm^{-1}, respectively, with the corresponding absorptance being 0.99, 0.98, and 0.93. The propagation direction of the HPPs of the first two hybrid polaritons is in consistent with the slightly changed resonance frequencies.

Practical experiments may have some discrepancies with the theoretical ideal structure. For example, fabricated metal gratings may not be perfectly flat and leave a vacuum gap between hBN film and grating. However, such an imperfection may not significantly alter the results since no identifiable difference are found in the three spectra shown in Figure 5.25 when a 1-nm gap between hBN and metal gratings is present, though not shown here. Meanwhile, the corners of the fabricated grating may not be as sharp as the ideal case, and thus the electric field would be expected to be somehow weaker around the grating edges. Such gratings may still be able to concentrate an electric field that is

strong enough to launch a strong HPP in hBN and achieve high absorption, but the excited polariton may be less distinguishable with lower spatial contrast. The above-discussed unique properties enabled by the hybrid hBN film and grating micro/nanostructures have potential applications in sub-wavelength imaging [122] and surface-enhanced Raman spectroscopy [26]. Considering that gratings made of high-temperature materials like tungsten [144] and SiC [52] also support MPs, the design presented here could be used to build stable perfect absorbers or spectral selective emitters for high-temperature applications [36].

In conclusion, this work demonstrates perfect and near-perfect absorption in hBN/metal grating hybrid anisotropic structures due to hybrid phonon-plasmon polaritons. The hybrid polaritons can be explained with an LC circuit model in which hBN behaves as either an inductor or capacitor depending on the frequency range. In the two hyperbolic regions of hBN, HPPs strongly couple with localized MPs, forming hybrid hyperbolic phonon-plasmon polaritons and boosting the absorptance. The majority of the power is dissipated inside the hBN film with a tunable location-dependent absorption profile. Outside the hyperbolic regions, the optical phonons in hBN can strongly couple with MPs and hBN dissipates significant power because of its intrinsic loss and the strong electric field produced by MP resonances. The height of the grating, the trench width, as well as the hBN film thickness, can be used to tune the perfect and near-perfect absorption to different frequencies. This work reveals the possibility of using hyperbolic 2D materials to achieve perfect absorption and sheds light on a new route to construct hybrid structures with unique radiative properties for sub-wavelength imaging and high-temperature energy harvesting.

5.4 Trapezoidal Gratings Made of Hyperbolic Materials

The previous work demonstrates a way to achieve perfect absorption at a specific wavelength using hyperbolic material hBN. However, for some applications such as energy harvesting, photodetection, chemical sensing, and color filtering, wavelength-selective broadband absorption may be much more desired to improve the efficiency and functionality [311-313]. In fact, hyperbolic materials can be engineered to efficiently absorb a broadband of radiation.

Various methods and structures have been proposed to achieve broadband absorption. Inspired by the high absorption of localized resonances like MPs at a single wavelength, one can put multiple localized resonators with different resonance wavelengths together. Such designs have been demonstrated using complex gratings [160], metal/dielectric/metal structures with a cluster of separated metal patches as the top layer [211], and structures assembled by nanoparticles of different sizes [314]. Nanowires made of different semiconductor materials such as doped silicon and indium phosphide can also support broadband absorption especially in visible range, which is important for solar cell applications [304,315,316]. Recently, it is found that metamaterials made of alternating layers of metal and dielectric can support broadband absorption when sculpted into a tapering sawtooth shape, thanks to the effective hyperbolic response [34,317,318]. Proper metals and dielectrics can be chosen to achieve broadband absorption in a desired frequency range, as long as hyperbolic responses are present. However, since this type of metamaterials involve depositing or etching metals and dielectrics that need to be controlled precisely, fabrications are typically very challenging [319]. Therefore, it is of great significance to explore whether natural hyperbole materials can be directly used to

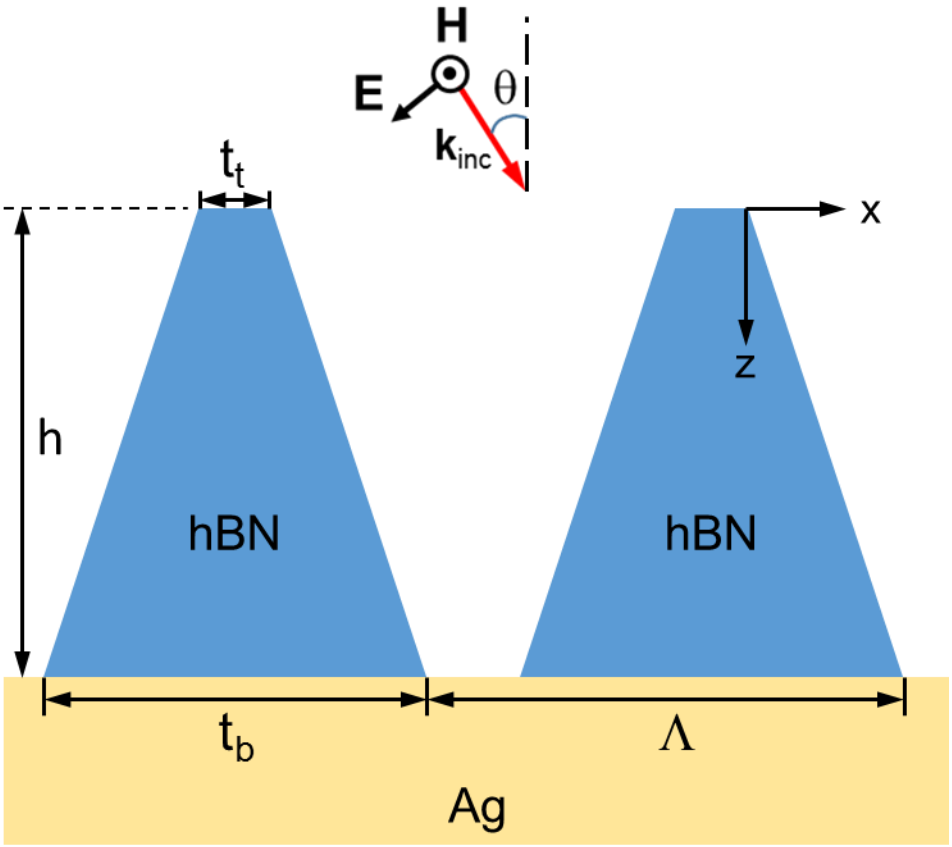

Figure 5.31 Schematic of the hBN trapezoidal grating.

achieve broadband absorption. Since various natural hyperbolic materials have been found that preserve hyperbolic response covering the whole visible and infrared range [320], such exploration becomes even more significant.

This work uses hBN as an example to demonstrate that broadband absorption can be achieved in trapezoidal gratings made of natural hyperbolic materials. Figure 5.31 shows a schematic of the proposed structure. The hBN grating is periodic in the *x*-direction with a period Λ and extended to infinity in the *y*-direction. In each period, hBN is shaped to an isosceles trapezoid with the height, short and long bases being h, t_t, and t_b, respectively. The optical axis of hBN is in the *z*-direction. The substrate is made of silver (Ag) and is thick enough to be treated as opaque. Therefore, the incident light will be either reflected

or absorbed, and the absorptance can be indirectly calculated from one minus the reflectivity. The incidence is a plane wave from vacuum and the plane of incidence is the *x*-*z* plane. The wavevector of the incident wave can be expressed as $\mathbf{k}_{\text{inc}} = k_x\ \hat{\mathbf{x}} + k_z\ \hat{\mathbf{z}} = k_0 \sin\theta\ \hat{\mathbf{x}} + k_0 \cos\theta\ \hat{\mathbf{z}}$, where θ is the incidence angle and k_0 is the magnitude of the wavevector in vacuum.

Figure 5.32 displays the absorptance of the proposed structure for TM waves (with an oscillating magnetic field in the *y*-direction) when h = 10 μm, Λ = 3 μm, t_t = 0.04 μm, and t_b = 2 μm. In the calculation, the trapezoid is divided into 100 layers in the *z*-direction.

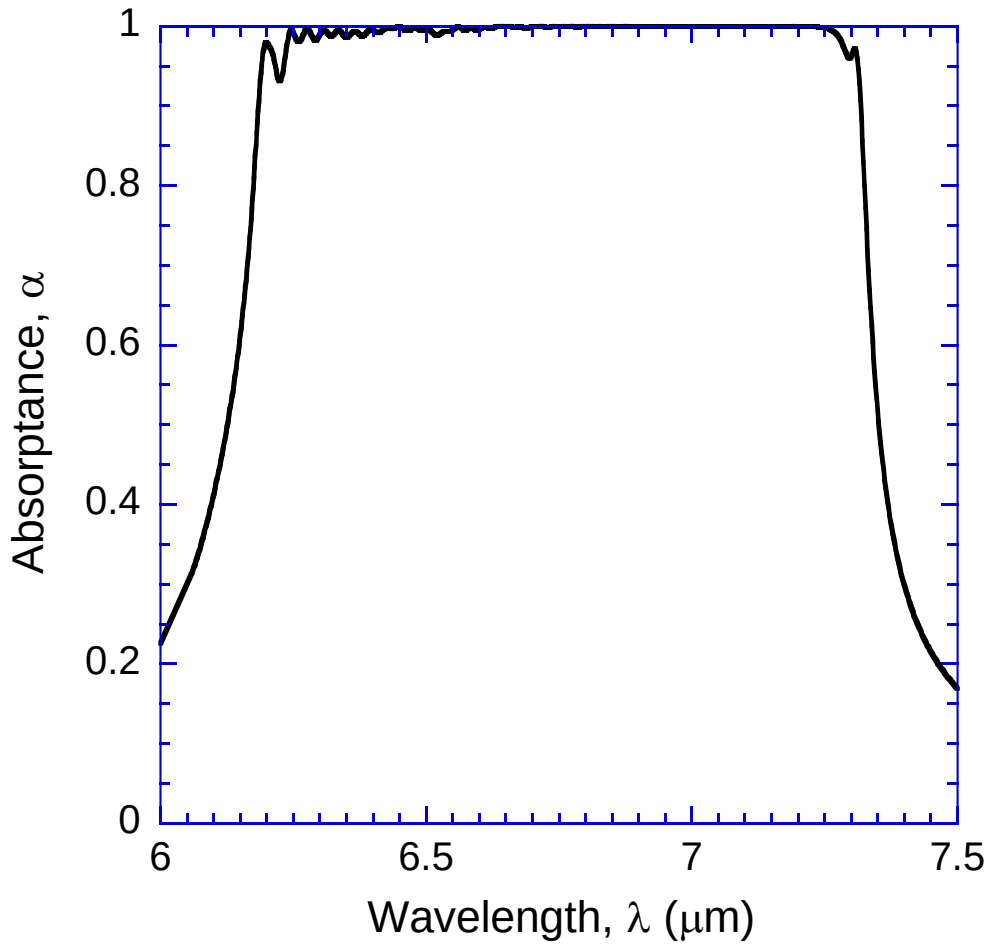

Figure 5.32 Absorptance of the structure shown in Figure 5.31 at normal incidence. The parameters are h = 10 μm, Λ = 3 μm, t_t = 0.04 μm, and t_b = 2 μm.

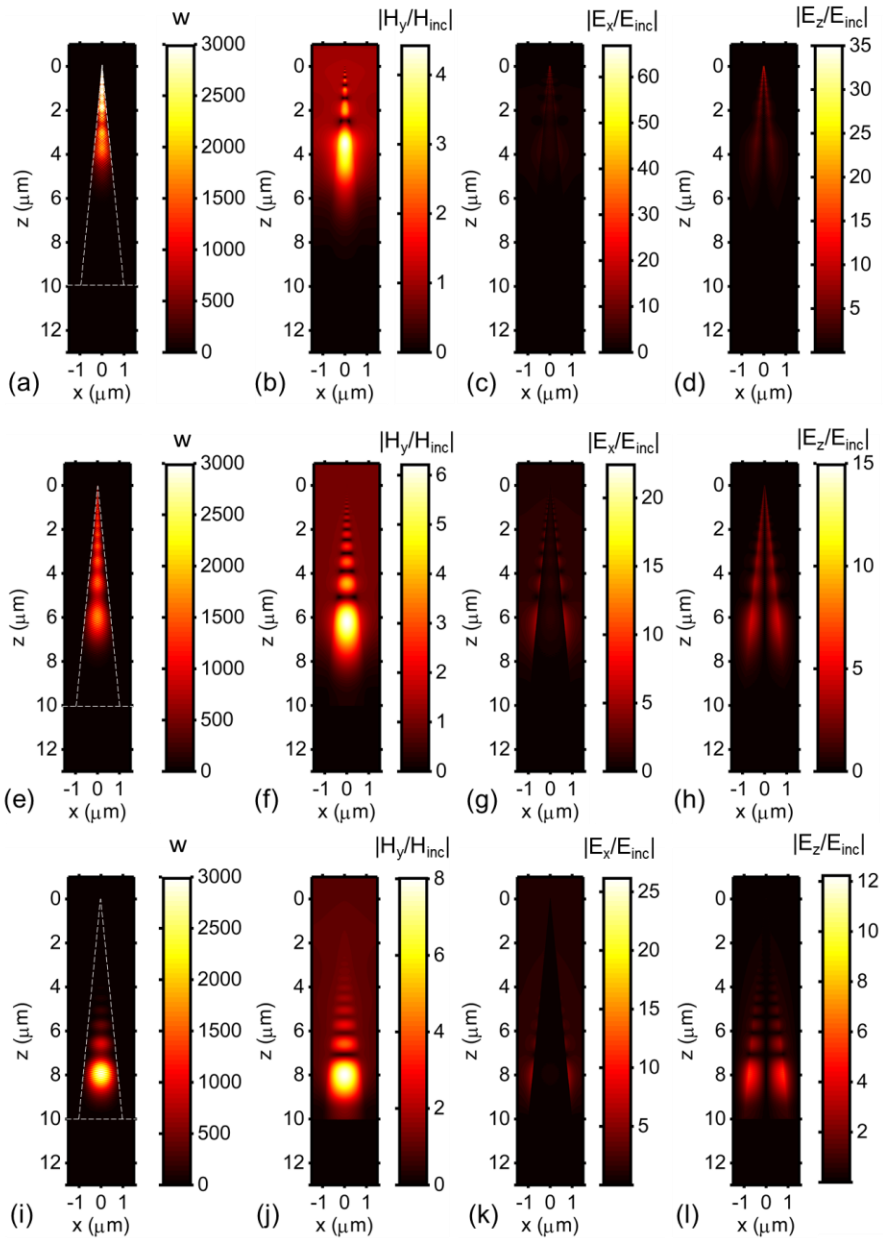

Figure 5.33 Field plots at different resonance wavelengths: (a-d) λ = 6.63 μm or ν = 1508 cm^{-1}, (e-h) λ = 7 μm or ν = 1429 cm^{-1}, and (i-l) λ = 7.2 μm or ν = 1389 cm^{-1}. The first column is the power dissipation density, the rest three columns show the magnitude of magnetic field, the *x*-component of electric field, and the *z*-component of the electric field, respectively. Values larger than 3000 W/m^3 are shown in white color in the plots for *w*. The electric and magnetic field are normalized using the incidence, whose electric field is 1 V/m. The surface profile of the hBN trapezoid and the Ag substrate is delineated using dashed lines in the power dissipation contours.

It is clear to see that the absorptance is close to unity in a broad wavelength range from about 6.2 μm to 7.2 μm, which is the Type-II hyperbolic region of hBN. The absorptance spectrum shows a sharp drop at the edges of this range, which indicates the broadband high absorptance is a result of the hyperbolic response of hBN.

To explain the mechanisms of the broadband absorption, the field plots at three different wavelengths are presented in Figure 5.33. The three rows are for λ = 6.63 μm, 7 μm, and 7.2 μm, respectively, and the four columns show the power dissipation density (w), magnetic field (H), the x-component of the electric field (E_x), and the z-component of the electric field (E_z), respectively. The absorptance at these wavelengths all equal to one. At the λ = 6.63 μm, only the upper part of the hBN trapezoid is lightened as shown in (a), indicating the majority of the power is dissipated there. When the resonance wavelength becomes longer, the dissipation profile moves down toward the bottom of the trapezoid, as shown in (e) and (i). Based on Eq. (3.49), it is found that for all three cases, almost all the power is dissipated inside the hBN trapezoid and the substrate absorption is negligibly small. The dissipation contours show a clear standing wave feature with relatively longer wavelength toward the bottom and the field plots echoes this pattern well. The field plots also reveal the resonances are highly localized and, thus, coupling between neighboring hBN trapezoid can be neglect. As shown next, these resonance features can be understood by considering the modes allowed in a hyperbolic waveguide.

Considering a waveguide made of an uniaxial anisotropic materials whose dielectric tenser are described by $\varepsilon_{\perp}$ and $\varepsilon_{||}$ that is similar to hBN, as shown in Figure 5.34. The cladding material is lossless with a dielectric function of ε_2. The core material width is denoted as t. For TM waves, the dispersion of the waveguide can be expressed as

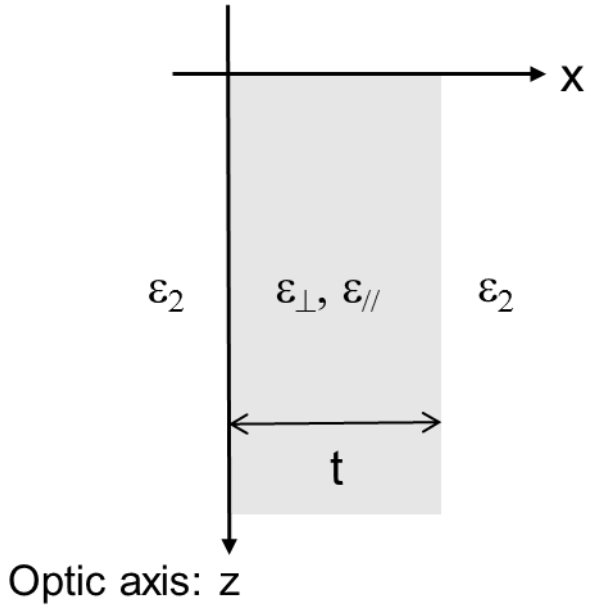

Figure 5.34 Schematic of a hyperbolic waveguide. The waveguide is made of an uniaxial materials with a dielectric tensor in the same form as hBN.

$$\frac{k_{x,2}\varepsilon_{\perp}}{k_{x,1}\varepsilon_2} = \tan\left(k_{1x}\frac{t}{2}\right) \tag{5.17}$$

where $k_{x,2} = \sqrt{\beta^2 - \varepsilon_2 k_0^2}$ and $k_{1x} = \sqrt{\varepsilon_{\|} k_0^2 - \left(\varepsilon_{\|}/\varepsilon_{\perp}\right)\beta^2}$ are the x-component of wavevector in vacuum and the waveguide, respectively, with β being the z-component of the wavevectors in both regions [317]. Figure 5.35 shows the obtained dispersion relationship of the fundamental waveguide mode at t = 0.2, 0.6, 1, 1.4, and 1.8 μm when the core material is hBN. Loss is neglected when solving the dispersion curves. One can see that, for a specific core width, the group velocity, $v_g = 2\pi c_0\, d\nu/d\beta$, is positive at small β, meaning that the power is flowing toward positive z-direction. However, the group velocity gradually decreases as β increases and finally becomes zero at the top of the dispersion curve, after which v_g becomes negative. The top point of the dispersion curve

thus indicates a slow light effect, meaning the power of the wave is trapped inside the waveguide [34,317]. Therefore, a hyperbolic waveguide with a specific core width can effectively trap the power flow at a certain wavelength, and when t becomes larger, the slow light effect can be generated at lower frequency.

For the trapezoidal grating considered, since the coupling between neighboring hBN is negligible, each of the hBN trapezoids can be viewed as a waveguide with a varying core width. For a specific incident wavelength, the incident wave enters the hBN trapezoid from the narrower end and the power can propagate downward. Since the core width becomes larger, v_g decreases gradually as the power flows down. At a certain t, v_g becomes zero and the power is trapped at this location without further flowing due to the slow light effect. For a longer wavelength or smaller wavenumber, the slow light effect happens at a wider core width. For example, for λ = 6.63 μm (ν = 1508 cm^{-1}), slow light effect can happen at t = 1 μm, which matches well with the field plots shown in Figure 5.33(a) where the power is trapped at near the middle of the trapezoid. For λ = 7 μm (ν = 1429 cm^{-1}) and λ = 7.2 μm (ν = 1389 cm^{-1}), the slow light effect occurs at t = 1.44 μm and 1.73 μm, respectively, corresponding well to the previous observations in the dissipation contours and field plots in Figure 5.33. At a specific t, the waveguide supports two modes with different β. The standing wave patterns are created due to interference effect of these two waves. Since the spatial period of interference patterns is inversely proportional to the difference between the two β, the hot spots in the contour plots in Figure 5.33 are larger at the location that supports slow light effect where the difference between the two β degenerates to zero [317]. This difference tends to be larger toward the top of the trapezoid where t becomes smaller, resulting in shorter spatial periods there.

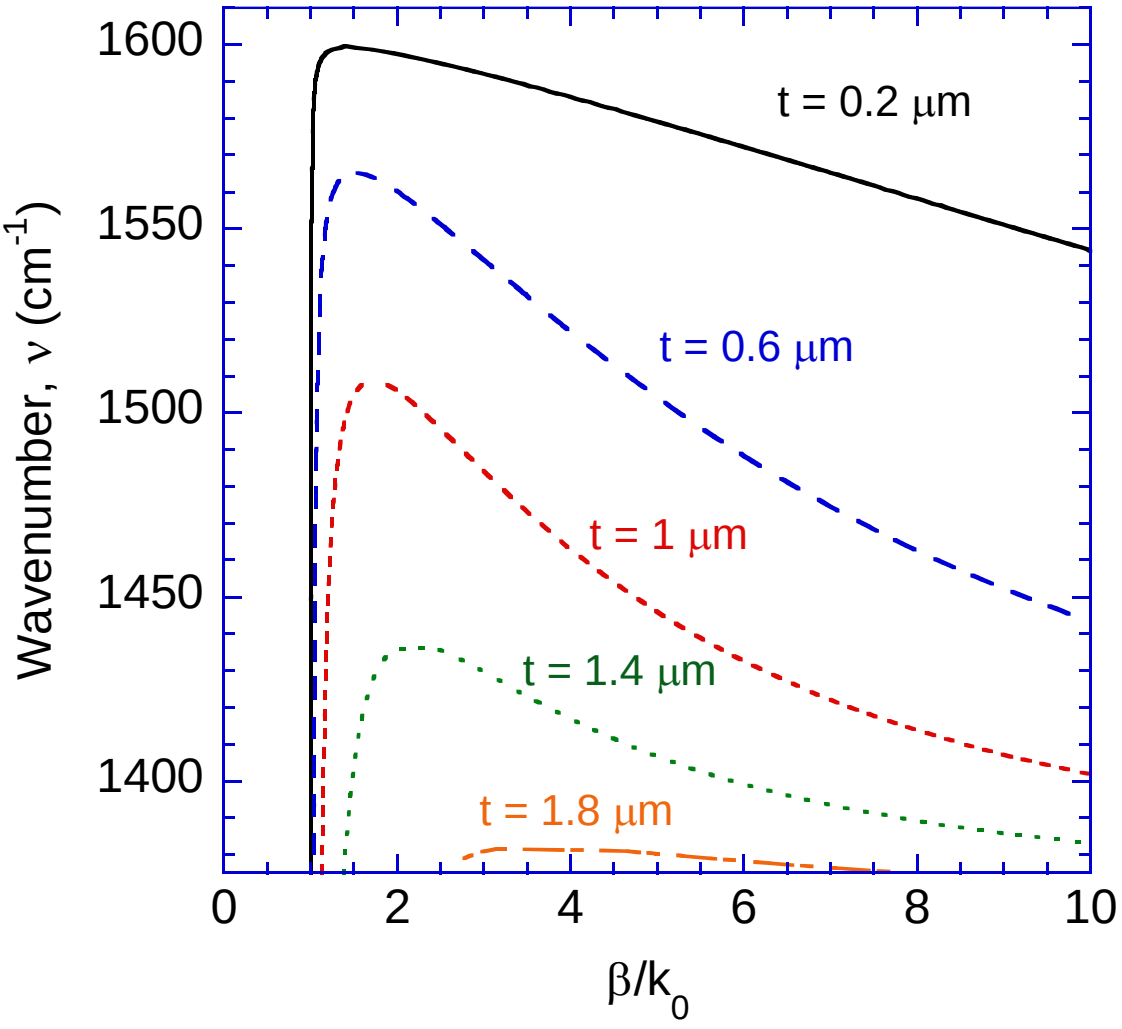

Figure 5.35 Dispersion relationship of the waveguide modes in a hyperbolic waveguide made of hBN.

Considering the absorption requires a slow light effect, one can engineer the absorption band by designing the shape of the trapezoid. Figure 5.36 demonstrates such an example, where only the top half or the lower half of the trapezoid of the structure in Figure 5.32 is present. For both scenarios, h = 5 μm and Λ = 3 μm. The solid line shows the case where the top half of the hBN trapezoid exists with t extending from 0.04 μm to 1 μm, corresponding to a wavelength range from λ = 6.22 μm to 6.63 μm that slow light effect

can be supported. Therefore, the high broadband absorptance can be achieved merely within this range as the spectrum shows. Similarly, the lower half of the trapezoid supports slow light effect for wavelengths from 6.63 μm to 7.29 μm and, thus, the high absorptance is supported within this band as the dashed spectrum indicates. The high absorptance peak at 6.2 μm is beyond the hyperbolic region potentially caused by the epsilon-near-zero effect. Since natural hyperbolic materials have been found in the wavelengths ranging from ultraviolet to microwave range, one may use proper trapezoid shape to achieve high absorptance over any desired wavelength range as along as the material has a hyperbolic response. Note that since the slow light effect requires a Type-II hyperbolicity, the featured broadband absorptance may not be achieved in Type-I hyperbolic region.

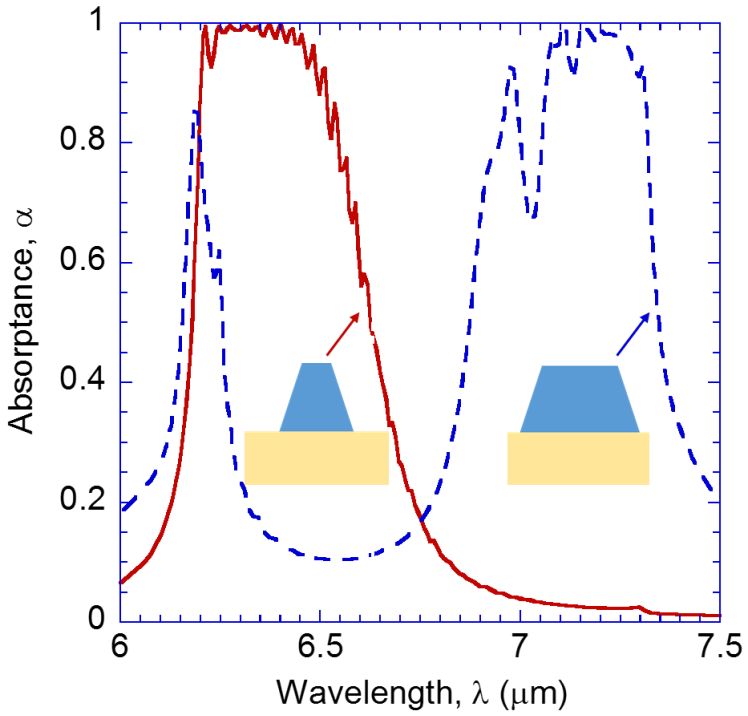

Figure 5.36 Absorptance of trapezoidal gratings when only the top half or the lower half of the trapezoid of the structure in Figure 5.32 is present. For both cases, h = 5 μm and Λ = 3 μm. The solid line represents the case where t_t = 0.04 μm and t_b = 1 μm, while the dashed line is when t_t = 1 μm and t_b = 2 μm.

Since the resonances are highly localized, the broadband absorptance is insensitive to the incident direction, as demonstrated in Figure 5.37. The absorptance spectrum maintains its broadband feature nearly omnidirectionally and the absorptance is still higher than 0.8 over a broadband even at $\theta = 80°$. When θ becomes larger, absorptance decreases possibly due to the difficulties for the incident wave to couple with the waveguide modes. This angle insensitivity is of great importance for energy harvesting applications. Moreover, since the 1D structure can achieve broadband absorption only for TM waves, one may use isolated hBN pyramids, which is a two-dimensional counterpart of the proposed hBN grating, to obtain high broadband absorption for both polaritons. Furthermore, the substrate plays little role in the high broadband absorption since almost all the power is absorbed inside hBN. This has been justified by taking away the Ag substrate and the suspended hBN trapezoidal grating yield almost unchanged absorptance spectrum, though not shown here. Therefore, in real fabrication, the substrate may be chosen with no strict requirements.

In conclusion, this work demonstrates that trapezoidal hBN gratings can achieve high broadband absorptance in its Type-II hyperbolic region. The mechanism is attributed to a localized resonance that caused by a slow light effect in hyperbolic waveguides. The absorption is nearly omnidirectional and the absorption bandwidth can be engineered by using different shapes of trapezoid. The results in this work may pave the way to utilize natural hyperbolic materials to achieve broadband absorption, which will benefit a wide spectrum of applications including solar thermal conversion, radiative cooling, and photodetection.

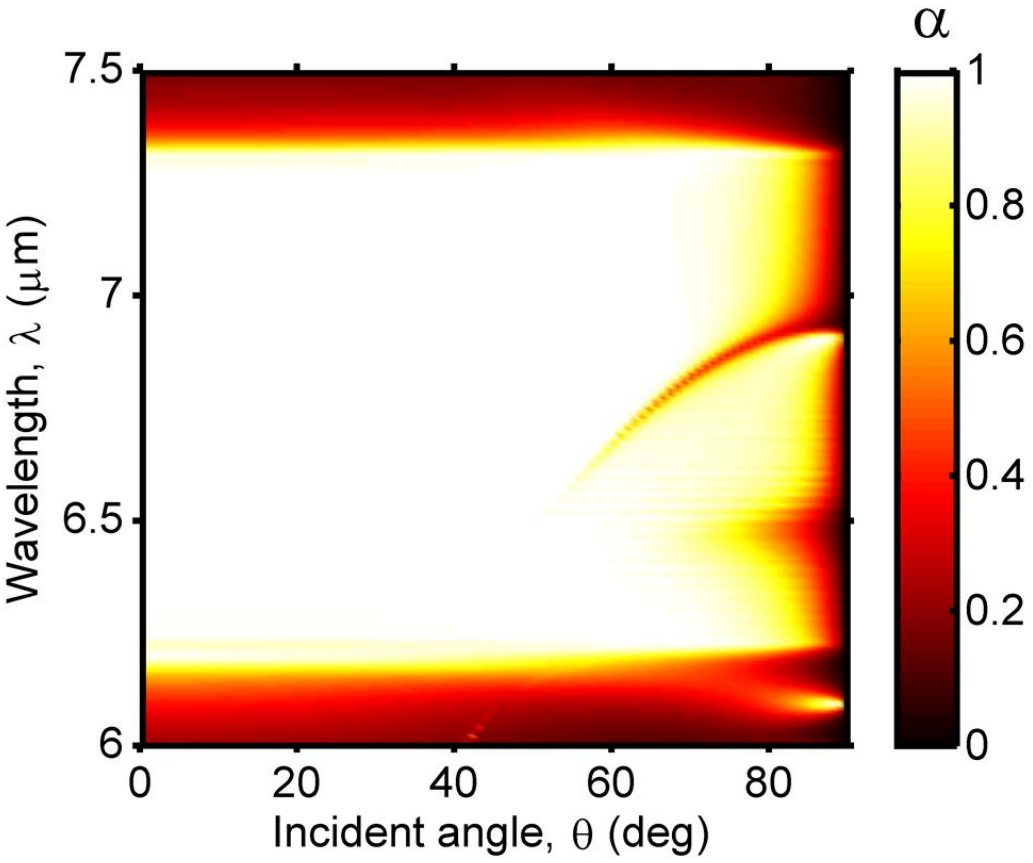

Figure 5.37 Absorptance of the trapezoidal grating with the same geometries as the structure shown in Figure 5.32.

5.5 Resonance Absorption by Hyperbolic Polaritons

The previous work demonstrates a way to achieve perfect absorption using trapezoidal hBN gratings due to the slow light effect. However, the analysis is based on a prerequisite that each hBN trapezoid is high enough to be considered as a waveguide. If the height of the grating becomes smaller, one can expect that the waveguide explanation may not work anymore. This work focuses such a case. It turns out that new phenomena occur when the hBN trapezoid becomes shorter.

The considered grating structures are the same as shown in Figure 5.31. The hBN

grating is 1D and with a period Λ in the *x*-direction and extends to infinity in the *y*-direction. In each period, hBN is shaped to a trapezoid with the height, short, and long bases being h, t_t and t_b, respectively. The optical axis of hBN is in the *z*-direction. The substrate is made of silver (Ag) and is thick enough to be treated as opaque. Figure 5.38 shows the absorptance spectrum when Λ = 3 μm, t_t = 0.04 μm, and t_b = 2 μm that are the same as the previous work, but the grating height is shortened to h = 1 μm. In the calculation, the trapezoid is divided into 100 layers in the *z*-direction. Compared to Figure 5.32, the broadband high absorptance changes to several isolated absorptance peaks, indicating that the short trapezoid cannot be approximated as a waveguide any more.

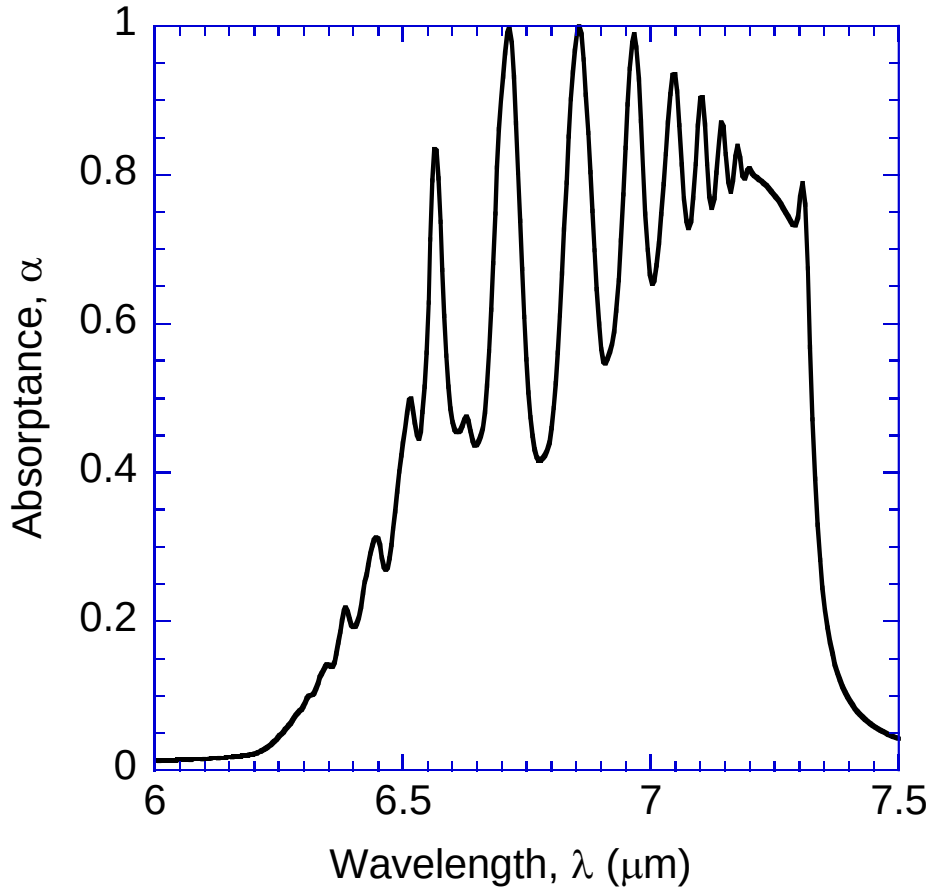

Figure 5.38 Absorptance of a trapezoidal grating shown in Figure 5.31 at normal incidence. The geometric parameters are h = 1 μm, Λ = 3 μm, t_t = 0.04 μm, and t_b = 2 μm.

To explore the mechanisms, the power dissipation plot is calculated at the first, third, and fifth predominant absorptance peaks at λ = 6.56 μm (ν = 1523 cm^{-1}), λ = 6.86 μm (ν = 1459 cm^{-1}), and λ = 7.05 μm (ν = 1419 cm^{-1}), as shown in Figure 5.39(a), (b), and (c), respectively. The power dissipation contours show a very different feature compared to Figure 5.33. The interference pattern disappears and some straight bright rays show up inside the hBN trapezoid. The absorptance at the these three wavelengths are α = 0.8, 0.98, and 0.93 and integration calculations show that almost all the power is absorbed inside hBN for all the cases, demonstrating the localized feature of the resonances. For all scenarios, the dissipation toward the top of the trapezoid is stronger, indicating a concentrated electric field therein. Actually, due to local scattering, electric field with high wavevectors are produced near the sharp edge of trapezoid [120], and HPPs can be launched predominantly from the two upper edges. This can be justified by a close analysis on the direction of the strips, which agrees well with the propagation angle of the HPPs predicted by Eq. (5.9). Based on this picture, the resonance conditions can be predicted as shown next.

Consider a trapezoidal resonator shown in Figure 5.40. The dashed lines show the trajectory of the two branches of HPPs initiated from the two corners of the top base. The HPPs experience total internal reflections on the sides, and based on the field plots, they end at the bottom corner of the trapezoid to form a resonance. Note that the reflection of the HPPs on the sides of the trapezoid are not specular but anomalous, meaning that the reflection of HPPs are not affected by the slope of the sides and the polaritons reflect as if the sides are vertical, as has been experimentally justified in a similar cone nanostructure [321]. Based on the geometries and the propagation angle of HPPs given in Eq. (5.9),

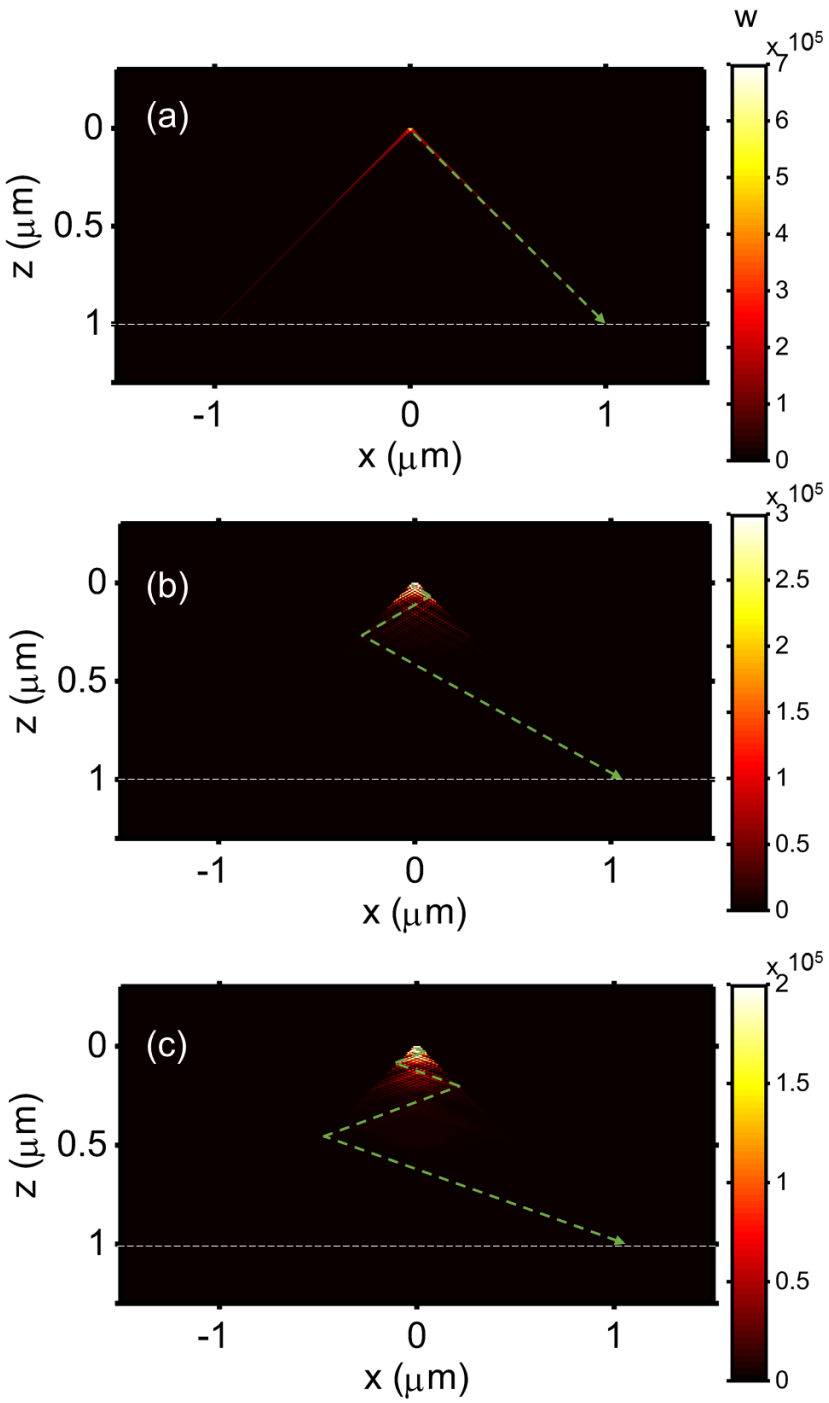

Figure 5.39 Power dissipation contours in the structure same as in Figure 5.38: (a) λ = 6.56 μm or ν = 1523 cm^{-1}; (b) λ = 6.86 μm or ν = 1459 cm^{-1}; and (c) λ = 7.05 μm or ν = 1419 cm^{-1}. The dashed line with an arrow shows the directional propagation of HPPs (one branch) inside the trapezoidal resonator. The white dashed line shows the interface below which is the Ag substrate.

one can obtain the order of the resonances, which equals the number of reflections HPPs experienced on the sides [321]:

$$n = \frac{\ln\left(1 - \frac{t_b - t_t}{t_b}\right)}{\ln\left(\frac{2h\tan\beta(\lambda) - t_b + t_t}{2h\tan\beta(\lambda) + t_b - t_t}\right)} \tag{5.18}$$

This order is associated with the resonance in the *z*-direction. Since propagation angle β depends on wavelength, only at a specific wavelength can the right-hand-side take integer values, yielding a way to predict the resonance conditions. Based on this method, the predicted wavelengths for the first five orders (i.e. n = 1 to 5) are 6.56 μm, 6.68 μm, 6.83 μm, 6.95 μm, and 7.03 μm, which correspond well with the simulated absorptance that peaks at 6.56 μm, 6.72 μm, 6.86 μm, 6.97 μm, and 7.05 μm. The three resonances shown in Figure 5.39 are the first three odd orders. The excellent agreement again justifies that the resonance is caused by the directional propagation of HPPs.

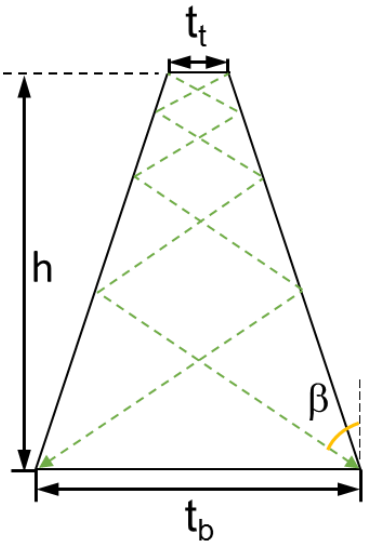

Figure 5.40 Directional propagation of HPPs in trapezoidal resonators. The height of the trapezoid is h and the short and long bases are t_t and t_b, respectively. The dashed line with an end arrow indicates the trajectory of the HPPs, which corresponds to order n = 4.

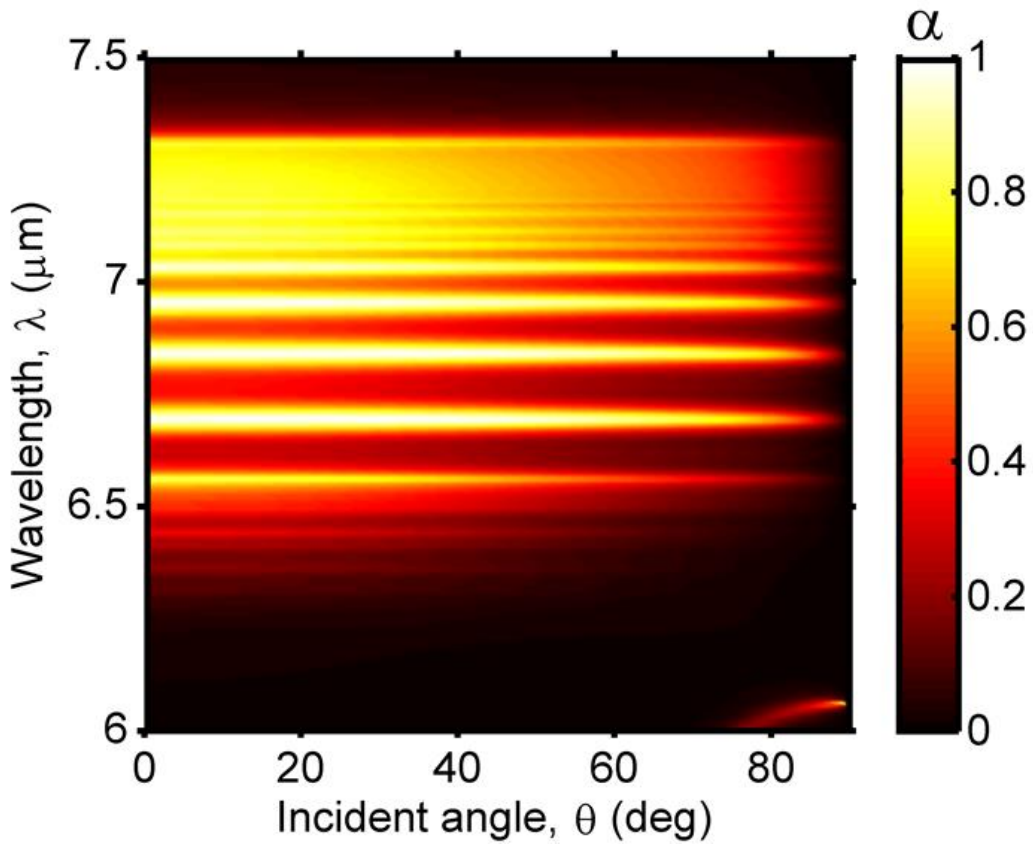

Figure 5.41 Absorptance of the trapezoidal grating with the same geometries as the structure shown in Figure 5.38.

Since the resonances are localized, they show little sensitive to the incidence angle, as demonstrated in Figure 5.41. The resonances can be excited almost omnidirectional by the incident light. Note that the resonances associated with lower orders are excited at shorter wavelengths or higher frequency. This is very different with traditional cavity resonances and a similar anomalous scaling law was demonstrated in a metal-dielectric multilayer hyperbolic metamaterials [322]. Moreover, since the directional propagation of HPPs can also happen in Type-I hyperbolic region [120], similar resonance effect is supported between 12.1 μm to 12.8 μm where hBN possesses Type-I hyperbolicity, though not shown here. This is another difference compared to the previously discussed broadband absorption that can be supported only in Type-II hyperbolic region.

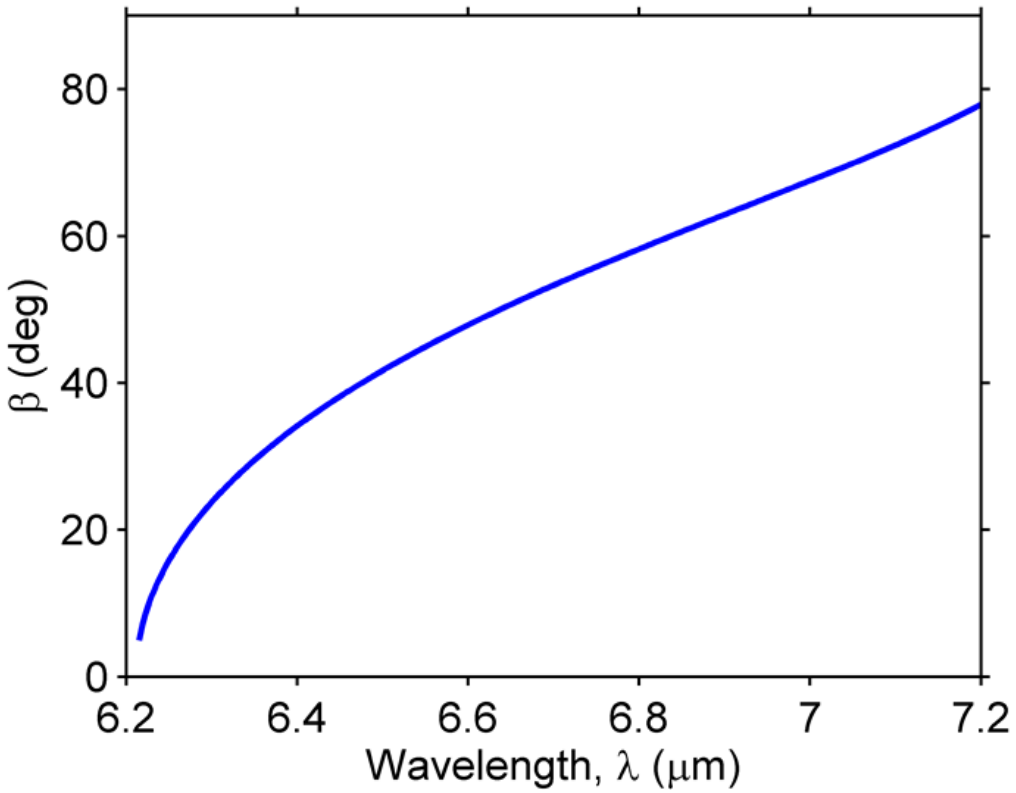

Figure 5.42 Propagation angle of HPPs in the Type-II hyperbolic region of hBN.

One may have noticed that the absorptance between 6.2 μm to 6.5 μm is not high even though this range is in the hyperbolic region. This is because the considered trapezoid possesses a base angle of $45.6°$, and HPPs initiated from the top corners have to have a propagation angle larger than this value to propagate inside the resonator. Since β increases with wavelength as shown in Figure 5.42, λ needs to be longer than about 6.5 μm, at which $\beta = 45.6°$, to form a resonance inside the resonator. This indicates a way to use the shape of the resonator to tune the absorptance spectrum. In fact, one can use resonators of other shapes to manipulate the HPPs and create resonances at a desired wavelength, as shown next.

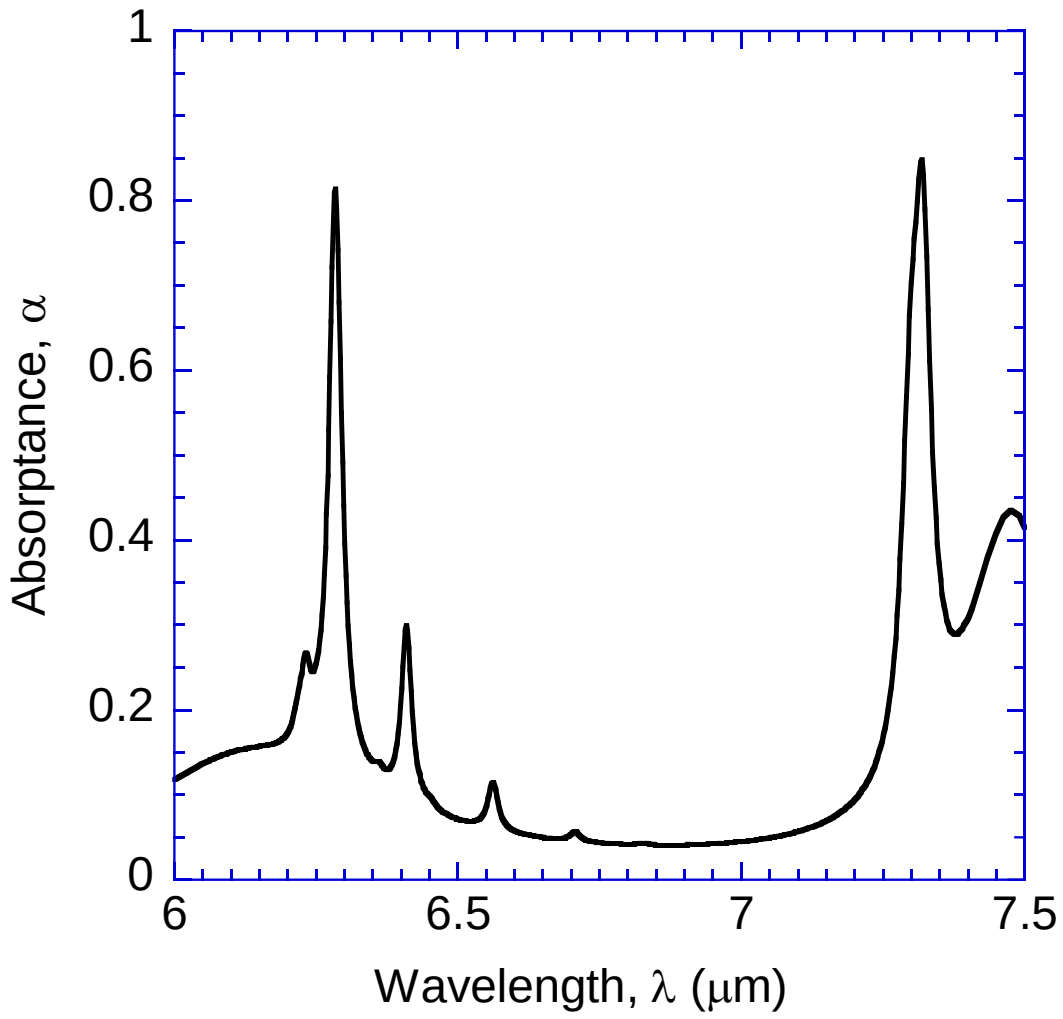

Figure 5.43 Absorptance of a hBN grating shown in Figure 5.31 at normal incidence. The geometric parameters are Λ = 3 μm and $h = t_t = t_b$ = 2 μm.

Figure 5.43 shows the absorptance of a hBN grating shown in Figure 5.31 with Λ = 3 μm and $h = t_t = t_b$ = 2 μm at normal incidence. In this case, the hBN grating strips has a square cross section. The resonance peaks can be clearly identified on the absorptance spectrum. The local power dissipation contours for the three dominate peaks at λ = 6.29 μm (ν = 1591 cm^{-1}), λ = 6.41 μm (ν = 1560 cm^{-1}), and λ = 6.56 μm (ν = 1524 cm^{-1}) are displayed in Figure 5.44 (a), (b), and (c), respectively. The resonance peak at λ = 7.32 μm

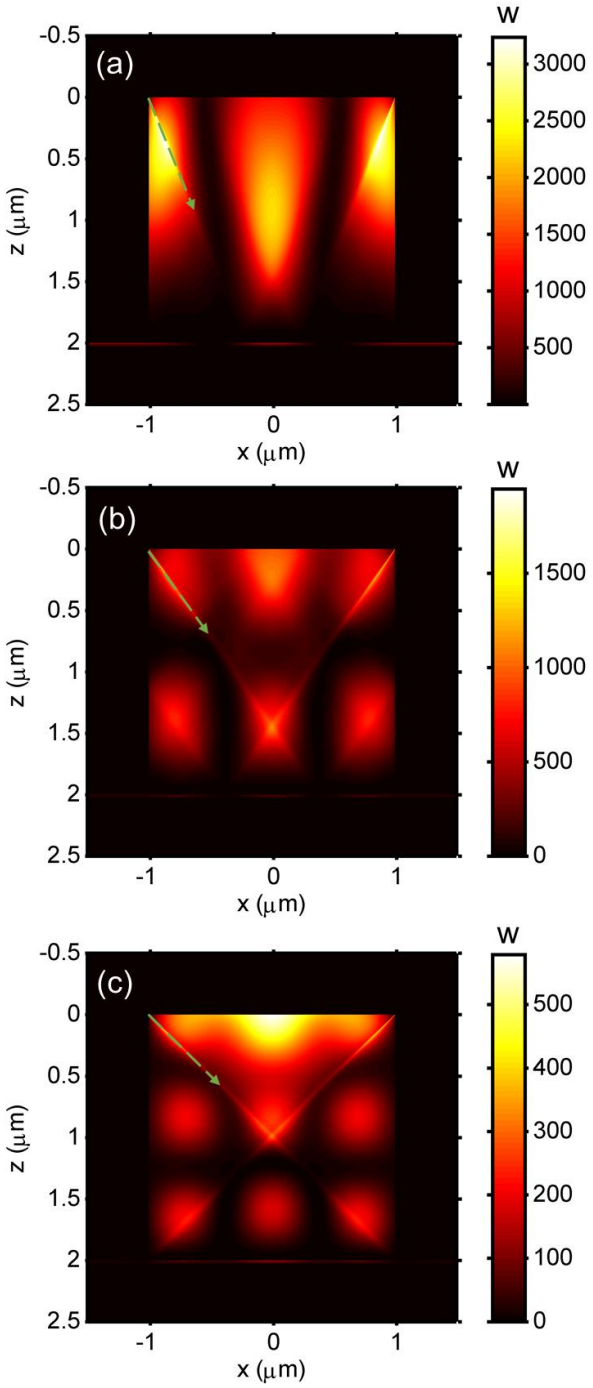

Figure 5.44 Power dissipation contours in the structure same as in Figure 5.43: (a) λ = 6.29 μm or ν = 1591 cm^{-1}; (b) λ = 6.41 μm or ν = 1560 cm^{-1}; and (c) λ = 6.56 μm or ν = 1524 cm^{-1}. They correspond to mode (3,1), (3,2), and (3,3), respectively. The dashed line with an arrow shows the directional propagation of HPPs. The electric field of the incident waves is 1V/m.

is very close to $\omega_{\mathrm{TO},\perp}$ and possibly caused by the high loss of hBN around this frequency. Since it is beyond the hyperbolic region, it will not be further discussed. One can clear see that the square resonators show Fabry–Pérot-like resonances inside with notes and antinodes in both the *z*- and *x*-directions. The order of the resonances can be denoted as (*m*,*n*), where *m* and *n* respectively denote the resonance order in the *x*- and *z*-directions. Under this convention, the order of the previous discussed resonances in trapezoid shape can be denoted as (1, *n*) based on the field plots. Note that resonances with $m > 1$ also exist in trapezoid resonators [317,319], but the fundamental modes cause the absorptance peaks as analyzed before. However, for the square shape resonator, absorptance peaks associated with high order resonances can be seen and the orders of the three resonances in Figure 5.44 can be identified based on the dissipation field plots as (3,1), (3,2), and (3,3), respectively. Based on the field plots, in order to form such a resonance, the direction of the HPPs for resonance (*m*,*n*) needs to satisfy

$$\tan\beta(\lambda) = \frac{n}{m} \tag{5.19}$$

This provides a method to predict the resonance wavelength. Based on this equation, the wavelengths of the three resonances are obtained as λ = 6.27 μm, 6.39 μm, and 6.55 μm, respectively, which agree well with the simulation and justify the previous analysis based on directional HPPs. Note that (5.19) does not contain any geometric parameters of the resonator, indicating a possibility to create resonators with similar shape but different dimensions to resonate at the same wavelength.

In conclusion, this work demonstrates that hyperbolic materials such as hBN can be used to build resonators with wavelength-selective absorption. The resonances are caused by the directional propagation of HPPs, and the resonance wavelength can be well

predicted based on the shape of the resonator. Different resonators with the same shape but different sizes may be designed to resonate at the same frequency. This methodology may be used to design wavelength-selective emitters or absorbers based on hyperbolic resonators made of natural hyperbolic materials. Since this method is expected to be valid as long as hyperbolic response is present, various natural hyperbolic materials that have been found can be used to achieve such resonance absorption in different frequency ranges, and thus can benefit various applications such as photodetection, color filters, and energy harvesting.

CHAPTER 6

NEAR-FIELD HEAT TRANSFER BETWEEN 2D MATERIALS

In this chapter, the near-field radiative heat transfer between 2D materials and their heterostructures are theoretically investigated based on fluctuational electrodynamics. Specifically, van der Waals heterostructures assembled by graphene and hBN are studied for their capability to enhance photon tunneling. The results are compared with the scenarios where only graphene monolayers or hBN films are present. The geometric effects and the chemical potential of graphene are investigated. A second layer of graphene on the backside of the heterostructure is further explored for its impact on the near-field heat transfer of the heterostructure.

6.1 Near-Field Heat Transfer Between Graphene/hBN Heterostructures

The well-known diffraction limit in optical imaging is caused by the disappearance of evanescent waves in the far field, which contain fine feature information of the sample surface and are critical for constructing images with high resolution [323]. The decay of the evanescent waves at large distances not only reduces the imaging resolution, but also limits the radiative heat transfer between two objects in the far field. Thermal radiation is initiated by the fluctuational motion of charges inside materials at above absolute zero Kelvin and contains both propagating and evanescent waves [3,89]. If the distance between two media is greater than the characteristic wavelength of thermal radiation, i.e., in the far field, only propagating waves generated by one medium can reach the other and contribute to radiative heat transfer. The disappearance of evanescent waves in the far field limits the radiative heat transfer to a rate that cannot exceed the blackbody limit governed by the

well-known Stefan-Boltzmann law. The limited radiative heat transfer greatly hinders the application where thermal radiation plays a major role, such as radiative energy harvesting, thermal management, and local heating and cooling [84,86-90]. To overcome this limit, the evanescent waves have to be collected, which can be done by enabling photon tunneling.

When two objects are at a distance comparable to or shorter than the characterized thermal radiation wavelength, i.e., in the near-field regime, the forward and backward evanescent waves can couple with each other and open paths for photons to tunnel through. This phenomenon is called photon tunneling and since there are more tunneling photons than propagating photons, the radiative heat transfer rate can be enhanced to orders of magnitude higher than the blackbody limit. The huge radiative heat flux in the near field opens the door to various applications like thermal rectification [85], thermophotovoltaics [76,153], noncontact refrigeration [324], and information processing [325]. Since a large heat transfer is of critical importance in these appealing applications, continuous efforts have been devoted to exploring innovative optical materials that can enhance photon tunneling.

Surface modes, such as SPPs or SPhPs, have been demonstrated to mediate photon tunneling between metallic surfaces and polar materials [91,92]. Nanostructures like photonic crystals, nanowire arrays, and gratings can effectively behave as hyperbolic metamaterials, which support propagating waves with large wavevectors and thus enhance photon tunneling [43,125,127,326]. Two-dimensional (2D) materials can enable plentiful resonances [57,58,61,65,272,310,327] to facilitate photon tunneling. For example, graphene supports SPPs that can enhance photon tunneling between graphene sheets

[328,329]. Graphene SPPs can also couple with the hyperbolic modes in nanowires, resulting in nearly perfect photon tunneling [95]. When graphene is patterned to ribbons, hyperbolic plasmons can be excited that can significantly enhance photon tunneling than with continuous graphene [94,330]. As a natural hyperbolic material, hexagonal boron nitride (hBN) can support multiple orders of phonon-polaritonic waveguide modes in its two infrared Reststrahlen bands [60,64,126], as discussed before. Recently, it has been demonstrated both theoretically and experimentally that van der Waals heterostructures assembled by graphene and hBN can support surface plasmon-phonon polaritons (SPPPs), which are resulted from the strong coupling between the phonon polaritons in hBN and the surface plasmons in graphene [80-82]. It is still a question whether SPPPs can enhance photon tunneling between such heterostructures and enable a higher heat flux than other 2D materials like graphene. Meanwhile, since graphene has been proposed for a number of promising nano-electronic applications, and hBN is an ideal substrate supporting high-quality graphene owing to its planar hexagonal lattice structure [118,119], it is imperative to explore the effect of hBN on graphene regarding radiative heat transfer performance.

The present study theoretically investigates SPPPs in enhancing the photon tunneling between graphene/hBN heterostructures. Figure 6.1(a) shows the configuration of near-field radiative heat transfer between two aligned heterostructures separated by a vacuum gap of *d*. Each heterostructure contains a monolayer graphene covered on a hBN film with a thickness denoted as *h*. The upper one is the emitter with a relatively higher temperature T_1 and the lower one is the receiver with a lower temperature T_2. Graphene is modeled with its sheet conductivity, σ_s, that includes the contributions from both the interband and intraband transitions. Here, $\tau = 10^{-13}$ s is chosen for all the calculations.

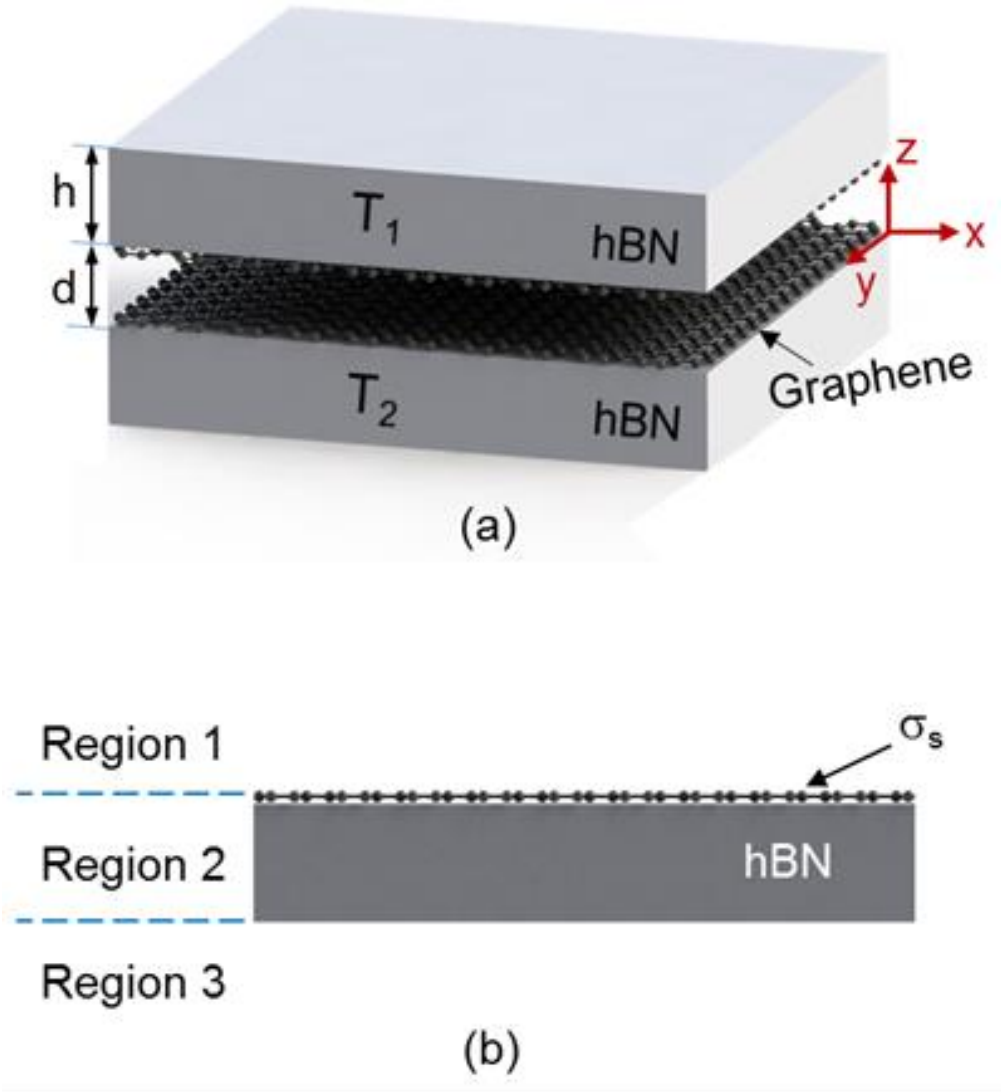

Figure 6.1 (a) Schematic of near-field radiative heat transfer between two graphene/hBN heterostructures. (b) Illustration of the regions for calculating the reflection coefficients.

The near-field radiative heat flux q is calculated based on fluctuational electrodynamics using dyadic Green's functions based on Eq. (2.17). The photon tunneling probability includes contributions of both polarizations, that is, $\xi(\omega,\beta) = \xi_s(\omega,\beta) + \xi_p(\omega,\beta)$. For the scenario interested here, since the optical axis of hBN is in the z direction, the cross-polarization components vanish. Thus, Eq. (2.18) can be rewritten as

$$\xi_j(\omega,\beta)=\begin{cases}\dfrac{\left(1-\left|r_j\right|^2\right)^2}{\left|1-r_j^2e^{2ik_{z0}d}\right|^2}, & \beta<k_0\\ \dfrac{4\left[\mathrm{Im}(r_j)\right]^2e^{-2|k_{z0}|d}}{\left|1-r_j^2e^{2ik_{z0}d}\right|^2}, & \beta>k_0\end{cases} \tag{6.1}$$

where *j* is for either *s* or *p* polarization, r_j signifies the corresponding reflection coefficient, and Im takes the imaginary part [127]. The magnitude and *z*-component of the wavevector in vacuum are denoted as k_0 and k_{z0}, respectively.

The reflection coefficient of TM waves for the graphene/hBN heterostructure takes the following form

$$r_p=\frac{r_{12,p}+\left(1-r_{12,p}-r_{21,p}\right)r_{23,p}\exp(2ik_{z,2}h)}{1-r_{21,p}r_{23,p}\exp(2ik_{z,2}h)} \tag{6.2}$$

where 1, 2, and 3 are the indexes for the vacuum region above hBN film, the hBN film region, and the vacuum region below hBN film, respectively, as defined in Figure 6.1(b). Also, the reflection coefficient between the vacuum and hBN or *vice versa* can be obtained by

$$r_{ab,p}=\frac{\dfrac{\varepsilon_{\perp,b}}{k_{z,b}}-\dfrac{\varepsilon_{\perp,a}}{k_{z,a}}+\dfrac{\sigma_s}{\omega\varepsilon_0}}{\dfrac{\varepsilon_{\perp,b}}{k_{z,b}}+\dfrac{\varepsilon_{\perp,a}}{k_{z,a}}+\dfrac{\sigma_s}{\omega\varepsilon_0}} \tag{6.3}$$

if there is a graphene layer in between media *a* and *b*, where *a* = 1 or 2 and *b* = 1, 2 or 3. The effect of graphene is included as a current sheet. If there is no graphene in between media *a* and *b*, then,

$$r_{ab,p} = \frac{\dfrac{\varepsilon_{\perp,b}}{k_{z,b}} - \dfrac{\varepsilon_{\perp,a}}{k_{z,a}}}{\dfrac{\varepsilon_{\perp,b}}{k_{z,b}} + \dfrac{\varepsilon_{\perp,a}}{k_{z,a}}} \tag{6.4}$$

In Eqs. (6.3) and (6.4), ε_0 is the vacuum permittivity and $k_{z,b} = \left(\varepsilon_{\perp,b} k_0^2 - \varepsilon_{\perp,b}\beta^2 / \varepsilon_{\|,b}\right)^{1/2}$ with *b* being 1, 2 or 3 is the *z*-component of the wavevector in a given region. For regions with isotropic medium like regions 1 and 3, $\varepsilon_1 = \varepsilon_3 = \varepsilon_\perp = \varepsilon_\| = 1$. For TE waves, the reflection coefficient can be expressed as

$$r_s = \frac{r_{12,s} + \left(1 + r_{12,s} + r_{21,s}\right) r_{23,s} \exp(2ik_{z,2}h)}{1 - r_{21,s} r_{23,s} \exp(2ik_{z,2}h)} \tag{6.5}$$

where

$$r_{ab,s} = \frac{\dfrac{k_{z,a}}{\mu_a} - \sigma_s \omega \mu_0 - \dfrac{k_{z,b}}{\mu_b}}{\dfrac{k_{z,a}}{\mu_a} + \sigma_s \omega \mu_0 + \dfrac{k_{z,b}}{\mu_b}} \quad , \text{ with a graphene sheet} \tag{6.6}$$

and

$$r_{ab,s} = \frac{\dfrac{k_{z,a}}{\mu_a} - \dfrac{k_{z,b}}{\mu_b}}{\dfrac{k_{z,a}}{\mu_a} + \dfrac{k_{z,b}}{\mu_b}} \quad , \text{ without a graphene sheet} \tag{6.7}$$

Here, μ_0 is the permeability of vacuum and μ_b (b = 1, 2 or 3) is the relative permeability for region *b*, which is unit for all regions since the materials are all nonmagnetic. Note that in Eqs. (6.5) to (6.7), $k_{z,b} = \left(\varepsilon_{\perp,b} k_0^2 - \beta^2\right)^{1/2}$ since TE waves are ordinary waves in the hBN film. As mentioned before, the near-field radiative heat transfer is dominated by TM waves. Equations (6.2) and (6.5) can also be used for structures with only graphene by

setting $r_{23} = 0$. They can also be used for the structure without graphene, with one graphene sheet as shown in Figure 6.1, or with a graphene monolayer on both sides of the hBN film to be discussed later. An alternative method can also be used is to treat graphene sheet as a layer of thickness Δ = 0.3 nm with an effective dielectric function $\varepsilon_{\text{eff}} = 1 + i\sigma_s / (\varepsilon_0 \omega \Delta)$ [70]. Both methods yield essentially identical results with less than

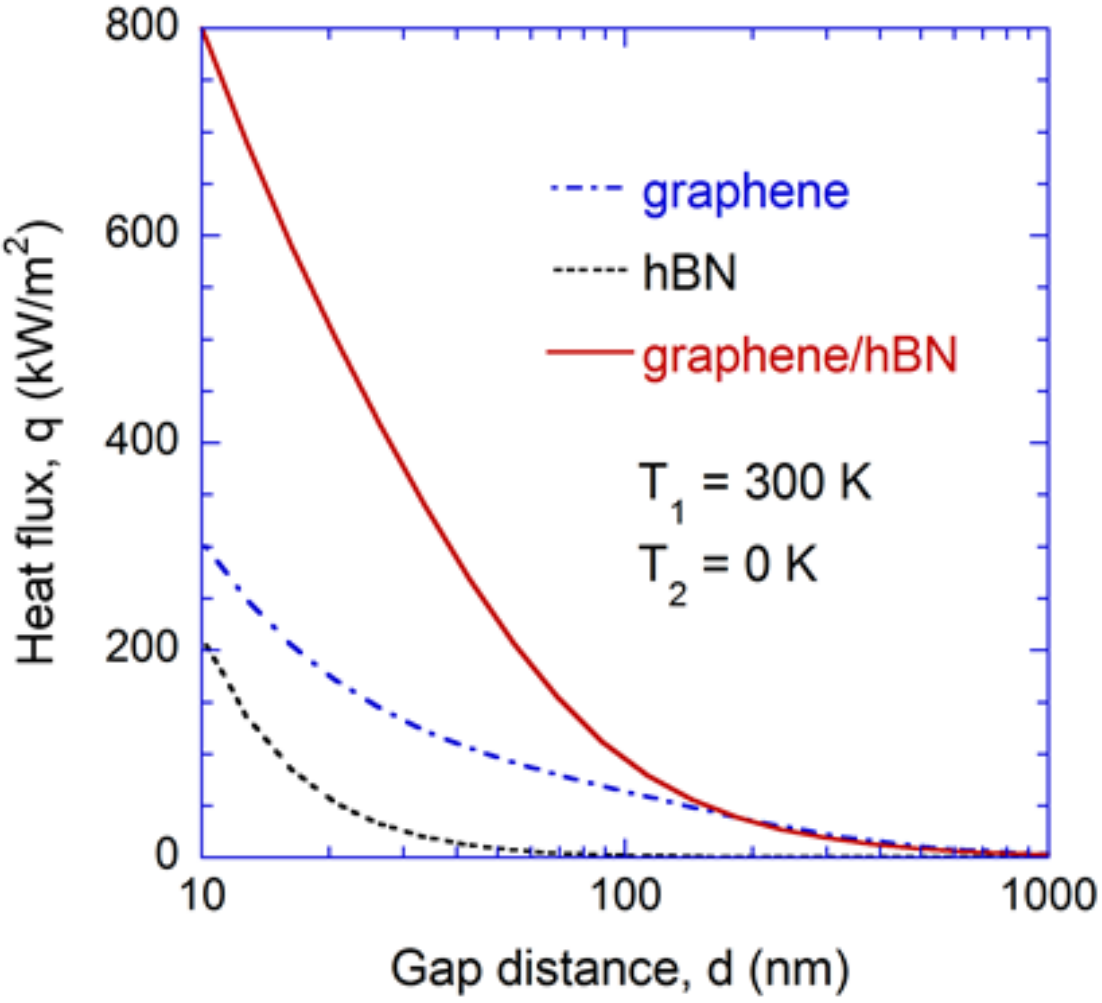

Figure 6.2 Comparison of the radiative heat flux as a function of gap spacing *d* between the heterostructures shown in Figure 6.1(a), graphene monolayers (same structures without the hBN film), and hBN films (same structures without graphene). The temperatures of the emitter and receiver are set at 300 and 0 K, respectively. The film thickness is h = 50 nm and the chemical potential of graphene is μ = 0.37 eV.

0.5% in the predicted total heat flux. The analytical expressions of the reflection coefficients presented here not only help elucidate the fundamental mechanisms of the coupled plasmonic resonances (to be discuss later), but also can save a lot of simulation time once implemented in the numerical algorithm.

Figure 6.2 compares the heat fluxes between a pair of graphene sheets, hBN films with h = 50 nm, and the heterostructures shown in Figure 6.1(a). The chemical potential of graphene is set to 0.37 eV, according to a previous experiment [81]. In the calculations, the temperature of the emitter and receiver are set as T_1 = 300 K and T_2 = 0 K, respectively. However, the optical properties of graphene and hBN are evaluated at room temperature of 300 K. In terms of the radiative heat flux, the heterostructure outperforms the other configurations, especially at small gap distances. At d = 10 nm, the heterostructure yields q = 800 kW/m^2 that is more than twice of that between graphene monolayers or hBN films, which are 305 and 212 kW/m^2, respectively. When d exceeds about 200 nm, the heat flux for the heterostructures is very close to that between suspended graphene sheets, indicating a negligible effect of the hBN film. Note that the radiative heat flux between blackbodies (in the far field) is 459 W/m^2, which is orders of magnitude smaller than the near-field heat flux shown in Figure 6.2.

The mechanism for the enhanced heat transfer between the heterostructures can be elucidated by the contours of photon tunneling probability displayed in Figure 6.3 for the three scenarios. Note that for the structures considered in this work, $\xi_p \gg \xi_s$ since the polaritons discussed here can only be excited for TM waves, which are the dominating contribution to the near-field radiative flux. The bright bands shown in Figure 6.3 indicate efficient photon tunneling due to the excitation of different polaritons, corresponding to the

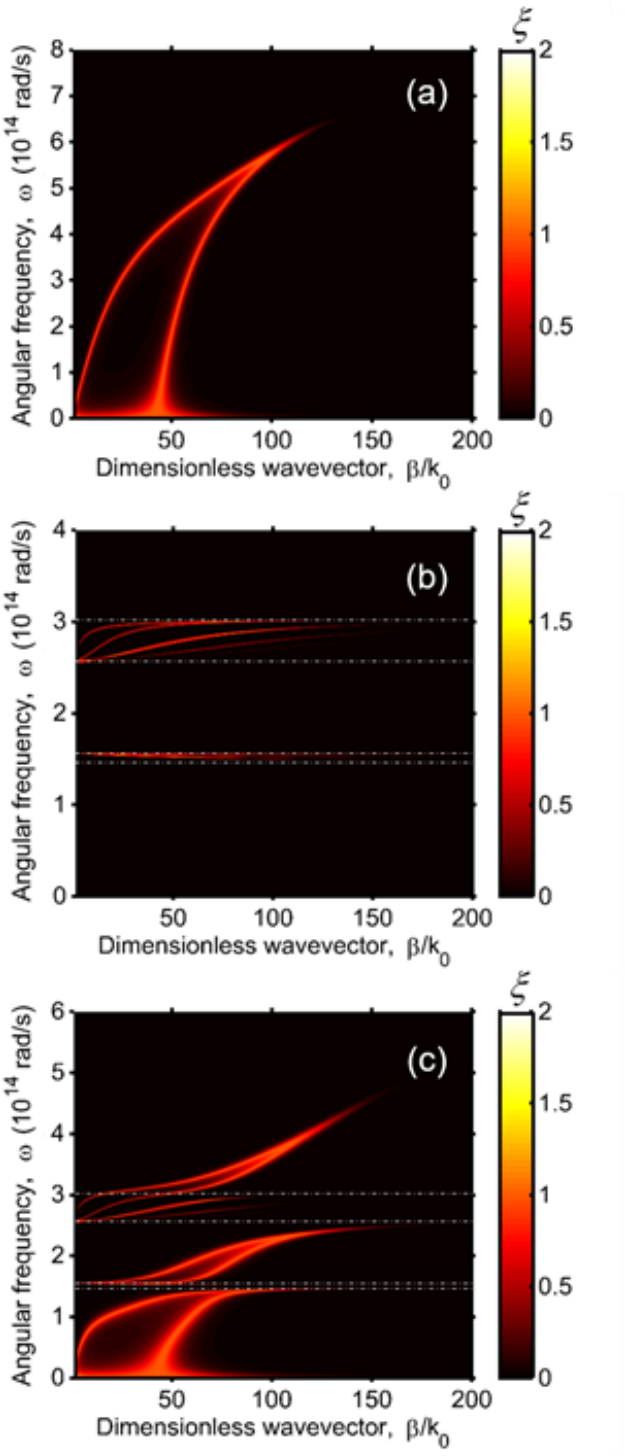

Figure 6.3 Photon tunneling probability contours for different structures: (a) graphene monolayers; (b) hBN films; and (c) heterostructures shown in Figure 6.1(a). The dashed lines indicate the two Reststrahlen bands of hBN. The parameters are d = 20 nm, h = 50 nm, and μ = 0.37 eV.

dispersion curves where the denominator of ξ_p in Eq. (6.1) approaches zero. The two bands in Figure 6.3(a) correspond to the symmetric (lower frequencies) and asymmetric (higher frequencies) branches of the coupled SPPs between two graphene sheets. They are the major contributors to the high near-field heat flux between graphene [330]. For hBN films shown in Figure 6.3(b), multiple phononic waveguide modes can be identified in each Reststrahlen band between the horizontal dashed lines. However, there exist strong tunneling branches outside the two Reststrahlen bands for the heterostructure, as shown in Figure 6.3(c). These additional polaritons, identified as SPPPs, are one kind of hybrid polaritons resulted from the coupling between surface plasmons in graphene and phonon polaritons in hBN [81,82]. Note that similar to the Figure 6.3(a), each order of the polariton bands in (b) and (c) splits into two branches. The mechanism of hybrid polaritons and their impact on near-field radiative transfer are elaborated in the following.

The hybrid polaritons in the heterostructure can be categorized into two kinds depending on whether they are inside or outside the Reststrahlen band of hBN. Specifically, the dispersion of the hybrid polaritons take two expressions based on the dielectric function of hBN [82]

$$\beta(\omega)=\begin{cases}-\dfrac{\delta}{h}\left[n\pi+\arctan\left(\dfrac{\omega\varepsilon_0\varepsilon_1+i\beta\sigma_s}{\delta\omega\varepsilon_0\varepsilon_{\perp,2}}\right)+\arctan\left(\dfrac{\varepsilon_3}{\delta\varepsilon_{\perp,2}}\right)\right], & \varepsilon_{\perp,2}\varepsilon_{\parallel,2}<0\\ \dfrac{|\delta|}{2h}\ln\left(\dfrac{\omega\varepsilon_0\varepsilon_1-\omega\varepsilon_0\varepsilon_{\perp,2}|\delta|+i\beta\sigma_s}{\omega\varepsilon_0\varepsilon_1+\omega\varepsilon_0\varepsilon_{\perp,2}|\delta|+i\beta\sigma_s}\times\dfrac{\varepsilon_3-\varepsilon_{\perp,2}|\delta|}{\varepsilon_3+\varepsilon_{\perp,2}|\delta|}\right), & \varepsilon_{\perp,2}\varepsilon_{\parallel,2}>0\end{cases} \tag{6.8}$$

When $\varepsilon_{\perp,2}\varepsilon_{\parallel,2}<0$, the isofrequency contour of hBN is hyperbolic and the hybrid polaritons are referred to as hyperbolic plasmon-phonon polaritons (HPPPs) [81] since they preserve the hyperbolic-waveguide-mode features as in an uncovered hBN film. Integer *n*

denotes the resonance order. Here, $\delta = \pm i\sqrt{\varepsilon_{\|,2}/\varepsilon_{\perp,2}}$ and the plus or minus sign is chosen based on the shape of the HPPPs bands [82]. If σ_s is set to zero, the first expression in Eq. (9) recovers the dispersion for the waveguide modes in hBN films. When $\varepsilon_{\perp,2}\varepsilon_{\|,2} > 0$, the isofrequency contour of hBN becomes elliptic, and SPPPs can be supported in the three frequency regions below, between, and above the two Reststrahlen bands, as shown in Figure 6.3(c). Unlike HPPPs, SPPPs are surface modes with a strong plasmonic characteristic when they are not so close to the Reststrahlen bands [81]. If σ_s is set to zero (i.e. without graphene), the second expression in Eq. (6.8) yields a negative β since $\varepsilon_{\perp,2} > 0$, suggesting that hBN films cannot support any resonances outside the two Reststrahlen bands. This provides an explanation why the resonances only exist within the Reststrahlen bands as Figure 6.3(b) shows.

It is worth pointing out that, the second expression in Eq. (6.8) does not require an anisotropic substrate to yield a valid solution. Thus, phononic polaritons in films made of isotropic polar materials like SiO_2 and SiC could also couple with SPPs in graphene to form a hybridized polariton, whose dispersion can be obtained by setting $|\delta| = 1$. Similar phenomena were demonstrated for the coupling between SPPs in graphene or thin metal layer with the SPhPs supported by semi-infinite polar material substrates [331,332]. Moreover, a prominent feature that can be identified in Figure 6.3(c) is the mode flatting when the SPPPs approach either Reststrahlen band near ω_{TO}. This is caused by the anticrossing effect or mode repulsion between SPPs in graphene and waveguide modes in hBN, and same effect was found to exist between SPPs in a thin metal layer and SPhPs in isotropic polar substrates [331]. Because of this effect, the two hyperbolic Reststrahlen

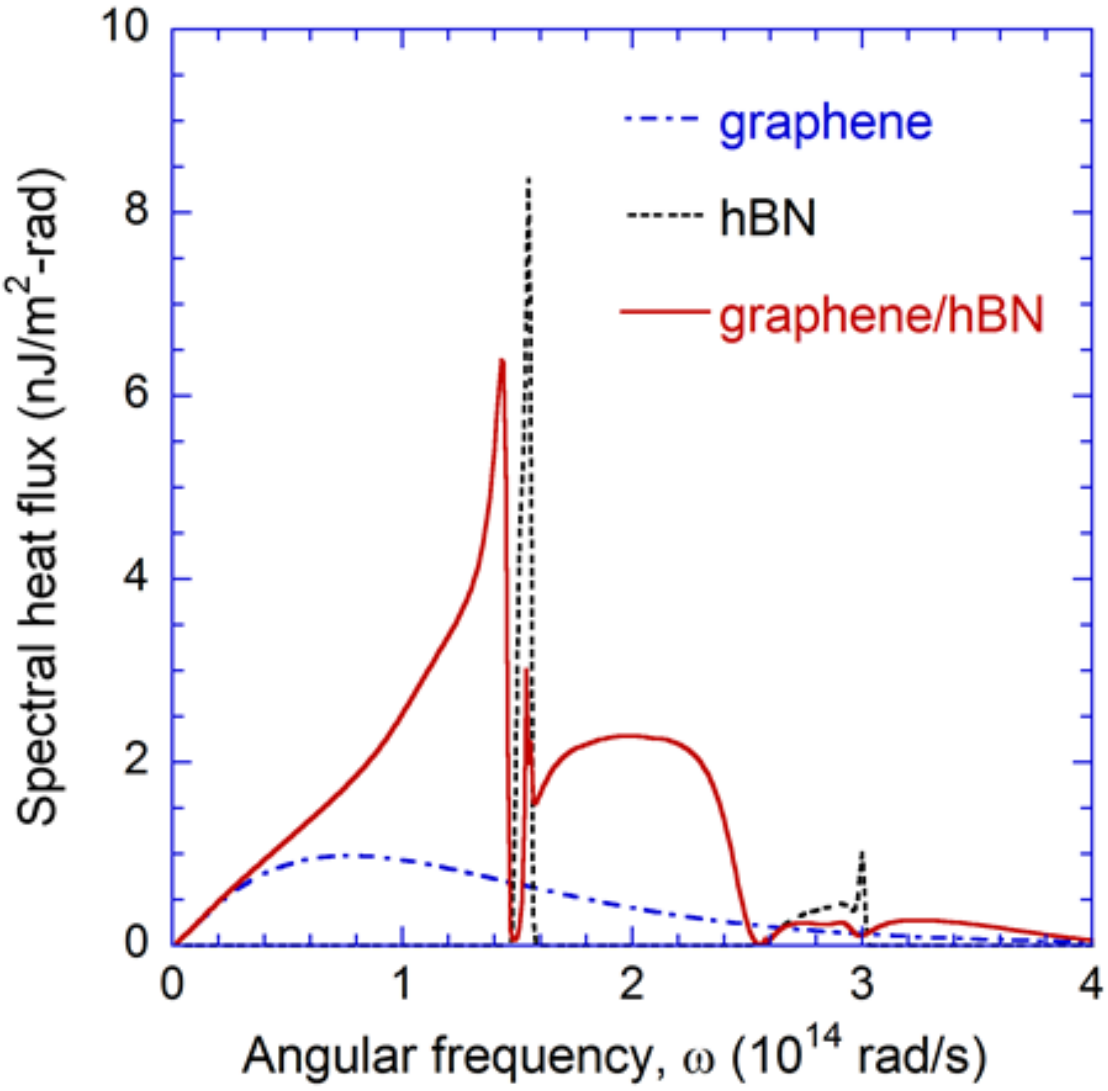

Figure 6.4 Spectral heat flux between two graphene monolayers, hBN films, and graphene/hBN heterostructures. The parameters used are the same as for Figure 6.2.

bands break the otherwise continuous SPPPs into three regions in frequency, allowing high density of state to occur at some band edges and boosting the photon tunneling, as will be discussed in the next.

If Eq. (2.17) is integrated over β only, the result is the spectral heat flux, which is shown in Figure 6.4 for the three configurations with d = 20 nm. It can be seen that the heat flux for hBN structures is mainly contributed by the waveguide modes, and the spectral

heat flux is nearly zero outside the two Reststrahlen bands. Graphene plasmons cover a frequency range up to 6×10^{14} rad/s as shown in Figure 6.3(a), and thus the spectral heat flux between graphene sheets has a nontrivial value over a broad band but fades away at high frequencies due to the frequency dependence of the Planck oscillator. The heterostructure combines the features of graphene and hBN film, and also shows a high spectral heat flux in the regions outside the Reststrahlen bands due to SPPPs, indicating that the major contribution to the radiative heat transfer between the heterostructures comes from SPPPs instead of HPPPs. The peak around 1.4×10^{14} rad/s is caused by the high density of state [333] of the SPPPs near $\omega_{\mathrm{TO},\parallel}$, as indicated by the flat dispersion in Figure 6.3(c), which is a result of the above-mentioned anticrossing effect. The flat dispersion allows high-β modes to exist and makes the term $\int_0^\infty \xi(\omega,\beta)\beta d\beta$ in Eq. (2.17) greater, leading to an increase in the spectral heat flux. However, the anticrossing effect plays the opposite role and suppresses the heat flux in the hyperbolic regions. As shown in Figure 6.3(b), the waveguide modes in hBN film are able to be supported when β is about $150k_0$. In contrast, the anticrossing causes an early truncation of the HPPPs, as shown in Figure 6.3(c), and these modes disappear at about $100k_0$. Similar effect was observed for the anticrossing between graphene SPPs and SPhPs in SiC and SiO_2, where SPPs truncate the SPhPs at large wavevectors [332,334]. This early truncation results in a lower spectral heat flux for the heterostructures in the two hyperbolic bands compared to the hBN films, as indicated in Figure 6.4.

The effect of loss on the hybrid polaritons are investigated by setting the loss of one of the materials to zero, though not shown here. When the graphene is assumed to have no

loss, calculations show that the contribution of SPPPs to the spectral flux becomes much less because the bands of SPPPs are much narrower. However, when the loss of hBN is set to zero, SPPPs are not affected too much, and the spectral heat flux is still very similar to Figure 6.4. HPPPs can extend to larger wavevectors in this case, but the spectral heat flux in the two hyperbolic regions drops since the bandwidth of HPPPs decreases.

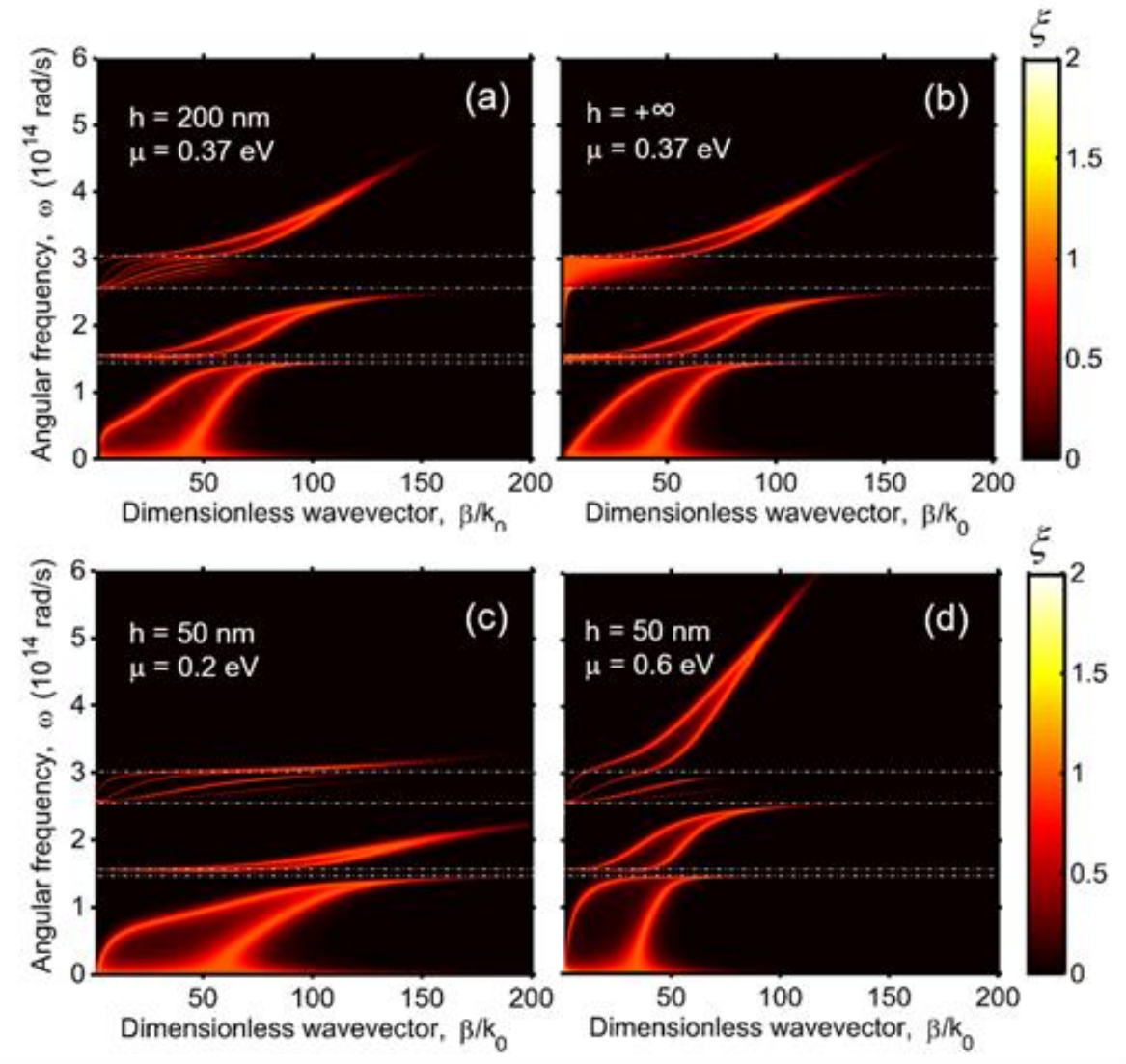

Figure 6.5 Photon tunneling probability contours for different graphene/hBN heterostructures. The gap distance is fixed at 20 nm and the other parameters are as follows: (a) h = 200 nm and μ = 0.37 eV; (b) h = +∞ (semi-infinite) and μ = 0.37 eV; (c) h = 50 nm and μ = 0.2 eV; and (d) h = 50 nm and μ = 0.6 eV.

The photon tunneling can be controlled by h since a thicker film allows higher orders of HPPPs to present at lower β. The upper panel of Figure 6.5 demonstrates this effect, in which the hBN film is changed to be 200 nm in (a) and semi-infinite in (b). Compared to the scenario in Figure 6.3(c) when h = 50 nm, more orders of HPPPs show up in Figure 6.5(a) and they eventually merge to a continuous band when the hBN layer becomes semi-infinite. However, the SPPPs do not experience significant changes. This can be understood since SPPPs are surface modes featured with a strong localized field on the interface of heterostructure that has graphene. The field intensity evanescently decays away from the interface and, thus, making the hBN film thicker has little effect on SPPPs. Since the enhanced heat flux is mainly due to the contribution of SPPPs, a thicker hBN film brings a slight increase in the heat flux, yielding 537 and 547 kW/m^2 for Figure 6.5(a) and (b), respectively, compared to 513 kW/m^2 for the case in Figure 6.3(c). This effect may offer a passive way to modify photon tunneling to some extent. Note that calculations show that the penetration depth in hBN is smaller than 300 nm over the spectral range with high spectral heat flux [335], and thus a thicker film exceeding 300 nm would bring little effect to near-field heat transfer.

On the other hand, a lower μ can push the SPPPs to larger wavevectors as indicated Eq. (6.8), and thus can affect the tunneling probability significantly. Figure 6.5(c) and (d) show the tunneling probability when μ is changed to 0.2 and 0.6 eV, respectively. The SPPP bands become flatter in (c) and steeper in (d) compared to Figure 6.3(c), and thus, q becomes 1131 kW/m^2 and 249 kW/m^2, respectively. The huge increase at $\mu = 0.2$ eV is attributed to the flat dispersion that allows the SPPPs to extend to larger β values. The same reason holds for the decrease of heat flux at $\mu = 0.6$ eV. Note that this does not mean

the maximum heat flux can be achieved at $\mu = 0$ eV because at this chemical potential, interband transitions dominate σ_s in the near-infrared region in which graphene does not support SPPs anymore [148,149]. Calculations show that the maximum heat flux occurs at around $\mu = 0.1$ eV with $q = 1700$ kW/m^2. Since μ can be changed by electrical gating [61], this effect may offer a potential way to actively control photon tunneling.

The photon tunneling probability can be further enhanced by placing an extra graphene layer on the other side of the graphene/hBN heterostructure. In this case, both sides of the hBN film are covered with graphene and the graphene on the backside can modify coefficient r_{23} such that additional solutions exist that can zero the denominator of ξ_p, as shown in Figure 6.6. Compared to Figure 6.3(c), two new branches of SPPPs occur

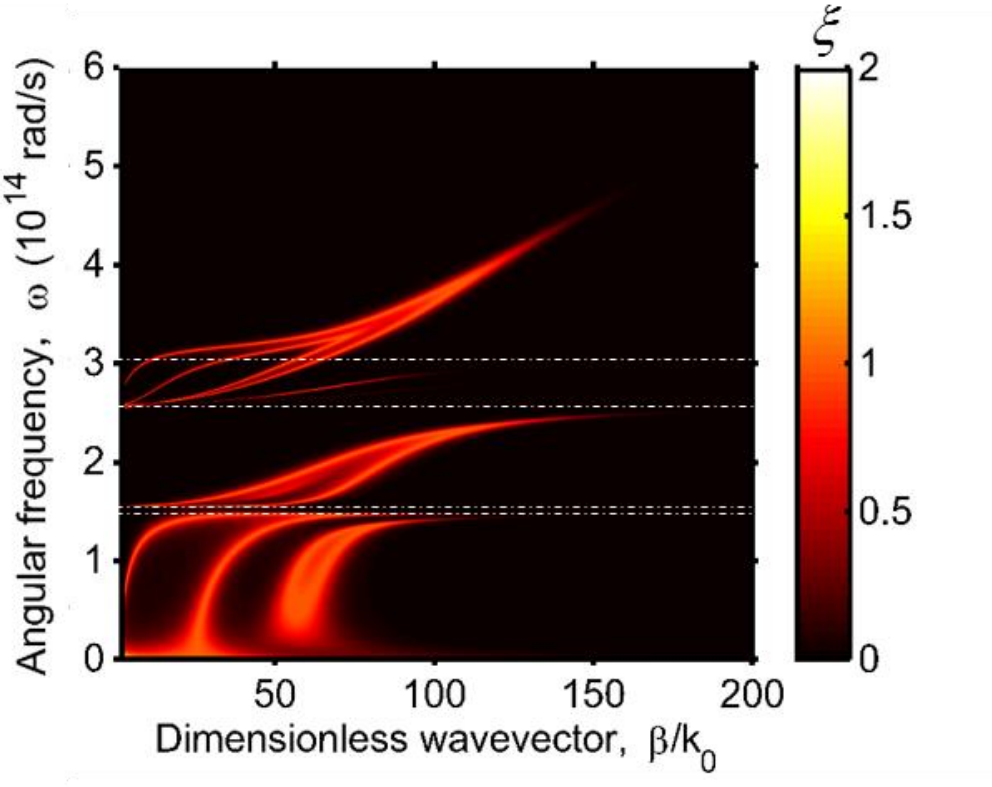

Figure 6.6 Photon tunneling probability contour for the graphene/hBN/graphene heterostructure.

outside the two hyperbolic Reststrahlen bands. These SPPP branches further enhance photon tunneling as demonstrated by the spectral heat flux shown in Figure 6.7, and the total heat flux q is increased to 643 kW/m^2 (a 25.3% increase for the same structure with only one side covered graphene). Note that the chemical potentials of the two graphene layers in this example are the same and they can be actively changed to tune the SPPPs as discussed previously. However, they do not have to be the same and may be controlled independently to allow more active tunability.

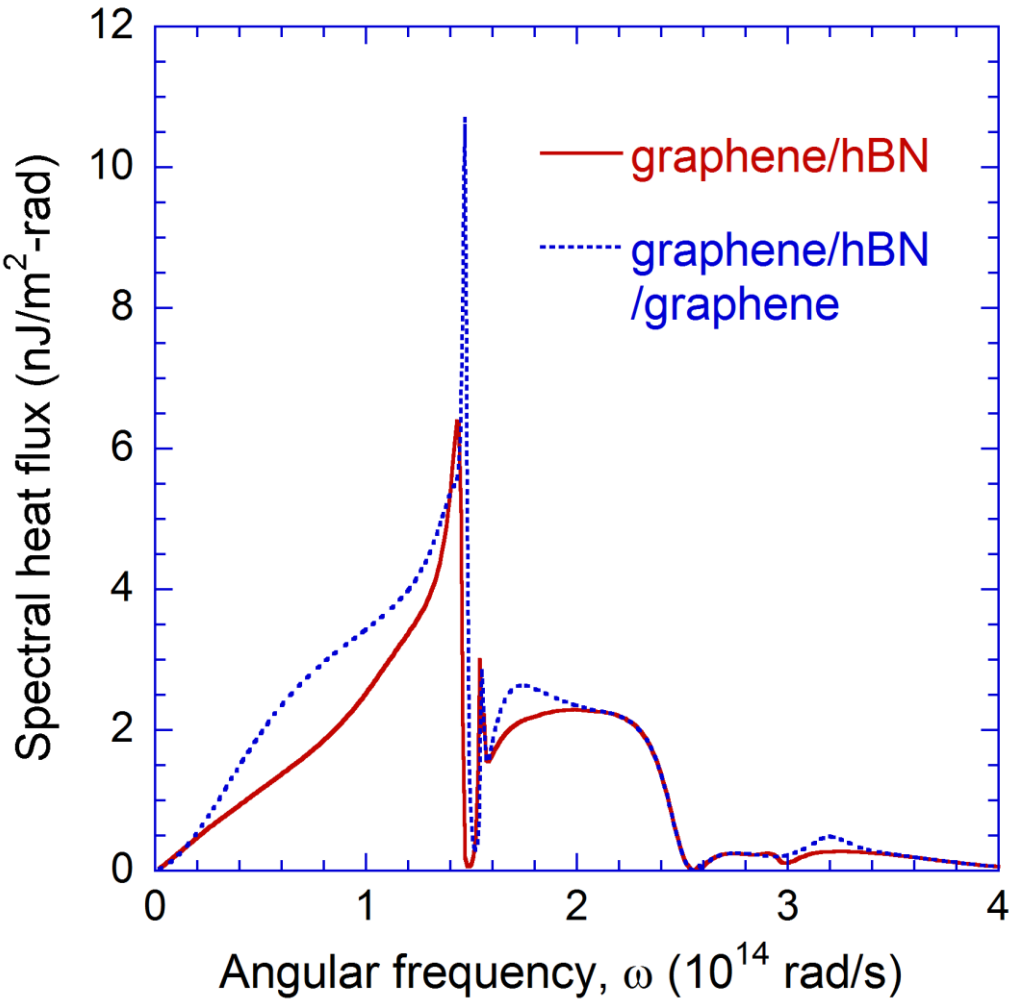

Figure 6.7 Comparison of the spectral heat flux for the graphene/hBN and graphene/hBN/graphene structures. The parameters are d = 20 nm, h = 50 nm, and μ = 0.37 eV.

In conclusion, this work demonstrates that graphene/hBN heterostructured optical materials can enhance photon tunneling and outperform graphene or hBN film in terms of achieving high near-field radiative heat transfer, thanks to the hybrid modes SPPPs. The SPPPs enhance the spectral heat flux outside the two Reststrahlen bands and can be controlled by the thickness of the hBN film and the chemical potential of graphene. Placing an additional graphene layer on the other side of the hBN film further enhances the heat transfer between the heterostructures by allowing extra SPPP branches. The findings in this work may facilitate the design of systems utilizing near-field thermal radiation with passively and actively tunable photon tunneling based on graphene and hBN.

CHAPTER 7

CONCLUSIONS AND RECOMMENDATIONS

This dissertation studies the radiative properties of various plasmonic nanostructures and 2D materials. Thanks to the excitation of various polaritons such as MPs and SPPs, diverse micro/nanostructures can be designed to control the optical and radiative properties for different practical application purposes. The emerging 2D materials provide even more plentiful resonances that can couple with the polaritons in the micro/nanostructures to yield exotic optical and radiative properties. Nano/micro structured 2D materials possess unusual properties such as broadband perfect absorption. Heterostructures of 2D materials enables hybrid polaritons that can enhance the photon tunneling and near-field heat transfer.

Anisotropic RCWA is summarized as a promising and competitive method to model periodic micro/nanostructures compared to FDTD and FEM. It can simulate the radiative properties and the field distribution in the frequency domain. Because of its meshless nature, it has advantages of modeling structures with small characteristic length like 2D materials. A 2D metal/dielectric/metal structure can be used to achieve wavelength-selective emittance that can be used to improve the efficiency of TPV system. MPs, SPPs, and WAs are responsible for the selective emittance spectrum. Different with a 1D grating, the 2D structure is insensitive to the polarization angle. Metal gratings can be used to excite SPPs and MPs. The wavevector of SPs can be compensated by the diffraction effect and thus help the incident electromagnetic wave to couple with the SPs to form a SPP. Localized resonance, MPs, can be excited inside the trench of the grating and LC model can be used to model the resonance frequency. Three-polarization-angle method is

discussed as a method to deduct the polarization of the eigenmodes from the reflectance or transmittance of three arbitrary polarization angles. The method may benefit the design of optical and radiative properties with polarization dependence.

Graphene can be used to tune radiative properties. By using a graphene/metal grating hybrid structure, strong absorption can be achieved in different frequency range. In the visible and near-infrared region, graphene couples with MPs and SPPs in grating and enhances the absorptance of the structure significantly without affecting the original resonance condition of MPs and SPPs. The majority of the power is dissipated by graphene, and that can be favorable in ultrafast optoelectronic applications. In the mid- and far-infrared, graphene ribbon plasmons strongly couple with MPs in gratings to create a hybrid resonance with significantly high absorptance. The coupled resonance can be tuned by electrical gating or chemical doping of graphene. Perfect absorption is achieved in hBN/metal grating hybrid anisotropic structures due to hybrid phonon-plasmon polaritons. In the two hyperbolic regions of hBN, HPPs strongly couple with localized MPs, forming hybrid hyperbolic phonon-plasmon polaritons and achieving strong absorption. The majority of the power is dissipated inside the hBN film with a tunable location-dependent absorption profile. Trapezoidal hBN gratings can achieve high broadband absorptance in its Type-II hyperbolic region due to a localized resonance that is caused by a slow light effect in hyperbolic waveguides. The absorption is nearly omnidirectional and the absorption bandwidth can be engineered by using different shapes of trapezoid. Hyperbolic materials can also be used to build resonators with wavelength-selective absorption resulted from directional propagation of HPPs. Different resonators with the same shape

but different sizes may be designed to resonate at the same frequency and the resonance wavelength can be well predicted based on the shape of the resonator.

This dissertation has enhanced the understanding of the radiative properties of micro/nanostructured plasmonic metamaterials and 2D materials. It is hoped that other 2D materials such as black phosphorus, silicene, and borophene can also be integrated with micro/nanostructures to achieve desired unusual properties. Moreover, since the plasmon-phonon coupling phenomena involves optical phonon, it is interesting to further study the light absorption and heat transfer in the hybrid structures. Other natural materials that possess hyperbolic response in visible and infrared range may be further explored to achieve broadband and resonance absorption. It is also hoped that structured 2D materials can provide even more plentiful routes to enhance photon tunneling and near-field heat transfer.

REFERENCES

[1] Hesketh, P. J., Zemel, J. N., and Gebhart, B., 1986, "Organ Pipe Radiant Modes of Periodic Micromachined Silicon Surfaces," Nature, **324**, pp. 549-551.

[2] Greffet, J.-J., Carminati, R., Joulain, K., Mulet, J.-P., Mainguy, S., and Chen, Y., 2002, "Coherent Emission of Light by Thermal Sources," Nature, **416**, pp. 61-64.

[3] Zhang, Z. M., 2007, *Nano/Microscale Heat Transfer*, McGraw-Hill, New York.

[4] Lee, B. J., Fu, C. J., and Zhang, Z. M., 2005, "Coherent Thermal Emission from One-Dimensional Photonic Crystals," Appl. Phys. Lett., **87**, p. 071904.

[5] Dahan, N., Niv, A., Biener, G., Gorodetski, Y., Kleiner, V., and Hasman, E., 2008, "Extraordinary Coherent Thermal Emission from Sic Due to Coupled Resonant Cavities," J. Heat Transfer, **130**, p. 112401.

[6] Cai, W., and Shalaev, V., 2009, *Optical Metamaterials: Fundamentals and Applications*, Springer, New York.

[7] Tan, Y., Liu, B., Shen, S., and Yu, Z., 2016, "Enhancing Radiative Energy Transfer through Thermal Extraction," Nanophotonics, **5**, p. 22.

[8] Chang, C.-C., Sharma, Y. D., Kim, Y.-S., Bur, J. A., Shenoi, R. V., Krishna, S., Huang, D., and Lin, S.-Y., 2010, "A Surface Plasmon Enhanced Infrared Photodetector Based on Inas Quantum Dots," Nano Lett., **10**, pp. 1704-1709.

[9] Kulkarni, A. P., Noone, K. M., Munechika, K., Guyer, S. R., and Ginger, D. S., 2010, "Plasmon-Enhanced Charge Carrier Generation in Organic Photovoltaic Films Using Silver Nanoprisms," Nano Lett., **10**, pp. 1501-1505.

[10] Li, W., and Valentine, J., 2014, "Metamaterial Perfect Absorber Based Hot Electron Photodetection," Nano Lett., **14**, pp. 3510-3514.

[11] Ebbesen, T. W., Lezec, H. J., Ghaemi, H. F., Thio, T., and Wolff, P. A., 1998, "Extraordinary Optical Transmission through Sub-Wavelength Hole Arrays," Nature, **391**, pp. 667-669.

[12] Porto, J. A., García-Vidal, F. J., and Pendry, J. B., 1999, "Transmission Resonances on Metallic Gratings with Very Narrow Slits," Phys. Rev. Lett., **83**, pp. 2845-2848.

[13] Baida, F. I., and Van Labeke, D., 2002, "Light Transmission by Subwavelength Annular Aperture Arrays in Metallic Films," Opt. Commun., **209**, pp. 17-22.

[14] Lee, B. J., Chen, Y.-B., and Zhang, Z. M., 2008, "Transmission Enhancement through Nanoscale Metallic Slit Arrays from the Visible to Mid-Infrared," J. Comput. Theor. Nanosci., **5**, pp. 201-213.

[15] Pendry, J. B., 2000, "Negative Refraction Makes a Perfect Lens," Phys. Rev. Lett., **85**, pp. 3966-3969.

[16] Shelby, R. A., Smith, D. R., and Schultz, S., 2001, "Experimental Verification of a Negative Index of Refraction," Science, **292**, pp. 77-79.

[17] Smith, D. R., Pendry, J. B., and Wiltshire, M. C. K., 2004, "Metamaterials and Negative Refractive Index," Science, **305**, pp. 788-792.

[18] Shalaev, V. M., Cai, W., Chettiar, U. K., Yuan, H.-K., Sarychev, A. K., Drachev, V. P., and Kildishev, A. V., 2005, "Negative Index of Refraction in Optical Metamaterials," Opt. Lett., **30**, pp. 3356-3358.

[19] Eleftheriades, G. V., and Balmain, K. G., 2005, *Negative-Refraction Metamaterials: Fundamental Principles and Applications*, John Wiley & Sons, New Jersey.

[20] Grady, N. K., Heyes, J. E., Chowdhury, D. R., Zeng, Y., Reiten, M. T., Azad, A. K., Taylor, A. J., Dalvit, D. A. R., and Chen, H.-T., 2013, "Terahertz Metamaterials for Linear Polarization Conversion and Anomalous Refraction," Science, **340**, pp. 1304-1307.

[21] Hou-Tong, C., Antoinette, J. T., and Nanfang, Y., 2016, "A Review of Metasurfaces: Physics and Applications," Rep. Prog. Phys., **79**, p. 076401.

[22] Pendry, J. B., Schurig, D., and Smith, D. R., 2006, "Controlling Electromagnetic Fields," Science, **312**, pp. 1780-1782.

[23] Schurig, D., Mock, J. J., Justice, B. J., Cummer, S. A., Pendry, J. B., Starr, A. F., and Smith, D. R., 2006, "Metamaterial Electromagnetic Cloak at Microwave Frequencies," Science, **314**, pp. 977-980.

[24] Cai, W., Chettiar, U. K., Kildishev, A. V., and Shalaev, V. M., 2007, "Optical Cloaking with Metamaterials," Nat. Photonics, **1**, pp. 224-227.

[25] Liu, R., Ji, C., Mock, J. J., Chin, J. Y., Cui, T. J., and Smith, D. R., 2009, "Broadband Ground-Plane Cloak," Science, **323**, pp. 366-369.

[26] Stiles, P. L., Dieringer, J. A., Shah, N. C., and Duyne, R. P. V., 2008, "Surface-Enhanced Raman Spectroscopy," Annu. Rev. Anal. Chem., **1**, pp. 601-626.

[27] Cai, W., Gao, T., Hong, H., and Sun, J., 2008, "Applications of Gold Nanoparticles in Cancer Nanotechnology," Nanotechnol. Sci. Appl., **2008**, p. 10.2147/NSA.S3788.

[28] Basu, S., Chen, Y.-B., and Zhang, Z. M., 2007, "Microscale Radiation in Thermophotovoltaic Devices—a Review," Int. J. Energy Res., **31**, pp. 689-716.

[29] Wang, L. P., and Zhang, Z. M., 2012, "Wavelength-Selective and Diffuse Emitter Enhanced by Magnetic Polaritons for Thermophotovoltaics," Appl. Phys. Lett., **100**, p. 063902.

[30] Watts, C. M., Liu, X., and Padilla, W. J., 2012, "Metamaterial Electromagnetic Wave Absorbers," Adv. Mater., **24**, pp. OP98-OP120.

[31] Boriskina, S. V., Ghasemi, H., and Chen, G., 2013, "Plasmonic Materials for Energy: From Physics to Applications," Mater. Today, **16**, pp. 375-386.

[32] Baxter, J., Bian, Z., Chen, G., Danielson, D., Dresselhaus, M. S., Fedorov, A. G., Fisher, T. S., Jones, C. W., Maginn, E., Kortshagen, U., Manthiram, A., Nozik, A., Rolison, D. R., Sands, T., Shi, L., Sholl, D., and Wu, Y., 2009, "Nanoscale Design to Enable the Revolution in Renewable Energy," Energy Environ. Sci., **2**, pp. 559-588.

[33] Atwater, H. A., and Polman, A., 2010, "Plasmonics for Improved Photovoltaic Devices," Nat. Mater., **9**, pp. 205-213.

[34] Cui, Y., Fung, K. H., Xu, J., Ma, H., Jin, Y., He, S., and Fang, N. X., 2012, "Ultrabroadband Light Absorption by a Sawtooth Anisotropic Metamaterial Slab," Nano Lett., **12**, pp. 1443-1447.

[35] Fan, S., 2014, "Photovoltaics: An Alternative 'Sun' for Solar Cells," Nat. Nanotechnol., **9**, pp. 92-93.

[36] Khodasevych, I. E., Wang, L., Mitchell, A., and Rosengarten, G., 2015, "Micro- and Nanostructured Surfaces for Selective Solar Absorption," Adv. Opt. Mater., **3**, pp. 852-881.

[37] Cheng, F., Gao, J., Luk, T. S., and Yang, X., 2015, "Structural Color Printing Based on Plasmonic Metasurfaces of Perfect Light Absorption," Sci. Rep., **5**, p. 11045.

[38] Raman, A. P., Anoma, M. A., Zhu, L., Rephaeli, E., and Fan, S., 2014, "Passive Radiative Cooling Below Ambient Air Temperature under Direct Sunlight," Nature, **515**, pp. 540-544.

[39] Raether, H., 1988, *Surface Plasmons on Smooth and Rough Surfaces and on Gratings*, Springer-Verlag, Berlin.

[40] Zayats, A. V., Smolyaninov, I. I., and Maradudin, A. A., 2005, "Nano-Optics of Surface Plasmon Polaritons," Phys. Rep., **408**, pp. 131-314.

[41] Williams, C. R., Andrews, S. R., Maier, S. A., Fernandez-Dominguez, A. I., Martin Moreno, L., and Garcia-Vidal, F. J., 2008, "Highly Confined Guiding of Terahertz Surface Plasmon Polaritons on Structured Metal Surfaces," Nat. Photonics, **2**, pp. 175-179.

[42] Krishnamoorthy, H. N. S., Jacob, Z., Narimanov, E., Kretzschmar, I., and Menon, V. M., 2012, "Topological Transitions in Metamaterials," Science, **336**, pp. 205-209.

[43] Poddubny, A., Iorsh, I., Belov, P., and Kivshar, Y., 2013, "Hyperbolic Metamaterials," Nat. Photonics, **7**, pp. 948-957.

[44] Othman, M. A. K., Guclu, C., and Capolino, F., 2013, "Graphene–Dielectric Composite Metamaterials: Evolution from Elliptic to Hyperbolic Wavevector Dispersion and the Transverse Epsilon-near-Zero Condition," J. Nanophotonics, **7**, pp. 073089-073089.

[45] Lee, B. J., Wang, L. P., and Zhang, Z. M., 2008, "Coherent Thermal Emission by Excitation of Magnetic Polaritons between Periodic Strips and a Metallic Film," Opt. Express, **16**, pp. 11328-11336.

[46] Zhao, B., and Zhang, Z. M., 2014, "Study of Magnetic Polaritons in Deep Gratings for Thermal Emission Control," J. Quant. Spectrosc. Radiat. Transfer, **135**, pp. 81-89.

[47] Xuan, Y., and Zhang, Y., 2014, "Investigation on the Physical Mechanism of Magnetic Plasmons Polaritons," J. Quant. Spectrosc. Radiat. Transfer, **132**, pp. 43-51.

[48] Luo, C., Narayanaswamy, A., Chen, G., and Joannopoulos, J. D., 2004, "Thermal Radiation from Photonic Crystals: A Direct Calculation," Phys. Rev. Lett., **93**, p. 213905.

[49] Zhang, Z., and Ye, H., 2012, "Measurements of Radiative Properties of Engineered Micro/Nanostructures," Annual Review of Heat Transfer, **12**, p. 345.

[50] Wang, L. P., and Zhang, Z. M., 2009, "Resonance Transmission or Absorption in Deep Gratings Explained by Magnetic Polaritons," Appl. Phys. Lett., **95**, p. 111904.

[51] Zhang, Z., Park, K., and Lee, B. J., 2011, "Surface and Magnetic Polaritons on Two-Dimensional Nanoslab-Aligned Multilayer Structure," Opt. Express, **19**, pp. 16375-16389.

[52] Wang, L. P., and Zhang, Z. M., 2011, "Phonon-Mediated Magnetic Polaritons in the Infrared Region," Opt. Express, **19**, pp. A126-A135.

[53] Wu, C., Neuner, B., III, Shvets, G., John, J., Milder, A., Zollars, B., and Savoy, S., 2011, "Large-Area Wide-Angle Spectrally Selective Plasmonic Absorber," Phys. Rev. B, **84**, p. 075102.

[54] Fang, N., Lee, H., Sun, C., and Zhang, X., 2005, "Sub-Diffraction-Limited Optical Imaging with a Silver Superlens," Science, **308**, pp. 534-537.

[55] Kabashin, A. V., Evans, P., Pastkovsky, S., Hendren, W., Wurtz, G. A., Atkinson, R., Pollard, R., Podolskiy, V. A., and Zayats, A. V., 2009, "Plasmonic Nanorod Metamaterials for Biosensing," Nat. Mater., **8**, pp. 867-871.

[56] Kang, L., Lan, S., Cui, Y., Rodrigues, S. P., Liu, Y., Werner, D. H., and Cai, W., 2015, "An Active Metamaterial Platform for Chiral Responsive Optoelectronics," Adv. Mater., **27**, pp. 4377-4383.

[57] Geim, A. K., and Grigorieva, I. V., 2013, "Van Der Waals Heterostructures," Nature, **499**, pp. 419-425.

[58] Xia, F., Wang, H., Xiao, D., Dubey, M., and Ramasubramaniam, A., 2014, "Two-Dimensional Material Nanophotonics," Nat. Photonics, **8**, pp. 899-907.

[59] Novoselov, K. S., Geim, A. K., Morozov, S. V., Jiang, D., Zhang, Y., Dubonos, S. V., Grigorieva, I. V., and Firsov, A. A., 2004, "Electric Field Effect in Atomically Thin Carbon Films," Science, **306**, pp. 666-669.

[60] Lin, Y., and Connell, J. W., 2012, "Advances in 2d Boron Nitride Nanostructures: Nanosheets, Nanoribbons, Nanomeshes, and Hybrids with Graphene," Nanoscale, **4**, pp. 6908-6939.

[61] Grigorenko, A. N., Polini, M., and Novoselov, K. S., 2012, "Graphene Plasmonics," Nat. Photonics, **6**, pp. 749-758.

[62] Koppens, F. H. L., Mueller, T., Avouris, P., Ferrari, A. C., Vitiello, M. S., and Polini, M., 2014, "Photodetectors Based on Graphene, Other Two-Dimensional Materials and Hybrid Systems," Nat. Nanotechnol., **9**, pp. 780-793.

[63] Bonaccorso, F., Colombo, L., Yu, G., Stoller, M., Tozzini, V., Ferrari, A. C., Ruoff, R. S., and Pellegrini, V., 2015, "Graphene, Related Two-Dimensional Crystals, and Hybrid Systems for Energy Conversion and Storage," Science, **347**, p. 1246501.

[64] Dai, S., Fei, Z., Ma, Q., Rodin, A. S., Wagner, M., McLeod, A. S., Liu, M. K., Gannett, W., Regan, W., Watanabe, K., Taniguchi, T., Thiemens, M., Dominguez, G., Neto, A. H. C., Zettl, A., Keilmann, F., Jarillo-Herrero, P., Fogler, M. M., and

Basov, D. N., 2014, "Tunable Phonon Polaritons in Atomically Thin Van Der Waals Crystals of Boron Nitride," Science, **343**, pp. 1125-1129.

[65] Wang, F., Wang, Z., Wang, Q., Wang, F., Yin, L., Xu, K., Huang, Y., and He, J., 2015, "Synthesis, Properties and Applications of 2d Non-Graphene Materials," Nanotechnol., **26**, p. 292001.

[66] Ling, X., Wang, H., Huang, S., Xia, F., and Dresselhaus, M. S., 2015, "The Renaissance of Black Phosphorus," Proc. Natl. Acad. Sci., **112**, pp. 4523-4530.

[67] Nair, R. R., Blake, P., Grigorenko, A. N., Novoselov, K. S., Booth, T. J., Stauber, T., Peres, N. M. R., and Geim, A. K., 2008, "Fine Structure Constant Defines Visual Transparency of Graphene," Science, **320**, p. 1308.

[68] Thongrattanasiri, S., Koppens, F. H. L., and García de Abajo, F. J., 2012, "Complete Optical Absorption in Periodically Patterned Graphene," Phys. Rev. Lett., **108**, p. 047401.

[69] Pop, E., Varshney, V., and Roy, A. K., 2012, "Thermal Properties of Graphene: Fundamentals and Applications," MRS Bulletin, **37**, pp. 1273-1281.

[70] Vakil, A., and Engheta, N., 2011, "Transformation Optics Using Graphene," Science, **332**, pp. 1291-1294.

[71] Xia, F., Mueller, T., Lin, Y.-m., Valdes-Garcia, A., and Avouris, P., 2009, "Ultrafast Graphene Photodetector," Nat. Nanotechnol., **4**, pp. 839-843.

[72] Liu, M., Yin, X., Ulin-Avila, E., Geng, B., Zentgraf, T., Ju, L., Wang, F., and Zhang, X., 2011, "A Graphene-Based Broadband Optical Modulator," Nature, **474**, pp. 64-67.

[73] Yao, Y., Kats, M. A., Shankar, R., Song, Y., Kong, J., Loncar, M., and Capasso, F., 2013, "Wide Wavelength Tuning of Optical Antennas on Graphene with Nanosecond Response Time," Nano Lett., **14**, pp. 214-219.

[74] Echtermeyer, T. J., Britnell, L., Jasnos, P. K., Lombardo, A., Gorbachev, R. V., Grigorenko, A. N., Geim, A. K., Ferrari, A. C., and Novoselov, K. S., 2011, "Strong Plasmonic Enhancement of Photovoltage in Graphene," Nat. Commun., **2**, p. 458.

[75] Miao, X., Tongay, S., Petterson, M. K., Berke, K., Rinzler, A. G., Appleton, B. R., and Hebard, A. F., 2012, "High Efficiency Graphene Solar Cells by Chemical Doping," Nano Lett., **12**, pp. 2745-2750.

[76] Messina, R., and Ben-Abdallah, P., 2013, "Graphene-Based Photovoltaic Cells for near-Field Thermal Energy Conversion," Sci. Rep., **3**, p. 1383.

[77] Wu, J., Agrawal, M., Becerril, H. A., Bao, Z., Liu, Z., Chen, Y., and Peumans, P., 2009, "Organic Light-Emitting Diodes on Solution-Processed Graphene Transparent Electrodes," ACS Nano, **4**, pp. 43-48.

[78] Mics, Z., Tielrooij, K.-J., Parvez, K., Jensen, S. A., Ivanov, I., Feng, X., Mullen, K., Bonn, M., and Turchinovich, D., 2015, "Thermodynamic Picture of Ultrafast Charge Transport in Graphene," Nat. Commun., **6**, p. 7655.

[79] Freitag, M., Chiu, H.-Y., Steiner, M., Perebeinos, V., and Avouris, P., 2010, "Thermal Infrared Emission from Biased Graphene," Nat. Nanotechnol., **5**, pp. 497-501.

[80] Brar, V. W., Jang, M. S., Sherrott, M., Kim, S., Lopez, J. J., Kim, L. B., Choi, M., and Atwater, H., 2014, "Hybrid Surface-Phonon-Plasmon Polariton Modes in Graphene/Monolayer H-Bn Heterostructures," Nano Lett., **14**, pp. 3876-3880.

[81] Dai, S., Ma, Q., Liu, M. K., Andersen, T., Fei, Z., Goldflam, M. D., Wagner, M., Watanabe, K., Taniguchi, T., Thiemens, M., Keilmann, F., Janssen, G. C. A. M., Zhu, S. E., Jarillo Herrero, P., Fogler, M. M., and Basov, D. N., 2015, "Graphene on Hexagonal Boron Nitride as a Tunable Hyperbolic Metamaterial," Nat. Nanotechnol., **10**, pp. 682-686.

[82] Kumar, A., Low, T., Fung, K. H., Avouris, P., and Fang, N. X., 2015, "Tunable Light–Matter Interaction and the Role of Hyperbolicity in Graphene–Hbn System," Nano Lett., **15**, pp. 3172-3180.

[83] Li, X., Zhu, J., and Wei, B., 2016, "Hybrid Nanostructures of Metal/Two-Dimensional Nanomaterials for Plasmon-Enhanced Applications," Chem. Soc. Rev., **45**, pp. 3145-3187.

[84] Basu, S., Zhang, Z. M., and Fu, C. J., 2009, "Review of near-Field Thermal Radiation and Its Application to Energy Conversion," Int. J. Energy Res., **33**, pp. 1203-1232.

[85] Otey, C. R., Lau, W. T., and Fan, S., 2010, "Thermal Rectification through Vacuum," Phys. Rev. Lett., **104**, p. 154301.

[86] Jones, A. C., and Raschke, M. B., 2012, "Thermal Infrared near-Field Spectroscopy," Nano Lett., **12**, pp. 1475-1481.

[87] De Wilde, Y., Formanek, F., Carminati, R., Gralak, B., Lemoine, P.-A., Joulain, K., Mulet, J.-P., Chen, Y., and Greffet, J.-J., 2006, "Thermal Radiation Scanning Tunnelling Microscopy," Nature, **444**, pp. 740-743.

[88] Yang, Y., Basu, S., and Wang, L. P., 2013, "Radiation-Based near-Field Thermal Rectification with Phase Transition Materials," Appl. Phys. Lett., **103**, p. 163101.

[89] Liu, X. L., Wang, L. P., and Zhang, Z. M., 2015, "Near-Field Thermal Radiation: Recent Progress and Outlook," Nanoscale Microscale Thermophys. Eng., **19**, pp. 98-126.

[90] Kim, K., Song, B., Fernández-Hurtado, V., Lee, W., Jeong, W., Cui, L., Thompson, D., Feist, J., Reid, M. T. H., García-Vidal, F. J., Cuevas, J. C., Meyhofer, E., and Reddy, P., 2015, "Radiative Heat Transfer in the Extreme near Field," Nature, **528**, pp. 387-391.

[91] Basu, S., Lee, B. J., and Zhang, Z. M., 2010, "Near-Field Radiation Calculated with an Improved Dielectric Function Model for Doped Silicon," J. Heat Transfer, **132**, p. 023302.

[92] Shen, S., Narayanaswamy, A., and Chen, G., 2009, "Surface Phonon Polaritons Mediated Energy Transfer between Nanoscale Gaps," Nano Lett., **9**, pp. 2909-2913.

[93] Svetovoy, V. B., van Zwol, P. J., and Chevrier, J., 2012, "Plasmon Enhanced near-Field Radiative Heat Transfer for Graphene Covered Dielectrics," Phys. Rev. B, **85**, p. 155418.

[94] Liu, B., Liu, Y., and Shen, S., 2014, "Thermal Plasmonic Interconnects in Graphene," Phys. Rev. B, **90**, p. 195411.

[95] Liu, X. L., Zhang, R. Z., and Zhang, Z. M., 2014, "Near-Perfect Photon Tunneling by Hybridizing Graphene Plasmons and Hyperbolic Modes," ACS Photonics, **1**, pp. 785-789.

[96] Modest, M. F., 2003, *Radiative Heat Transfer*, Academic Press, San Diego.

[97] Howell, J. R., Menguc, M. P., and Siegel, R., 2015, *Thermal Radiation Heat Transfer*, CRC Press, Florida.

[98] Xuan, Y., 2014, "An Overview of Micro/Nanoscaled Thermal Radiation and Its Applications," Phot. Nano. Fund. Appl., **12**, pp. 93-113.

[99] Barnes, W. L., Dereux, A., and Ebbesen, T. W., 2003, "Surface Plasmon Subwavelength Optics," Nature, **424**, pp. 824-830.

[100] Srituravanich, W., Fang, N., Sun, C., Luo, Q., and Zhang, X., 2004, "Plasmonic Nanolithography," Nano Lett., **4**, pp. 1085-1088.

[101] Homola, J., 2008, "Surface Plasmon Resonance Sensors for Detection of Chemical and Biological Species," Chem. Rev., **108**, pp. 462-493.

[102] Ozbay, E., 2006, "Plasmonics: Merging Photonics and Electronics at Nanoscale Dimensions," Science, **311**, pp. 189-193.

[103] Ghaemi, H. F., Thio, T., Grupp, D. E., Ebbesen, T. W., and Lezec, H. J., 1998, "Surface Plasmons Enhance Optical Transmission through Subwavelength Holes," Phys. Rev. B, **58**, pp. 6779-6782.

[104] Marquier, F., Laroche, M., Carminati, R., and Greffet, J. J., 2007, "Anisotropic Polarized Emission of a Doped Silicon Lamellar Grating," J. Heat Transfer, **129**, pp. 11-16.

[105] Chen, Y.-B., and Chen, C.-J., 2013, "Interaction between the Magnetic Polariton and Surface Plasmon Polariton," Opt. Commun., **297**, pp. 169-175.

[106] Maier, S. A., 2007, *Plasmonics: Fundamentals and Applications*, Springer Science & Business Media, Berlin, Germany.

[107] Mattiucci, N., D'Aguanno, G., Alu, A., Argyropoulos, C., Foreman, J. V., and Bloemer, M. J., 2012, "Taming the Thermal Emissivity of Metals: A Metamaterial Approach," Appl. Phys. Lett., **100**, pp. 201109-201104.

[108] Pardo, F., Bouchon, P., Haïdar, R., and Pelouard, J.-L., 2011, "Light Funneling Mechanism Explained by Magnetoelectric Interference," Phys. Rev. Lett., **107**, p. 093902.

[109] Wang, L. P., and Zhang, Z. M., 2012, "Measurement of Coherent Thermal Emission by Exciting Magnetic Polaritons in Subwavelength Grating Structures.," J. Heat Transfer, **135**, p. 091505.

[110] Linden, S., Enkrich, C., Wegener, M., Zhou, J., Koschny, T., and Soukoulis, C. M., 2004, "Magnetic Response of Metamaterials at 100 Terahertz," Science, **306**, pp. 1351-1353.

[111] Podolskiy, V. A., Sarychev, A. K., and Shalaev, V. M., 2002, "Plasmon Modes in Metal Nanowires and Left-Handed Materials," Journal of Nonlinear Optical Physics & Materials, **11**, pp. 65-74.

[112] Zhang, S., Fan, W., Panoiu, N. C., Malloy, K. J., Osgood, R. M., and Brueck, S. R. J., 2005, "Experimental Demonstration of near-Infrared Negative-Index Metamaterials," Phys. Rev. Lett., **95**, p. 137404.

[113] Solymar, L., and Shamonina, E., 2009, *Waves in Metamaterials*, Oxford University Press, Oxford.

[114] Engheta, N., 2007, "Circuits with Light at Nanoscales: Optical Nanocircuits Inspired by Metamaterials," Science, **317**, pp. 1698-1702.

[115] Zhou, J., Economon, E. N., Koschny, T., and Soukoulis, C. M., 2006, "Unifying Approach to Left-Handed Material Design," Opt. Lett., **31**, pp. 3620-3622.

[116] Falkovsky, L. A., 2008, "Optical Properties of Graphene," J. Phys. Conf. Ser., **129**, p. 012004.

[117] García de Abajo, F. J., 2014, "Graphene Plasmonics: Challenges and Opportunities," ACS Photonics, **1**, pp. 135-152.

[118] Dean, C. R., Young, A. F., Meric, I., Lee, C., Wang, L., Sorgenfrei, S., Watanabe, K., Taniguchi, T., Kim, P., Shepard, K. L., and Hone, J., 2010, "Boron Nitride Substrates for High-Quality Graphene Electronics," Nat. Nanotechnol., **5**, pp. 722-726.

[119] Yan, Z., Chen, L., Yoon, M., and Kumar, S., 2016, "Phonon Transport at the Interfaces of Vertically Stacked Graphene and Hexagonal Boron Nitride Heterostructures," Nanoscale, **8**, pp. 4037-4046.

[120] Caldwell, J. D., Kretinin, A. V., Chen, Y., Giannini, V., Fogler, M. M., Francescato, Y., Ellis, C. T., Tischler, J. G., Woods, C. R., Giles, A. J., Hong, M., Watanabe, K., Taniguchi, T., Maier, S. A., and Novoselov, K. S., 2014, "Sub-Diffractional Volume-Confined Polaritons in the Natural Hyperbolic Material Hexagonal Boron Nitride," Nat. Commun., **5**, p. 5221.

[121] Dai, S., Ma, Q., Andersen, T., McLeod, A. S., Fei, Z., Liu, M. K., Wagner, M., Watanabe, K., Taniguchi, T., Thiemens, M., Keilmann, F., Jarillo-Herrero, P., Fogler, M. M., and Basov, D. N., 2015, "Subdiffractional Focusing and Guiding of Polaritonic Rays in a Natural Hyperbolic Material," Nat. Commun., **6**, p. 6963.

[122] Li, P., Lewin, M., Kretinin, A. V., Caldwell, J. D., Novoselov, K. S., Taniguchi, T., Watanabe, K., Gaussmann, F., and Taubner, T., 2015, "Hyperbolic Phonon-Polaritons in Boron Nitride for near-Field Optical Imaging and Focusing," Nat. Commun., **6**, p. 7507.

[123] Jacob, Z., Smolyaninov, I. I., and Narimanov, E. E., 2012, "Broadband Purcell Effect: Radiative Decay Engineering with Metamaterials," Appl. Phys. Lett., **100**, p. 181105.

[124] Nefedov, I. S., Valagiannopoulos, C. A., Hashemi, S. M., and Nefedov, E. I., 2013, "Total Absorption in Asymmetric Hyperbolic Media," Sci. Rep., **3**, p. 2662.

[125] Biehs, S. A., Tschikin, M., and Ben-Abdallah, P., 2012, "Hyperbolic Metamaterials as an Analog of a Blackbody in the near Field," Phys. Rev. Lett., **109**, p. 104301.

[126] Jacob, Z., 2014, "Nanophotonics: Hyperbolic Phonon-Polaritons," Nat. Mater., **13**, pp. 1081-1083.

[127] Liu, X. L., Zhang, R. Z., and Zhang, Z. M., 2014, "Near-Field Radiative Heat Transfer with Doped-Silicon Nanostructured Metamaterials," Int. J. Heat Mass Transfer, **73**, pp. 389-398.

[128] Kane, Y., 1966, "Numerical Solution of Initial Boundary Value Problems Involving Maxwell's Equations in Isotropic Media," IEEE Transactions on Antennas and Propagation, **14**, pp. 302-307.

[129] Taflove, A., and Hagness, S. C., 2005, *Computational Electrodynamics: The Finite Difference Time Domain Method*, Artech House, Boston.

[130] Davidson, D. B., 2010, *Computational Electromagnetics for Rf and Microwave Engineering*, Cambridge University Press, United Kingdom.

[131] Moharam, M. G., and Gaylord, T. K., 1981, "Rigorous Coupled-Wave Analysis of Planar-Grating Diffraction," J. Opt. Soc. Am., **71**, pp. 811-818.

[132] Oskooi, A. F., Roundy, D., Ibanescu, M., Bermel, P., Joannopoulos, J. D., and Johnson, S. G., 2010, "Meep: A Flexible Free-Software Package for Electromagnetic Simulations by the Fdtd Method," Comput. Phys. Commun., **181**, pp. 687-702.

[133] Liu, V., and Fan, S., 2012, "S4 : A Free Electromagnetic Solver for Layered Periodic Structures," Comput. Phys. Commun., **183**, pp. 2233-2244.

[134] http://zhang-nano.gatech.edu/.

[135] Glytsis, E. N., and Gaylord, T. K., 1990, "Three-Dimensional (Vector) Rigorous Coupled-Wave Analysis of Anisotropic Grating Diffraction," J. Opt. Soc. Am. A, **7**, pp. 1399-1420.

[136] Li, L., 1996, "Use of Fourier Series in the Analysis of Discontinuous Periodic Structures," J. Opt. Soc. Am. A, **13**, pp. 1870-1876.

[137] Li, L., 1998, "Reformulation of the Fourier Modal Method for Surface-Relief Gratings Made with Anisotropic Materials," J. Mod. Opt., **45**, pp. 1313-1334.

[138] Popov, E., and Nevière, M., 2001, "Maxwell Equations in Fourier Space: Fast-Converging Formulation for Diffraction by Arbitrary Shaped, Periodic, Anisotropic Media," J. Opt. Soc. Am. A, **18**, pp. 2886-2894.

[139] Lin, C.-H., Leung, K. M., and Tamir, T., 2002, "Modal Transmission-Line Theory of Three-Dimensional Periodic Structures with Arbitrary Lattice Configurations," J. Opt. Soc. Am. A, **19**, pp. 2005-2017.

[140] Li, L., 2003, "Fourier Modal Method for Crossed Anisotropic Gratings with Arbitrary Permittivity and Permeability Tensors," J. Opt. A: Pure Appl. Opt., **5**, p. 345.

[141] Zhang, Z. M., and Wang, L. P., 2013, "Measurements and Modeling of the Spectral and Directional Radiative Properties of Micro/Nanostructured Materials," Int. J. Thermophys., **34**, pp. 2209-2242.

[142] Chen, Y.-B., and Tan, K. H., 2010, "The Profile Optimization of Periodic Nano-Structures for Wavelength-Selective Thermophotovoltaic Emitters," Int. J. Heat Mass Transfer, **53**, pp. 5542-5551.

[143] Bräuer, R., and Bryngdahl, O., 1993, "Electromagnetic Diffraction Analysis of Two-Dimensional Gratings," Opt. Commun., **100**, pp. 1-5.

[144] Zhao, B., Wang, L., Shuai, Y., and Zhang, Z. M., 2013, "Thermophotovoltaic Emitters Based on a Two-Dimensional Grating/Thin-Film Nanostructure," Int. J. Heat Mass Transfer, **67**, pp. 637-645.

[145] Yeh, P., 1979, "Electromagnetic Propagation in Birefringent Layered Media," J. Opt. Soc. Am., **69**, pp. 742-756.

[146] Moharam, M. G., Grann, E. B., Pommet, D. A., and Gaylord, T. K., 1995, "Formulation for Stable and Efficient Implementation of the Rigorous Coupled-Wave Analysis of Binary Gratings," J. Opt. Soc. Am. A, **12**, pp. 1068-1076.

[147] Zhao, J. M., and Zhang, Z. M., 2015, "Electromagnetic Energy Storage and Power Dissipation in Nanostructures," J. Quant. Spectrosc. Radiat. Transfer, **151**, pp. 49-57.

[148] Zhao, B., Zhao, J. M., and Zhang, Z. M., 2014, "Enhancement of near-Infrared Absorption in Graphene with Metal Gratings," Appl. Phys. Lett., **105**, p. 031905.

[149] Zhao, B., Zhao, J. M., and Zhang, Z. M., 2015, "Resonance Enhanced Absorption in a Graphene Monolayer Using Deep Metal Gratings," J. Opt. Soc. Am. B, **32**, pp. 1176-1185.

[150] Palik, E. D., 1985, *Handbook of Optical Constants of Solids*, Academic Press, San Diego, CA.

[151] Coutts, T. J., 1999, "A Review of Progress in Thermophotovoltaic Generation of Electricity," Renewable Sustainable Energy Rev., **3**, pp. 77-184.

[152] Teofilo, V. L., Choong, P., Chang, J., Tseng, Y. L., and Ermer, S., 2008, "Thermophotovoltaic Energy Conversion for Space," J. Phys. Chem. C, **112**, pp. 7841-7845.

[153] Park, K., Basu, S., King, W. P., and Zhang, Z. M., 2008, "Performance Analysis of near-Field Thermophotovoltaic Devices Considering Absorption Distribution," J. Quant. Spectrosc. Radiat. Transfer, **109**, pp. 305-316.

[154] Francoeur, M., Vaillon, R., and Mengüç, M. P., 2011, "Thermal Impacts on the Performance of Nanoscale-Gap Thermophotovoltaic Power Generators," IEEE Trans. Energy Convers., **26**, pp. 686-698.

[155] Mao, L., and Ye, H., 2010, "New Development of One-Dimensional Si/Sio2 Photonic Crystals Filter for Thermophotovoltaic Applications," Renew. Energ., **35**, pp. 249-256.

[156] Kristensen, R. T., Beausang, J. F., and DePoy, D. M., 2004, "Frequency Selective Surfaces as near-Infrared Electromagnetic Filters for Thermophotovoltaic Spectral Control," J. Appl. Phys., **95**, pp. 4845-4851.

[157] Bauer, T., Forbes, I., Penlington, R., and Pearsall, N., 2005, "Heat Transfer Modelling in Thermophotovoltaic Cavities Using Glass Media," Sol. Energy Mater. Sol. Cells, **88**, pp. 257-268.

[158] Bermel, P., Ghebrebrhan, M., Chan, W., Yeng, Y. X., Araghchini, M., Hamam, R., Marton, C. H., Jensen, K. F., Soljacic, M., Joannopoulos, J. D., Johnson, S. G., and Celanovic, I., 2010, "Design and Global Optimization of High-Efficiency Thermophotovoltaic Systems," Opt. Express, **18**, pp. A314-A334.

[159] Nguyen-Huu, N., Chen, Y.-B., and Lo, Y.-L., 2012, "Development of a Polarization-Insensitive Thermophotovoltaic Emitter with a Binary Grating," Opt. Express, **20**, pp. 5882-5890.

[160] Chen, Y.-B., and Zhang, Z. M., 2007, "Design of Tungsten Complex Gratings for Thermophotovoltaic Radiators," Opt. Commun., **269**, pp. 411-417.

[161] Sergeant, N. P., Agrawal, M., and Peumans, P., 2010, "High Performance Solar-Selective Absorbers Using Coated Sub-Wavelength Gratings," Opt. Express, **18**, pp. 5525-5540.

[162] Nagpal, P., Han, S. E., Stein, A., and Norris, D. J., 2008, "Efficient Low-Temperature Thermophotovoltaic Emitters from Metallic Photonic Crystals," Nano Lett., **8**, pp. 3238-3243.

[163] Narayanaswamy, A., and Chen, G., 2004, "Thermal Emission Control with One-Dimensional Metallodielectric Photonic Crystals," Phys. Rev. B, **70**, p. 125101.

[164] Lee, J. H., Kim, Y. S., Constant, K., and Ho, K. M., 2007, "Woodpile Metallic Photonic Crystals Fabricated by Using Soft Lithography for Tailored Thermal Emission," Adv. Mater., **19**, pp. 791-794.

[165] Heinzel, A., Boerner, V., Gombert, A., Bläsi, B., Wittwer, V., and Luther, J., 2000, "Radiation Filters and Emitters for the Nir Based on Periodically Structured Metal Surfaces," J. Mod. Opt., **47**, pp. 2399-2419.

[166] Pralle, M. U., Moelders, N., McNeal, M. P., Puscasu, I., Greenwald, A. C., Daly, J. T., Johnson, E. A., George, T., Choi, D. S., El-Kady, I., and Biswas, R., 2002, "Photonic Crystal Enhanced Narrow-Band Infrared Emitters," Appl. Phys. Lett., **81**, pp. 4685-4687.

[167] Sai, H., and Yugami, H., 2004, "Thermophotovoltaic Generation with Selective Radiators Based on Tungsten Surface Gratings," Appl. Phys. Lett., **85**, pp. 3399-3401.

[168] Sai, H., Kanamori, Y., and Yugami, H., 2003, "High-Temperature Resistive Surface Grating for Spectral Control of Thermal Radiation," Appl. Phys. Lett., **82**, pp. 1685-1687.

[169] Sai, H., Kanamori, Y., and Yugami, H., 2005, "Tuning of the Thermal Radiation Spectrum in the near-Infrared Region by Metallic Surface Microstructures," J. Micromech. Microeng., **15**, p. S243.

[170] Bouchon, P., Koechlin, C., Pardo, F., Haïdar, R., and Pelouard, J.-L., 2012, "Wideband Omnidirectional Infrared Absorber with a Patchwork of Plasmonic Nanoantennas," Opt. Lett., **37**, pp. 1038-1040.

[171] Wang, C.-M., Chang, Y.-C., Tsai, M.-W., Ye, Y.-H., Chen, C.-Y., Jiang, Y.-W., Chang, Y.-T., Lee, S.-C., and Tsai, D. P., 2007, "Reflection and Emission Properties of an Infraredemitter," Opt. Express, **15**, pp. 14673-14678.

[172] Cui, Y., Xu, J., Fung, K. H., Jin, Y., Kumar, A., He, S., and Fang, N. X., 2011, "A Thin Film Broadband Absorber Based on Multi-Sized Nanoantennas," Appl. Phys. Lett., **99**, p. 253101.

[173] Hendrickson, J., Guo, J., Zhang, B., Buchwald, W., and Soref, R., 2012, "Wideband Perfect Light Absorber at Midwave Infrared Using Multiplexed Metal Structures," Opt. Lett., **37**, pp. 371-373.

[174] Lévêque, G., and Martin, O. J. F., 2006, "Tunable Composite Nanoparticle for Plasmonics," Opt. Lett., **31**, pp. 2750-2752.

[175] Liu, X., Tyler, T., Starr, T., Starr, A. F., Jokerst, N. M., and Padilla, W. J., 2011, "Taming the Blackbody with Infrared Metamaterials as Selective Thermal Emitters," Phys. Rev. Lett., **107**, p. 045901.

[176] Liu, N., Mesch, M., Weiss, T., Hentschel, M., and Giessen, H., 2010, "Infrared Perfect Absorber and Its Application as Plasmonic Sensor," Nano Lett., **10**, pp. 2342-2348.

[177] Puscasu, I., and Schaich, W. L., 2008, "Narrow-Band, Tunable Infrared Emission from Arrays of Microstrip Patches," Appl. Phys. Lett., **92**, pp. 233102-233103.

[178] Wang, J., Fan, C., Ding, P., He, J., Cheng, Y., Hu, W., Cai, G., Liang, E., and Xue, Q., 2012, "Tunable Broad-Band Perfect Absorber by Exciting of Multiple Plasmon Resonances at Optical Frequency," Opt. Express, **20**, pp. 14871-14878.

[179] Liu, H., Li, T., Wang, Q. J., Zhu, Z. H., Wang, S. M., Li, J. Q., Zhu, S. N., Zhu, Y. Y., and Zhang, X., 2009, "Extraordinary Optical Transmission Induced by Excitation of a Magnetic Plasmon Propagation Mode in a Diatomic Chain of Slit-Hole Resonators," Phys. Rev. B, **79**, p. 024304.

[180] Tsai, M.-W., Chuang, T.-H., Meng, C.-Y., Chang, Y.-T., and Lee, S.-C., 2006, "High Performance Midinfrared Narrow-Band Plasmonic Thermal Emitter," Appl. Phys. Lett., **89**, p. 173116.

[181] Ye, Y.-H., Jiang, Y.-W., Tsai, M.-W., Chang, Y.-T., Chen, C.-Y., Tzuang, D.-C., Wu, Y.-T., and Lee, S.-C., 2008, "Localized Surface Plasmon Polaritons in Ag/Sio_2/Ag Plasmonic Thermal Emitter," Appl. Phys. Lett., **93**, p. 033113.

[182] Jiang, Y.-W., Wu, Y.-T., Tsai, M.-W., Chang, P.-E., Tzuang, D.-C., Ye, Y.-H., and Lee, S.-C., 2009, "Characteristics of a Waveguide Mode in a Trilayer Ag/Sio2/Au Plasmonic Thermal Emitter," Opt. Lett., **34**, pp. 3089-3091.

[183] Mauk, M. G., and Andreev, V. M., 2003, "Gasb-Related Materials for Tpv Cells," Semicond. Sci. Technol., **18**, p. S191.

[184] Pillai, S., Catchpole, K. R., Trupke, T., and Green, M. A., 2007, "Surface Plasmon Enhanced Silicon Solar Cells," J. Appl. Phys., **101**, pp. 093105-093108.

[185] Yang, L., Xuan, Y., Han, Y., and Tan, J., 2012, "Investigation on the Performance Enhancement of Silicon Solar Cells with an Assembly Grating Structure," Energy Convers. Manage., **54**, pp. 30-37.

[186] Hajimirza, S., El Hitti, G., Heltzel, A., and Howell, J., 2012, "Specification of Micro-Nanoscale Radiative Patterns Using Inverse Analysis for Increasing Solar Panel Efficiency," J. Heat Transfer, **134**, p. 102702.

[187] Hesketh, P. J., Zemel, J. N., and Gebhart, B., 1988, "Polarized Spectral Emittance from Periodic Micromachined Surfaces. I. Doped Silicon: The Normal Direction," Phys. Rev. B, **37**, pp. 10795-10802.

[188] Maruyama, S., Kashiwa, T., Yugami, H., and Esashi, M., 2001, "Thermal Radiation from Two-Dimensionally Confined Modes in Microcavities," Appl. Phys. Lett., **79**, pp. 1393-1395.

[189] Kusunoki, F., Kohama, T., Hiroshima, T., Fukumoto, S., Takahara, J., and Kobayashi, T., 2004, "Narrow-Band Thermal Radiation with Low Directivity by Resonant Modes inside Tungsten Microcavities," Jpn. J. Appl. Phys., **43**, p. 5253.

[190] Huang, J., Xuan, Y., and Li, Q., 2011, "Narrow-Band Spectral Features of Structured Silver Surface with Rectangular Resonant Cavities," J. Quant. Spectrosc. Radiat. Transfer, **112**, pp. 839-846.

[191] Gordon, R., and Brolo, A., 2005, "Increased Cut-Off Wavelength for a Subwavelength Hole in a Real Metal," Opt. Express, **13**, pp. 1933-1938.

[192] Suckling, J. R., Hibbins, A. P., Lockyear, M. J., Preist, T. W., Sambles, J. R., and Lawrence, C. R., 2004, "Finite Conductance Governs the Resonance Transmission of Thin Metal Slits at Microwave Frequencies," Phys. Rev. Lett., **92**, p. 147401.

[193] Dahan, N., Niv, A., Biener, G., Gorodetski, Y., Kleiner, V., and Hasman, E., 2007, "Enhanced Coherency of Thermal Emission: Beyond the Limitation Imposed by Delocalized Surface Waves," Phys. Rev. B, **76**, p. 045427.

[194] Sobnack, M. B., Tan, W. C., Wanstall, N. P., Preist, T. W., and Sambles, J. R., 1998, "Stationary Surface Plasmons on a Zero-Order Metal Grating," Phys. Rev. Lett., **80**, pp. 5667-5670.

[195] Wanstall, N. P., Preist, T. W., Tan, W. C., Sobnack, M. B., and Sambles, J. R., 1998, "Standing-Wave Surface-Plasmon Resonances with Overhanging Zero-Order Metal Gratings," J. Opt. Soc. Am. A, **15**, pp. 2869-2876.

[196] Nishiyama, H., and Nakamura, M., 1994, "Form and Capacitance of Parallel-Plate Capacitors," Components, Packaging, and Manufacturing Technology, Part A, IEEE Transactions on, **17**, pp. 477-484.

[197] Rinnerbauer, V., Ndao, S., Yeng, Y. X., Senkevich, J. J., Jensen, K. F., Joannopoulos, J. D., SoljaCic, M., Celanovic, I., and Geil, R. D., 2013, "Large-Area Fabrication of High Aspect Ratio Tantalum Photonic Crystals for High-Temperature Selective Emitters," J. Vac. Sci. Technol. B, **31**, pp. 011802-011807.

[198] Guo, L. J., 2007, "Nanoimprint Lithography: Methods and Material Requirements," Adv. Mater., **19**, pp. 495-513.

[199] Basu, S., Lee, B. J., and Zhang, Z. M., 2010, "Infrared Radiative Properties of Heavily Doped Silicon at Room Temperature," J. Heat Transfer, **132**, p. 023301.

[200] Chen, C.-J., Chen, J.-S., and Chen, Y.-B., 2011, "Optical Responses from Lossy Metallic Slit Arrays under the Excitation of a Magnetic Polariton," J. Opt. Soc. Am. B, **28**, pp. 1798-1806.

[201] Pala, R. A., Liu, J. S. Q., Barnard, E. S., Askarov, D., Garnett, E. C., Fan, S., and Brongersma, M. L., 2013, "Optimization of Non-Periodic Plasmonic Light-Trapping Layers for Thin-Film Solar Cells," Nat. Commun., **4**.

[202] Tok, R. U., and Şendur, K., 2013, "Engineering the Broadband Spectrum of Close-Packed Plasmonic Honeycomb Array Surfaces," J. Quant. Spectrosc. Radiat. Transfer, **120**, pp. 70-80.

[203] Cheng, Q., Li, P., Lu, J., Yu, X., and Zhou, H., "Silicon Complex Grating with Different Groove Depths as an Absorber for Solar Cells," J. Quant. Spectrosc. Radiat. Transfer, **132**, pp. 70-79.

[204] Borisov, A. G., García de Abajo, F. J., and Shabanov, S. V., 2005, "Role of Electromagnetic Trapped Modes in Extraordinary Transmission in Nanostructured Materials," Phys. Rev. B, **71**, p. 075408.

[205] Lu, Y., Cho, M. H., Lee, Y., and Rhee, J. Y., 2008, "Polarization-Independent Extraordinary Optical Transmission in One-Dimensional Metallic Gratings with Broad Slits," Appl. Phys. Lett., **93**, pp. 061102-061103.

[206] Selcuk, S., Woo, K., Tanner, D. B., Hebard, A. F., Borisov, A. G., and Shabanov, S. V., 2006, "Trapped Electromagnetic Modes and Scaling in the Transmittance of Perforated Metal Films," Phys. Rev. Lett., **97**, p. 067403.

[207] Grant, J., Ma, Y., Saha, S., Khalid, A., and Cumming, D. R. S., 2011, "Polarization Insensitive, Broadband Terahertz Metamaterial Absorber," Opt. Lett., **36**, pp. 3476-3478.

[208] Canfield, B. K., Kujala, S., Jefimovs, K., Vallius, T., Turunen, J., and Kauranen, M., 2005, "Polarization Effects in the Linear and Nonlinear Optical Responses of Gold Nanoparticle Arrays," J. Opt. A: Pure Appl. Opt., **7**, p. S110.

[209] Tong, P., Zhang, S., Cui, Y., Lin, Y., Ji, T., and Hao, Y., "Thin Film Dual Band Metamaterial Absorber Based on Gold Triangular Patches," Proc. Asia Communications and Photonics Conference, Optical Society of America, p. AF2B.50.

[210] Tok, R. U., Ow-Yang, C., and Şendur, K., 2011, "Unidirectional Broadband Radiation of Honeycomb Plasmonic Antenna Array with Broken Symmetry," Opt. Express, **19**, pp. 22731-22742.

[211] Wang, H., and Wang, L., 2013, "Perfect Selective Metamaterial Solar Absorbers," Opt. Express, **21**, pp. A1078-A1093.

[212] Bossard, J. A., and Werner, D. H., 2013, "Metamaterials with Angle Selective Emissivity in the near-Infrared," Opt. Express, **21**, pp. 5215-5225.

[213] Chen, J., Wang, P., Chen, C., Lu, Y., Ming, H., and Zhan, Q., 2011, "Plasmonic Eit-Like Switching in Bright-Dark-Bright Plasmon Resonators," Opt. Express, **19**, pp. 5970-5978.

[214] Cao, J., Liu, H., Li, T., Wang, S., Li, T., Zhu, S., and Zhang, X., 2009, "Steering Polarization of Infrared Light through Hybridization Effect in a Tri-Rod Structure," J. Opt. Soc. Am. B, **26**, pp. B96-B101.

[215] Cao, J. X., Liu, H., Li, T., Wang, S. M., Dong, Z. G., and Zhu, S. N., 2010, "High Sensing Properties of Magnetic Plasmon Resonance in the Double-Rod and Tri-Rod Structures," Appl. Phys. Lett., **97**, p. 071905.

[216] Tok, R. U., and Şendur, K., 2013, "Absorption Efficiency Enhancement in Inorganic and Organic Thin Film Solar Cells Via Plasmonic Honeycomb Nanoantenna Arrays," Opt. Lett., **38**, pp. 3119-3122.

[217] Liu, X., Starr, T., Starr, A. F., and Padilla, W. J., 2010, "Infrared Spatial and Frequency Selective Metamaterial with near-Unity Absorbance," Phys. Rev. Lett., **104**, p. 207403.

[218] Hao, J., Wang, J., Liu, X., Padilla, W. J., Zhou, L., and Qiu, M., 2010, "High Performance Optical Absorber Based on a Plasmonic Metamaterial," Appl. Phys. Lett., **96**, p. 251104.

[219] Zhang, B., Zhao, Y., Hao, Q., Kiraly, B., Khoo, I.-C., Chen, S., and Huang, T. J., 2011, "Polarization-Independent Dual-Band Infrared Perfect Absorber Based on a Metal-Dielectric-Metal Elliptical Nanodisk Array," Opt. Express, **19**, pp. 15221-15228.

[220] Chen, K., Adato, R., and Altug, H., 2012, "Dual-Band Perfect Absorber for Multispectral Plasmon-Enhanced Infrared Spectroscopy," ACS Nano, **6**, pp. 7998-8006.

[221] Liu, N., Liu, H., Zhu, S., and Giessen, H., 2009, "Stereometamaterials," Nat. Photonics, **3**, pp. 157-162.

[222] Qiu, J., Hsu, P. f., and Liu, L. H., 2014, "Infrared Radiative Properties of Two-Dimensional Square Optical Black Holes with Materials of Insulators and Semiconductors," J. Quant. Spectrosc. Radiat. Transfer, **132**, pp. 99-108.

[223] Sung, J., Sukharev, M., Hicks, E. M., Van Duyne, R. P., Seideman, T., and Spears, K. G., 2008, "Nanoparticle Spectroscopy: Birefringence in Two-Dimensional Arrays of L-Shaped Silver Nanoparticles," J. Phys. Chem. C, **112**, pp. 3252-3260.

[224] Chen, J., and Hu, J., 2014, "Strong Coupling between Localized and Propagating Surface Plasmon Modes in a Noncentrosymmetric Metallic Photonic Slab," J. Opt. Soc. Am. B, **31**, pp. 1600-1606.

[225] Nanfang, Y., Genevet, P., Aieta, F., Kats, M. A., Blanchard, R., Aoust, G., Tetienne, J. P., Gaburro, Z., and Capasso, F., 2013, "Flat Optics: Controlling Wavefronts with Optical Antenna Metasurfaces," Selected Topics in Quantum Electronics, IEEE Journal of, **19**, pp. 4700423-4700423.

[226] Aydin, K., Ferry, V. E., Briggs, R. M., and Atwater, H. A., 2011, "Broadband Polarization-Independent Resonant Light Absorption Using Ultrathin Plasmonic Super Absorbers," Nat. Commun., **2**, p. 517.

[227] Husu, H., Siikanen, R., Mäkitalo, J., Lehtolahti, J., Laukkanen, J., Kuittinen, M., and Kauranen, M., 2012, "Metamaterials with Tailored Nonlinear Optical Response," Nano Lett., **12**, pp. 673-677.

[228] Montelongo, Y., Tenorio-Pearl, J. O., Milne, W. I., and Wilkinson, T. D., 2013, "Polarization Switchable Diffraction Based on Subwavelength Plasmonic Nanoantennas," Nano Lett., **14**, pp. 294-298.

[229] Syrenova, S., Wadell, C., and Langhammer, C., 2014, "Shrinking-Hole Colloidal Lithography: Self-Aligned Nanofabrication of Complex Plasmonic Nanoantennas," Nano Lett., **14**, pp. 2655-2663.

[230] Menzel, C., Helgert, C., Rockstuhl, C., Kley, E. B., Tünnermann, A., Pertsch, T., and Lederer, F., 2010, "Asymmetric Transmission of Linearly Polarized Light at Optical Metamaterials," Phys. Rev. Lett., **104**, p. 253902.

[231] Pfeiffer, C., Zhang, C., Ray, V., Guo, L. J., and Grbic, A., 2014, "High Performance Bianisotropic Metasurfaces: Asymmetric Transmission of Light," Phys. Rev. Lett., **113**, p. 023902.

[232] Luk'yanchuk, B., Zheludev, N. I., Maier, S. A., Halas, N. J., Nordlander, P., Giessen, H., and Chong, C. T., 2010, "The Fano Resonance in Plasmonic Nanostructures and Metamaterials," Nat. Mater., **9**, pp. 707-715.

[233] Howell, J. R., Siegel, R., and Menguc, M. P., 2010, *Thermal Radiation Heat Transfer*, Taylor & Francis, New York.

[234] Husu, H., Mäkitalo, J., Laukkanen, J., Kuittinen, M., and Kauranen, M., 2010, "Particle Plasmon Resonances in L-Shaped Gold Nanoparticles," Opt. Express, **18**, pp. 16601-16606.

[235] Capolino, F., 2009, *Applications of Metamaterials*, CRC Press, Florida.

[236] Sakurai, A., Zhao, B., and Zhang, Z. M., 2015, "Effect of Polarization on Dual-Band Infrared Metamaterial Emitters or Absorbers," J. Quant. Spectrosc. Radiat. Transfer, **158**, pp. 111-118.

[237] Schubert, M., 1996, "Polarization-Dependent Optical Parameters of Arbitrarily Anisotropic Homogeneous Layered Systems," Phys. Rev. B, **53**, pp. 4265-4274.

[238] Yariv, A., and Yeh, P., 2002, *Optical Waves in Crystals: Propagation and Control of Laser Radiation*, Wiley-Interscience, New York.

[239] Born, M., and Wolf, E., 1999, *Principles of Optics*, Cambridge University Press, Cambridge.

[240] Azzam, R. M. A., and Bashara, N. M., 1977, *Ellipsometry and Polarized Light*, North Holland, Amsterdam.

[241] Engel, M., Steiner, M., Lombardo, A., Ferrari, A. C., Löhneysen, H. v., Avouris, P., and Krupke, R., 2012, "Light–Matter Interaction in a Microcavity-Controlled Graphene Transistor," Nat. Commun., **3**, p. 906.

[242] Xia, F., Mueller, T., Lin, Y.-m., Valdes-Garcia, A., and Avouris, P., 2009, "Ultrafast Graphene Photodetector," Nat. Nanotechnol., **4**, pp. 839-843.

[243] Mueller, T., Xia, F., and Avouris, P., 2010, "Graphene Photodetectors for High-Speed Optical Communications," Nat. Photonics, **4**, pp. 297-301.

[244] Furchi, M., Urich, A., Pospischil, A., Lilley, G., Unterrainer, K., Detz, H., Klang, P., Andrews, A. M., Schrenk, W., Strasser, G., and Mueller, T., 2012, "Microcavity-Integrated Graphene Photodetector," Nano Lett., **12**, pp. 2773-2777.

[245] Fang, Z., Liu, Z., Wang, Y., Ajayan, P. M., Nordlander, P., and Halas, N. J., 2012, "Graphene-Antenna Sandwich Photodetector," Nano Lett., **12**, pp. 3808-3813.

[246] Wang, F., Zhang, Y., Tian, C., Girit, C., Zettl, A., Crommie, M., and Shen, Y. R., 2008, "Gate-Variable Optical Transitions in Graphene," Science, **320**, pp. 206-209.

[247] Basov, D. N., Fogler, M. M., Lanzara, A., Wang, F., and Zhang, Y., 2014, "Colloquium: Graphene Spectroscopy," Rev. Mod. Phys., **86**, pp. 959-994.

[248] Fang, Z., Wang, Y., Schlather, A. E., Liu, Z., Ajayan, P. M., García de Abajo, F. J., Nordlander, P., Zhu, X., and Halas, N. J., 2013, "Active Tunable Absorption Enhancement with Graphene Nanodisk Arrays," Nano Lett., **14**, pp. 299-304.

[249] Popov, V. V., Bagaeva, T. Y., Otsuji, T., and Ryzhii, V., 2010, "Oblique Terahertz Plasmons in Graphene Nanoribbon Arrays," Phys. Rev. B, **81**, p. 073404.

[250] Nikitin, A. Y., Guinea, F., Garcia-Vidal, F. J., and Martin-Moreno, L., 2012, "Surface Plasmon Enhanced Absorption and Suppressed Transmission in Periodic Arrays of Graphene Ribbons," Phys. Rev. B, **85**, p. 081405.

[251] Ju, L., Geng, B., Horng, J., Girit, C., Martin, M., Hao, Z., Bechtel, H. A., Liang, X., Zettl, A., Shen, Y. R., and Wang, F., 2011, "Graphene Plasmonics for Tunable Terahertz Metamaterials," Nat. Nanotechnol., **6**, pp. 630-634.

[252] Jang, M. S., Brar, V. W., Sherrott, M. C., Lopez, J. J., Kim, L., Kim, S., Choi, M., and Atwater, H. A., 2014, "Tunable Large Resonant Absorption in a Midinfrared Graphene Salisbury Screen," Phys. Rev. B, **90**, p. 165409.

[253] Fallahi, A., and Perruisseau-Carrier, J., 2012, "Design of Tunable Biperiodic Graphene Metasurfaces," Phys. Rev. B, **86**, p. 195408.

[254] Andryieuski, A., and Lavrinenko, A. V., 2013, "Graphene Metamaterials Based Tunable Terahertz Absorber: Effective Surface Conductivity Approach," Opt. Express, **21**, pp. 9144-9155.

[255] Jiang-Tao, L., Nian-Hua, L., Li, W., Xin-Hua, D., and Fu-Hai, S., 2013, "Gate-Tunable Nearly Total Absorption in Graphene with Resonant Metal Back Reflector," EPL (Europhysics Letters), **104**, p. 57002.

[256] Yuan, H., Yang, H., Liu, P., Jiang, X., and Sun, X., 2014, "Mode Manipulation and near-Thz Absorptions in Binary Grating-Graphene Layer Structures," Nanoscale Res. Lett., **9**, p. 90.

[257] Slipchenko, T. M., Nesterov, M. L., Martin-Moreno, L., and Nikitin, A. Y., 2013, "Analytical Solution for the Diffraction of an Electromagnetic Wave by a Graphene Grating," J. Opt., **15**, p. 114008.

[258] Xu, B.-z., Gu, C.-q., Li, Z., and Niu, Z.-y., 2013, "A Novel Structure for Tunable Terahertz Absorber Based on Graphene," Opt. Express, **21**, pp. 23803-23811.

[259] Zhang, Y., Feng, Y., Zhu, B., Zhao, J., and Jiang, T., 2014, "Graphene Based Tunable Metamaterial Absorber and Polarization Modulation in Terahertz Frequency," Opt. Express, **22**, pp. 22743-22752.

[260] Ying, X., Pu, Y., Li, Z., Liu, Z., and Jiang, Y., 2014, "Absorption Enhancement of Graphene Salisbury Screen in the Mid-Infrared Regime," J. Opt., **44**, pp. 1-9.

[261] Alaee, R., Farhat, M., Rockstuhl, C., and Lederer, F., 2012, "A Perfect Absorber Made of a Graphene Micro-Ribbon Metamaterial," Opt. Express, **20**, pp. 28017-28024.

[262] Peres, N. M. R., and Yu, V. B., 2013, "Enhancing the Absorption of Graphene in the Terahertz Range," EPL (Europhysics Letters), **101**, p. 58002.

[263] Gao, W., Shu, J., Qiu, C., and Xu, Q., 2012, "Excitation of Plasmonic Waves in Graphene by Guided-Mode Resonances," ACS Nano, **6**, pp. 7806-7813.

[264] Zhan, T. R., Zhao, F. Y., Hu, X. H., Liu, X. H., and Zi, J., 2012, "Band Structure of Plasmons and Optical Absorption Enhancement in Graphene on Subwavelength Dielectric Gratings at Infrared Frequencies," Phys. Rev. B, **86**, p. 165416.

[265] Yao, Y., Shankar, R., Rauter, P., Song, Y., Kong, J., Loncar, M., and Capasso, F., 2014, "High-Responsivity Mid-Infrared Graphene Detectors with Antenna-Enhanced Photocarrier Generation and Collection," Nano Lett., **14**, pp. 3749-3754.

[266] Stauber, T., Gómez-Santos, G., and de Abajo, F. J. G., 2014, "Extraordinary Absorption of Decorated Undoped Graphene," Phys. Rev. Lett., **112**, p. 077401.

[267] Mahdieh, H., Mahmood Hosseini, F., Mortensen, N. A., and Sanshui, X., 2013, "Enhanced Absorption of Graphene in the Visible Region by Use of Plasmonic Nanostructures," J. Opt., **15**, p. 055003.

[268] Zhao, W., Shi, K., and Lu, Z., 2013, "Greatly Enhanced Ultrabroadband Light Absorption by Monolayer Graphene," Opt. Lett., **38**, pp. 4342-4345.

[269] Grande, M., Vincenti, M. A., Stomeo, T., Bianco, G. V., de Ceglia, D., Aközbek, N., Petruzzelli, V., Bruno, G., De Vittorio, M., Scalora, M., and D'Orazio, A., 2014, "Graphene-Based Absorber Exploiting Guided Mode Resonances in One-Dimensional Gratings," Opt. Express, **22**, pp. 31511-31519.

[270] Hu, J.-H., Huang, Y.-Q., Duan, X.-F., Wang, Q., Zhang, X., Wang, J., and Ren, X.-M., 2014, "Enhanced Absorption of Graphene Strips with a Multilayer Subwavelength Grating Structure," Appl. Phys. Lett., **105**, p. 221113.

[271] Piper, J. R., and Fan, S., 2014, "Total Absorption in a Graphene Monolayer in the Optical Regime by Critical Coupling with a Photonic Crystal Guided Resonance," ACS Photonics, **1**, pp. 347-353.

[272] Lim, M., Lee, S. S., and Lee, B. J., 2013, "Near-Field Thermal Radiation between Graphene-Covered Doped Silicon Plates," Opt. Express, **21**, pp. 22173-22185.

[273] Garcia-Vidal, F. J., Sanchez-Dehesa, J., Dechelette, A., Bustarret, E., Lopez-Rios, T., Fournier, T., and Pannetier, B., 1999, "Localized Surface Plasmons in Lamellar Metallic Gratings," J. Lightwave Technol., **17**, pp. 2191-2195.

[274] López-Rios, T., Mendoza, D., García-Vidal, F. J., Sánchez-Dehesa, J., and Pannetier, B., 1998, "Surface Shape Resonances in Lamellar Metallic Gratings," Phys. Rev. Lett., **81**, pp. 665-668.

[275] Chen, J., Wang, P., Zhang, Z. M., Lu, Y., and Ming, H., 2011, "Coupling between Gap Plasmon Polariton and Magnetic Polariton in a Metallic-Dielectric Multilayer Structure," Phys. Rev. E, **84**, p. 026603.

[276] Barnes, W. L., Preist, T. W., Kitson, S. C., and Sambles, J. R., 1996, "Physical Origin of Photonic Energy Gaps in the Propagation of Surface Plasmons on Gratings," Phys. Rev. B, **54**, pp. 6227-6244.

[277] Gan, C. H., Chu, H. S., and Li, E. P., 2012, "Synthesis of Highly Confined Surface Plasmon Modes with Doped Graphene Sheets in the Midinfrared and Terahertz Frequencies," Phys. Rev. B, **85**, p. 125431.

[278] Jablan, M., Soljacic, M., and Buljan, H., 2013, "Plasmons in Graphene: Fundamental Properties and Potential Applications," Proc. IEEE, **101**, pp. 1689-1704.

[279] Low, T., and Avouris, P., 2014, "Graphene Plasmonics for Terahertz to Mid-Infrared Applications," ACS Nano, **8**, pp. 1086-1101.

[280] Chugh, S., Man, M., Chen, Z., and Webb, K. J., 2015, "Ultra-Dark Graphene Stack Metamaterials," Appl. Phys. Lett., **106**, p. 061102.

[281] Brar, V. W., Jang, M. S., Sherrott, M., Lopez, J. J., and Atwater, H. A., 2013, "Highly Confined Tunable Mid-Infrared Plasmonics in Graphene Nanoresonators," Nano Lett., **13**, pp. 2541-2547.

[282] Strait, J. H., Nene, P., Chan, W.-M., Manolatou, C., Tiwari, S., Rana, F., Kevek, J. W., and McEuen, P. L., 2013, "Confined Plasmons in Graphene Microstructures: Experiments and Theory," Phys. Rev. B, **87**, p. 241410.

[283] Yan, H., Low, T., Zhu, W., Wu, Y., Freitag, M., Li, X., Guinea, F., Avouris, P., and Xia, F., 2013, "Damping Pathways of Mid-Infrared Plasmons in Graphene Nanostructures," Nat. Photonics, **7**, pp. 394-399.

[284] Yi, S., Zhou, M., Shi, X., Gan, Q., Zi, J., and Yu, Z., 2015, "A Multiple-Resonator Approach for Broadband Light Absorption in a Single Layer of Nanostructured Graphene," Opt. Express, **23**, pp. 10081-10090.

[285] Koppens, F. H. L., Chang, D. E., and García de Abajo, F. J., 2011, "Graphene Plasmonics: A Platform for Strong Light–Matter Interactions," Nano Lett., **11**, pp. 3370-3377.

[286] Yan, H., Li, X., Chandra, B., Tulevski, G., Wu, Y., Freitag, M., Zhu, W., Avouris, P., and Xia, F., 2012, "Tunable Infrared Plasmonic Devices Using Graphene/Insulator Stacks," Nat. Nanotechnol., **7**, pp. 330-334.

[287] Gao, W., Shi, G., Jin, Z., Shu, J., Zhang, Q., Vajtai, R., Ajayan, P. M., Kono, J., and Xu, Q., 2013, "Excitation and Active Control of Propagating Surface Plasmon Polaritons in Graphene," Nano Lett., **13**, pp. 3698-3702.

[288] Thareja, V., Kang, J.-H., Yuan, H., Milaninia, K. M., Hwang, H. Y., Cui, Y., Kik, P. G., and Brongersma, M. L., 2015, "Electrically Tunable Coherent Optical Absorption in Graphene with Ion Gel," Nano Lett., **15**, pp. 1570-1576.

[289] Papasimakis, N., Luo, Z., Shen, Z. X., De Angelis, F., Di Fabrizio, E., Nikolaenko, A. E., and Zheludev, N. I., 2010, "Graphene in a Photonic Metamaterial," Opt. Express, **18**, pp. 8353-8359.

[290] Gilbertson, A. M., Francescato, Y., Roschuk, T., Shautsova, V., Chen, Y., Sidiropoulos, T. P. H., Hong, M., Giannini, V., Maier, S. A., Cohen, L. F., and Oulton, R. F., 2015, "Plasmon-Induced Optical Anisotropy in Hybrid Graphene–Metal Nanoparticle Systems," Nano Lett., **15**, pp. 3458-3464.

[291] Li, Z., and Yu, N., 2013, "Modulation of Mid-Infrared Light Using Graphene-Metal Plasmonic Antennas," Appl. Phys. Lett., **102**, p. 131108.

[292] Alonso-González, P., Nikitin, A. Y., Golmar, F., Centeno, A., Pesquera, A., Vélez, S., Chen, J., Navickaite, G., Koppens, F., Zurutuza, A., Casanova, F., Hueso, L. E., and Hillenbrand, R., 2014, "Controlling Graphene Plasmons with Resonant Metal Antennas and Spatial Conductivity Patterns," Science, **344**, pp. 1369-1373.

[293] Chen, J., Nesterov, M. L., Nikitin, A. Y., Thongrattanasiri, S., Alonso-González, P., Slipchenko, T. M., Speck, F., Ostler, M., Seyller, T., Crassee, I., Koppens, F. H. L., Martin-Moreno, L., García de Abajo, F. J., Kuzmenko, A. B., and Hillenbrand, R., 2013, "Strong Plasmon Reflection at Nanometer-Size Gaps in Monolayer Graphene on Sic," Nano Lett., **13**, pp. 6210-6215.

[294] Garcia-Pomar, J. L., Nikitin, A. Y., and Martin-Moreno, L., 2013, "Scattering of Graphene Plasmons by Defects in the Graphene Sheet," ACS Nano, **7**, pp. 4988-4994.

[295] Nikitin, A. Y., Low, T., and Martin-Moreno, L., 2014, "Anomalous Reflection Phase of Graphene Plasmons and Its Influence on Resonators," Phys. Rev. B, **90**, p. 041407.

[296] Du, L., Tang, D., and Yuan, X., 2014, "Edge-Reflection Phase Directed Plasmonic Resonances on Graphene Nano-Structures," Opt. Express, **22**, pp. 22689-22698.

[297] Khavasi, A., 2013, "Fast Convergent Fourier Modal Method for the Analysis of Periodic Arrays of Graphene Ribbons," Opt. Lett., **38**, pp. 3009-3012.

[298] Hao, W., Yue, Y., and Liping, W., 2015, "Infrared Frequency-Tunable Coherent Thermal Sources," J. Opt., **17**, p. 045104.

[299] Landy, N. I., Sajuyigbe, S., Mock, J. J., Smith, D. R., and Padilla, W. J., 2008, "Perfect Metamaterial Absorber," Phys. Rev. Lett., **100**, p. 207402.

[300] Feng, R., Ding, W., Liu, L., Chen, L., Qiu, J., and Chen, G., 2014, "Dual-Band Infrared Perfect Absorber Based on Asymmetric T-Shaped Plasmonic Array," Opt. Express, **22**, pp. A335-A343.

[301] Zhao, B., Sakurai, A., and Zhang, Z. M., 2016, "Polarization Dependence of the Reflectance and Transmittance of Anisotropic Metamaterials," J. Thermophys Heat Transfer, **30**, pp. 240-246.

[302] Zhao, Y., and Fu, C., 2016, "Numerical Simulation on the Thermal Radiative Properties of a 2d Sio2/W/Sio2/W Layered Grating for Thermophotovoltaic Applications," J. Quant. Spectrosc. Radiat. Transfer, **182**, pp. 35-44.

[303] Song, J., Si, M., Cheng, Q., and Luo, Z., 2016, "Two-Dimensional Trilayer Grating with a Metal/Insulator/Metal Structure as a Thermophotovoltaic Emitter," Appl. Opt., **55**, pp. 1284-1290.

[304] Liu, X. L., Wang, L. P., and Zhang, Z. M., 2013, "Wideband Tunable Omnidirectional Infrared Absorbers Based on Doped-Silicon Nanowire Arrays," J. Heat Transfer, **135**, pp. 061602-061602.

[305] Nikitin, A., Guinea, F., Garcia-Vidal, F., and Martin-Moreno, L., 2012, "Surface Plasmon Enhanced Absorption and Suppressed Transmission in Periodic Arrays of Graphene Ribbons," Phys. Rev. B, **85**, p. 081405.

[306] Liu, Z., and Aydin, K., 2016, "Localized Surface Plasmons in Nanostructured Monolayer Black Phosphorus," Nano Lett., **16**, pp. 3457-3462.

[307] Zhu, L., Liu, F., Lin, H., Hu, J., Yu, Z., Wang, X., and Fan, S., 2016, "Angle-Selective Perfect Absorption with Two-Dimensional Materials," Light Sci. Appl., **5**, p. e16052.

[308] Liu, Z., Gong, Y., Zhou, W., Ma, L., Yu, J., Idrobo, J. C., Jung, J., MacDonald, A. H., Vajtai, R., Lou, J., and Ajayan, P. M., 2013, "Ultrathin High-Temperature

Oxidation-Resistant Coatings of Hexagonal Boron Nitride," Nat. Commun., **4**, p. 2541.

[309] Chen, Y.-B., and Chiu, F.-C., 2013, "Trapping Mid-Infrared Rays in a Lossy Film with the Berreman Mode, Epsilon near Zero Mode, and Magnetic Polaritons," Opt. Express, **21**, pp. 20771-20785.

[310] Zhao, B., and Zhang, Z. M., 2015, "Strong Plasmonic Coupling between Graphene Ribbon Array and Metal Gratings," ACS Photonics, **2**, pp. 1611-1618.

[311] Ni, G., Li, G., Boriskina, Svetlana V., Li, H., Yang, W., Zhang, T., and Chen, G., 2016, "Steam Generation under One Sun Enabled by a Floating Structure with Thermal concentration," Nat. Energy, **1**, p. 16126.

[312] Zhou, L., Tan, Y., Wang, J., Xu, W., Yuan, Y., Cai, W., Zhu, S., and Zhu, J., 2016, "3d Self-Assembly of Aluminium Nanoparticles for Plasmon-Enhanced Solar Desalination," Nat. Photonics, **10**, pp. 393-398.

[313] Zhou, L., Tan, Y., Ji, D., Zhu, B., Zhang, P., Xu, J., Gan, Q., Yu, Z., and Zhu, J., 2016, "Self-Assembly of Highly Efficient, Broadband Plasmonic Absorbers for Solar Steam Generation," Science Advances, **2**, p. e1501227.

[314] Li, X., Choy, W. C. H., Lu, H., Sha, W. E. I., and Ho, A. H. P., 2013, "Efficiency Enhancement of Organic Solar Cells by Using Shape-Dependent Broadband Plasmonic Absorption in Metallic Nanoparticles," Adv. Funct. Mater., **23**, pp. 2728-2735.

[315] Zhu, J., Yu, Z., Fan, S., and Cui, Y., 2010, "Nanostructured Photon Management for High Performance Solar Cells," Mat. Sci. Eng. R-Reports, **70**, pp. 330-340.

[316] Tsakalakos, L., Balch, J., Fronheiser, J., Shih, M.-Y., LeBoeuf, S. F., Pietrzykowski, M., Codella, P. J., Korevaar, B. A., Sulima, O. V., Rand, J., Davuluru, A., and Rapol, U., 2007, "Strong Broadband Optical Absorption in Silicon Nanowire Films," J. Nanophotonics, **1**, pp. 013552-013552-013510.

[317] Hu, H., Ji, D., Zeng, X., Liu, K., and Gan, Q., 2013, "Rainbow Trapping in Hyperbolic Metamaterial Waveguide," Sci. Rep., **3**, p. 1249.

[318] Ferrari, L., Wu, C., Lepage, D., Zhang, X., and Liu, Z., 2015, "Hyperbolic Metamaterials and Their Applications," Prog. Quant. Electron., **40**, pp. 1-40.

[319] Zhou, J., Kaplan, A. F., Chen, L., and Guo, L. J., 2014, "Experiment and Theory of the Broadband Absorption by a Tapered Hyperbolic Metamaterial Array," ACS Photonics, **1**, pp. 618-624.

[320] Narimanov, E. E., and Kildishev, A. V., 2015, "Metamaterials: Naturally Hyperbolic," Nat. Photonics, **9**, pp. 214-216.

[321] Giles, A. J., Dai, S., Glembocki, O. J., Kretinin, A. V., Sun, Z., Ellis, C. T., Tischler, J. G., Taniguchi, T., Watanabe, K., Fogler, M. M., Novoselov, K. S., Basov, D. N., and Caldwell, J. D., 2016, "Imaging of Anomalous Internal Reflections of Hyperbolic Phonon-Polaritons in Hexagonal Boron Nitride," Nano Lett., **16**, pp. 3858-3865.

[322] Yang, X., Yao, J., Rho, J., Yin, X., and Zhang, X., 2012, "Experimental Realization of Three-Dimensional Indefinite Cavities at the Nanoscale with Anomalous Scaling Laws," Nat. Photonics, **6**, pp. 450-454.

[323] Zhang, X., and Liu, Z., 2008, "Superlenses to Overcome the Diffraction Limit," Nat. Mater., **7**, pp. 435-441.

[324] Chen, K., Santhanam, P., Sandhu, S., Zhu, L., and Fan, S., 2015, "Heat-Flux Control and Solid-State Cooling by Regulating Chemical Potential of Photons in near-Field Electromagnetic Heat Transfer," Phys. Rev. B, **91**, p. 134301.

[325] Ben-Abdallah, P., and Biehs, S.-A., 2014, "Near-Field Thermal Transistor," Phys. Rev. Lett., **112**, p. 044301.

[326] Guo, Y., Cortes, C. L., Molesky, S., and Jacob, Z., 2012, "Broadband Super-Planckian Thermal Emission from Hyperbolic Metamaterials," Appl. Phys. Lett., **101**, p. 131106.

[327] Xu, M., Liang, T., Shi, M., and Chen, H., 2013, "Graphene-Like Two-Dimensional Materials," Chem. Rev., **113**, pp. 3766-3798.

[328] Ilic, O., Jablan, M., Joannopoulos, J. D., Celanovic, I., Buljan, H., and Soljačić, M., 2012, "Near-Field Thermal Radiation Transfer Controlled by Plasmons in Graphene," Phys. Rev. B, **85**, p. 155422.

[329] Drosdoff, D., Phan, A. D., and Woods, L. M., 2014, "Transverse Electric Mode for near-Field Radiative Heat Transfer in Graphene–Metamaterial Systems," Adv. Opt. Mater., **2**, pp. 1038-1042.

[330] Liu, X. L., and Zhang, Z. M., 2015, "Giant Enhancement of Nanoscale Thermal Radiation Based on Hyperbolic Graphene Plasmons," Appl. Phys. Lett., **107**, p. 143114.

[331] Dubois, L. H., Schwartz, G. P., Camley, R. E., and Mills, D. L., 1984, "Inelastic Scattering of Electrons from Ionic Crystals with a Highly Conducting Overlayer," Phys. Rev. B, **29**, pp. 3208-3216.

[332] Messina, R., Hugonin, J.-P., Greffet, J.-J., Marquier, F., De Wilde, Y., Belarouci, A., Frechette, L., Cordier, Y., and Ben-Abdallah, P., 2013, "Tuning the Electromagnetic Local Density of States in Graphene-Covered Systems Via Strong Coupling with Graphene Plasmons," Phys. Rev. B, **87**, p. 085421.

[333] Jones, A. C., O'Callahan, B. T., Yang, H. U., and Raschke, M. B., 2013, "The Thermal near-Field: Coherence, Spectroscopy, Heat-Transfer, and Optical Forces," Prog. Surf. Sci., **88**, pp. 349-392.

[334] Liu, X. L., and Zhang, Z. M., 2014, "Graphene-Assisted near-Field Radiative Heat Transfer between Corrugated Polar Materials," Appl. Phys. Lett., **104**, p. 251911.

[335] Bright, T. J., Liu, X. L., and Zhang, Z. M., 2014, "Energy Streamlines in near-Field Radiative Heat Transfer between Hyperbolic Metamaterials," Opt. Express, **22**, pp. A1112-A1127.

VITA

BO ZHAO

Bo Zhao was born in Shuozhou, Shanxi Province, China in 1989. He received his Bachelor's degree from the University of Science and Technology of China in 2011 with a best thesis award. Afterward, he joined Professor Zhuomin Zhang's group in Mechanical Engineering at Georgia Institute of Technology. His research is concentrated on near- and far-field thermal radiation, plasmonics, electromagnetic metamaterials, and radiative properties of 2D materials. During his Ph.D., he coauthored 15 journal publications with more than 200 citations according to Google Scholar. His work on graphene was entitled the top downloads of the Optical Society (OSA) in June 2015. He has given over ten conference presentations and several invited talks and received the best poster award in 2013 ASME International Mechanical Engineering Congress & Exposition. He is a reviewer for *Nature Communications*, *Optics Express*, *Optics Letters*, *Journal of Quantitative Spectroscopy and Radiative Transfer*, *Journal of Applied Physics*, and *Materials Research Express*. He is a student member of the American Society of Mechanical Engineers (ASME), the American Institute of Aeronautics and Astronautics (AIAA), and the Optical Society.

In addition to the research experience, Bo Zhao has worked as a lead graduate teaching assistant for the thermal-fluids labs of ME4056 Mechanical Engineering System Laboratory since Fall 2014. He has also taught the fundamentals of nanoscale radiative heat transfer in ME4803/6309A Nanoscale Heat Transfer (graduate level) in Spring 2016. His teaching was highly recognized by students.